DOE/MC/11580-5

DOE/MC/11580-5
DE82 000896

FOSSIL ENERGY

EFFECTS OF POROSITY TYPE, PORE GEOMETRY, AND DIAGENETIC HISTORY ON TERTIARY RECOVERY OF PETROLEUM FROM CARBONATE RESERVOIRS

Final Report
July 1, 1979—Nov. 30, 1980

Work Performed for the Department of Energy
Under Contract No. DE-AC21-79MC11580

Date Published—September 1981

Rensselaer Polytechnic Institute
Troy, New York

U. S. DEPARTMENT OF ENERGY

DISCLAIMER

"This book was prepared as an account of work sponsored by an agency of the United States Government. Neither the United States Government nor any agency thereof, nor any of their employees, makes any warranty, express or implied, or assumes any legal liability or responsibility for the accuracy, completeness, or usefulness of any information, apparatus, product, or process disclosed, or represents that its use would not infringe privately owned rights. Reference herein to any specific commercial product, process, or service by trade name, trademark, manufacturer, or otherwise, does not necessarily constitute or imply its endorsement, recommendation, or favoring by the United States Government or any agency thereof. The views and opinions of authors expressed herein do not necessarily state or reflect those of the United States Government or any agency thereof."

Available from the National Technical Information Service, U.S. Department of Commerce, Springfield, Virginia 22161.

NTIS price codes
Paper copy: $18.50
Microfiche copy: $3.50

DOE/MC/11580-5
Distribution Category UC-92a

EFFECTS OF POROSITY TYPE, PORE GEOMETRY, AND DIAGENETIC HISTORY ON TERTIARY RECOVERY OF PETROLEUM FROM CARBONATE RESERVOIRS

Final Report
July 1, 1979—Nov. 30, 1980

Gerald M. Friedman, Kenneth Ruzyla, and
Anne Reeckmann, *Principal Investigators*
Rensselaer Polytechnic Institute
Office of Contracts and Grants
Troy, New York 12181

Royal J. Watts, *Technical Project Officer*
Morgantown Energy Technology Center
P.O. Box 880
Morgantown, West Virginia 26505

Work Performed for the Department of Energy
Under Contract No. DE-AC21-79MC11580

Date Published—September 1981

UNITED STATES DEPARTMENT OF ENERGY

CONTENTS

	Page
ACKNOWLEDGEMENTS	vii
ABSTRACT	viii
INTRODUCTION	1
PREVIOUS INVESTIGATIONS	4
METHODS OF INVESTIGATION	11
DESCRIPTION OF STUDY AREA	13
STRATIGRAPHY	18
Winnipeg Formation	18
Red River Formation	18
Stony Mountain Formation	22
LITHOFACIES	24
Lithofacies 1	24
Lithofacies 2	27
Lithofacies 3	27
Lithofacies 4	28
Lithofacies 5	29
Lithofacies 6	29
DEPOSITIONAL ENVIRONMENTS	35
Subtidal Zone	35
Intertidal Zone	38
Supratidal Zone	41
Depositional Cycles in the Upper Red River Formation	42

	Page
Regional Depositional Evironments	45
Origin of Laminae in Supratidal Dolostones	47
DIAGENESIS	50
Vadose Leaching	50
Dolomitization	54
Anhydrite Cementation	64
Silica Cementation	67
Pressure Solution	71
DISTRIBUTION OF POROSITY WITHIN UPPER RED RIVER RESERVOIRS	73
Porosity Types and Associations	73
Vertical Distribution of Porosity	78
Lateral Distribution of Porosity	82
PORE GEOMETRY FROM CAPILLARY-PRESSURE CURVES	91
Pore-throat Geometry of U4 Reservoir Rocks	92
Pore-throat Geometry of U6 Reservoir Rocks	100
QUALITATIVE OBSERVATIONS OF PORE GEOMETRY	103
Pore Geometry From Thin Sections	103
Pore Geometry From Resin Casts	104
Summary and Discussion	110
PETROPHYSICAL RELATIONSHIPS OF UPPER RED RIVER RESERVOIRS	128
Permeability Versus Porosity	128
Permeability Versus Mean Throat Size	129
Porosity Versus Mean Throat Size	135
Influence of Lithology and Depositional Environment on Reservoir Petrophysics	139

Page

DIAGENETIC CONTROLS ON THE DEVELOPMENT AND GEOMETRY OF UPPER RED RIVER PORE SYSTEMS 142

Pore System Development 142

Pore Geometry as an Index to Carbonate Reservoir Characteristics 147

CONCLUSIONS 156

LITERATURE CITED 158

APPENDIX 163

FIGURES

	Page
Figure 1	3
Figure 2	15
Figure 3	16
Figure 4	23
Figure 5	26
Figure 6	32
Figure 7	34
Figure 8	36
Figure 9	40
Figure 10	43
Figure 11	53
Figure 12	60
Figure 13	62
Figure 14	66
Figure 15	70
Figure 16	77
Figure 17	83
Figure 18	84
Figure 19	85
Figure 20	86
Figure 21	98
Figure 22	99
Figure 23	113
Figure 24	115
Figure 25	117
Figure 26	119
Figure 27	121
Figure 28	123
Figure 29	125
Figure 30	127
Figure 31	130
Figure 32	131
Figure 33	132
Figure 34	133
Figure 35	134
Figure 36	136
Figure 37	137
Figure 38	138
Figure 39	143
Figure 40	148
Figure 41	151
Figure 42	152
Figure A-0	165
Figure A-1	170
Figure A-2	171
Figure A-3	172
Figure A-4	173
Figure A-5	174
Figure A-6	175
Figure A-7	176
Figure A-8	177
Figure A-9	178

Figure A-10 179
Figure A-11 180
Figure A-12 181
Figure A-13 182
Figure A-14 183
Figure A-15 184
Figure A-16 185
Figure A-17 186
Figure A-18 187
Figure A-19 188
Figure A-20 189
Figure 1-A 200
Figure 2-A 201
Figure 2-A Supplement 202
Figure 3-A 203
Figure 4-A 204
Figure 5-A 205
Figure 6-A 206
Figure 6-A Supplement 207
Figure 7-A 208
Figure 7-A Supplement 209
Figure 8-A 210
Figure 9-A 211
Figure 10-A 212
Figure 11-A 213
Figure 12-A 214
Figure 13-A 215
Overlays for location maps 216, 217

TABLES

Table 1 25
Table 2 37
Table 3 74
Table 4 93
Table 5 94
Table 6 144
Table 7 153
Table 8 153
Table 1-A 193
Table 2-A 195
Table 3-A 197

ACKNOWLEDGEMENTS

Funding for this study was provided by the United States Department of Energy under contract number DE-AC21-79MC11580. The author wishes to express his appreciation to Dr. Gerald M. Friedman for his guidance in initiating this research and for his constructive criticism. Additional comments and suggestions were provided by Anne Reeckmann. I gratefully acknowledge the Shell Oil Company, and especially Frank E. Coupal, for generous cooperation in providing the cores and additional materials necessary for this study. James H. Clement of Shell Oil Company was most helpful in providing cores and in initiating this research. Pressure-chamber equipment for impregnation work was provided by Barker Air & Hydraulic Division, and designed by Wyatt B. Strickland.

ABSTRACT

The Upper Ordovician Red River Formation at Cabin Creek Field, Montana, consists of several carbonate peritidal sequences deposited on a broad, shallow-marine, carbonate bank under arid conditions. Sediments of the upper part of the Red River Formation were deposited as shoaling-upwards cycles which display diagenetic overprinting. Cabin Creek is one of many fields located on the Cedar Creek Anticline, a linear feature, 100 miles long, which lies along the southwest margin of the Williston Basin. The upper Red River Formation is about 150 feet thick and is composed of alternating limestone and dolostone, units U1 through U6; these units are stratigraphically equivalent to the Herald Formation and to the A, B, and C zones used widely by industry operators. Oil production is from the U2, U4, and U6 dolstones. The interstratified U1, U3, and U5 limestone units are non-productive. Six lithofacies are recognized in the upper Red River Formation of Cabin Creek Field: (1) mottled dolomitic biomicrite-wackestone to packstone, (2) mottled dolomitic biomicrite-mudstone, (3) finely crystalline dolomite, (4) microcrystalline dolomite, (5) skeletal dolomite, and (6) laminated black shale stringers.

The predominant pore types are vug, moldic, interparticle, and intercrystal. Vug pores originated in supratidal sediments as a result of vadose leaching of evaporitic sulfate minerals. Moldic porosity occurs most abundantly in the intertidal and subtidal zones, and resulted from leaching of calcium-carbonate grains remaining after

dolomitization of matrix material. Moldic pores also developed by leaching of gypsum crystals in the phreatic zone. Interparticle porosity is of primary origin and occurs most commonly in intertidal and lower supratidal zones. Intercrystal porosity resulting from pervasive dolomitization is best developed in the uppermost part of the U6 subtidal zone. Porosity was occluded locally by late diagenetic anhydrite and silica cements.

Pore geometry of the upper Red River carbonate reservoirs is a function of depositional environment and diagenetic history. The size, shape, and sorting of pores is related to porosity type. Geometry of pore throats is primarily a function of the size and shape of dolomite crystals composing the matrix of the reservoir rock. Study of petrographic thin sections, mercury capillary-pressure curves, and resin pore casts showed that several different types of pore systems occur and that each is associated with particular depositional environments and diagenetic regimes.

An important relationship was established between porosity and pore geometry. Mean pore-throat size, a statistical measure of pore geometry, was found to increase as percent porosity increases, depending on reservoir rock type. Using this relationship and electric log porosity values, it is possible to predict pore geometry and, as a consequence, recovery efficiency, if lithofacies distribution, porosity type, and diagenetic history are known for the reservoir. Residual oil saturation caused by capillary forces is strongly dependent on the pore

system characteristics of the reservoir rock. This approach to predicting reservoir pore geometry is thus capable of identifying areas of potentially high residual oil saturation which can be targeted for enhanced recovery.

INTRODUCTION

The objective of this study is to determine the mechanisms controlling porosity in Red River Formation (Upper Ordovician) carbonate reservoirs, and to determine what types of pore systems result from a given set of depositional and diagenetic conditions. The term pore system refers to the total void space in a reservoir rock, which consists of larger spaces, referred to as pores, connected by smaller spaces, which are referred to as throats. The geometry of pore systems have a great effect on reservoir characteristics, or stated another way, the reservoir characteristics of any rock depend on how the pores are interconnected. In order to determine the reservoir characteristics of a stratigraphic unit with regard to either primary or enhanced recovery, it is necessary to know the pore-system geometry and to determine its continuity across the field. However, in order to predict pore geometry and determine the distribution of reservoir characteristics within any oil field, it is necessary to establish relationships between pore geometry and petrophysical parameters applicable to the study of electric logs, since cores are usually cut in only a few selected wells of any given field. Geological trends, such as lithofacies, depositional environments and diagenetic regimes must also be established to permit interpolation of data between existing well control.

The formation under study is the Red River Formation (Upper Ordovician) of Cabin Creek Field, a producing oil field located in southeast Montana (Figure 1). This particular field and formation were chosen mostly on account of the availability of cores and other data. Drilling density provides enough control for stratigraphic correlation and mapping data. The Red River Formation is a major oil-producing reservoir in the area and Cabin Creek Field is a good candidate to undergo tertiary recovery in the future.

The first sections of this paper discuss the stratigraphy, distribution of lithofacies, depositional environments, and diagenesis of the study area. The section on distribution of porosity discusses the various types of porosity present, their origin, how they are distributed throughout the upper Red River reservoirs, and how they relate to depositional environment. Size and shape of pores and pore throats are discussed in the sections on pore geometry, first in terms of statistical measures from capillary-pressure curves, then by interpretation of scanning-electron micrographs of resin-pore casts. The last two sections discuss petrophysical relationships, diagenetic controls on the development and geometry of pore systems, and the role of pore geometry in the determination of carbonate reservoir characteristics.

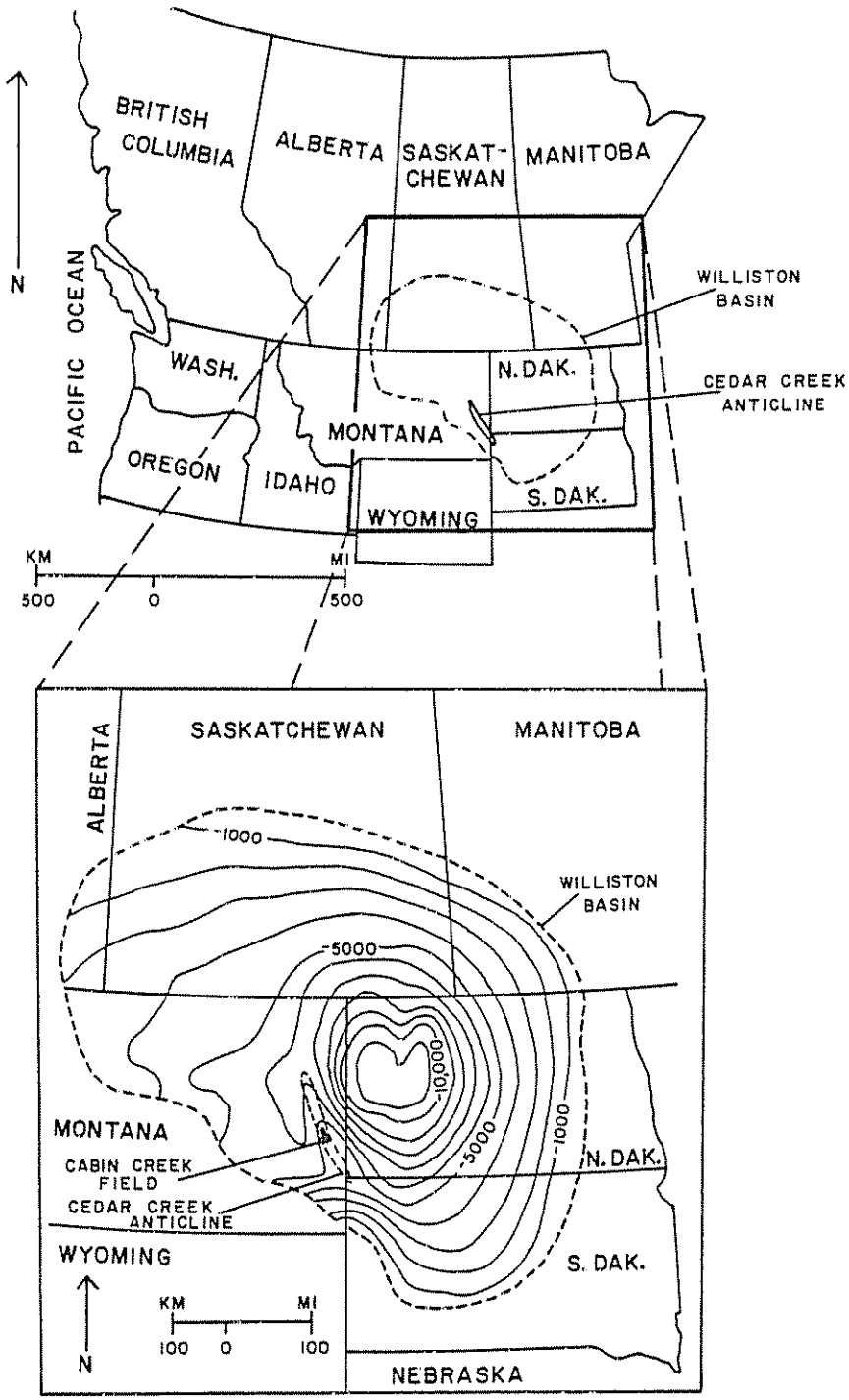

FIGURE 1. Location maps showing Williston Basin, Cedar Creek Anticline, and Cabin Creek Field. Lower map includes regional structure contours of the top of the Red River Formation. Contour interval is 1000 feet.

PREVIOUS INVESTIGATIONS

Heterogeneity of Porosity In Carbonate Reservoirs

Recognition of rapid lateral variations of porosity within carbonate reservoirs and the need to predict the type of porosity or permeability expected under operative geologic conditions was emphasized by Imbt and Ellison (1946). Dowling (1970) related dolomitic reservoir porosity and permeability to depositional environment for the Monahans Clearfork Field, Texas. He pointed out that the lack of knowledge of porosity heterogeneity of this field seriously hampered secondary recovery operation.

The fact that the distribution of porosity and permeability within carbonate reservoirs can vary greatly over short distances both laterally and vertically was shown by Jardine et al (1977) and also Reitzel and Callow (1977). Wayhan and McCaleb (1969) have discussed such heterogeneity in the Madison limestone reservoir of Elk Basin Field, Montana and Wyoming. They concluded that porosity zonation resulted from (1) differential depositional environments, (2) variations in the degree of dolomitization, (3) later erosion and solution of the reservoir rocks, and (4) various amounts of ground-water leaching and remineralization. They also concluded that it is first necessary to understand reservoir geology and heterogeneities before reservoir performance can be understood.

Gvirtzman and Friedman (1977) studied the effects of diagenetic trends on porosity distribution in modern and Pleistocene carbonate reefs of the Red Sea. They recognized several diagenetic stages affecting porosity. Cussey and Friedman (1977) reported on carbonate porosity heterogeneity in the Chailly Oil Field of France. Primary porosity has been preserved in parts of this field, but in other parts the pore space has been obliterated due to either (1) pressure solution with its attendant reduction of porosity and generation of cement, or (2) fresh-water cementation in the phreatic zone below the ground water table. Porosity heterogeneity in the Chailly reservoir can thus be explained in relation to variations of depositional environment and stages of diagenesis.

Depositional and diagenetic controls on upper Red River Formation porosity development in North Dakota were investigated by Carroll (1978). He concluded that porosity development was favored by high topography which exposed sediment to dolomitization in the supratidal zone. Kohm and Louden (1978) concluded that all Red River porosity in eastern Montana and western North Dakota is related to diagenetic dolomitization. They also found that despite occurrence of persistent, laterally continuous depositional lithofacies, abrupt lateral changes in dolomitization and porosity can occur.

Pore Geometry and Classification of Pore Systems

The relation for determining the distribution of pore sizes in a porous material via mercury capillary-pressure was developed by Washburn (1921). Thomeer (1960) developed a mathematical description of capillary-pressure curves which reflects differences in pore geometry of samples. This technique is based on the observation that graphical location and shape of a capillary-pressure curve reflect pore-structure characteristics of the rock sample.

Important aspects of pore geometry as determined by capillary-pressure data in carbonate reservoirs were summarized by Stout (1964). He classified Williston Basin carbonate-reservoir rocks on the basis of pore-size distribution and reservoir properties. A method of determining the distribution of pore volume by both pore and throat diameters was developed by Dullien and Dhawan (1974 and 1975), who concluded that pore throats contribute very little to the total pore volume of a reservoir rock. The pore geometry of carbonate rocks as revealed by pore casts and capillary-pressure data has been discussed by Wardlaw (1976). He concluded that pore connections in dolomites are sheet-like rather than tubular, and that pore geometry is related to the manner in which growth of dolomite crystals occurs. Wardlaw and Taylor (1976) have evaluated various factors that influence the form of mercury capillary-pressure curves and define the extent to which the form of the curves can be used to interpret pore and throat geometry. They also considered idealized, model pore systems as a means of illustrating the influence of pore and throat geometry on the form of capillary-pressure curves.

Aschenbrenner and Achauer (1960) attempted to classify carbonate pore space, as observed in thin section, according to shape, size and types of interconnections. They also attempted to define maximum conditions for migration of oil in water-wet carbonate rocks based on pore-space type. They concluded that minimum conditions for migration through carbonates seem to be determined to a large degree by the prevailing pore-space type. In cases where a great difference exists between pore and throat dimensions, the small size of the latter is inherent and conditions for migration were found to be least favorable.

Robinson (1966) classified reservoir rock pore-size distribution using the following three parameters from mercury capillary-pressure curves: (1) pore-entry pressure, (2) minimum unsaturated pore volume, and (3) a geological description of the curve taken to be a measure of pore sorting. He found a good correlation between textural types and reservoir properties. Saccharoidal dolomite, composed of euhedral to subhedral crystals and having well-sorted intercrystalline pore space, was found to have optimum reservoir properties.

Pickett and Artus (1970) found that the ratio of air permeability to porosity, K/Ø, was a useful parameter for classifying rock types by pore size in the case of the upper Red River reservoirs at Pennel Field, Montana, as demonstrated by a plot of K/Ø ratio versus capillary pressure, a measure of pore size. They also devised a method for estimating K/Ø ratios from logs in uncored wells, and for predicting the quantity of recoverable oil by primary depletion.

Effects of Pore Geometry on Reservoir Properties

The applications of capillary-pressure data in the determination of distribution and mobility of carbonate reservoir fluids were summarized by Aufricht and Koept (1957). They attempted to find a correlation betwen interstitial water, as a function of permeability and porosity, and gross porosity types over a wide area. Lack of such correlation was attributed to the wide range in carbonate pore geometry.

Pickell et al (1966) gave evidence to show that the fluid distribution in a porous medium is a function of pore-size distribution, pore configurations, interfacial properties, and previous saturation history. They also showed that residual non-wetting phase saturations are a function of both pore geometry and initial saturation. Thus, pore geometry was determined to be an important parameter for reliable estimation of recoverable reserves. It was found that in most cases residual saturations determined from capillary-pressure data reasonably approximate residual oil saturation following waterflood of a strongly water-wet medium.

Jordy (1972) investigated the relationship between carbonate rock types and families of capillary-pressure curves. He concluded that the pore geometry of carbonate rocks is as important as porosity and permeability in determining the reservoir potential of the rock. He also pointed out that reservoir characteristics must be determined by identifying the depositional or diagenetic processes that create large pore throats and then locating areas where such processes were active.

The influence of rock and fluid properties on the magnitude of irreducible saturations was experimentally determined by Morrow (1970 and 1971). He concluded that the magnitude of irreducible saturation is an index of packing heterogeneity, or local variation in pore-size distribution, which may reflect depositional environment and post-depositional history. In particular, residual oil saturation is important because it is one of the factors that limits the amount of oil displaced during a waterflood.

Melrose and Brandner (1974) reviewed factors controlling the distribution of immiscible fluids, such as oil and water, within the interstices of a porous solid. One such factor is small-scale packing heterogeneity, which if present in a reservoir rock, increases the magnitude of residual wetting phase saturation. They also indicate that experimental results for various porous systems clearly show that the broader the pore-size distribution, the larger the residual non-wetting phase saturation.

The effects of pore system properties on recovery efficiency were investigated by Wardlaw and Cassan (1978). They believe that pore-to-throat size ratio, throat-to-pore coordination number, or the number of throats that connect with each pore, type and degree of heterogeneity, and surface roughness are important factors affecting recovery efficiency. On the basis of these characteristics, they proposed a scheme for estimation of recovery efficiency from visual observations made from resin pore casts of carbonate-reservoir rocks. Their main conclusion was that non-wetting-phase trapping caused by capillary forces is

strongly dependent on the characteristics of the pore system of a reservoir rock. They also concluded that samples of high porosity with pores and throats of relatively uniform size and low pore-to-throat size ratio exhibit high recovery efficiencies, and that samples having large pores with large pore-to-throat size ratios exhibit low recovery efficiencies.

METHODS OF INVESTIGATION

Approximately 1450 feet of upper Red River Formation core from 12 different wells was studied. Selected pieces of core slab were polished with abrasive grit, then etched in dilute hydrochloric acid to enhance sedimentary structures and aid in identification of particles and matrix material by binocular microscope inspection. Staining methods described by Friedman (1959) were used to aid in mineralogical determination. Alizarine Red-S was routinely applied to distinguish calcite from dolomite.

Samples for thin sectioning were taken at approximately 3 to 4 foot intervals within oil-producing zones, and in selected parts of the nonproducing intervals. Thin-section preparation was done by commercial petrographic lab. Finished thin sections were stained with Alizarine Red-S and examined with a petrographic microscope for mineralogy, petrography, and porosity characteristics. Point-counting methods were used to determine relative amounts of each pore type, average pore size (longest dimension), and pore shape. A visual estimate was made of the pore sorting.

In order to determine the three-dimension geometry of pore-throat systems in the upper Red River reservoirs, pore casts were prepared by plastic impregnation of approximately 70 selected samples. A representative suite of samples was chosen to include all of the various porosity types, as well as a diversity of porosity percents and permeability values. Liquid resin was forced into the pore space of the

samples under 1200 psi pressure and allowed to harden. Samples were then placed in very dilute hydrochloric acid for several days to dissolve the host rock (dolomite), leaving only the plastic cast of the pore space. Pore casts were examined under a binocular microscope. Eight casts and their corresponding rock specimens were selected for further study with a scanning electron microscope.

The instrument used was a Japan Electron Optics Laboratory Co., Ltd., type JSM, U2, scanning electron microscope. Each sample was mounted on a carbon planchet and coated with approximately 200 A of gold in order to insure sample conductivity. Scanning electron micrographs were taken at 6000X, 2800X, 1600X, 1100X, 600X and 300X magnifications to exhibit the surface morphology of each sample.

Porosity values were obtained from neutron logs, and core-plug analysis reports supplied by Shell Oil Company. Values of permeability, water saturation, and oil saturation were also obtained from the core analysis reports. Capillary-pressure curves, also supplied by Shell Oil Company, were used to obtain pore geometry data as described in the Appendix.

DESCRIPTION OF STUDY AREA

The Upper Ordovician Red River Formation at Cabin Creek Field, Montana, consists of several carbonate peritidal sequences whose porosity depends mostly on dolomitization. Diagenetic processes, including dolomitization, were greatly influenced by depositional environment. Porous lithofacies are laminated finely crystalline dolomite, laminated microcrystalline dolomite, and skeletal dolomite. Non-porous lithofacies are shale stringers, dolomitic biomicrite-wackestone to packstone, and dolomitic biomicrite-mudstone.

Cabin Creek Field, discovered in 1953 by seismic methods, is located along the southwest margin of the Williston Basin, Montana (Figure 1). The Williston Basin is a wide, circular, indistinctly bounded, shallow depression on the southwestern side of the Canadian Shield (Fuller, 1961). At the basin center, Lower Paleozoic rocks attain maximum thickness in excess of 3000 feet and are overlain by about 12,000 feet of Upper Paleozoic, Mesozoic, and Tertiary deposits.

Structurally, Cabin Creek is part of the Cedar Creek Anticline, an asymmetrical, remarkably straight, 100 mile-long feature which came into existence in the early Paleozoic, apparently as a result of basement faulting (Roehl, 1967). Subsequent periods of uplift have occurred at the following times: pre-Mississippian-post-Silurian, Mississippian-Triassic, and post-Paleocene. The anticline is accentuated by northwest-southeast linear faulting. The fold is asymmetrical with the

steeper side to the southwest. The axis of the anticline rises and falls along its length, creating a series of nodes and antinodes. Figure 2 is a structure contour map of Cabin Creek Field.

Previous studies indicate that oil migration from Ordovician source-rocks began in the middle Late Cretaceous, and that accumulation was controlled by paleostructural closures, faulting, geomorphology, facies variations, and hydrodynamic conditions (Clement, 1976). According to Williams (1974), the Winnipeg Shale (Middle Ordovician) is the most probable source of oil in the Red River Formation (Figure 3). This is because the soluble organic matter extracted from the Winnipeg Shale correlates with Red River oil, as well as most other lower Paleozoic oil in the Williston Basin. However, the Winnipeg Shale lies stratigraphically below impermeable limestones of the Red River Formation, and any oil originating in Winnipeg source rocks must have been emplaced in the Red River by vertical migration through fracture systems (Dow, 1974). A more likely source of oil was indigenous stromatolites of the Red River peritidal sequences. Such indigenous source rocks eliminate the problem of vertical migration through impermeable rock.

Within the field area, the Red River Formation averages about 500 feet in thickness and consists of a sequence of alternating limestones and dolostones. Production is from the U2, U4, and U6 dolostone units in the upper 150 feet of the Red River Formation, which is stratigraphically equivalent to the A through C zones used widely by industry operators of the Williston Basin (Clement, 1978); and also

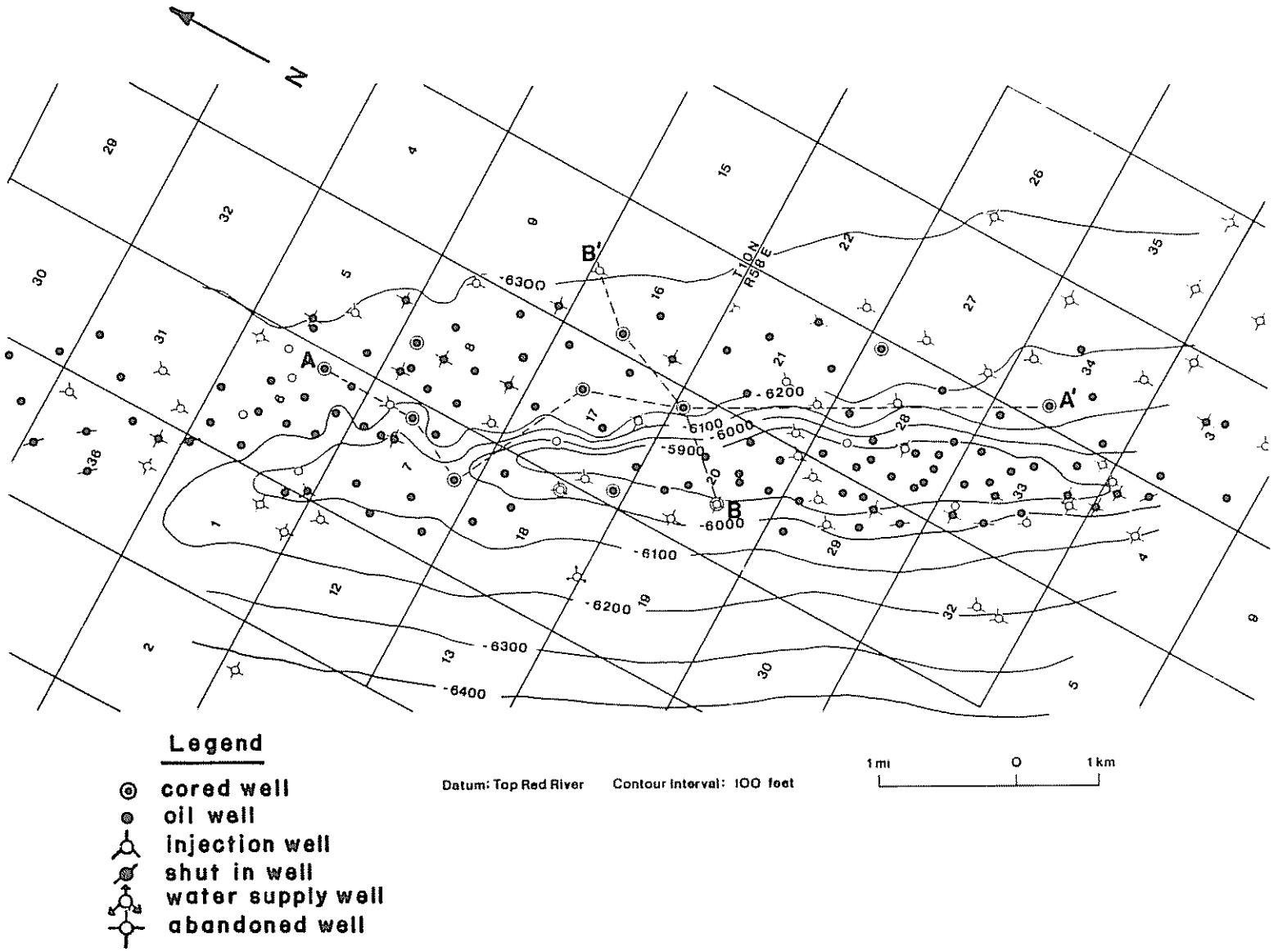

FIGURE 2. Structure contour map of Cabin Creek Field.

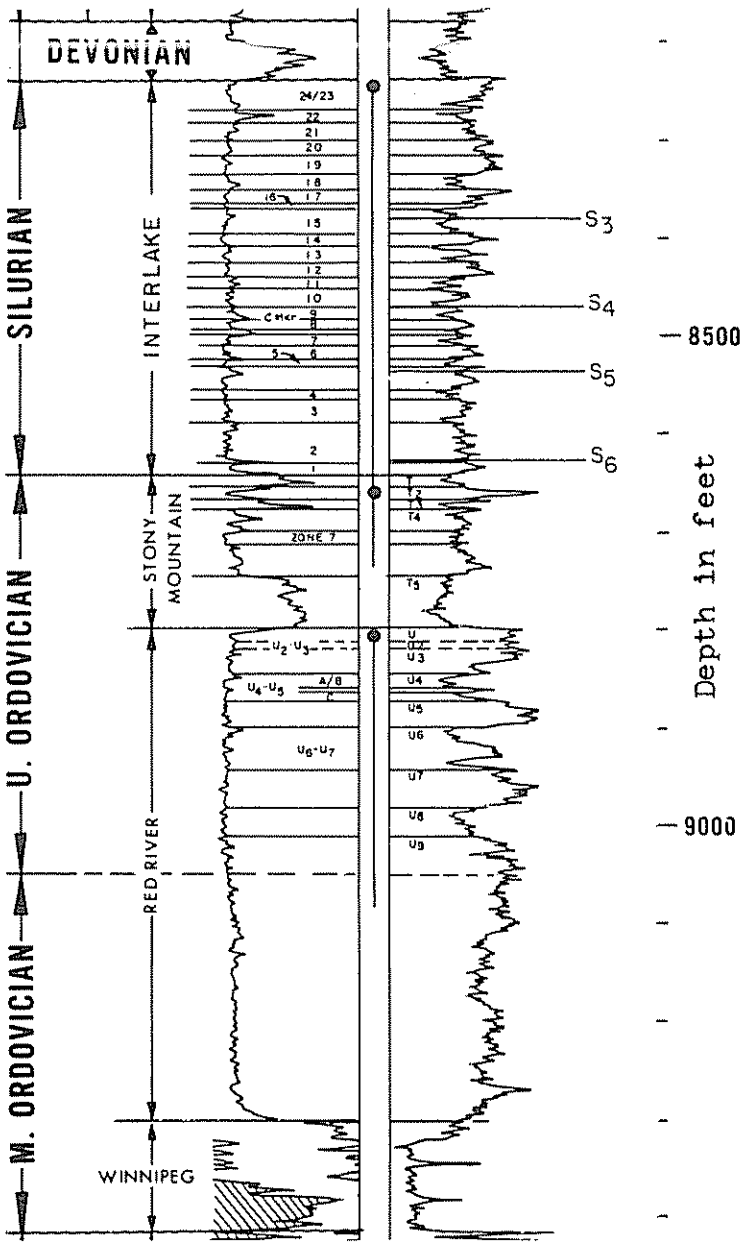

FIGURE 3. Type radioactivity log of Lower Paleozoic formations, Cedar Creek Anticline, Montana.

equivalent to the Herald Formation (Kendall, 1976). The interstratified U1, U3 and U5 limestone units are non-productive. Lateral and vertical variations of dolomitization are mostly responsible for variations in reservoir properties and effective pay thicknesses (Clement, 1978).

Red River production is commingled with Silurian productive intervals. Combined Ordovician and Silurian reservoir production is 61,574,000 barrels of oil as of September 1979, with reserves of 13,624,000 barrels. The field has been on waterflood since April 1964, and is considered to be a good candidate for tertiary recovery by carbon dioxide miscible process.

STRATIGRAPHY

Winnipeg Formation

The Winnipeg Formation (Middle Ordovician) underlies the Red River Formation. The Winnipeg Formation consists of a quartz-sandstone and shale series about 110 feet in thickness (Porter and Fuller, 1959). The sandstones occur in the lower part and are well sorted and cross-bedded. Thin siltstones and shales occur mainly in the upper part and are typically bluish green and pyritic. The contact between the Red River Formation and the underlying Winnipeg Formation is abrupt but conformable.

Red River Formation

Lower Red River

The lower part of the Red River Formation is about 350 feet thick and is a gray and brown mottled, bioturbated, dolomitic, fossiliferous wackestone and mudstone (Kohm and Louden, 1978). Fragmented brachiopods, bryozoa, crinoids, trilobites, and cephalopods are common and indicate normal marine salinities. The lower Red River is stratigraphically equivalent to the Yeoman Formation (Kendall, 1976).

Upper Red River

U6 dolostone. The U6 dolostone abruptly underlies the U5 limestone and is about 55 feet thick. This unit consists of microcrystalline dolomite (less than 10 micron size) in the upper part and skeletal dolomite in the lower part. A thick black shale locally lies at the top of the U6 dolostone. In places, this shale is found to contain a flat pebble conglomerate or breccia. The upper part of the U6 contains rare skeletal remains, abundant wavy laminae, anhydrite, solution breccias, and locally abundant relict pellets. Downward, the U6 becomes cross-bedded and contains abundant peloids, intraclasts, ooids, bedded and imbricate shell debris. The lower part of the U6 consists of massive, burrowed, skeletal dolomite containing local beds of limestone (biomicrite-wackestone).

U5 limestone. The U5 limestone is about 35 feet thick and conformably underlies the U4 dolostone. It consists of biomicrite-wackestone. The upper part of the U5 limestone is massive and contains abundant burrows, dolomitic mottling, and locally distributed imbricate shells. Dolomitic mottling decreases downward. Stylolites occur throughout the U5 and generally have horizontal orientation. The base of the U5 contains abundant peloids, intraclasts, bedded and imbricate shell debris, and is locally crossbedded.

U4 dolostone. The U4 dolostone is about 20 feet thick and abruptly underlies the U3 limestone. It consists of finely crystalline dolomite (10-60 micron size) in the upper part and skeletal dolomite in the lower part. A thin, black, finely laminated shale occurs locally at the top

of the U4 dolostone. The upper part of the U4 contains rare skeletal remains, local concentrations of relict pellets, locally distributed flat-pebble breccias and conglomerates, abundant wavy laminae, nodular anhydrite, solution breccias, desiccation cracks, and stylolites. Downward, the U4 becomes massive, with local cross-bedding and ripple bedding; and contains intraclasts, peloids, bedded and imbricate shell debris, and conglomerates. The lower part of the U4 dolostone is massive and contains abundant skeletal remains, burrows, chert nodules, and anhydrite nodules. A bed of limestone (biomicrite-wackestone) occurs locally in the lower part of the U4, and is up to 8 feet thick.

U3 limestone. The U3 limestone is about 20 feet thick and conformably underlies the U4 dolostone. It consists of biomicrite-wackestone very similar to the U5 limestone. The upper part of the U3 limestone is massive with abundant dolomitic mottling. It contains peloids, intraclasts, imbricate brachiopod shells, and locally exhibits cross-bedding and graded bedding. Downward, the U3 becomes intensely burrowed. The base of the U3 limestone contains structures similar to those in the upper part: local graded bedding, bedded and imbricate shell debris. Abundant peloids and intraclasts, and scattered concentrations of ooids occur in the lower part of the U3 limestone. Stylolites are common throughout the U3 limestone.

U2 dolostone. The U2 dolostone is about 6 feet thick and underlies the U1 limestone. It consists of finely crystalline dolomite (10-60 micron size), skeletal dolomite, and dolomitic biomicrite-mudstone. The upper part of the U2 dolostone contains rare skeletal remains, abundant

wavy laminae, locally distributed flat pebble conglomerates, truncation surfaces, nodular anhydrite, oncolites, and solution breccias. The U2 becomes massive downward. The lower part of the U2 contains locally abundant peloids and intraclasts. Burrows, chert nodules, anhydrite nodules, cross-bedding, and bedded skeletal debris are common in the lower U2. Horizontal stylolite surfaces are common throughout the U2. The base of the U2 is transitional with the underlying U3 limestone.

U1 limestone. The U1 limestone is about 25 feet thick and consists of biomicrite-wackestone very similar to the U3 and U5 limestones. Skeletal debris is composed of echinoderm, brachiopod, bryozoa, trilobite, mollusk, ostracod, and gastropod remains. Matrix material is generally structureless micrite with locally preserved pelletal fabric. The entire U1 limestone is massive to very poorly bedded as a result of intense burrowing. Larger skeletal grains locally exhibit preferred horizontal orientation. Dolomitic mottling commonly occurs in the upper part of the U1 limestone. Stylolites occur throughout and generally have horizontal orientation. The base of the U1 limestone generally contains imbricate brachiopod shells, oncolites, high concentations of peloids, and low amounts of skeletal debris.

The above units of the upper Red River Formation total about 150 feet in thickness. These units (U1 through U6) are stratigraphically equivalent to the A through C zones used widely by industry operators of the Williston Basin (Clement, 1978); and also equivalent to the Herald Formation (Kendall, 1976). Lateral continuity of the U1 through U6 units across Cabin Creek Field is shown in Figure 4.

Stony Mountain Formation

The Red River Formation is overlain disconformably by the Stony Mountain Formation (Upper Ordovician). From base to top, the Stony Mountain Formation is composed of (1) the Stony Mountain "Shale" Member, a very argillaceous, calcareous, fossiliferous dolomite about 50 feet in thickness, (2) the Gunton Member, a mottled and laminated dolomite about 70 feet thick, and (3) the Stonewall Member, an argillaceous, arenaceous, fossiliferous dolomite about 40-50 feet thick (Roehl, 1967).

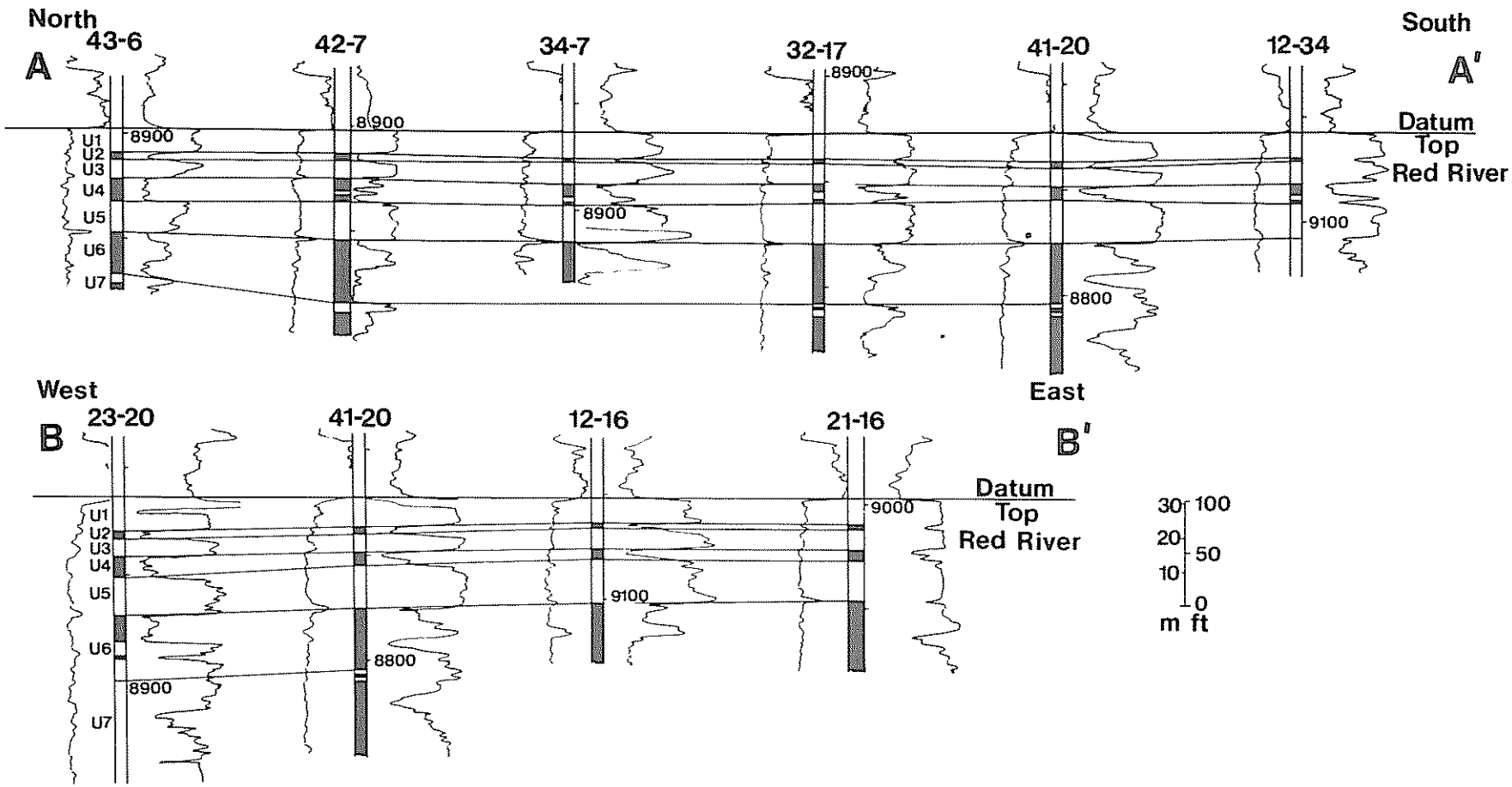

FIGURE 4. Stratigraphic cross sections A-A' and B-B' through Cabin Creek Field (see Fig. 2 for locations). Dolomite is indicated in black, limestone in white. All logs shown are gamma ray-neutron.

LITHOFACIES

Six lithofacies are recognized within the upper Red River Formation at Cabin Creek Field. The lithology, environmental setting, stratigraphic occurrence, and other features of the lithofacies are summarized in Table 1. Figure 5 shows the lateral distribution of the lithofacies across Cabin Creek Field, and relates them to the stratigraphic units.

Lithofacies 1

Description

Lithofacies 1 is a mottled dolomitic biomicrite-wackestone to packstone (Figure 6A). The major allochems are skeletal grains consisting of echinoderm, brachiopod, bryozoa, trilobite, mollusk, ostracod, gastropod, coral, and stramatoporoid fragments. Concentrations of peloids, intraclasts, and ooids are locally distributed. Matrix material consists of pelletal lime-mud. Pellets occurring within or adjacent to large shells survived the effects of compaction.

Bedding within this lithofacies is poorly preserved due to intense burrowing activity. Burrows have been selectively dolomitized resulting in mottling. Most burrows exhibit preferred horizontal orientation, although vertical burrows are common. Burrow shape has been greatly modified by the combined effects of selective dolomitization and pressure solution. Stylolites are common throughout and are generally irregular, low amplitude, and exhibit preferred horizontal orientation. Cross bedding and graded bedding occur locally.

Table 1. Description and occurrence of upper Red River Lithofacies for Cabin Creek Field

	Lithology	Texture and Grain Types	Fossils	Sedimentary Structures	Environmental Setting	Stratigraphic Occurrence
Lithofacies 1	Mottled dolomitic biomicrite-wackestone to packstone	Mainly skeletal grains in pelletal-mud matrix. Peloids, intraclasts and ooids occur locally	Echinoderm, brachiopod, bryozoa, trilobite, mollusk, ostracod, and gastropod common. Rare solitary corals and stromatoporoids.	Massive to poorly bedded, intensely burrowed, abundant horizontal stylolites. Local cross bedding and graded bedding.	Subtidal to intertidal zones	Composes U1, U3, and U5 limestones. Occurs locally in lower part of U4 and U6 dolostones.
Lithofacies 2	Mottled dolomitic biomicrite-mudstone	Skeletal grains in pelletal-mud matrix	Same as Lithofacies 1.	Massive to poorly bedded, intensely burrowed, horizontal stylolites.	Subtidal zone	Locally distributed in U2 dolostone.
Lithofacies 3	Finely crystalline dolomite (10-60 μ)	Hypidiotopic dolomite	Traces of small shell debris, mostly ostracod or small brachiopod.	Wavy laminae predominate. Flat-pebble breccias, desiccation cracks, truncation surfaces, oncolites, nodular anhydrite, and solution breccias are common.	Supratidal zone	Occurs in upper part of U2 and U4 dolostones
Lithofacies 4	Microcrystalline dolomite (less than 10 μ)	Xenotopic dolomite	Same as Lithofacies 3	Same as Lithofacies 3	Supratidal zone	Occurs in upper part of U6 dolostone.
Lithofacies 5	Skeletal dolomite	Dolomitized biomicrite, wackestone to packstone. Locally abundant peloids and intraclasts.	Same as Lithofacies 1	Same as Lithofacies 1	Subtidal to intertidal zones	Occurs in lower part of U4 and U6 dolostones.
Lithofacies 6	Laminated black shale stringers	Fissile Carbonaceous	Unfossiliferous	Locally contain flat-pebble breccia clasts of microcrystalline dolomite. Graded bedding	Supratidal zone marsh deposits	Occurs locally atop U4 and U6 dolostones

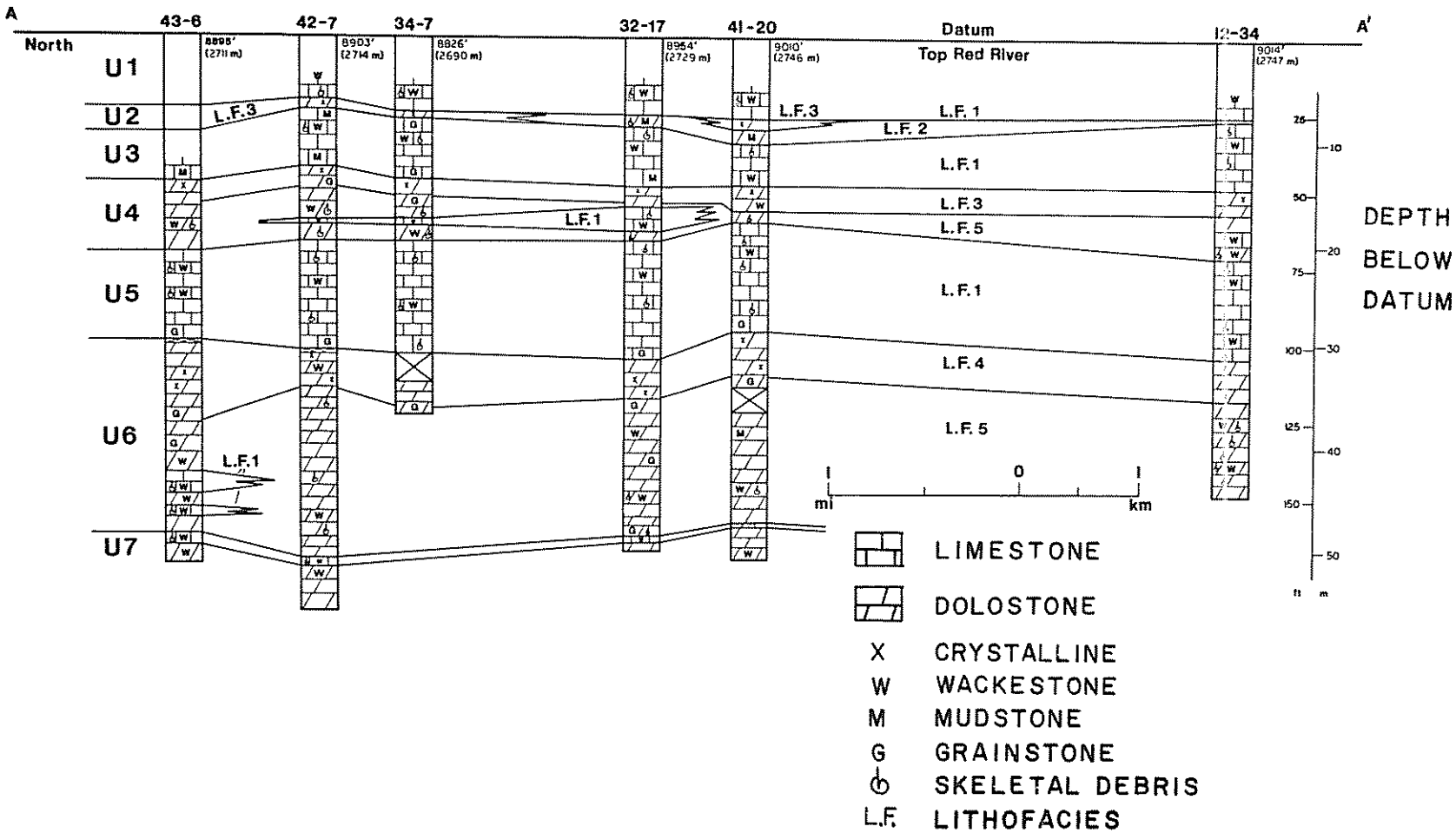

FIGURE 5. Lithofacies cross section A-A' showing relationship among upper Red River lithofacies and stratigraphic units (see Fig. 2 for location).

Stratigraphic Distribution

Lithofacies 1 composes essentially all of the U1, U3 and U5 limestones. Thickness varies from 14 to 40 feet across Cabin Creek Field. Lithofacies 1 also occurs locally within the U4 and U6 dolostones, attaining maximum thickness of 9 feet in these units.

Lithofacies 2

Description

Lithofacies 2 is a mottled dolomitic biomicrite-mudstone. Allochems consist of skeletal grains very similar to those which occur in lithofacies 1. Matrix material consists of pelletal lime-mud. Lithofacies 2 is massive to poorly bedded and intensely burrowed. Burrows have been selectively dolomitized resulting in mottling similar to that of lithofacies 1. Horizontally oriented stylolites are common.

Stratigraphic Distribution

Lithofacies 2 occurs locally within the U2 dolostone only. Maximum thickness is 4 feet. Laterally, lithofacies 2 interfingers with lithofacies 3.

Lithofacies 3

Description

Lithofacies 3 is a finely crystalline dolomite (10-60 micron size) having a predominantly hypidiotopic fabric. Wavy laminae are the

predominant structure (Figure 6B). Other common structures of this lithofacies are flat-pebble breccias, desiccation cracks (Figure 6C), truncation surfaces, ohcolites (Figure 6D), nodular anhydrite, and solution breccias healed by secondary anhydrite. Pelletal fabric is locally preserved. Lithofacies 3 is mostly unfossiliferous, although scattered, small bits of skeletal debris consisting of ostracod and brachiopod shells occur.

Stratigraphic Distribution

Lithofacies 3 occurs locally in the U3 dolostone. It also occurs in the upper part of the U4 dolostone. Maximum thickness is 8 feet.

Lithofacies 4

Description

Lithofacies 4 is a microcrystalline dolomite (less than 10 micron size) having a predominantly xenotopic fabric. Structures are similar to those of lithofacies 3 (Figure 6E). Rare fossil remains occur in lithofacies 4.

Stratigraphic Distribution

The occurrence of lithofacies 4 is restricted to the upper part of the U6 dolostone. Thickness varies from 10 to 25 feet.

Lithofacies 5

Description

Lithofacies 5 is a skeletal dolomite (Figure 6F). Allochems consist of skeletal grains derived largely from the same faunal assemblage as that of lithofacies 1. In addition to skeletal grains, lithofacies 5 contains locally abundant peloids and intraclasts. Bedding is poorly developed due to burrowing activity (Figures 7A and 7B). Other structures include local cross bedding and graded bedding (Figures 7C and 7D), stylolites, chert nodules, and anhydrite nodules (Figure 7E). Prior to being dolomitized, lithofacies 5 was a biomicrite wackestone.

Stratigraphic Distribution

Lithofacies 5 occurs in the lower part of the U4 and U6 dolostones. Thickness varies from 5 to 54 feet. Lithofacies 5 locally interfingers with lithofacies 1.

Lithofacies 6

Description

Lithofacies 6 consists of laminated black shale stringers. The shales are fissile, carbonaceous, and unfossiliferous. Locally they contain flat-pebble breccia clasts of microcrystalline dolomite (Figure 7F) which exhibit graded bedding.

Stratigraphic Distribution

Lithofacies 6 is locally distributed atop the U4 and U6 dolostones. Thickness is less than one foot. It is recognized on gamma-ray logs by a characteristic sharp increase in radioactivity, which is readily correlated.

FIGURE 6

A. Mottled dolomitic biomicrite-wackestone (lithofacies 1) containing small brachiopods with micrite geopetal fill, and various fragments of skeletal debris. Specimen was stained with Alizarin Red-S. The dolomite mottling is light-colored. Cabin Creek 42-7, 8936 ft. U3 limestone subtidal zone.

B. Finely crystalline dolomite (lithofacies 3) with wavy laminae. In many cases the laminae are separated by stylolitic surfaces containing organic matter. Cabin Creek 42-7, 8949 ft. U4 dolostone supratidal zone.

C. Laminated finely crystalline dolomite (lithofacies 3) locally containing small fragments of skeletal debris. Desiccation crack is filled with clasts of laminated dolomite as well as skeletal debris. Cabin Creek 42-7, 8925 ft. U2 dolostone supratidal zone.

D. Truncation surface within a laminated finely crystalline dolomite (lithofacies 3) containing oncolites (arrow). Cabin Creek 34-7, 8851 ft. U2 dolostone intertidal to supratidal zone.

E. Laminated microcrystalline dolomite (lithofacies 4) which has undergone solution collapse and fracturing. Secondary anhydrite now fills fractures and solution voids. Cabin Creek 42-7, 9030 ft. U6 dolostone intertidal to supratidal zone.

F. Skeletal dolomite (lithofacies 5) with crude bedding and horizontal stylolites. Many skeletal molds are present and the larger ones have been filled by secondary anhydrite (arrow). Molds exhibit crude horizontal stratification. Cabin Creek 41-28, 9048 ft. U4 dolostone intertidal zone.

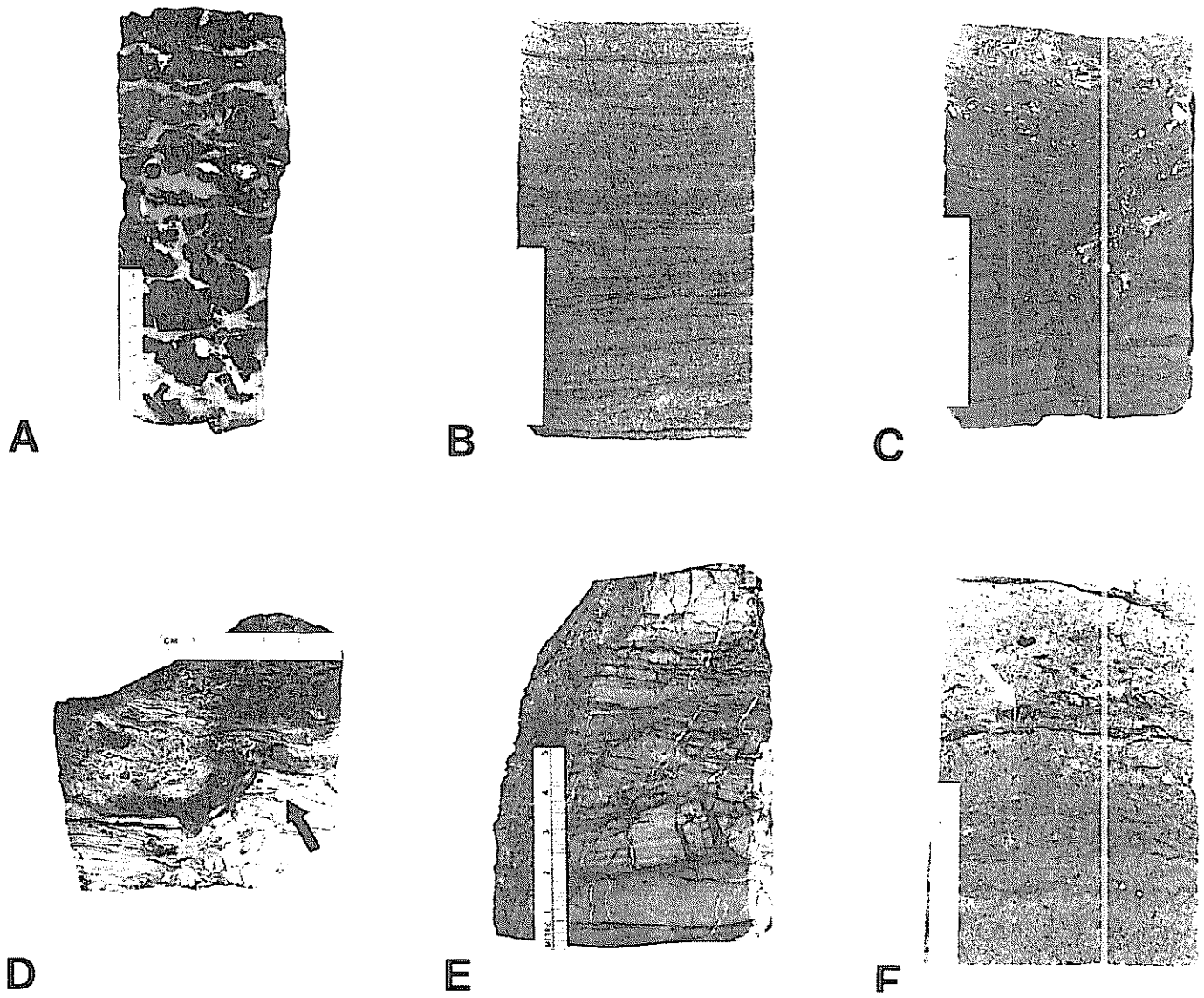

Figure 6

FIGURE 7

A. Skeletal dolomite (lithofacies 5) containing tabulate coral debris and burrow mottles. Cabin Creek 41-28, 9054 ft. U4 dolostone subtidal zone.

B. Skeletal dolomite (lithofacies 5) which has undergone intense burrowing. Note random orientation of burrow mottles. Cabin Creek 42-7, 9064 ft. U6 dolostone subtidal zone.

C. Cross bedded, oolitic, skeletal dolomite (lithofacies 5) containing multiple horizontal stylolites. Cabin Creek 42-7, 9016 ft. U6 dolostone intertidal zone.

D. Cross bedded skeletal dolomite (lithofacies 5) consisting of a peloidal grainstone. Bedding has been enhanced by oil stain. Cabin Creek 42-7, 9020 ft. U6 dolostone intertidal zone.

E. Skeletal dolomite (lithofacies 5) at contact with a large anhydrite nodule (arrow). Bedding within the dolomite has been displaced downward by nodule growth. The dolomite contains several chert nodules, one of which is cross cut by a vein of secondary anhydrite (below arrow). Cabin Creek 34-7, 8884 ft. U4 dolostone intertidal zone.

F. Black shale (lithofacies 6) containing flat-pebble breccia clasts of microcrystalline dolomite. The breccia clasts exhibit graded bedding and are topped by a layer of fissile organic shale. Note horizontal orientation of the breccia clasts. Cabin Creek 43-18, 8890 ft. U6 dolostone supratidal zone.

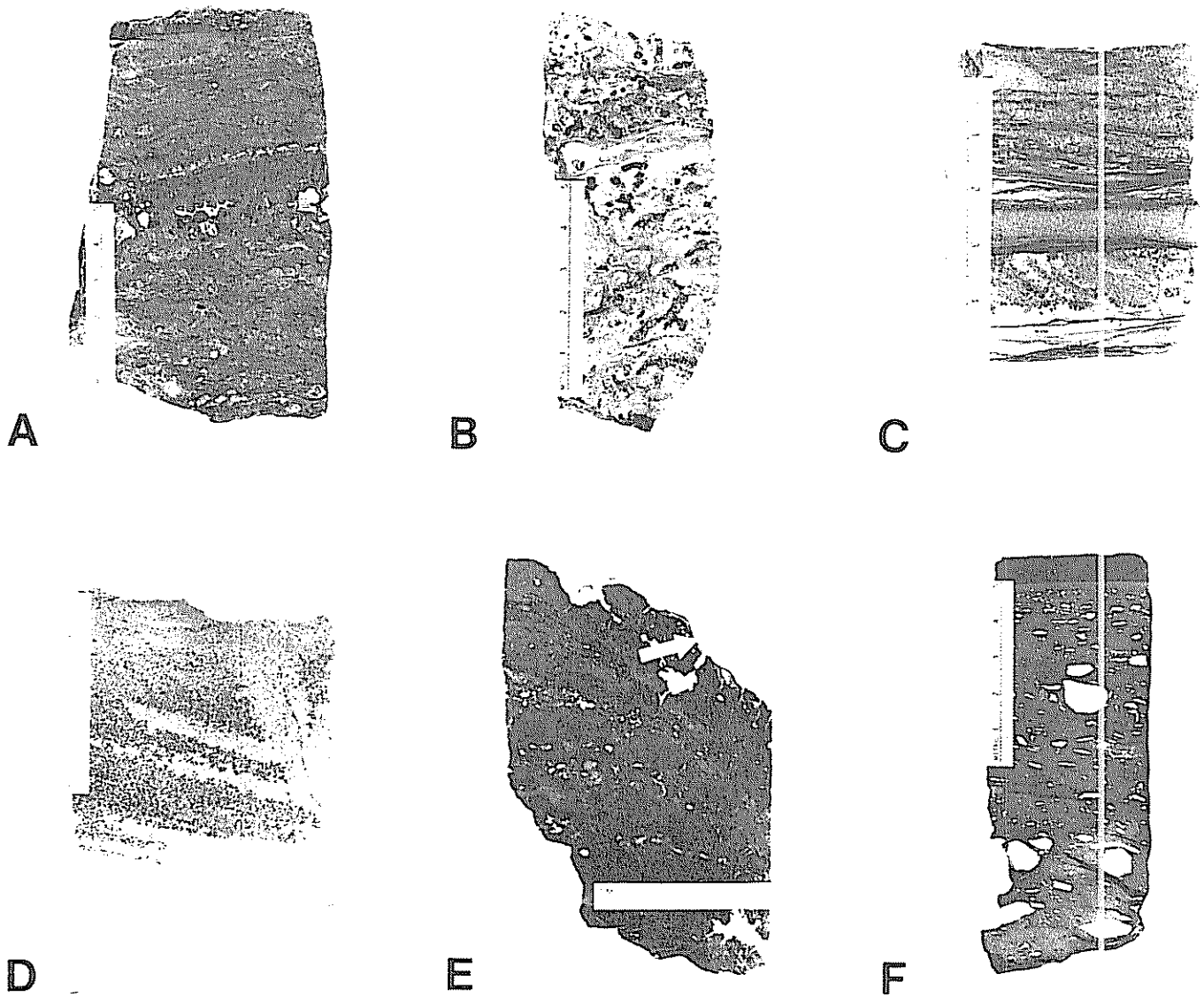

Figure 7

DEPOSITIONAL ENVIRONMENTS

Depositional environments of the upper Red River Formation are shown in Figure 8. Three cycles of subtidal through supratidal deposition occurred on a broad, shallow-marine, carbonate bank under arid conditions. The relationship between lithofacies and environment is shown in Table 1. The relative occurrence of sedimentary structures and grain types of the upper Red River supratidal, intertidal, and subtital zones appear in Table 2.

Subtidal Zone

The dominance of mud supported sediments and poorly developed bedding indicate that subtidal conditions of relatively low energy predominated during deposition of much of lithofacies 1, 2, and 5. The relative abundance and diversity of fossils, and the abundance of burrow mottling may indicate normal salinity and open marine conditions.

Indications of currents, such as cross bedding or ripple marks, are generally absent in subtidal deposits of the upper Red River Formation. Subtidal deposition occurred under relatively quiet conditions below effective wave base. Rate of sedimentation did not exceed the rate of sediment reworking by burrowing organisms. Thin beds of packstone, which generally contain imbricated skeletal debris, occur locally and indicate periodic winnowing and sorting of bottom sediments by storm waves. Packstone grains consist mostly of skeletal debris and peloids,

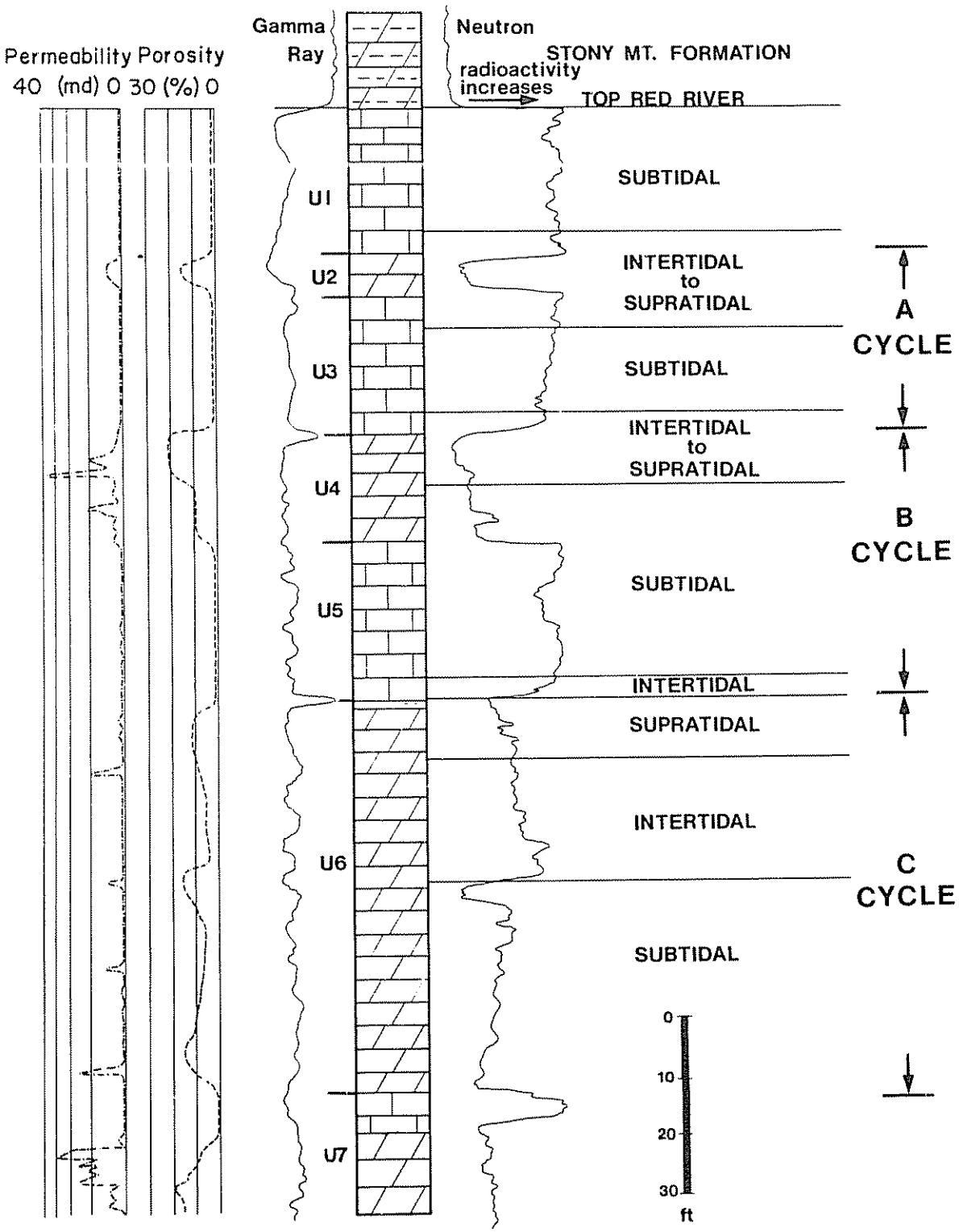

FIGURE 8. Typical columnar section of the upper Red River Formation showing depositional environments, porosity, and permeability determined by core analysis and gamma ray-neutron curves.

TABLE 2. Sedimentary Structures and Grain Types of the Red River Supratidal, Intertidal and Subtidal Zones

Structures	Supratidal	Intertidal	Subtidal
Bedding > 1 cm		C	R
Parallel laminae (< 1 cm)	C	C	
Wavy laminae	D		
Cross laminae		A	R
Ripple laminae		C	
Contorted laminae	C	C	
Graded bedding	C	C	R
Flat pebble conglomerates	C		
Imbricate shells		A	C
Shale	C		
Erosional truncations	C	C	
Chert nodules	R	C	C
Anhydrite nodules	C	C	R
Oncolites		C	R
Stylolites	C	C	D
Mottling (bioturbation)	R	R	D
Solution brecciation	C		
Lag conglomerate	C	C	R
Desiccation features	R-C		
Grain Types			
Skeletal	R	C-A	A-D
Peloids	A	C	C-A
Intraclasts	R	C-A	R-C
Ooids	R	C	R

D = dominant, A = abundant, C = common, R = rare

with some concentrations of intraclasts and ooids. Presence of packstones with imbricated shells suggests that the rate of sediment churning by burrowing organisms was relatively slow. Most skeletal debris is intact and unabraided, as would be expected under low energy conditions. Fragmentation of shells and other skeletal remains can be attributed to effects of boring organisms (Figure 9A) and sediment churning by burrowing organisms. Occurrence of pyrite and local thin black kerogenites within the biomicrite wackestones indicate periods of euxinic bottom conditions (Kohm and Louden, 1978). Stratigraphically, subtidal conditions predominated during deposition of the lower U6 dolostone, again during deposition of the upper U5 limestone, and lower U4 dolostone units; and during deposition of the middle U3 and upper U1 limestone units (Figure 8).

Intertidal Zone

Parts of lithofacies 1 and 5 were deposited under relatively high energy intertidal conditions, as indicated by the presence of cross bedding, graded bedding, ripple bedding, imbricate shells, conglomerates, and oncolites. In addition to skeletal debris, intertidal sediments contain abundant intraclasts, peloids, and ooids. Burrow mottling occurs in the intertidal sediments, but is much less abundant than in the subtidal zone. Intertidal conditions predominated during deposition of middle to lower-upper U6 dolostone, basal part of the U5 limestone, middle part of the U4 dolostone, basal and upper parts of the U3 limestone, and during deposition of the basal U1 limestone.

FIGURE 9

A. Algal borings (arrow) in an unidentified fossil which is totally silicified. Algal borings and skeletal walls are composed of chalcedony while interior of fossil has been filled with megaquartz crystals. Thin section photomicrograph, crossed nicols. Cabin Creek 34-7, 8894 ft. U5 limestone subtidal zone.

B. Folded laminae in a finely crystalline dolomite (lithofacies 3). The folding may have resulted from soft sediment deformation or possibly shrinkage of an algal mat. Arrow indicates stratigraphic-up direction. Cabin Creek 41-28, 9045 ft. U4 dolostone supratidal zone.

C. Pelletal, finely crystalline dolomite. Pore space is white. Thin section photomicrograph, plane-polarized light. Cabin Creek 41-28, 9043 ft. U4 dolostone supratidal zone.

D. Laminated finely crystalline dolomite. Thin films of organic material occur between many laminae. In many cases the laminae appear to be separated by stylolites. Arrow indicates stratigraphic-up direction. Cabin Creek 41-28, 9047 ft. U4 dolostone supratidal zone.

E. Anhydrite crystal (arrow) in a finely crystalline dolomite matrix. Such anhydrite crystals which occur in supratidal sediments, have survived early dissolution by fresh meteoric waters which percolated down through the vadose zone. Thin section photomicrograph, crossed nicols. Cabin Creek 34-7, 8876 ft. U4 dolostone supratidal zone.

F. Partly leached anhydrite (arrow) in finely crystalline dolomite. Thin section photomicrograph, crossed nicols. Cabin Creek 34-7, 8876 ft. U4 dolostone supratidal zone.

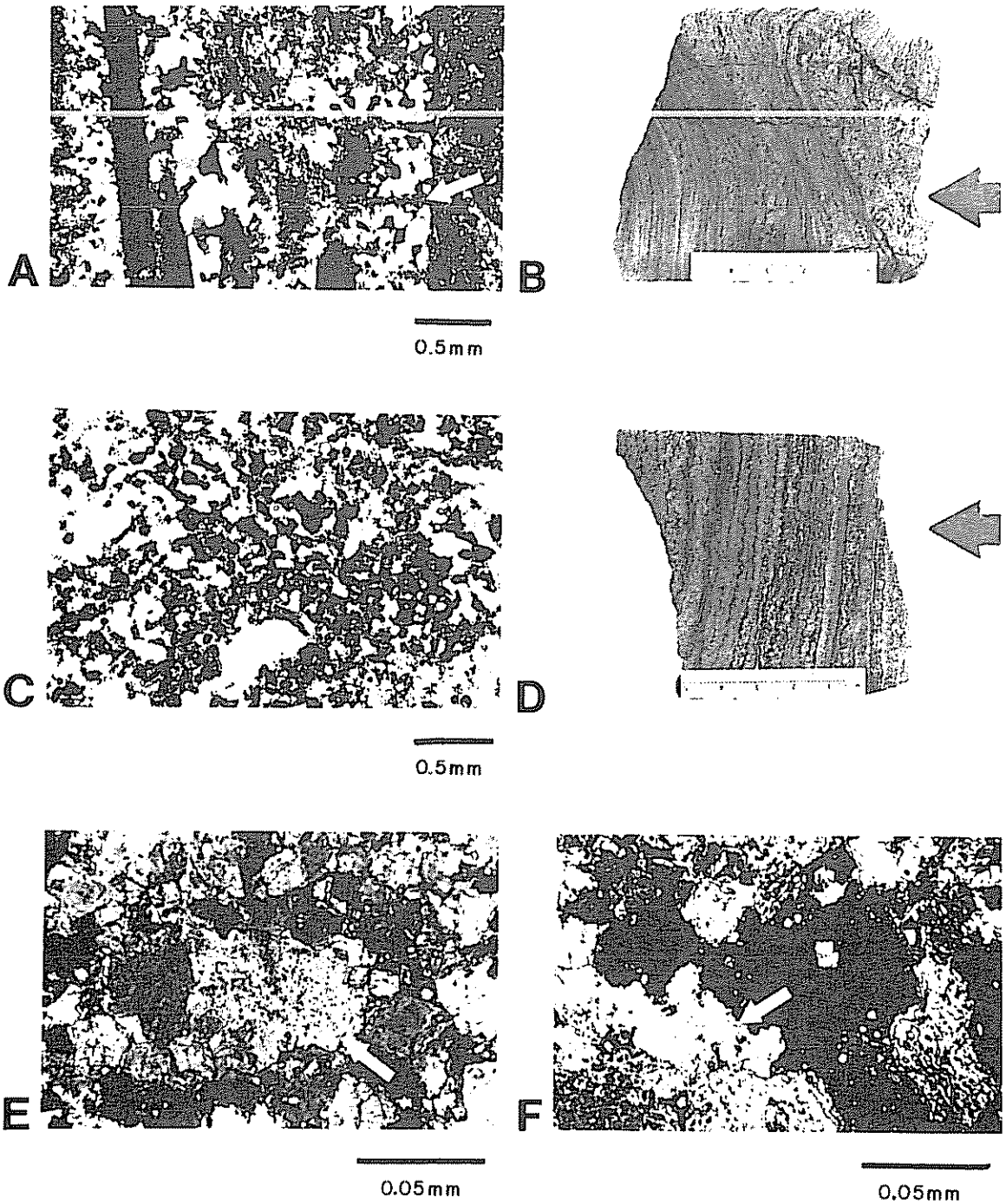

Figure 9

Supratidal Zone

Supratidal conditions prevailed during deposition of lithofacies 3, 4 and 6, as indicated by the presence of desiccation cracks, truncation surfaces, flat-pebble breccias, wavy laminated dolomite, rare fossil remains, and lack of burrows. Solution breccias are common in the supratidal sediments and probably formed by dissolution of evaporitic sulfate minerals and collapse of the overlying sediment. Deposition of laminae occurred by periodic flooding of the supratidal surface by marine waters laden with fine grained calcium-carbonate sediment.

It has been suggested that algae have contributed to the formation of laminated dolomites of the upper Red River Formation (Asquith, 1978, and Carroll, 1978). Organic-rich laminae are regarded by Carroll (1978) as poorly preserved algal structures. Wavy laminae strongly resembling stromatolites are conspicuous in Red River supratidal sediments at Cabin Creek Field. In many examples the laminae are separated by stylolitic surfaces. Local folding of laminae resulted from soft-sediment deformation (Figure 9B).

Organic-rich muds accumulated locally in marshes on the supratidal surface as indicated by occurrence of laminated black shales (lithofacies 6). These shales commonly contain flat-pebble breccias of microcrystalline dolomite, indicating desiccation and erosion of adjacent sediment. The shales are laterally persistent across the basin and have been described by Carrol (1978) as argillaceous marker beds consisting of non-calcareous, dark gray fissile shale about one inch thick. He interpreted the shales as diastems, representing times of

subaerial exposure and non-deposition or erosion. The shale stringers occur at the interface of upper supratidal and subtidal sediments, further indicating that the shales represent a major change in environment conditions.

Anhydrite occurs as porphyrotopic, anhedral crystals up to 60 micron size, and generally constitutes less than 1% of the total supratidal sediments. Presence of anhydrite indicates the occurrence of evaporitic conditions in the supratidal zone. Displacive nodular anhydrite occurs locally in the lower supratidal sediments. Former abundance of evaporitic sulfate minerals in the supratidal zone is indicated by the occurrence of solution breccias and also vug porosity, which are interpreted as having formed by leaching of sulfate minerals. Supratidal conditions prevailed during deposition of the upper parts of the U6, U4, and U2 dolostones.

Depositional Cycles in the Upper Red River Formation

Three cycles of subtidal through supratidal deposition are recognized in the upper Red River Formation at Cabin Creek Field. A summary of sedimentary features occurring within these cycles appears in Figure 10. Each cycle represents a shoaling-upward sedimentary sequence. An ideal, fully developed cycle consists of the following units: a basal biomicrite-wackestone deposited under subtidal conditions; a cross bedded and ripple marked biomicrite packstone containing intraclasts, peloids, and ooids deposited under intertidal conditions; a laminated unfossiliferous dolomite containing anhydrite and solution

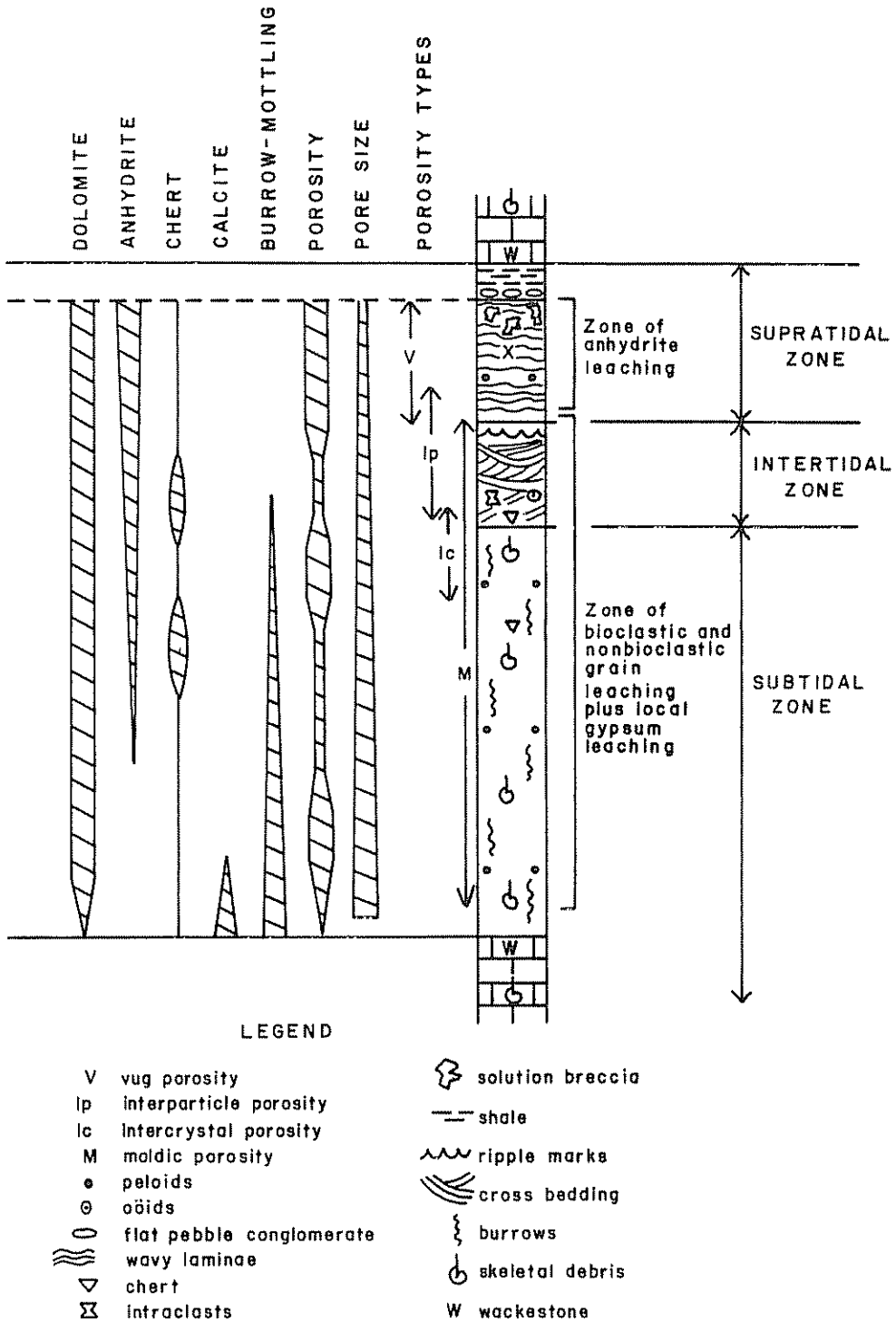

FIGURE 10. Depositional and diagenetic features of the upper Red River dolostone units.

breccias, deposited under high intertidal to supratidal conditons; and a black laminated fissile shale containing flat-pebble breccias of microcrystalline dolomite, deposited under supratidal conditions.

The lowest part of each cycle was deposited under low energy, subtidal, open-marine conditions. Regression of the Upper Ordovician Sea resulted in shoaling, relatively high energy intertidal conditions. Continued regression resulted in emergence of the tidal flats. At this time, the Cedar Creek Anticline area was a broad supratidal flat which was periodically inundated by marine waters, and on which evaporitic conditions prevailed. Ponding of marine waters and meteoric fresh waters created widespread marshes on the supratidal surface, in which organic-rich terrigenous muds were accumulated. Desiccation of lithified carbonate sediments occurred in the intermarsh areas. Clasts of this carbonate material were ripped-up and redeposited in low-lying marsh areas by storm waves which inundated the supratidal surface. Shortly after or synchronous with this erosional activity the Upper Ordovician sea transgressed over the area resulting in renewed subtidal, open marine conditions. Such transgression marked the beginning of a new subtidal through supratidal cycle.

The first two (oldest) depositional cycles are complete and consist of the U6 through U4 stratigraphic units. The third and last cycle consists of the U3 and U2 stratigraphic units and is incomplete as it lacks the capping black shale. The biomicrite-wackestone of the U1 unit lies directly above the laminated dolomite of the U2.

Regional Depositional Environments

Deposition of upper Red River Formation stratigraphic units began in a shallow carbonate epeiric sea under normal-salinity, open-marine conditions (Kendall, 1976). At this time, the Williston Basin was bordered by broad intertidal and supratidal flats (Carroll, 1978). The Cedar Creek Anticline area was included within the tidal flats fringing the basin (Roehl, 1967).

Depositional environments of upper Red River equivalent sediments in the southeastern Saskatchewan part of the Williston Basin have been discussed by Kendall (1976). He concluded that Upper Ordovician sedimentary cycles in the Williston Basin resulted from cycles of increasing basin hypersalinity, which may have been accompanied by shallowing and basin edge emergence as a consequence of evaporative downdraw. Evidence cited for this interpretation are (1) the thickness and lateral continuity of some cycle members, (2) the basin-central location of anhydrites, (3) absence of indicators of subaerial exposure, and (4) the bedded character of the anhydrite beds. These features, according to Kendall, are inconsistent with a progradational model of sedimentation.

Kohm and Louden (1978) have studied the Red River Formation of eastern Montana and western North Dakota (exclusive of the Cedar Creek Anticline), and are in agreement with the basic depositional model of Kendall (1976). They concluded that the laminated dolomites and anhydrite beds of the upper Red River were deposited in a restricted penesaline sea under subtidal conditions. As evidence, they cite

(1) lack of evidence of subaerial exposure (e.g., mud cracks, desiccation breccias) of laminated dolomite units and anhydrite units, (2) lack of oxidation (e.g., paleosols, red staining), (3) lateral continuity of facies character and thickness from northeast Montana wells to deeper parts of the basin in North Dakota. This, according to Kohm and Louden, precludes the possibility of a sabkha deposit which might be expected to have an equivalent marine facies in the center of the basin.

Upper Ordovician and Silurian carbonate cycles on the Cedar Creek Anticline have been interpreted to be a result of lateral or progradational sedimentation episodes (Roehl, 1967). In this model, the mottled biomicrite wackestones are considered subtidal to low intertidal; the laminated dolomites and bedded anhydrites as supratidal deposits. According to Roehl, the thickness and lateral continuity of basin-center anhydrites do not preclude a supratidal saline-playa origin. It is possible for the basin-center anhydrites to be the result of precipitation in a series of shallow saline playas interconnected by wadis and tidal channels across a supratidal (sabkha) evaporite plain.

Carroll (1978) and Asquith, et al (1978) have also interpreted the laminated dolomites and anhydrites of the upper Red River as being of supratidal origin. Evidence for this conclusion consists of desiccation fractures, acicular anhydrite crystals, relict algal structures, and flat-pebble breccias.

Origin of Laminae in Supratidal Dolostones

It is possible that at least part of the laminated dolostones of the upper Red River supratidal zone are of cryptalgal origin. Cryptalgal sedimentary rocks have been defined by Aitken (1967) as those believed to originate through the sediment-binding and/or carbonate-precipitating activities of nonskeletal algae. The term cryptalgalaminite refers to carbonate rocks displaying a distinctive form of discontinuous, more or less planar lamination believed to have resulted from algal activity.

Characteristics of cryptalgalaminae have been discussed by Aitken (1967). Features of upper Red River supratidal sediments which conform to characteristics of cryptalgalaminae are (1) the laminae do not show indications of having been deposited from currents of variable velocity, (2) locally the laminae appear to have an encrusting relationship to the underlying surface, (3) small-scale disconformities occur, (4) desiccation cracks are present locally, (5) laminae are composed of dense and light-colored dolomite, rather than limestone, (6) pellets are common and locally abundant (Figure 9C), (7) domes and bubbles on the scale of a few millimeters occur in some localities, (8) stromatolites occur and are locally well developed, (9) fenestral fabric is locally developed, but fenestral pores are filled with dolomite.

Despite the above comparisons of upper Red River supratidal laminae to cryptalgalaminae as defined by Aitken (1967), several characteristics of cryptalgalaminae are absent or rare in upper Red River supratidal sediments. Although stromatolites occur, they are not polygonal and are

only rarely domal in shape. Thin breccia chips do not occur except at the very top of the laminated dolostones. No traces of algal filaments or sub-millimeter diameter burrows were found. However, not every cryptalgalaminate rock has all of the characteristics proposed, and Aitken concluded that any laminated carbonate rock lacking cross lamination is suspect as being of cryptalgal origin.

The upper Red River U4 laminated dolostones commonly display round and elongate to irregular vugs aligned with and parallel to the laminae. These vugs range from 0.03 to 0.80 mm in length, and average about 0.15 mm in length. According to Monty (1976) cavities of this type may develop within an algal mat due to oxidation of organic matter. The vugs may in fact be fenestral pores. Other possible causes of aligned vugs will be discussed in the section on porosity.

The supratidal surfaces of the upper Red River were periodically inundated by marine waters during storms or unusually high tides. Following the deposition of suspended sediment and the receding of the waters, it is likely that algal mats were developed locally on the wet supratidal surface. As suggested by Laporte (1967), peloids may be the weathering products from exposed and dried-out carbonate mud. Similar pellet-shaped weathering products have been reported to have formed in modern subaerially exposed flats of Laguna Madre by deflation of algal crusts (Fisk, 1959).

Mudcracks are healed by mud, skeletal debris, and small wedges of laminated sediment. Mud cracks are up to 2 centimeters wide and up to several centimeters in depth. Thin bituminous films separating laminae

may represent the remains of algal mats which covered the supratidal sediments from time to time (Figure 9D). As these mats dried, they would have crinkled and curled, thereby disturbing the laminated sediment just underneath (Figure 9B). Gentle convex-up warps which overhang adjacent lows on the sediment surface imply a cohesive sediment character as would be provided by the algal mats (Laporte, 1967).

DIAGENESIS

Each shoaling-upwards cycle of upper Red River subtidal through supratidal sediments displays diagenetic overprinting. Early stages of diagenesis include vadose leaching of evaporitic sulfate minerals and formation of dolomite in the supratidal zone. Later stages of diagenesis include continued dolomitization followed by leaching of undolomitized calcite, reprecipitation of sulfate minerals as cement, replacement and cementation by silica, and pressure solution.

Vadose Leaching

The supratidal sediments of the upper Red River Formation were periodically subjected to leaching by fresh meteoric water percolating down through the vadose zone. Under these conditions, early diagenetic minerals such as calcium sulfate are ephemeral and easily destroyed (Kinsman, 1969). The occurrence of this process is indicated by (1) corroded edges of relict anhydrite crystals, (2) presence of vugs which closely approximate the size and shape of relict anhydrite crystals, (3) presence of gypsum and anhydrite pseudomorphs preserved as pore space, and (4) the occurrence of solution-collapse breccias and fractures.

Porphyrotopic crystals of anhydrite occur in varying stages of dissolution within upper Red River supratidal sediments. Undissolved anhydrite crystals are generally 0.05 mm in size, anhedral, and surrounded by dolomite matrix (Figure 9E). In many examples the size

and shape of such anhydrite crystals closely approximate the size and shape of vugs which contribute to a large part of the porosity in upper Red River supratidal zones. Partially leached anhydrite is common (Figures 9F and 11A).

Gypsum and anhydrite pseudomorphs, now present as moldic porosity, occur within supratidal, intertidal, and subtidal sediments. They are recognized by their characteristic straight sides and rectangular re-entrants and projections (Figure 11B) and are on the order of 0.1 to 0.5 mm in size. In many examples a distinction can be made between gypsum and anhydrite molds on the basis of shape. The occurrence of gypsum and anhydrite in modern sabkha environments has been well documented as has leaching of such evaporitic sulfate minerals (Murray, 1960). Undoubtedly, the supratidal sediments underwent many episodes of vadose leaching, depending upon local climatic conditions. Gypsum and anhydrite could have been leached before, after or concurrent with dolomitization of the host sediments. Dolomitization after leaching would have resulted in modification of original gypsum or anhydrite mold shape.

In addition to vadose leaching of evaporitic sulfate minerals, there is evidence to suggest that skeletal and peloidal grains of calcite or aragonite were also leached from supratidal sediments. Round to ovoid-shaped molds up to 1.0 mm size are locally interlaminated with supratidal sediments and exhibit preferred horizontal orientation (Figure 11C). The shape and orientation of these molds indicates that small skeletal remains and peloids were deposited on the supratidal

FIGURE 11

A. Partly leached anhydrite (arrow) in microcrystalline dolomite matrix. Note the straight-sided, rectangular boundaries of the vug left after the anhydrite was leached. Thin section photomicrograph, crossed nicols. Cabin Creek 34-7, 8944 ft. U6 dolostone supratidal zone.

B. Gypsum mold (arrow) in finely crystalline dolomite. It is likely that much of the other pore space is of the same origin, but that dolomitization has altered the shape of the original gypsum molds. Thin section photomicrograph, crossed nicols. Cabin Creek 34-7, 8881 ft. U4 dolostone intertidal zone.

C. Stratified molds in microcrystalline dolomite. Long dimensions of the molds are aligned parallel to bedding. Thin section photomicrograph, crossed nicols. Cabin Creek 21-8, 9036 ft. U6 dolostone supratidal zone.

D. Solution collapse breccia in a microcrystalline dolomite. Clasts were downwarped with a common orientation and later modified by pressure solution. Void space has been healed with secondary anhydrite. Arrow indicates stratigraphic-up direction. Cabin Creek 41-20, 9108 ft. U6 dolostone supratidal zone.

E. Solution collapse breccia in a laminated microcrystalline dolomite. Secondary anhydrite (arrow) fills the fractures and much void space. Top of breccia zone is bounded by a planar stylolite. Arrow indicates stratigraphic-up direction. Cabin Creek 42-7, 9032 ft. U6 dolostone intertidal zone.

F. Dedolomite in a finely crystalline dolomite of the uppermost supratidal zone. Calcite (stained with Alizarin Red-S) has partly replaced many of the dolomite rhombs, especially along the edges (arrow). Calcite pseudomorphs after dolomite are also present (left of arrow). Thin section photomicrograph, plane-polarized light. Cabin Creek 23-20, 8778 ft. U4 dolostone supratidal zone.

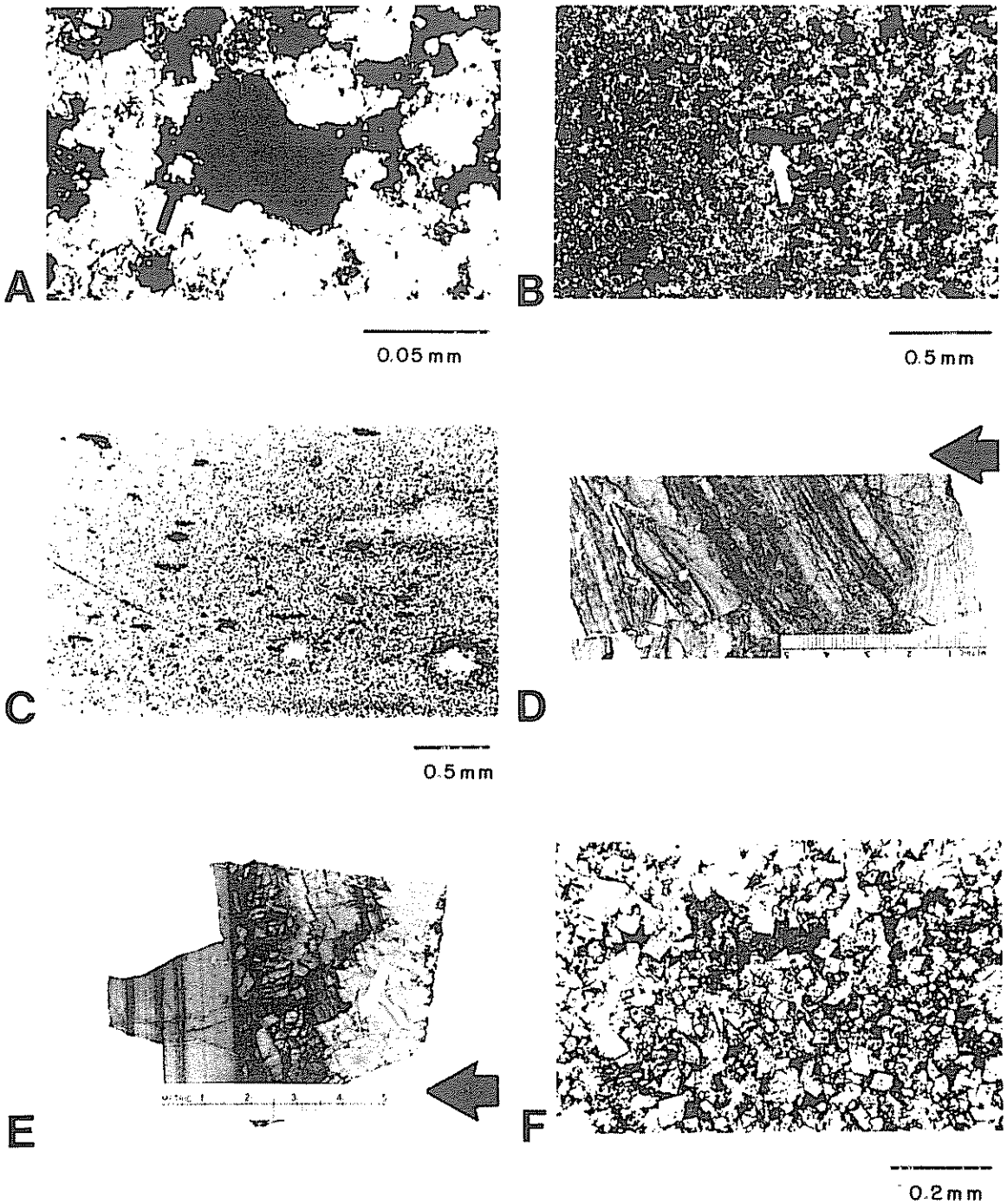

Figure 11

surface and selectively dissolved after dolomitization of the matrix sediment.

Breccias and fractures produced by solution-collapse are common in the supratidal sediments and are most likely the result of dissolution of gypsum or anhydrite crystals and nodules. Criteria for the recognition of evaporite solution breccias have been summarized by Beales and Oldershaw (1969). Evidence for solution-collapse origin of the breccias are (1) association with evaporite deposits, (2) clast lithology, which consists of laminated dolomite identical to the surrounding host sediments, (3) the absence of foreign detritus incorporated within the breccia matrix, (4) the settled and downwarped nature of the breccias (Figure 11D), and (5) the absence of preferred orientation of individual clasts. Dissolution of evaporitic minerals and collapse of the overlying strata resulted in downwarping, fracturing, and rotation of breccia clasts. Size distribution of breccia clasts is uniform (non-graded). The solution breccias are healed by secondary anhydrite (Figure 11E). Clasts are up to several centimeters in size, angular, and very poorly sorted.

Dolomitization

Dolomitization of upper Red River sediments may be considered as having occurred in two stages. The first stage is syngenetic (penecontemporaneous) dolomitization occurring in the supratidal zone. The second stage is diagenetic dolomitization occurring in the

intertidal and subtidal zones. Thus dolomitization proceeded from top to bottom, beginning first in the supratidal zone and progressively affecting deeper and deeper sediments.

Syngenetic Dolomitization

Environmental conditions suggest that syngenetic dolomite formed in the supratidal sediments of the upper Red River (Asquith et al, 1978, 1979; Carroll, 1978). Original sediment of the supratidal zone consisted of pelletal lime-mud. Dolomitization occurred under hypersaline conditions resulting from capillary concentration (Friedman and Sanders, 1967). Hypersalinity is indicated by presence of anhydrite within the supratidal sediments. Evaporitic sulfate precipitation increased the Mg/Ca ratio of the interstitial brines and thus induced dolomitization of the pre-existing calcium carbonate sediments (Murray and Pray, 1965). The chemical, climatic, and physiographic setting of upper Red River syngenetic dolomites was somewhat analogous to the sabkha environments of the Persian Gulf as described by Kinsman (1969).

Evidence which suggests that syngenetic dolomitization occurred in supratidal sediments of the upper Red River Formation at Cabin Creek Field is (1) preservation of the original pelletal fabric of the sediment, and (2) the shape of vugs formed as a result of early vadose leaching of anhydrite from the supratidal sediments.

The fact that pelletal fabric has been preserved through much of the upper Red River supratidal sediments implies that dolomitization

occurred soon after deposition, before significant burial and compaction. Studies on the experimental compaction of lime sediment have shown that pellets in soft mud are readily obliterated under conditions of shallow burial (Shinn et al, 1980). These same studies showed that slightly hardened pellets were preserved during experimental compaction. Shinn et al (1980) suggest that well-preserved pellets in ancient carbonates indicate predepositional hardening or synsedimentary cementation. It is therefore reasonable to suggest that pellets within the upper Red River supratidal sediments survived compaction by being replaced and cemented by syngenetic dolomite.

Vugs formed in upper Red River supratidal sediments as a result of early vadose leaching of anhydrite typically have rather sharp, distinct boundaries (Figure 11A). In most examples seen dolomite rhombs do not invade the vugs. This implies that dolomitization of the host sediment occurred before vadose leaching of the anhydrite.

Syngenetic dolomitization of the upper Red River Formation occurred in lithofacies 3 and lithofacies 4. These lithofacies consist of locally pelletal, finely crystalline hypidiotopic dolomite and microcrystalline xenotopic dolomite respectively. The textural laminae of the original sediment has been largely preserved in both examples. Size and textural differences between lithofacies 3 and lithofacies 4 dolomites may have resulted from differences of the original supratidal sediments, or from chemical differences during the dolomitization process. Carbonate crystal morphology may be related to rate of crystallization and also effects of magnesium and other ions present in

the precipitating waters (Folk, 1974). The microcrystalline texture of lithofacies 4 may have resulted from rapid precipitation, whereas the relatively coarser (finely crystalline) texture of lithofacies 3 indicates a slow rate of precipitation.

Dolomite of the uppermost supratidal zone has locally been replaced by calcite (dedolomitization). Evidence for dedolomitization is the occurrence of relicts of incompletely replaced dolomite crystals, and the presence of calcite pseudomorphs after dolomite (Figure 11F). Dedolomitization is believed to be a near-surface weathering process related to unconformities (Schmidt, 1965; Evamy, 1967). The occurrence of dedolomite in the uppermost parts of supratidal dolomites of the upper Red River Formation is consistent with the subaerial desiccation and erosion interpretation of these units.

Diagenetic Dolomitization

The occurrence of diagenetic dolomitization of the intertidal and subtidal zones is indicated by the selective replacement of former calcium-carbonate grains and matrix, and also by the transition from dolomite to the underlying limestone units. Note for example, the limestone beds which occur locally in lower parts of the U4 and U6 dolostones (Figure 5).

Dolomitization began in the supratidal zone as described above. Evaporation in the near-surface intertidal and supratidal zones resulted in increased density and gravitational instability of interstitial waters. Permeability of the sediments was sufficient to permit these

heavy upper waters to sink (reflux) into earlier deposited sediments. Sediments beneath the supratidal surface were progressively dolomitized by downward refluxing brines which slowly penetrated the intertidal and subtidal zones.

In general, the grains which composed the original calcium-carbonate sediments are preserved as relicts in the dolomite. Such relict grains include pellets, intraclasts, peloids, ooids, and skeletal grains (Figures 12A through 12F). The abundance of molds of the various grains indicates that the original lime-mud matrix was dolomitized before the grains. Molds were formed by selective dissolution of calcium carbonate grains as the result of the solubility contrast between the calcium-carbonate grains and the dolomite-mud matrix. Contacts of dolostone units are transitional with underlying limestones. As this contract is approached, less and less dolomitized skeletal grains occur until only the matrix consists of dolomite (Figure 12E). The vertical lower limit of dolomitization resulted both from the presence of compacted, impermeable sediment, and a downward decrease in Mg/Ca ratio.

Dolomitic mottling. Dolomitic mottling is very common throughout the limestone units of the upper Red River. The mottling resulted from selective dolomitization of burrows. Although vertical burrows are common, most have a preferred horizontal orientation. Dolomite within burrows is generally finely crystalline and hypidiotopic. Rhombs are not strictly confined within burrows but tend to be scattered into the surrounding sediment (Figure 13A) except in areas where shells have obstructed the passage of dolomitizing solutions (Figure 13B). Burrow

FIGURE 12

A. Dolomitic biomicrite-wackestone with pellets locally preserved within and next to a fossil shell. Only part of the matrix has been replaced by dolomite. Thin section photomicrograph, crossed nicols. Cabin Creek 43-6, 8966 ft. U5 limestone subtidal zone.

B. Dolomitized intraclasts cemented by finely crystalline dolomite. Long dimensions of intraclasts are aligned parallel to bedding. Thin section photomicrograph, plane-polarized light. Cabin Creek 42-7, 9018 ft. U6 dolostone intertidal zone.

C. Dolomitized intraclast and pelletal grainstone. Intraclasts are well rounded and many contain ostracod shells or bryozoa remains. Thin section photomicrograph, crossed nicols. Cabin Creek 41-20, 9121 ft. U6 dolostone intertidal zone.

D. Dolomitized skeletal grains in a micrite (calcium carbonate) matrix which itself is largely replaced by dolomite rhombs. No skeletal grains have been leached. Thin section photomicrograph, plane-polarized light. Cabin Creek 34-7, 8890 ft. U4 dolostone subtidal zone.

E. Skeletal grains are calcite but some have been partly replaced by dolomite. Matrix was originally a pelletal micrite but has been mostly replaced by dolomite. Thin section photomicrograph, plane-polarized light. Cabin Creek 43-18, 8854 ft. U4 dolostone subtidal zone.

F. Partly leached skeletal grain (arrow) of dolomite in a pelletal dolomite matrix. Grain probably underwent partial leaching before being dolomitized. Thin section photomicrograph, crossed nicols. Cabin Creek 12-34, 9074 ft. U4 dolostone subtidal zone.

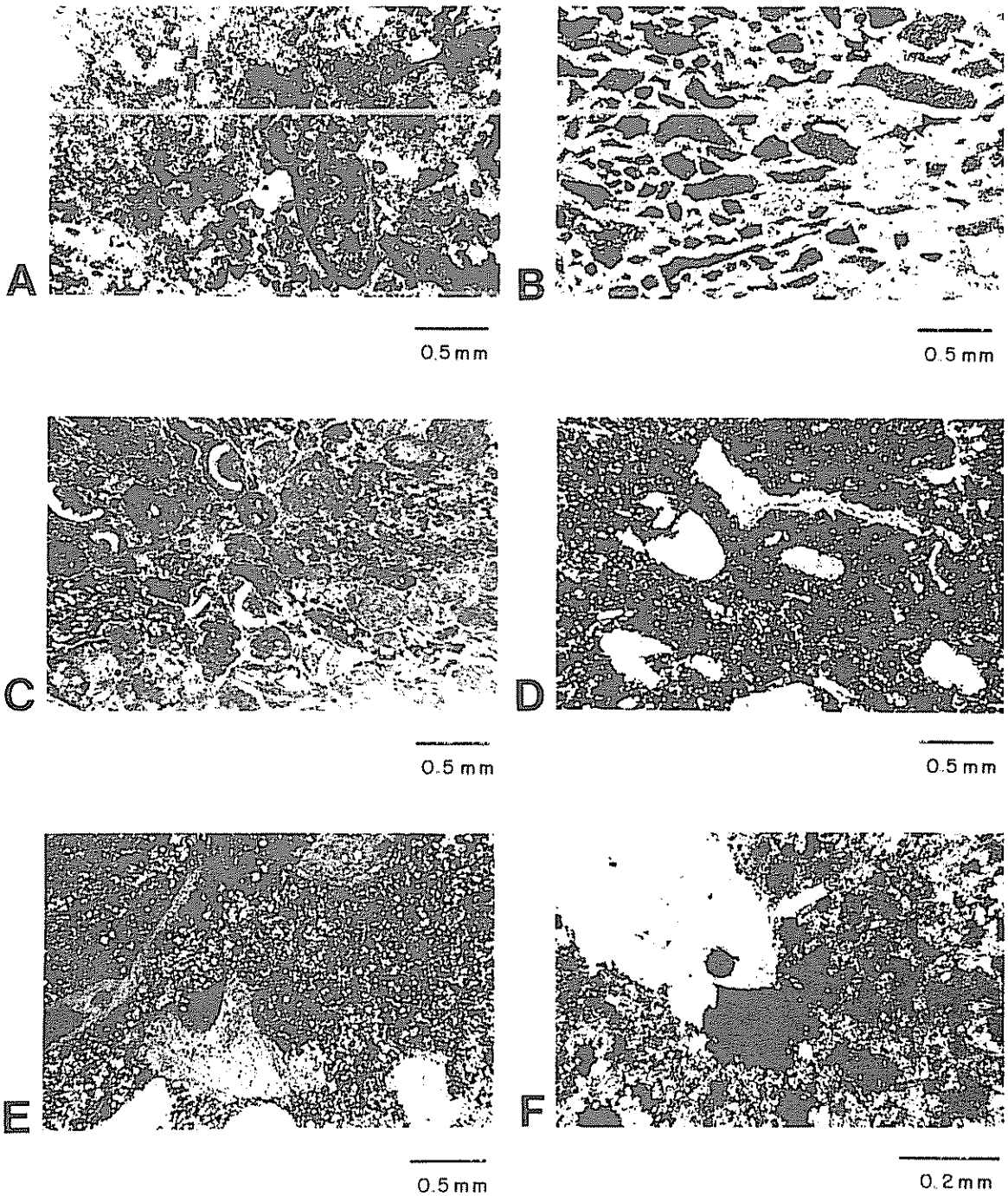

Figure 12

FIGURE 13

A. Edge of a dolomitized burrow protruding into matrix of a biomicrite-wackestone. Additional dolomite rhombs are scattered through the limestone matrix (arrow). Thin section photomicrograph, plane-polarized light. Cabin Creek 43-6, 8971 ft. U5 limestone subtidal zone.

B. Partly dolomitized biomicrite-wackestone. Dolomitization was obstructed by presence of brachiopod shell (arrow). Note how the sharp boundary of dolomitization extends well beyond the end of the shell. Thin section photomicrograph, plane-polarized light. Cabin Creek 34-7, 8907 ft. U5 limestone subtidal zone.

C. Pervasive dolomite occurring in the upper subtidal zone. Crystals are finely crystalline, idiotopic to hypidiotopic. Intercrystal pore space is black. Thin section photomicrograph, crossed nicols. Cabin Creek 41-20, 9150 ft. U6 dolostone subtidal zone.

D. Saddle dolomite crystals have filled a large vug in a biomicrite-wackestone. Note undulose extinction and curved crystal faces typical of saddle dolomite. Thin section photomicrograph, crossed nicols. Cabin Creek 43-18, 8885 ft. U5 limestone subtidal zone.

E. Finely crystalline dolomite (arrow) cementing dolomitized peloids. Interparticle and moldic pores are black. Thin section photomicrograph, crossed nicols. Cabin Creek 12-34, 9156 ft. U6 dolostone subtidal zone.

F. Fractures in a microcrystalline dolomite are healed by secondary anhydrite. The fractures originated from solution collapse. Thin section photomicrograph, crossed nicols. Cabin Creek 41-20, 9111 ft. U6 dolostone supratidal zone.

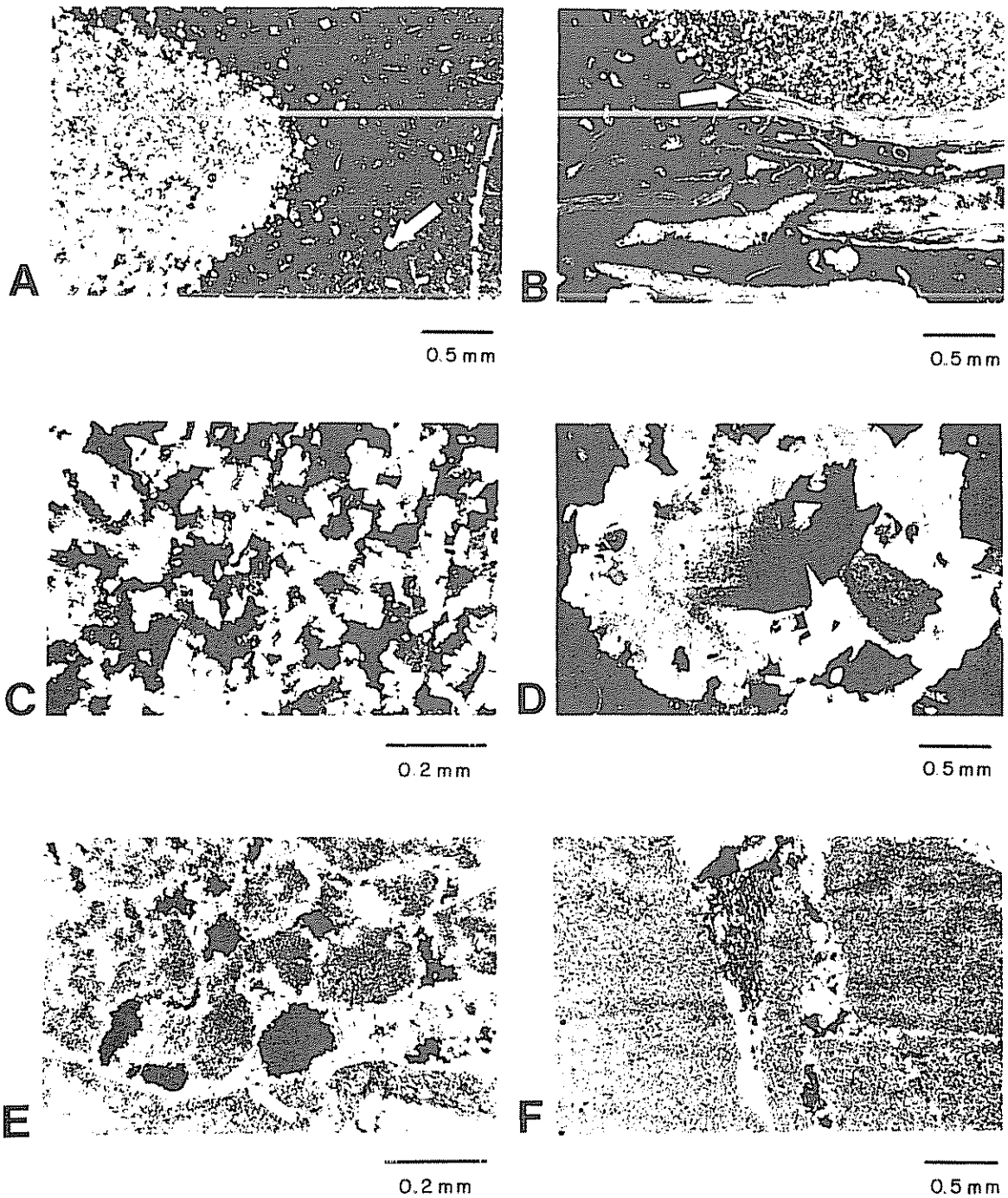

Figure 13

shapes have been modified by dolomitization and also by pressure solution. Where sediments of the upper Red River were compacted or partly lithified, burrows acted as a major conduit of dolomitizing solutions.

Pervasive dolomite. Pervasive dolomitization occurred locally in the supratidal, intertidal, and subtidal zones, but was most widespread in the uppermost part of the U6 subtidal sediments. This zone of pervasive dolomite is about 2 to 4 feet thick and occurs in most of the cores studied. It consists of finely crystalline, mostly idiotopic dolomite (Figure 13C). Idiotopic dolomite is believed to form when nonreplaced calcite is dissolved from within a framework of euhedral dolomite crystals, leaving a highly porous idiotopic fabric of euhedral dolomite crystals (Friedman and Sanders, 1978, p.178). The occurrence of this type of dolomite near the contact of subtidal and intertidal facies suggests a possible relationship to depositional environment.

Dolomite cement. Dolomite occurs locally as a void filling cement and also as an interparticle cement in grainstones. Void-filling dolomite cements consist of euhedral rhombs of saddle dolomite up to 1.0 mm in size (Figure 13D). Saddle dolomite fills some large vugs and shells, and also occurs on the undersides of large skeletal grains. Interparticle dolomite cements consist of finely crystalline to microcrystalline xenotopic dolomite between pellets, peloids, or intraclasts of subtidal to intertidal grainstones (Figure 13E). In some cases, dolomite cement also heals fractures.

Anhydrite Cementation

Secondary anhydrite occurs locally as a pore-filling cement throughout the dolostone units of the upper Red River. In the supratidal sediments, anhydrite cement heals solution-breccias and fractures (Figure 13F). In intertidal and subtidal sediments, anhydrite fills moldic, interparticle, and intercrystal porosity. Several zones of anhydrite cement, generally less than one foot in thickness, can be correlated among cored wells. Source of secondary anhydrite is the primary evaporitic sulfate minerals which underwent vadose leaching in the supratidal zone. Saturated brines seeped downward through intertidal and subtidal sediments resulting in local precipitation of anhydrite or gypsum in shell molds, fractures, and void space left after solution brecciation. Anhydrite was also found to replace fossil fragments, a process found to be common in the geologic record (Murray, 1960).

Petrographic evidence indicates that in most cases, cementation by anhydrite postdated dolomitization. Vugs and molds, formed as a result of dissolution of calcium-carbonate skeletal grains after matrix dolomitization, were later filled with anhydrite (Figure 14A). Mold-filling anhydrite may be either a single crystal or an array of bladed crystals. Anhydrite has an affinity for the larger molds and generally does not fill molds less than about 0.1 mm size. Anhydrite which fills intercrystal pore space in the dolomites is usually massive (Figure 14B). In some examples the edges of dolomite rhombs have been replaced by

FIGURE 14

A. Fossil molds in a matrix of microcrystalline dolomite. The larger molds have been filled with single crystals of secondary anhydrite (arrow). Thin section photomicrograph, crossed nicols. Cabin Creek 32-17, 9114 ft. U6 dolostone subtidal zone.

B. Anhydrite cement in a finely crystalline dolomite. Note that edges of some dolomite rhombs have been replaced by anhydrite (arrow). Thin section photomicrograph, crossed nicols. Cabin Creek 42-7, 9068 ft. U6 dolostone subtidal zone.

C. Megaquartz and chalcedony cement have filled the cavity of a gastropod occurring in a skeletal dolomite. Dark area outside shell is chert which has replaced dolomite matrix. Thin section photomicrograph, crossed nicols. Cabin Creek 43-6, 9023 ft. U6 dolostone subtidal zone.

D. Chert nodule (dark area) occurring adjacent to a large anhydrite nodule. Note preferred orientation of the individual anhydrite crystals. Some particles of the original sediment, such as the bryozoa, have survived the silicification process. Thin section photomicrograph, crossed nicols. Cabin Creek 34-7, 8884 ft. U4 dolostone intertidal zone.

E. Chert nodules in a microcrystalline dolomite which are elongated parallel to bedding. Arrow indicates stratigraphic-up direction. Cabin Creek 23-20, 8856 ft. U6 dolostone intertidal zone.

F. Megaquartz crystals (arrow) cementing dolomitized peloidal grains. Quartz crystals are equant, graded, and anhedral. Thin section photomicrograph, crossed nicols. Cabin Creek 41-20, 9146 ft. U6 dolostone intertidal zone.

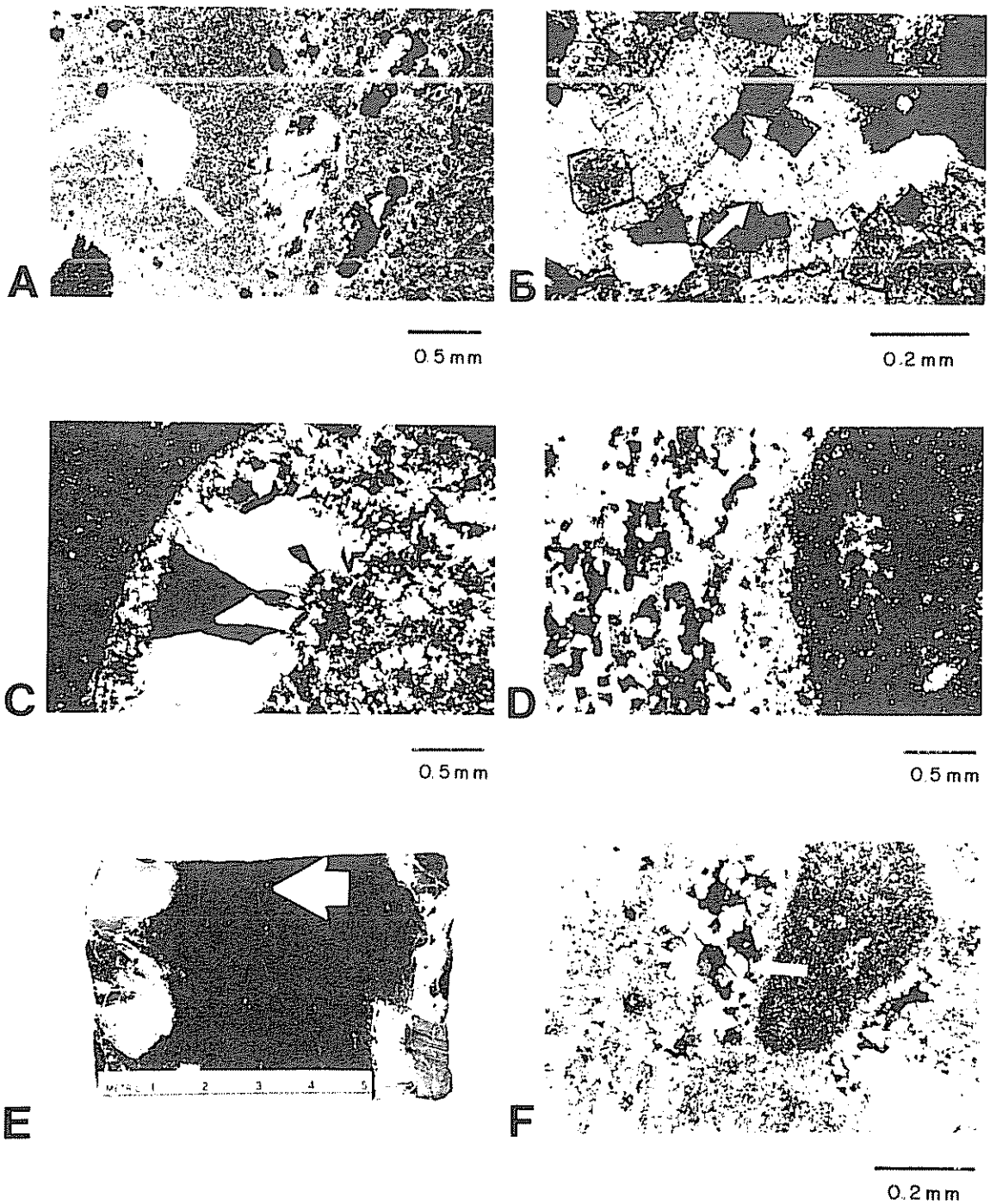

Figure 14

anhydrite. Some larger anhydrite crystals grown within the enclosing sediments contain inclusions of dolomite crystals.

Silica Cementation

Local zones of silica cement occur within upper Red River dolostone units as chert, megaquartz, and chalcedony. Silica cements may be either void filling or of replacement origin. Void-filling silica cement fills some of the larger fossils, particularly gastropods and corals, and also occurs most commonly in intertidal and subtidal sediments and generally postdates both dolomitization and anhydrite cementation.

Chert occurs as nodules up to several centimeters in size, in which original sediment fabric is usually preserved (Figure 14D). Chert nodules tend to occur concentrated as zones, generally less than one foot in thickness. Some nodular chert zones can be correlated across the field within both U4 and U6 dolostones. Chert is light brown to gray in color and is replacive and infilling, rather than displacive. Many nodules exhibit elongation parallel to bedding planes (Figure 14E). Chert replacement of skeletal grains, especially echinoderm debris, is common.

Megaquartz and chalcedony occur as void-filling cements and locally occlude moldic and interparticle porosity (Figure 14F). These cements are most abundant in intertidal zone sediments. Megaquartz cement crystals are equant, subhedral to anhedral, and usually about 0.01 mm

size, although they occur up to 1.0 mm. The crystals are also typically graded, the largest occurring in the central parts of the voids, the smallest along the perimeter. In some examples, peloids or ooids are cemented by megaquartz and the grains themselves have been partly or entirely replaced by chert (Figure 15A). Chert and megaquartz together commonly fill interskeletal pore space of tabulate corals, bryozoa, and other fossils, and also may partly or entirely replace the skeleton itself (Figure 9A).

Radial fibrous chalcedony and zebraic chalcedony most commonly line large cavities (Figure 15B). Chalcedony may fill the entire cavity, or may form an inner lining, the remainder of space being empty or filled by megaquartz. In cases where both megaquartz and anhydrite cements occur, the anhydrite crystals show evidence of being replaced by the quartz and are generally surrounded by it. Such associations indicate that replacement and cementation by quartz postdates anhydrite cementation. The association between zebraic chalcedony and evaporite minerals was described by McBride and Folk (1977).

FIGURE 15

A. Peloids which have been mostly replaced by chert, and are cemented by megaquartz. Peloid in top center of photo is composed of dolomite. Thin section photomicrograph, crossed nicols. Cabin Creek 21-8, 9049 ft. U6 dolostone intertidal zone.

B. Tabulate coral chambers replaced and filled by zebraic chalcedony, megaquartz, and anhydrite. The anhydrite laths (arrow) have been partly replaced by megaquartz. Anhydrite was probably an early cement which predates silicification. Thin section photomicrograph, crossed nicols. Cabin Creek 34-7, 8885 ft. U4 dolostone subtidal zone.

C. High amplitude stylolite in a skeletal dolomite. Additional effects of pressure solution are apparent from the presence of squashed grains (arrow) whose long dimensions are aligned parallel to bedding. Thin section photomicrograph, plane-polarized light. Cabin Creek 12-34, 9141 ft. U6 dolostone intertidal zone.

D. Multiple microstylolites in a biomicrite-wackestone which are subparallel to bedding. Note how microstylolite zones circumvent and do not cross cut skeletal grains. Thin section photomicrograph, plane-polarized light. Cabin Creek 34-7, 8894 ft. U5 limestone subtidal zone.

E. Undulatory microstylolites subparallel to laminae in a finely crystalline dolomite. Such microstylolites are often difficult to distinguish from organic-rich laminae. Thin section photomicrograph, plane-polarized light. Cabin Creek 12-34, 9064 ft. U4 dolostone supratidal zone.

F. Pressure solution surface (arrow) between interpenetrating intraclasts composed of calcite. Black area extending across top of photo is a thick stylolite filled with dead oil. Thin section photomicrograph, plane-polarized light. Cabin Creek 34-7, 8872 ft. U3 limestone intertidal zone.

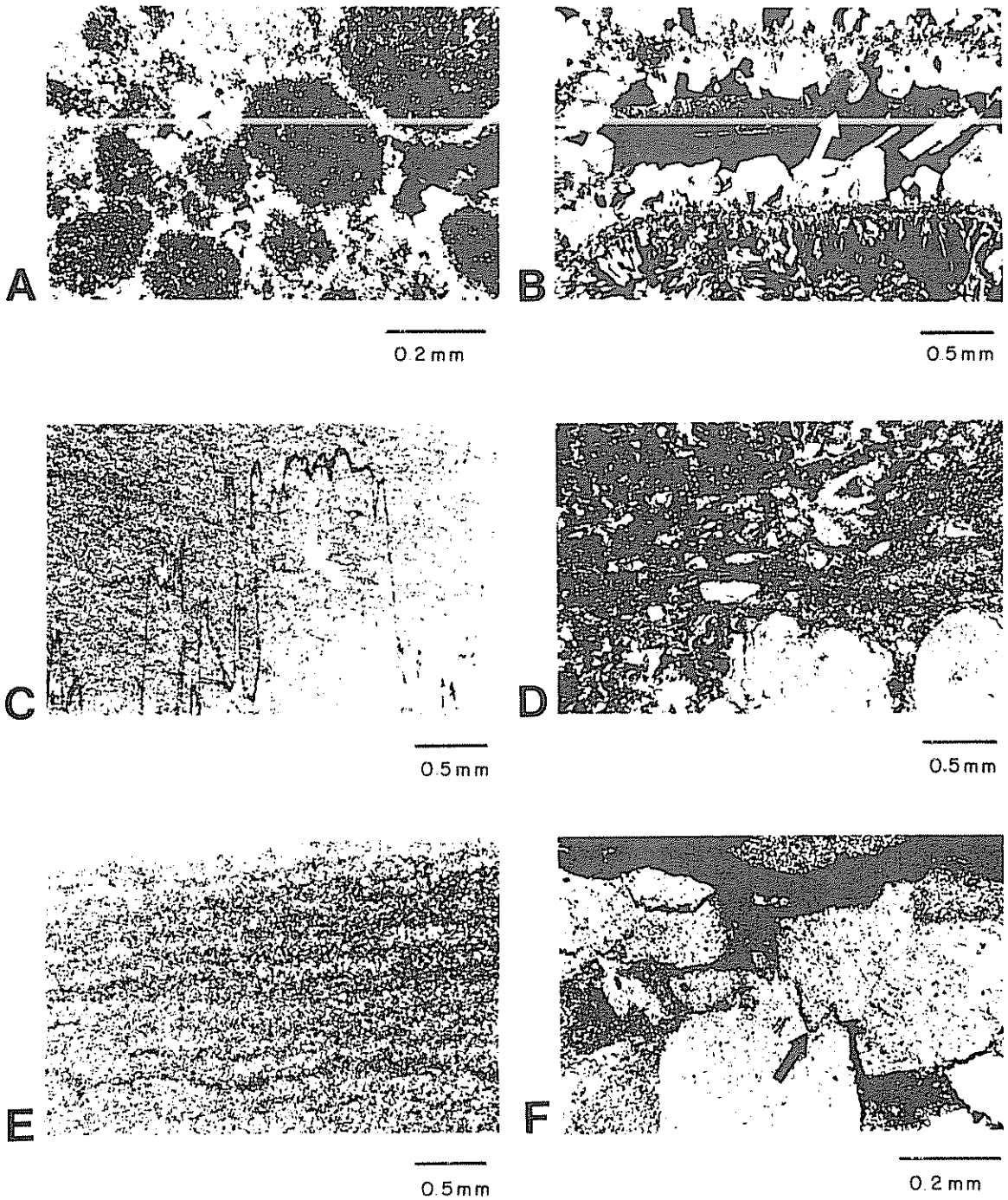

Figure 15

Pressure Solution

The effects of late diagenetic pressure solution are ubiquitous throughout the upper Red River as indicated by the abundance of stylolites. The stylolites are mostly irregular, low amplitude, subhorizontal, and are commonly multiple, although high amplitude stylolites occur locally (Figure 15C). Stylolites are most abundant in subtidal biomicrite-wackestones (lithofacies 1) and least abundant in supratidal dolostones (lithofacies 3 and 4). The lower abundance of stylolites in fine-grained dolomites was also noted by Carroll (1978) in the upper Red River Formation of North Dakota. This contrast of stylolite abundance may be the result of the lower solubility of dolomite in comparison to calcium carbonate.

The fact that dolomite is less susceptible to pressure solution than calcium carbonate is supported by the relationship between stylolites and dolomitic mottling in the limestone units. Stylolites commonly border but do not cross-cut dolomitic mottling. The irregular and distorted nature of dolomitized burrow mottling is a result of pressure solution. The presence of dolomite in the burrows thus appears to control stylolite shape and occurrence. In general, stylolites do not cross-cut skeletal or non-skeletal grains, nor do they cross-cut chert or anhydrite nodules. These findings are in concurrence with Wanless (1979) who concluded that primary sedimentary structures, composition, texture and fabric exert strong control on pressure solution.

Wispy, multiple microstylolites are common and may be too small to be detected in hand specimen (Figure 15D). Zones of multiple stylolites

are commonly undulatory, subparallel to bedding, and up to 3 or 4 centimeters thick. Horizontal microstylolites occur along laminae of fine-grained dolostones (lithofacies 3 and 4) and are difficult to distinguish from laminae composed of organic matter (Figure 15E). Effects of pressure solution are evident in examples where grains interpenetrate one another. The contact between such grains is usually a microstylolitic surface (Figure 15F).

Kendall (1976) estimated that the amount of rock volume removed from the Red River Formation by pressure solution may be on the order of 5 to 10 percent. Parts of the Red River more susceptible to pressure solution may have lost in excess of 25 percent.

Effects of pressure solution on permeability of Red River reservoir rocks have been discussed by Kendall (1976). He concluded that pressure solution has created tight and compact rocks in which the stylolitic planes themselves may account for much of the permeability. The presence of clay and organic insoluble residue along stylolite planes should, however, tend to obstruct fluid flow across stylolitic surfaces.

DISTRIBUTION OF POROSITY WITHIN UPPER RED RIVER RESERVOIRS

Porosity of the upper Red River Formation is restricted to the dolostone units and is a function of diagenetic overprint which in turn is a function of depositional environment. Four major types of porosity occur: vug, moldic, intercrystal, and interparticle. Typical vertical distributions of porosity percentage and permeability as determined by core analysis appear in Figure 8. Occurrence of the various porosity types with respect to environment of deposition is shown in Figure 10. Table 3 summarizes porosity, permeability, and saturation data for the U4 and U6 units as average values for cored wells and also shows the relative amounts of each porosity type.

Porosity Types and Associations

The important diagenetic events controlling porosity were dolomitization and post-depositional leaching of evaporitic sulfate minerals and calcium-carbonate grains. Occurrence of several types of interparticle porosity indicates that some primary porosity survived compaction and diagenesis; however, the vast majority of pore space originated as secondary porosity.

Interparticle Porosity

Interparticle porosity occurs most abundantly in the high energy intertidal zone of the U6 reservoir. The predominant sediment of this

Table 3. Summary of porosity, permeability, and saturation data for upper Red River reservoirs of Cabin Creek Field.

Zone	Porosity %	Perm (md)	Oil sat. (%)	Water sat. (%)	Total sat. (%)	Pore size (mm)	Relative amounts of each pore type			
							V	M	Ip	Ic
U4 supratidal	16.8	11.7	29.3	21.4	50.7	0.13	48%	13%	13%	26%
U6 supratidal	7.4	0.6	16.3	47.4	63.7	0.04	95%	5%	-	-
U4 intertidal	15.3	7.1	30.2	23.5	53.7	0.19	19%	81%	-	-
U6 intertidal	7.1	3.6	17.2	39.4	56.6	0.13	31%	31%	26%	11%
U4 subtidal	10.7	1.4	15.3	41.3	56.6	0.19	32%	64%	-	4%
U6 subtidal	9.4	2.3	16.2	44.3	60.5	0.17	25%	44%	10%	21%

V = vug, M = moldic, Ip = interparticle, Ic = intercrystal

zone consists of peloids, interclasts, ooids, and skeletal debris with varying amounts of lime-mud matrix. Interpelletal porosity occurs locally in supratidal sediments.

Vug Porosity

Vug porosity developed in the supratidal sediments as a result of vadose eogenetic leaching of evaporitic sulfate minerals. This mechanism was more effective in the U4, resulting in an average of 16.8% porosity (Figure 16A). In contrast, porosity of the U6 supratidal zone averages only 7.4%. This difference resulted from greater abundance of sulfate minerals in the U4, and also from textural differences between the U4 and U6 supratidal dolomites. Dolomite composing the U4 supratidal zone is finely crystalline and hypidiotopic, whereas dolomite composing the U6 supratidal zone is microcrystalline and xenotopic (Figure 16B). Scarcity of sulfate minerals in the U6 supratidal zone is due to climatic conditions being unfavorable to their formation at the time of deposition. Fewer sulfate minerals were available for leaching from the U6 supratidal zone and the fabric of the dolomite made it less permeable to percolating vadose waters.

Moldic Porosity

Moldic porosity occurs most abundantly in the intertidal and subtidal zones, and resulted from leaching of calcite and aragonite particles remaining after dolomitization of matrix material

FIGURE 16

A. Vug porosity in the supratidal zone of the U4 reservoir. Pores in black. Matrix is finely crystalline hypidiotopic dolomite. Cabin Creek 34-7, 8876 ft. Porosity = 17.6%. Permeability = 2.2 md. Cross-polarized light.

B. Vug porosity in the supratidal zone of the U6 reservoir. Arrow points to a partially dissolved anhydrite lath. Matrix is microcrystalline xenotopic dolomite. Cabin Creek 12-34, 9122 ft. Porosity = 3.8%. Permeability = 0.0 md. Cross-polarized light.

C. Moldic porosity in the subtidal zone of the U6 reservoir. Pores are black. Porosity resulted from dissolution of skeletal material. Note mold of brachiopod shell. Porosity has been partly occluded by anhydrite (see arrow). Matrix is microcrystalline dolomite. Cabin Creek 32-17, 9114 ft. Porosity = 13.4%. Permeability = 0.3 md. Cross-polarized light.

D. Moldic porosity in intertidal zone of the U4 reservoir. Pores are black. Arrow points to mold of gypsum rosette. Matrix is microcrystalline dolomite. Cabin Creek 34-7, 8881 ft. Porosity = 18.8%. Permeability = 3.7 md. Cross-polarized light.

E. Intercrystalline porosity in the subtidal zone of the U6 reservoir. Pores are black. Note zoning of dolomite crystals. Cabin Creek 41-20, 9176 ft. Porosity = 13.1%. Permeability = 92.1 md. Cross-polarized light.

F. Silica-filled moldic and interparticle porosity in the intertidal zone of the U6 reservoir. Matrix consists of peloidal dolomite. Cabin Creek 41-20, 9132 ft. Porosity = 2.0%. Permeability = 0.0 md. Cross-polarized light.

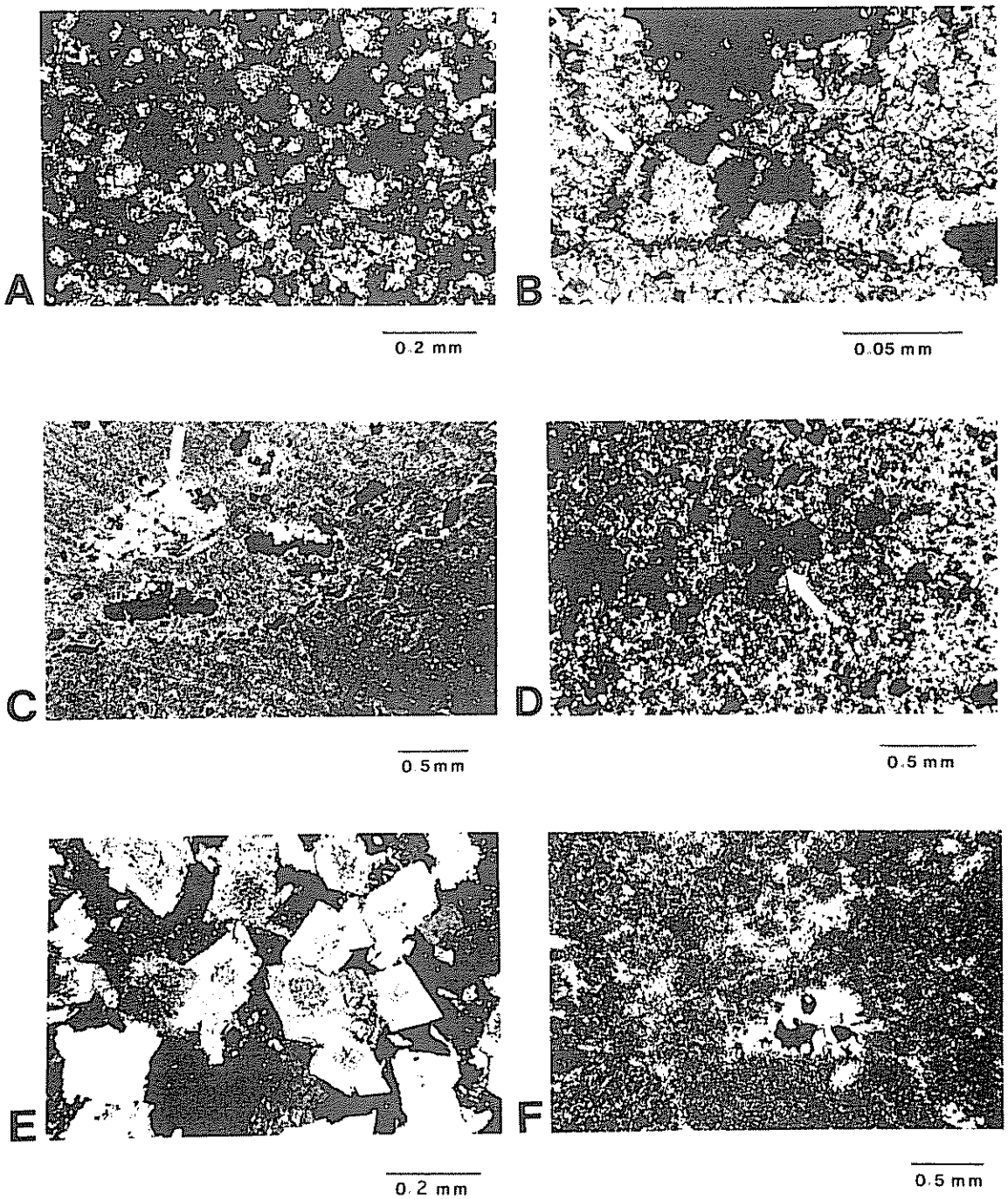

Figure 16

(Figure 16C). Some moldic porosity also developed by leaching of gypsum crystals from sediment prior to dolomitization (Figure 16D). Size and shape of moldic pores are a function of size and shape of leached particles and crystals. In many examples, molds have been enlarged by solution to form vugs which are much larger than vugs of the supratidal zone.

Intercrystal Porosity

Intercrystal porosity commonly occurs in the upper part of the U6 subtidal zone and resulted from pervasive dolomitization (Figure 16E). It also occurs locally in some supratidal and intertidal zones. Porosity measurements up to 20% and permeabilities over 100 md. occur where intercrystal porosity is well developed.

Vertical Distribution of Porosity

Figures A-1 through A-20 in the Appendix show the vertical distribution of porosity for cored wells of the U4 and U6 reservoirs. In addition to porosity, oil saturations, permeability, type of porosity, pore size (determined from thin section), and pore-throat size (determined from available capillary-pressure data) are also indicated, as are lithology and depositional environment. Most of this data is summarized in Table 3. Data concerning pore-throat size will be discussed in the section on pore geometry.

U4 Reservoir

It is evident from Figures A-1 through A-11 (see Appendix) that the vertical distribution of porosity and other related petrophysical parameters vary greatly in the case of the U4 reservor. In general, porosity of the U4 reservoir decreases downward. Porosity is greatest in the supratidal and intertidal zones of the U4 reservoir, and lowest in the subtidal zone (Table 3). Average porosity for the supratidal and intertidal zones is 16.8% and 15.3% respectively whereas average porosity of the subtidal zone is only 10.7%. The general downward decrease in U4 reservoir porosity is also illustrated by neutron logs as shown in Figures 4 and 8. Radioactivity, as measured by the neutron log, increases downward through the U4 reservoir,indicating a corresponding decrease in porosity.

Permeability is likewise of greater magnitude in the supratidal and intertidal zones; average values are 11.7 md and 7.1 md respectively. Permeability of the subtidal zone averages only 1.4 md. Oil saturation is also generally greater in the supratidal and intertidal zones.

The dominant porosity types of the U4 reservoir are vuggy, moldic, interparticle, and intercrystal. Vug porosity is most abundant in the supratidal zone. Vugs which occur in the intertidal and subtidal zones originated mostly by solution enlargement of what was originally moldic porosity, and are generally much larger in size than vugs of the supratidal zone. Moldic porosity is most abundant in the intertidal and subtidal zones but does occur locally in the supratidal zone, especially in the lower part. Interparticle porosity occurs only in the lower part

of the supratidal zone. Intercrystal porosity is common within the supratidal zone. It also occurs in the subtidal zone, but was found in only one well, the Cabin Creek #43-6.

Pore size within the U4 reservoir tends to increase downward. Pores within the intertidal and subtidal zones are generally larger than pores of the supratidal zone. Average size of pores in the supratidal zone is 0.13 mm, whereas average size of pores in both the intertidal and subtidal zones is 0.19 mm; 32% larger than pores of the supratidal zone. Pore size is basically a function of the kind of porosity. Larger pore sizes predominate in the subtidal zone where most of the porosity consists of molds and enlarged molds. In contrast, smaller pore sizes predominate in the supratidal zone where most of the porosity is vug or intercrystal.

U6 Reservoir

In contrast to the U4 reservoir, porosity of the U6 reservoir is most abundant in the subtidal zone; the average being 9.4% (Table 3). Average total porosity values for the U6 supratidal and intertidal zones are 7.4% and 7.1% respectively. Note that porosity values for all three depositional zones of the U6 are lower than the corresponding U4 reservoir porosity values. In comparision to the U4, porosity values of the U6 reservoir tend to increase downward rather than decrease. This contrast between the U4 and U6 reservoirs is also apparent from Figures A-1 through A-20 in the Appendix, and also Figures 4 and 8.

Permeability of the U6 reservoir is highest in the intertidal zone, where the average value is 3.6 md. Next highest is the subtidal zone, where permeability averages 2.3 md. Lowest permeability values of the U6 reservoir occur in the supratidal zone, where the average value is 0.6 md. These values of U6 permeability contrast sharply with those of the U4 reservoir. Permeability values of the U6 supratidal and intertidal zones are much lower than the corresponding values of the U4 reservoir, whereas permeability of the U6 subtidal zone is higher than that of the U4 subtidal zone. The vertical distribution of oil saturation is quite consistent throughout the U6 reservoir. Supratidal and intertidal zone oil saturations of the U6 are generally lower than those of the corresponding U4 reservoir zones.

The vertical distribution of porosity types in the U6 reservoir is more complex than that of the U4. Vug porosity is dominant in the U6 supratidal zone, as it is in the U4 supratidal zone. However, the vugs of the U6 supratidal zone are much smaller than those of the U4 (Table 3). Interparticle and intercrystal pores were not found to occur in the U6 supratidal zone. Small amounts of moldic porosity occur in the U6 supratidal zone. Whereas moldic porosity predominates in the intertidal zone of the U4, all four porosity types (vug, moldic, interparticle, and intercrystal) occur commonly in the intertidal zone of the U6 reservoir. Distribution of porosity types in the U6 subtidal zone is similar to that of the U4 subtidal zone, since moldic and enlarged moldic (vug) pores predominate in each. However, a zone of intercrystal porosity several feet thick occurs in the uppermost part of the U6 subtidal zone

(see Figures A-12 through A-20). This intercrystal porosity zone adds significantly to the reservoir quality of the U6 subtidal zone.

Pore size tends to increase downward through the U6 reservoir, as it does in the U4, since large molds are abundant in the intertidal and subtidal zones. Pores of the U6 subtidal zone are 76% larger than those of the U6 supratidal zone. Average pore sizes in the U6 reservoir are smaller than those of the U4. Note for example that the average pore size of the U6 supratidal zone is only 0.04 mm, where that of the U4 supratidal zone is 0.13 mm.

Lateral Distribution of Porosity

General variations in porosity across Cabin Creek Field are shown by electric log cross sections A-A' and B-B' (Figure 4). Figures 17 and 18 are fence diagrams constructed from core-analysis data, which show in detail the lateral distribution of porosity within the U4 and U6 reservoirs. The lateral heterogeneity of porosity in the U4 and U6 reservoirs is further illustrated by Figures 19 and 20, which are isopachous porosity maps of the respective reservoirs. These maps show amount of vertical feet of porosity greater than 10%, as determined from neutron logs, and serve to quantify the distribution of porosity over the field area.

U4 Reservoir

Areas of high porosity concentration within the U4 reservoir are apparent from Figures 17 and 19. Note that porosity-feet contours

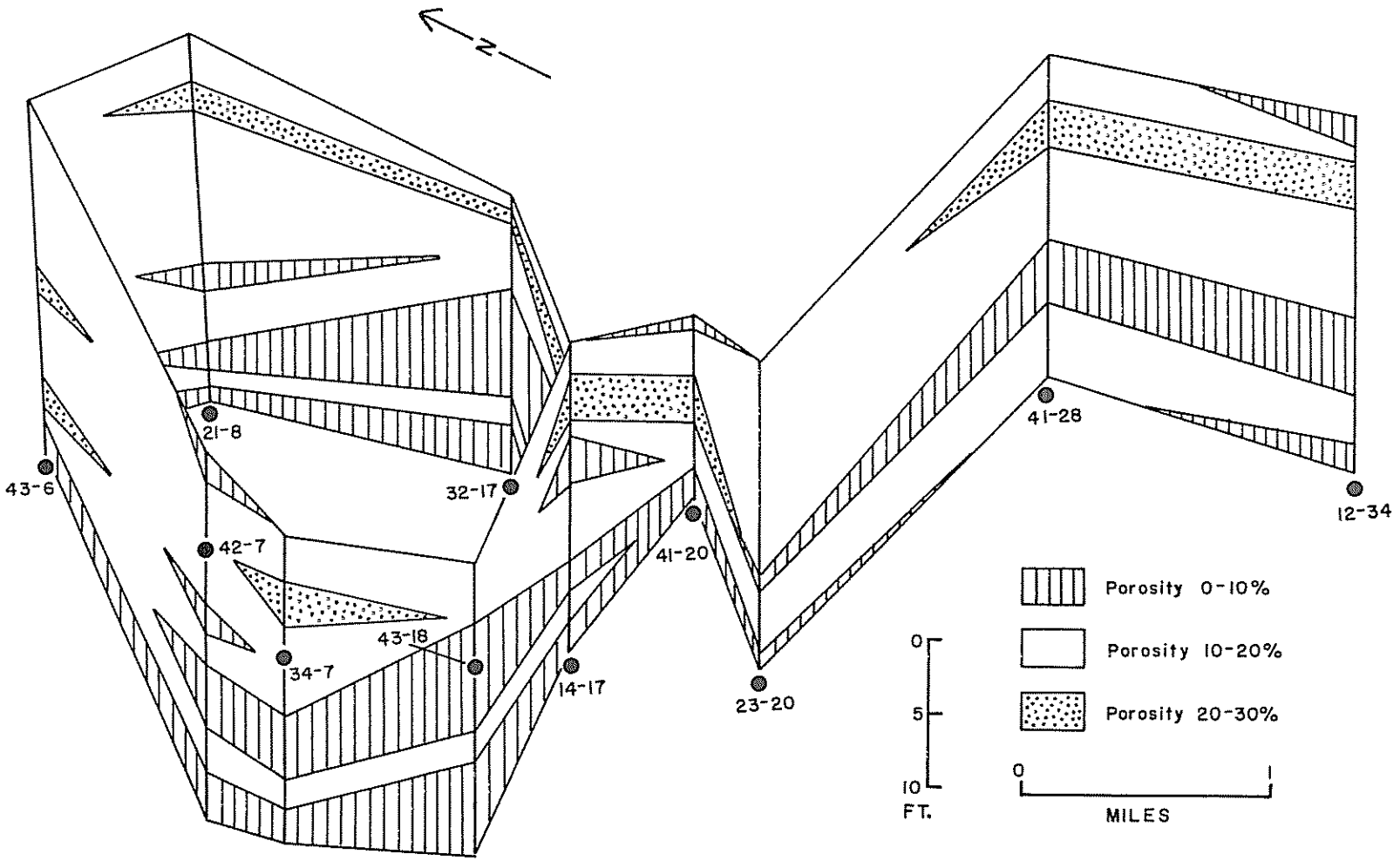

FIGURE 17. Fence diagram of U4 reservoir porosity distribution.

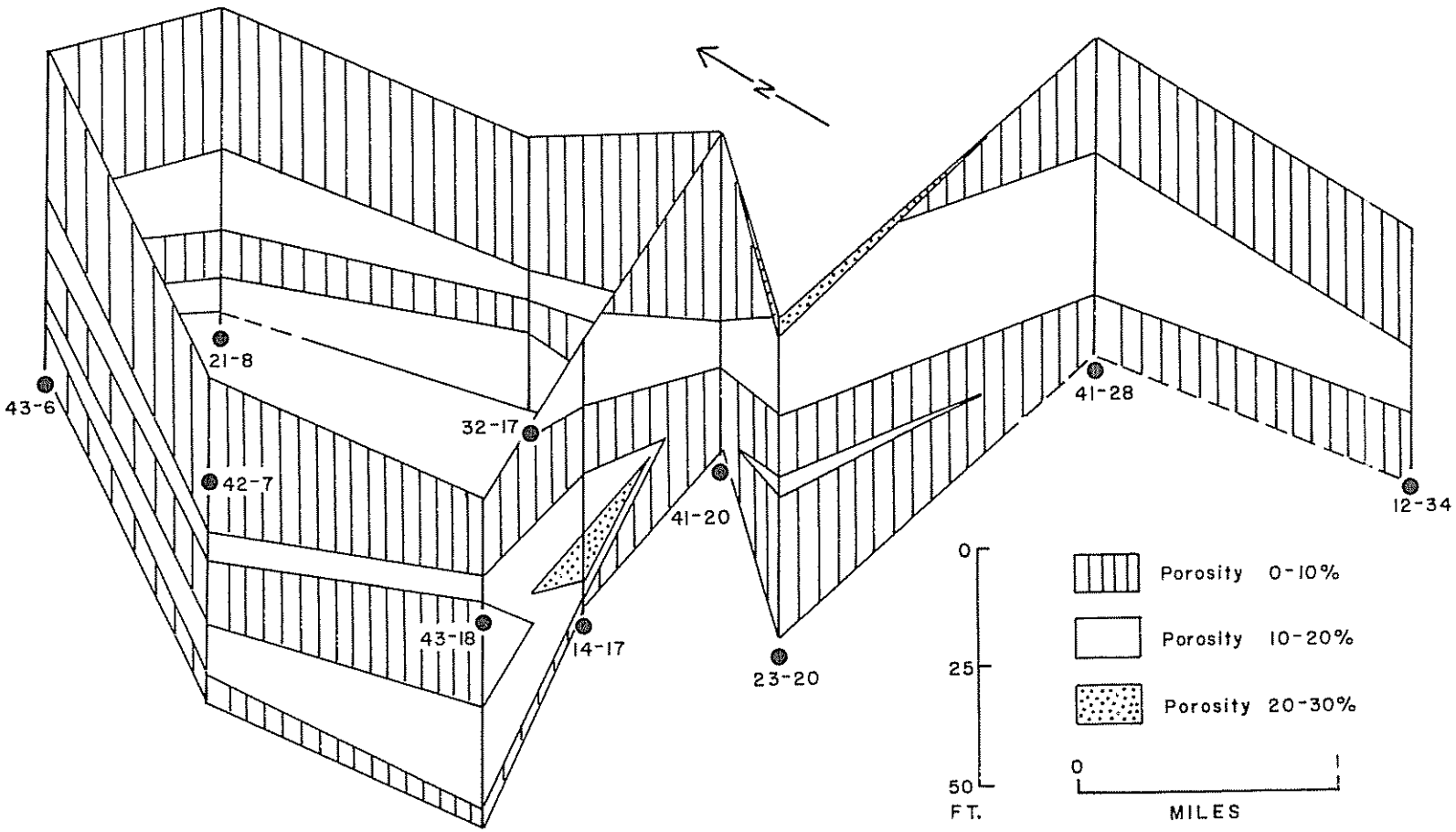

FIGURE 18. Fence diagram of U6 reservoir porosity distribution.

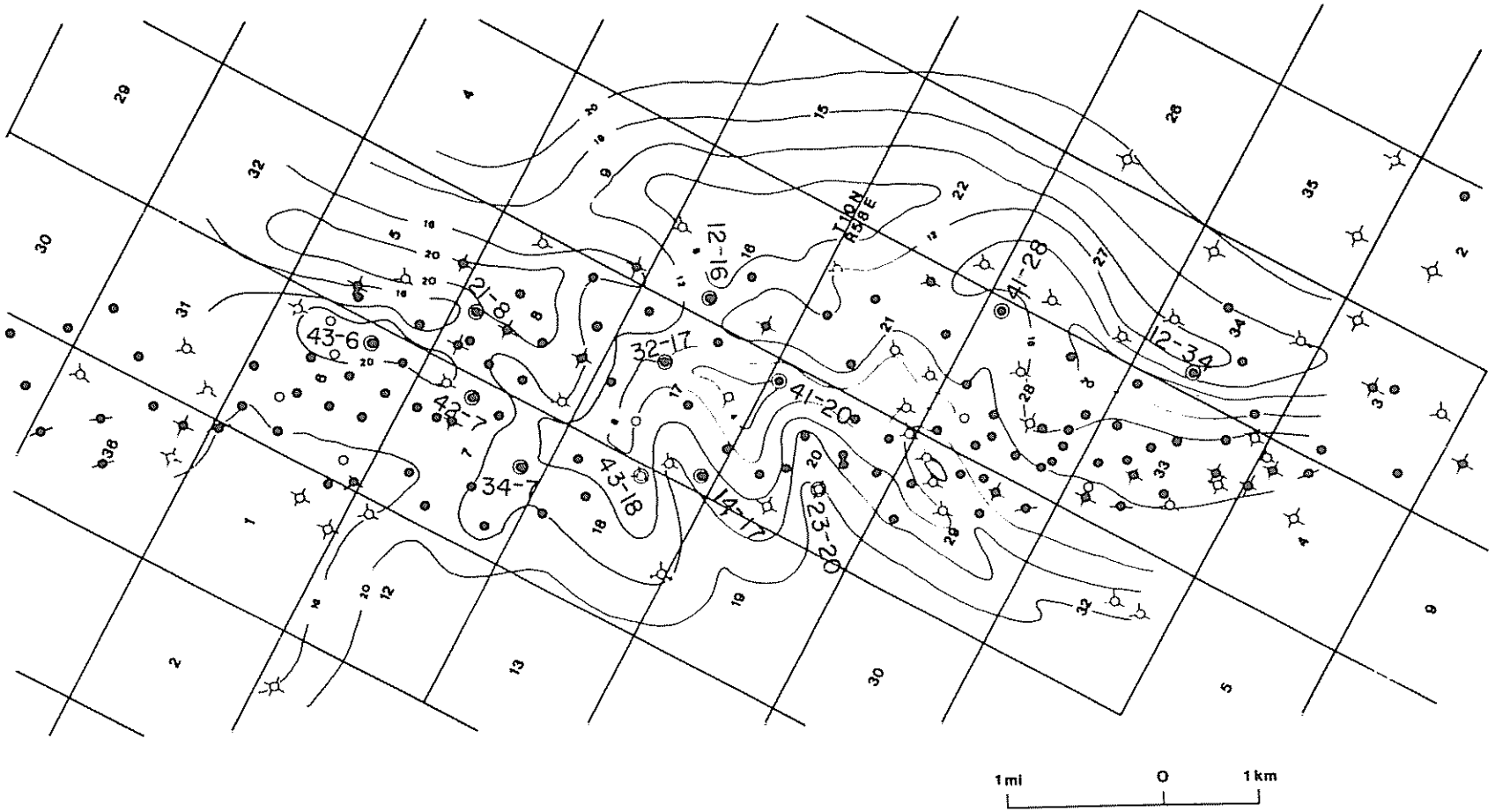

Contour interval = 4 feet

FIGURE 19. Isopachous porosity map of U4 reservoir showing feet of porosity greater than 10%.

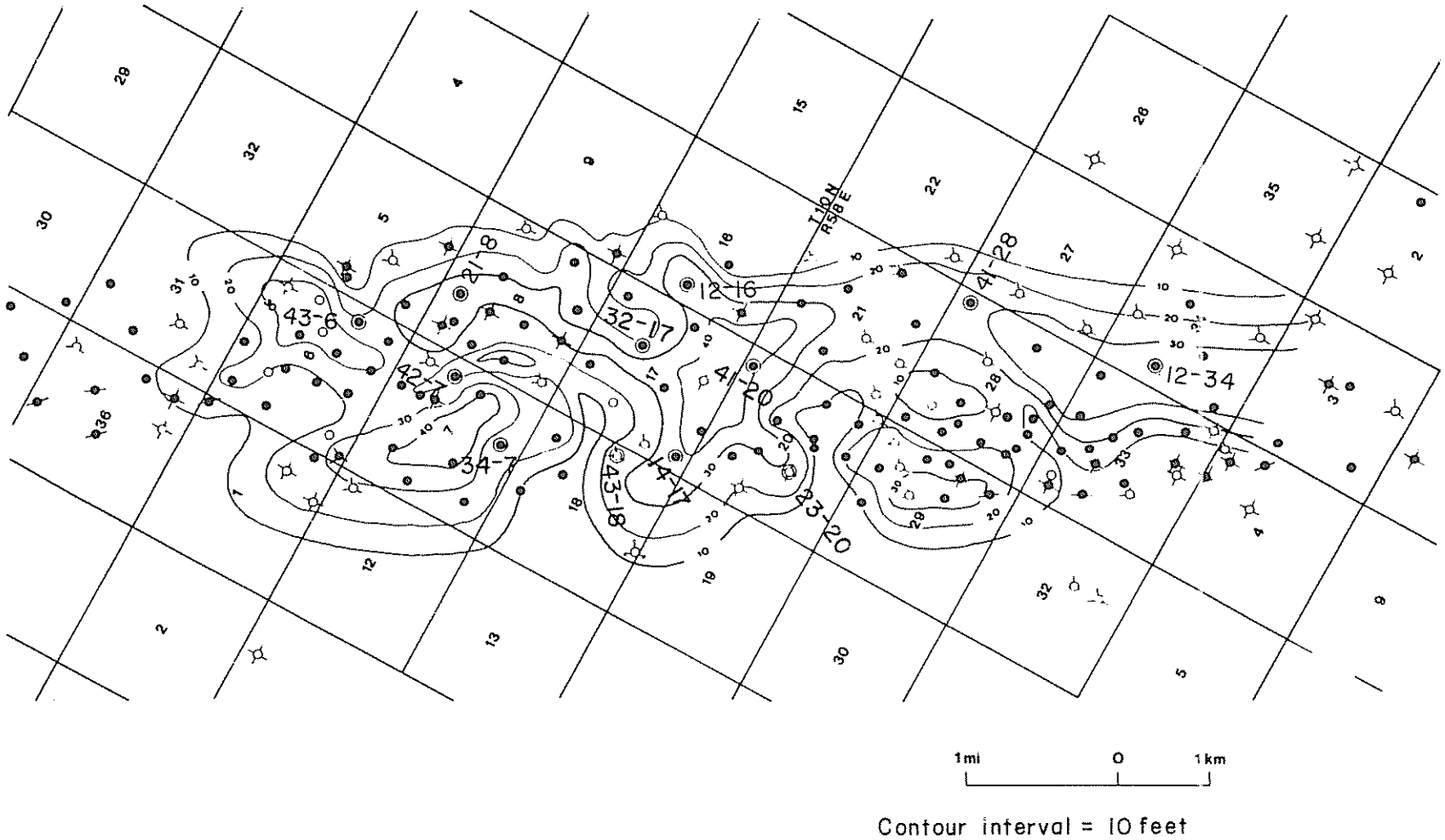

FIGURE 20. Isopachous porosity map of U6 reservoir showing feet of porosity greater than 10%.

(Figure 19) trend in a general north-south direction, roughly parallel to depositional strike. Comparing Figure 19 with Figures A-1 through A-11 (see Appendix), it is apparent that areas of high porosity-feet are related to lithology. Areas where the U4 reservoir has not been totally dolomitized have correspondingly low values of porosity-feet. Where the U4 has been completely dolomitized and is not interbedded with biomicrite-wackestone, these areas have correspondingly high values of porosity-feet. For example, the U4 reservoir of the Cabin Creek #43-6 well contains a thickness of 23 feet of dolomite (Figure A-10), and has 22 feet of porosity greater than 10%. In contrast, the U4 reservoir of the Cabin Creek #32-17 well contains 9 feet of dolomite (Figure A-9) and has only 8 feet of porosity greater than 10%.

Variations in dolomite fabric within the U4 reservoir have a great effect on the lateral distribution of porosity. As shown in Figure 5, the upper part of the U4 reservoir consists of finely crystalline dolomite (lithofacies 3) and the lower part consists of skeletal dolomite (lithofacies 5). The amount of porosity in the finely crystalline dolomite is typically much greater than that which occurs in the skeletal dolomite. Thickness of each lithofacies varies across the field, resulting in a corresponding variation in amount of porosity from well to well. For example, the U4 reservoir of the Cabin Creek #12-34 well contains 9 feet of finely crystalline dolomite (Figure A-6), whereas the Cabin Creek #43-18 well contains only 4 feet of finely crystalline dolomite (Figure A-2). Note that the corresponding porosities for these wells each show a sharp decline below the finely

crystalline/skeletal dolomite boundary. This difference in thickness accounts for a greater amount of porosity-feet in the Cabin Creek #12-34 well. Since finely crystalline dolomite occurs mostly within the supratidal zone, it can be said that porosity distribution relates indirectly to depositional environment. However, the porous, finely crystalline dolomite often overlaps into other environmental zones. In the Cabin Creek #12-34 well for example (Figure A-6), it extends down through the intertidal zone.

Distribution of porosity-feet across the field is also affected by the occurrence of chert and anhydrite cement zones. Reduction of porosity-feet is evident in wells which contain either or both cements. For example, the Cabin Creek #43-18 well contains a zone of chert cement at a depth of 8850 feet which has resulted in a corresponding reduction of porosity (Figure A-2). Silica and anhydrite cement zones of the U4 reservoir are, however, generally less than one foot in thickness and thus do not account for a major reduction of porosity-feet across the field. These cement zones are important in that they may act as permeability barriers to vertical movements of fluids within the reservoir. In some examples, chert cement zones are thick enough to show as anomalies on neutron logs, which can be correlated.

U6 Reservoir

Figure 18 is a fence diagram which shows distribution of U6 reservoir porosity across Cabin Creek Field and is based on core analysis data. Figure 20 is an isopachous porosity map of the U6

reservoir which shows amount of vertical feet of porosity greater than 10%. Note that high porosity-feet concentrations occur in areas which roughly coincide with high porosity-feet concentrations in the U4 reservoir (Figure 19). Porosity-feet contours of the U6 also trend in a north-south direction. The occurrence of dolomite, fabric of dolomite, and occurrence of chert and anhydrite cement zones, all account for lateral variations of porosity within the U6, just as in the case of the U4 reservoir.

Comparison of Figure 20 with Figures A-12 through A-20 (see Appendix) shows the relationship between dolomitization of the U6 and areas of high porosity-feet. For example, the U6 reservoir of the Cabin Creek #21-8 well contains a thickness of over 46 feet of dolomite (Figure A-17), and has 35 feet of porosity greater than 10%. In contrast, the U6 reservoir of the Cabin Creek #23-20 well contains 25 feet of dolomite (Figure A-20) and has only 27 feet of porosity greater than 10%. The relationship between dolomitization and distribution of porosity-feet within the U6 reservoir is not as consistent as for the U4 reservoir. Note that the U6 of the Cabin Creek #42-7 well contains 67 feet of dolomite (Figure A-14), yet has only 19 feet of porosity greater than 10%.

The fabric of the U6 dolomite is the most important factor controlling porosity distribution within this reservoir. As shown in Figure 5, the upper part of the U6 reservoir consists of microcrystalline dolomite (lithofacies 4) and the lower part consists of skeletal dolomite (lithofacies 5). Within the skeletal dolomite facies is a zone

of pervasive dolomite, the intercrystal porosity zone of the upper subtidal environment discussed previously. This pervasive dolomite, together with the rest of the skeletal dolomite facies, account for most U6 porosity. Porosity values within the microcrystalline dolomite facies are typically quite low. Distribution of porosity within the U6 depends mostly on thickness of the skeletal dolomite and the associated pervasive dolomite.

As in the case of the U4, thin zones of chert and anhydrite cement also affect porosity distribution within the U6 reservoir. A laterally persistent zone of chert cement, about one foot thick, occurs in the upper intertidal zone of the U6. In some cores this chert zone is nodular, in others, such as the Cabin Creek #21-8, the chert is massive. Chert and anhydrite cement zones of the U6 are thin and, as in the case of the U4, do not account for much reduction of porosity-feet.

PORE GEOMETRY FROM CAPILLARY PRESSURE CURVES

The pore system of a reservoir rock consists of larger spaces, referred to as pores, connected by smaller spaces, which are referred to as throats. Studies have shown that pore throats contribute very little to the total pore volume of a reservoir rock (Dullien and Dhawan, 1975). However, in order for a fluid, such as oil, to successively fill the pore spaces in any given reservoir rock, it must pass through the pore throats. The size, shape, and distribution of pore throats thus determines, to a great extent, the producibility of the reservoir rock. The physical makeup of the pore throats, together with that of the pores, defines the pore geometry of the reservoir rock.

Pore geometry may be determined quantitatively by study of mercury capillary-pressure curves, or qualitatively by study of thin sections and three-dimensional casts of the pore system. The theory, interpretation and use of mercury capillary-pressure curves are explained in the Appendix. It has been determined that capillary-pressure-curve shape is dependent on the size of the pore throats, and not on the size of the pores (Dullien and Dhawan, 1974 and 1975). This is because the mercury must pass through the throats in order to invade more and more of the rock sample being tested. Measurements obtained from capillary-pressure curves thus describe the geometry of the pore throats rather than geometry of the pores. Size and shape of pores are determined from thin section study. Pore throats are generally too small to be visually examined in thin section; most pore throats of dolomite reservoir rocks

are less than one micron in size. Examination of plastic resin casts of pore systems with a scanning electron microscope does provide an adequate method of qualitatively describing the geometry of throats.

Capillary-pressure curves were available for five cores of the U4 reservoir and one core of the U6 reservoir. Throat size at 50 percent saturation (d_{50}) for these cores is indicated in Figures A-1 through A-20 (see Appendix). Tables 4 and 5 are a summary of all pore-system geometry data for the U4 and U6 reservoirs respectively. The columns labeled pore size, pore shape, and pore sorting refer to measurements made on pores by thin-section analysis to be discussed in a later section. The remaining columns in Tables 4 and 5 refer to pore-throat geometry measurements from capillary-pressure curve data. Pore throat data include mean throat diameter (Dm), throat diameter at 50% mercury saturation (d_{50}), throat sorting (Sp), and throat skewness (Skp). Corresponding values of total porosity (Øt), effective porosity (Øe), and permeability are also indicated.

Pore-Throat Geometry of U4 Reservoir Rocks

Table 4 is a summary of U4 reservoir pore-system geometry data for five wells having available capillary-pressure curves. In addition to the above data, irreducible water saturation (Swi), critical pressure (Pcr), and threshold pressure (Pt) also appear in Table 4, since these parameters are also useful for comparison. Data for Table 4 are listed as average values for the supratidal, intertidal, and subtidal zones of

Table 4. Summary of pore system geometry and capillary pressure data for the U4 reservoir.

Well	Zone	Pore size (mm)	Pore shape	Pore sorting	Dm (μ)	d_{50} (μ)	Sp	Skp	φT (%)	φE (%)	Perm (md)	Swi (%)	Pcr (Kg/cm^2)	Pt (Kg/cm^2)
	Supratidal	0.06	SA	MS	1.40	1.02	0.64	+0.22	15.8	12.0	2.1	27	17.9	3.8
34-7	Intertidal	0.15	SR	PS	1.40	1.02	0.78	+0.19	17.1	13.0	2.1	30	16.3	4.2
	Subtidal	-	-	-	0.52	0.28	0.68	-0.35	10.8	6.0	0.4	76	27.0	-
23-20	Supratidal	0.13	SA	MS	1.80	1.60	0.95	+0.11	16.5	14.9	9.4	11	14.1	1.9
	Subtidal	0.25	SR	MS	0.64	0.26	0.65	-0.28	12.4	8.0	1.3	61	27.0	5.2
41-20	Supratidal	0.05	A	WS	3.90	3.73	0.91	+0.12	18.0	16.8	11.1	5	9.3	1.3
	Intertidal	0.20	R	PS	1.80	1.70	1.02	+0.23	21.3	19.6	9.3	12	14.4	1.6
	Supratidal	0.08	SA	MS	2.60	2.50	1.05	+0.09	17.9	16.7	27.0	5	18.6	4.0
32-17	Intertidal	0.09	SA	MS	2.00	2.15	1.00	+0.26	15.5	14.7	9.1	5	12.9	1.9
	Subtidal	0.44	SR	PS	0.42	0.19	1.57	-0.48	11.9	4.2	0.7	68	44.0	24.1
	Supratidal	0.12	SA	MS	2.20	2.10	0.89	+0.23	18.8	17.1	17.9	10	15.0	2.0
41-28	Intertidal	0.17	SR	MS	2.90	2.70	1.09	+0.92	19.5	16.8	31.5	13.1	16.3	2.7
	Subtidal	0.13	SR	PS	0.65	0.52	1.07	+0.08	12.3	10.0	1.6	20.6	35.3	4.9
		Average values for all 5 wells												
	Supratidal	0.09	SA	MS	2.38	2.19	0.89	+0.15	17.4	15.5	13.5	12	15.0	2.6
	Intertidal	0.15	SR	MS	2.03	1.89	0.97	+0.40	18.4	16.0	13.0	15	15.0	2.6
	Subtidal	0.27	SR	PS	0.56	0.31	0.99	-0.26	11.9	7.1	1.0	57	33.3	11.4

A = angular, R = rounded, SA = subangular, SR = subrounded

WS = well sorted, MS = moderately sorted, PS = poorly sorted

Table 5. Summary of pore system geometry and capillary pressure data for the U6 reservoir (one well only).

Well	Zone	Pore size (mm)	Pore shape	Pore sorting	Dm (μ)	d_{50} (μ)	Sp	Skp	φT (%)	φE (%)	Perm (md)	Swi (%)	Pcr (Kg/cm^2)	Pt (Kg/cm^2)
23-20	Supratidal	0.04	A	WS-MS	0.69	0.61	0.46	+0.16	13.5	11.8	1.9	21	22.2	7.2
	Intertidal	0.11	A-R	MS	0.16	0.07	0.41	-0.18	15.6	10.3	0.6	79	27.0	12.5
	Subtidal	0.12	A-R	MS-PS	1.7	1.8	0.67	+0.50	12.5	10.3	0.5	20	10.1	2.5

A = Angular, R= rounded, SA = subangular, SR = subrounded

WS = well sorted, MS = moderately sorted, PS = poorly sorted

the respective wells. Also shown are the average values for all five wells combined.

Throat Size

Mean throat diameter (Dm) generally decreases downward from the supratidal to the subtidal zone. Average throat diameter for the U4 supratidal zone is 2.38 microns, whereas those of intertidal and subtidal zones average 2.03 microns and 0.56 microns respectively. Values of throat diameter measured at 50% mercury saturation (d_{50}) exhibit the same downward decrease in magnitude as those of Dm. This is particularly evident for the Cabin Creek #41-28 well (Figure A-7), where D_{50} averages 2.10 micron in the supratidal zone, increases to 2.70 micron in the intertidal zone, and decreases sharply to an average of 0.52 micron in the subtidal zone.

Throat Sorting

Values of throat-size sorting (Sp) are a standard deviation measure and were determined graphically from cumulative-percent probability curves, constructed in turn from capillary-pressure curve data. As shown in Table 4, there is a slight trend toward poorer throat sorting downward from the U4 supratidal to subtidal zones (Sp increases downward). Average throat sorting value for the U4 supratidal zone is 0.89, whereas average values for the intertidal and subtidal zones are 0.97 and 0.99 respectively. All three average values are within the moderately sorted class.

Throat Skewness

Throat skewness (Skp) was also determined graphically and serves to indicate nonnormality of throat-size distribution. Skewness values indicate that a substantial difference in U4 reservoir throats exists among the various environmental zones. Average throat skewness value for the U4 supratidal zone is +0.15, indicating a fine-skewed throat-size distribution (excess of small throat sizes). Average throat skewness value for the U4 intertidal zone is +0.40, indicating a strongly fine-skewed throat-size distribution (large excess of small throat sizes). Average throat skewness value for the U4 subtidal zone is -0.26, indicating a coarse-skewed throat-size distribution (excess of large throat sizes).

Figure 21 is a plot of throat skewness (Skp) versus mean throat size (Dm) for U4 reservoir data. In this plot, the data points have been differentiated according to depositional zone. Note that the plot shows good distinction (dashed line) between pore throats of the subtidal zone and those of the supratidal and intertidal zones combined; on the basis of both throat size and skewness. Pore throats occurring in the subtidal zone are almost exclusively of negative skewness (coarse-skewed distribution), and have mean throat sizes less than 0.7 microns. In contrast, pore throats occurring in both the intertidal and supratidal zones generally have positive skewness (fine-skewed distribution), and tend to have mean throat sizes greater than 0.7 microns. The significance of this plot is that if U4 depositional environment is known for a particular part of Cabin Creek Field, then a

value range for both mean throat size and throat skewness can be predicted. Figure 21 thus establishes an important link between depositional environment and pore-throat geometry of the U4 reservoir. Of the 108 wells drilled in the development of Cabin Creek Field, only 5 have available capillary-pressure data with which to determine pore-throat geometry of the U4 reservoir. The necessity of being able to extrapolate pore geometry data across Cabin Creek, or any other oil field, cannot be overemphasized. It must however be understood that prediction of pore geometry is no easy matter even under the best of geological conditions. The effects of diagenesis account for many variables in reservoir pore geometry, as will be discussed in the sections to follow.

Figure 22 summarizes the basic similarities and differences among capillary-pressure curves of the U4 reservoir environmental zones. The curves shown are representative of the U4 supratidal, intertidal, and subtidal zones respectively. The shapes of the supratidal and intertidal capillary-pressure curves are quite similar and reflect the large pore-throat diameters, moderate throat sorting, and positive skewness typical of pore systems within these zones. Threshold pressure (Pt) averages 2.6 kg/cm^2 (52 psia) for both zones (Table 4), indicating the relative ease with which the mercury is able to begin penetrating the pore system. Average values of irreducible water saturations (Swi) for U4 supratidal and intertidal zones are 12% and 15% respectively. This indicates good interconnection between pores by throats of sufficient size to saturate most of the reservoir rock. Average value

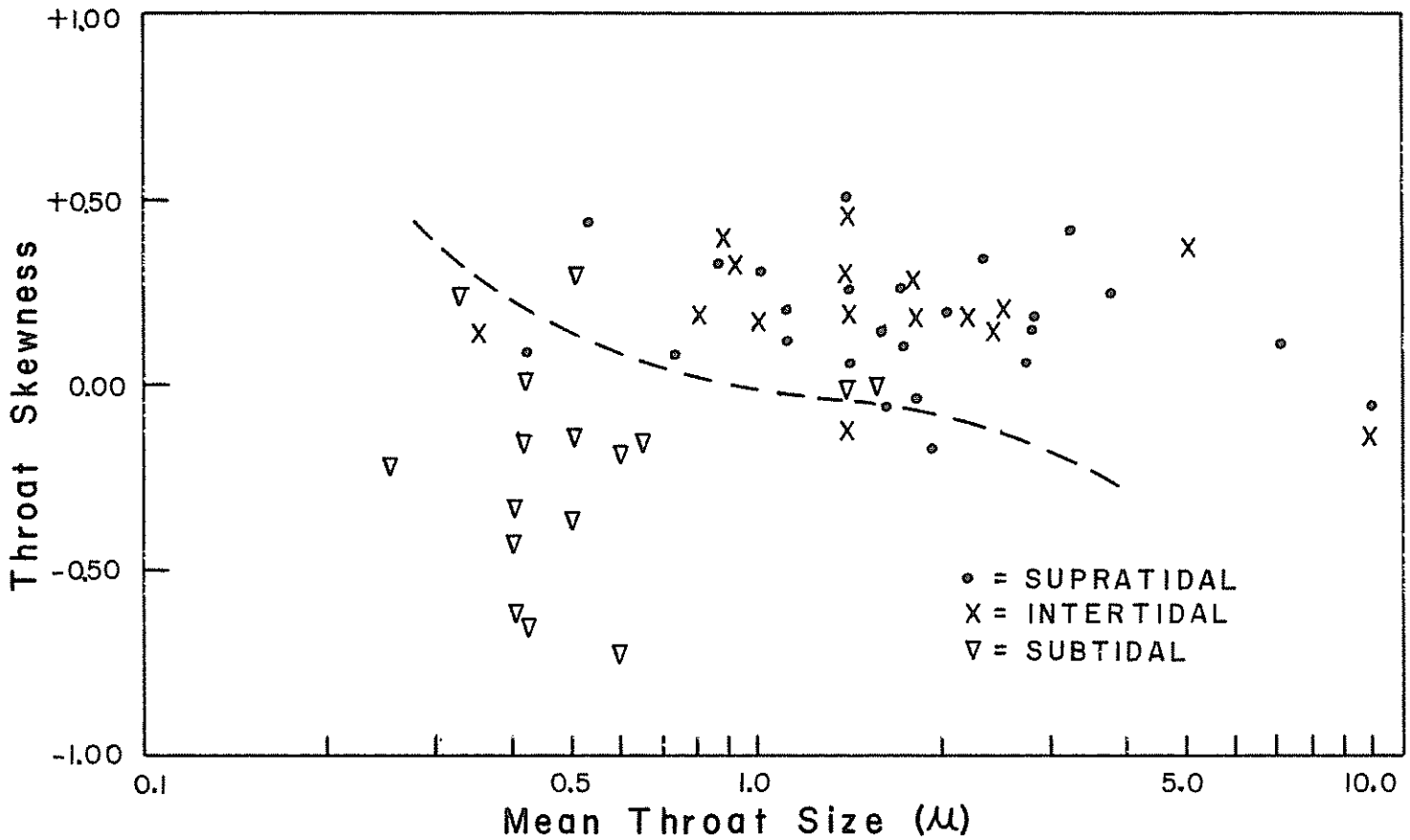

FIGURE 21. Plot of throat skewness versus mean throat size for U4 reservoir data.

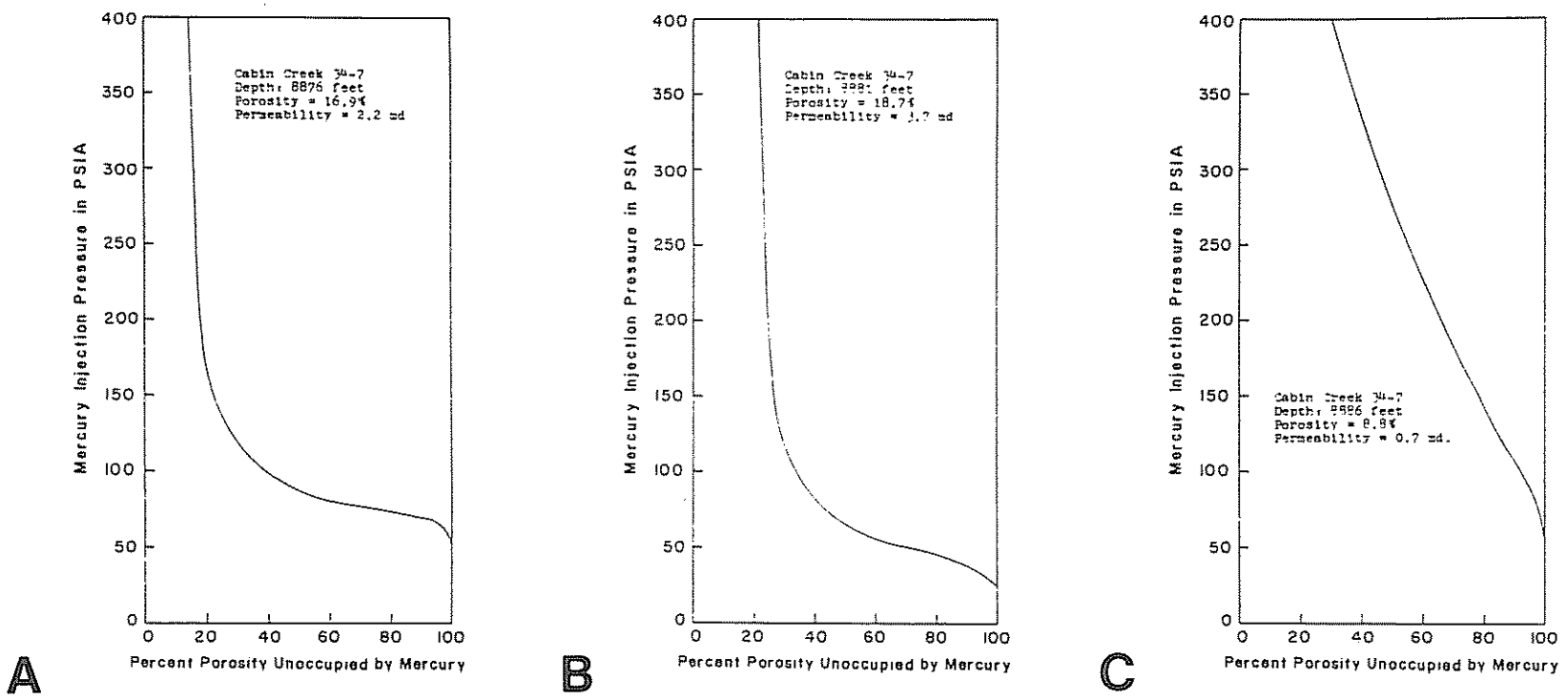

FIGURE 22. Typical U4 reservoir capillary pressure curves for (A) supratidal zone, (B) intertidal zone, and (C) subtidal zone.

of critical pressure is 15.0 kg/cm^2 (228 psia) for both zones, indicating that all available interconnected pores are saturated at relatively low pressure.

The shape of the subtidal capillary-pressure curve (Figure 22C) is quite different from those of the supratidal and intertidal zones and reflects the small pore throat diameters, moderate throat sorting, and negative skewness typical of pore systems within this zone. Threshold pressure (Pt) averages 11.4 kg/cm^2 (177 psia) for the subtidal zone, indicating that over four times as much pressure is needed to begin moving mercury through the pore system than is needed for the supratidal and intertidal zones. Average value of irreducible water saturation (Swi) for the U4 subtidal zones is 57%, indicating that pore throats are not of sufficient size or abundance to saturate most of the reservoir rock. Average value of critical pressure for pore systems of the U4 subtidal zone is 33.3 kg/cm^2 (488 psia), a value over twice as great as for the supratidal and intertidal zones. This indicates that high pressures are needed to saturate available pore space of the subtidal zone.

Pore-Throat Geometry of U6 Reservoir Rocks

Table 5 is a summary of U6 reservoir pore-system geometry data. Among the available core control, capillary-pressure curves were available for the Cabin Creek #23-20 well only. The data in Table 5 should not be construed as representative, but it does allow some comparison with U4 reservoir pore-system geometry data.

Throat Size

Mean throat size (Dm) of the U6 reservoir is highest in the subtidal zone (1.7 micron), and thus does not decrease downward from the supratidal to the subtidal zone as it does for the U4 reservoir. Mean throat diameters of the U6 supratidal and intertidal zones are 0.69 micron and 0.16 micron respectively, much smaller than the equivalent pore throats in the U4. Note, however, that mean throat size for the U6 subtidal zone is much larger than that of the U4 subtidal zone, reflecting the occurrence of intercrystalline porosity in the U6 subtidal zone. This is also shown by throat diameter values measured at 50% mercury saturation (Figure A-20).

Throat Sorting

Average throat sorting value (Sp) of the U6 reservoir all fall within the well to moderately sorted class. Highest values of Sp occur in the subtidal zone (0.67). Throat sorting values of the U6 supratidal and intertidal zones are quite similar, 0.46 and 0.41 respectively.

Throat Skewness

Average throat skewness value (Skp) of the U6 supratidal zone is similar to that of the U4 supratidal zone, +0.16 and +0.15 respectively. Thus pore throats of each reservoir have a fine-skewed size distribution (excess of small throat sizes) in the supratidal zone. Intertidal and subtidal throat skewness values of the U6, however, are quite different

from those of the U4. Average throat skewness value for the U6 intertidal zone is -0.18, indicating a coarse-skewed size distribution (excess of large throat sizes). Average throat skewness value for the U6 subtidal zone is +0.50, indicating a strongly fine-skewed size distribution (large excess of small throat sizes).

The large size and abundance of pore throats in the U6 subtidal zone are further documented by the low average values of threshold pressure (Pt), critical pressure (Pcr), and irreducible water saturation (Swi). Average threshold pressure for the U6 subtidal zone is 2.5 kg/cm^2 (50 psia), lower than any zone of the U4 reservoir. Threshold pressures for the U6 supratidal and intertidal zones average 7.2 kg/cm^2 (117 psia) and 12.5 kg/cm^2 (192 psia) respectively, indicating the relative difficulty of moving mercury through the small pore throats of these zones. Note, however, that despite the small size of U6 supratidal zone pore throats, the irreducible water saturation is 21%, indicating that most available pore space is interconnected by throats large enough for the mercury to pass through.

QUALITATIVE OBSERVATIONS OF PORE GEOMETRY

Pore geometry determined from capillary-pressure curve data applies mostly to pore throats, the interconnections between the actual pores. Determination of the geometry of the pores themselves is best done by study of thin sections, which present a two-dimensional view of pores, the size and shape of which can be determined petrographically. Plastic resin casts present a three-dimensional representation of pores and pore throats which can be studied with a scanning electron microscope. Resin casts of pore throats are particularly useful, since throats are usually too small and intricate for ordinary petrographic analysis by thin section. Optical microscopes lack sufficient depth of field for study of three-dimensional casts of pores and pore throats. As previously discussed, capillary-pressure curve data can be used to determine size and distribution of pore throats, but not the actual shape of the throats. Pore-throat shape is a function of the shape and arrangement of the dolomite crystals which line the throats of the reservoir rock.

Pore Geometry From Thin Sections

Pore size, shape, and sorting as determined by visual observation of thin sections are listed in Tables 4 and 5 for the U4 and U6 reservoirs respectively. Pore size is mostly a function of porosity type, as was previously discussed in the section on vertical distribution of porosity. The shape and sorting of pores also depend upon pore type. For example, in those parts of the reservoir where moldic porosity

predominates, the shape and sorting of the pores is mostly a function of the shape and sorting of the particles leached to produce the pores.

Pores of the U4 and U6 supratidal zones are subangular to angular in shape and are well to moderately sorted, because in both zones most of the pores were created by leaching of angular, well sorted anhydrite crystals from the original sediment. Subrounded, moderately sorted pores of the intertidal zones reflect the geometry of the original sediment particles (peloids, ooids, pellets, skeletal grains, etc.) which were leached out to create moldic and enlarged moldic porosity. Subtidal zone pores are subrounded and moderate to poorly sorted. The moldic porosity of the subtidal zone resulted from leaching of skeletal grains consisting of many different types and sizes. Enlargement of molds by dissolution of the enclosing sediment results in rounding of the pores.

Pore Geometry From Resin Casts

Examples of the various U4 and U6 reservoir pore systems are illustrated in Figures 23 through 30. Each figure consists of (A) a scanning-electron micrograph of the reservoir rock, (B) a scanning-electron micrograph of the resin cast corresponding to the reservoir rock pore-system, (C) the equivalent mercury capillary-pressure curve, and (D) a photomicrograph of the reservoir rock pore space. The scanning-electron micrographs present a comparison between the morphology of the dolomite crystals composing the various reservoir rocks and morphology of the corresponding pore space as revealed by the resin

cast. The equivalent mercury capillary-pressure curve is shown in each case so that the curve shapes can be related to the actual pore-throat geometry as revealed by the scanning-electron micrographs. The photomicrographs show geometry of the pore spaces as seen in thin section. Porosity percent and permeability are indicated for each case.

Supratidal Zone Pore Geometry

Pores of the U4 supratidal zone consist of vugs which resulted from the dissolution of anhydrite, as well as molds, interparticle, and intercrystal types (Table 3). Figure 23 shows the pore and pore-throat geometry for U4 supratidal dolomite in which the porosity consists of vug and interpelletal types. Crystals composing the U4 supratidal dolomite are finely crystalline (10-60 micron size) and have a predominantly hypidiotopic fabric. As a result, many voids between individual crystals are tabular in shape and are about 2 microns in thickness (Figure 23B). Throats of this shape, which occur as sheet-like spaces at crystal boundaries are termed "interboundary-sheet pores" and have been found to range in thickness from less than 0.1 micron to 4.0 micron (Wardlaw, 1976). Other throats of this sample are complex in shape, being bounded by many planar surfaces. Voids of this nature may be described as polyhedral (Wardlaw, 1976). This void space, existing between the dolomite crystals, comprises the pore throats which interconnect the pores. Hydrocarbons must pass through these voids to reach the adjoining pores. Capillary-pressure curve shape indicates good reservoir properties, since 80% of the pore system is filled by mercury at less than 150 psia pressure (Figure 23C).

Figure 24 shows the pore-system geometry for a sample containing vug pores. In this particular example the sample has 9.6% porosity but very low permeability. The dolomite crystals are packed more closely than was shown in the previous example, resulting in smaller throat sizes, many of which are less than one micron in size (Figure 24B). As a result, only about 55% of the pore space is interconnected, as shown by the corresponding capillary-pressure curve (Figure 24C).

Pores of the U6 supratidal zone consist mostly of vugs of similar origin to those of the U4 supratidal zone (Table 3). However, vugs of the U6 supratidal zone are generally much smaller (compare Figure 25D with Figure 24D). Figure 25 shows pore-system geometry typical of the U6 supratidal dolomites. Crystals composing the U6 supratidal dolomite are microcrystalline (less than 10 micron size) and have a predominantly xenotopic fabric. The resulting pore throats are tabular to irregular in shape and much smaller in thickness than throats of the U4 supratidal zone. Although throats of the U4 supratidal dolomite may locally occur up to several microns in size, these usually taper down to submicron size in a short distance. Capillary-pressure curve shape indicates poor reservoir quality, since a pressure in excess of 350 psia is required to saturate 50% of the pore space (Figure 25C). Note that although porosity for this sample is 10.0%, permeability is very low.

Figure 26 shows the pore geometry for a sample containing some moldic as well as vug pores. In this example, porosity is 16.0% and permeability is 1.2md, much higher than average for the U6 supratidal zone. The dolomite crystals are more of a hypidiotopic fabric and thus

the throats have more planar boundaries and are larger in size than the previous example. Capillary-pressure-curve shape indicates much better reservoir quality (Figure 26C).

Intertidal Zone Pore Geometry

Pores of both the U4 and U6 reservoir intertidal zones consist mostly of molds and enlarged molds (vugs) created by the dissolution of a variety of sedimentary particle types and also leaching of gypsum crystals. In addition, the U6 intertidal zone contains a substantial amount of interparticle porosity (Table 3). Available data indicates that pore throats of intertidal U6 dolomites are similar in shape but smaller than those of the intertidal U4 dolomites (Tables 4 and 5). Small throat size, as well as the occurrence of silica cement, account for the low porosity, low permeability, and poor reservoir quality of the U6 intertidal zone.

Figure 27 shows the pore geometry of a highly porous and permeable dolomite of the U4 intertidal zone. The dolomite crystals are hypidiotopic to xenotopic and range in size from about 3 micron to 30 micron. Crystal shape and the wide range of crystal size has resulted in irregular-shaped throats which may locally be over 10 microns in width (Figure 27B). Large throat size has created an excellent reservoir rock as shown by the capillary-pressure curve (Figure 27C). Over 80% of the available pore space is saturated at a pressure of only 100 psia. The amount, size and distribution of pores also contributes to the good reservoir properties of this rock, in that since the pores

are large and close to one another, fluids moving through the throats have only a short distance to traverse in order to reach the next pore (Figure 27D).

Subtidal Zone Pore Geometry

Moldic porosity predominates in subtidal sediments of the upper Red River reservoirs. Pore geometry of subtidal dolomites associated with moldic pores is shown in Figures 28 and 29. Figure 28 shows the pore geometry of a U4 subtidal dolomite with moderate porosity but low permeability. The dolomite crystals are predominantly hypidiotopic and are bimodal in size, the larger mode being 20-80 microns and the smaller mode 1-5 microns. The associated throats have a wide range of sizes, are irregular in shape, and have a heterogeneous distribution (Figure 28B). Capillary-pressure curve shape indicates that 80% of the pore space is saturated by mercury, but high pressure (350 psia) is required to attain this amount of saturation. Note that the mercury begins to enter the rock pore system at a pressure of only about 15 psia and maximum saturation is not attained until 400 psia pressure has been applied. Such a gradual filling of the available pore space results from the wide range (poor sorting) of throat sizes.

Figure 29 shows the pore geometry of a U4 subtidal dolomite having very low permeability and extremely poor reservoir characteristics, as indicated by the capillary-pressure curve. Only 5% of the available pore space has been saturated by mercury at a pressure of 400 psia (Figure 29C). Despite this low penetration by the mercury, porosity is

11.0% and pore throats were found to exist, but are very small in size. Dolomite crystals composing the rock matrix are xenotopic and microcrystalline, with larger dolomite crystals occurring locally. Pore throats are polyhedral to irregular in shape.

Observations of pore casts and thin sections have shown that pore throats associated with moldic porosity of the U6 subtidal zone are similar to those of the U4 subtidal zone, the matrix dolomite crystals being hypidiotopic to xenotopic and microcrystalline to finely crystalline size. However, within the uppermost part of the U6 subtidal dolomite is a zone of intercrystal porosity which occurs up to several feet in thickness. The finely crystalline, idiotopic to hypidiotopic dolomite crystals composing the matrix has resulted in corresponding pore throats which are tabular to polyhedral and quite large (Figure 30B). Note that in areas where the crystals were packed closely to one another, interboundary sheet-pores occur. Where the crystals are widely separated, tabular pore throats several microns in thickness occur. In many areas it is difficult to distinguish pore throats from pores.

The large, moderately sorted, open pore system of this intercrystal porosity zone has resulted in an excellent reservoir rock, as indicated by the capillary-pressure curve (Figure 30C). About 70% of the available pore space is saturated by mercury at 150 psia pressure. Note that porosity in this case is a moderate 11.3% and permeability is only 0.2 md, yet the size and arrangement of pore space and throats provide good reservoir properties.

Summary and Discussion

The examples of reservoir-rock pore system geometry discussed above show that size and shape of pore throats depend on size and shape of the dolomite crystals composing the matrix of the rock. The most important pore-geometry factor affecting reservoir quality is the size of the pore throats. In general, reservoir rocks of higher porosity, say over 15%, have pore throats large enough to insure good reservoir properties. In contrast, throat size in reservoir rocks of moderate porosity, ranging from about 9-14%, may be highly variable. Two reservoir rocks having the same porosity percentage may thus have vastly different reservoir properties resulting from a difference in throat size (compare Figures 29 and 30).

The relationship between pore-throat geometry and growth of dolomite matrix crystals has been discussed by Wardlaw (1976), who concluded that progressive changes in pore geometry occur as dolomite crystals grow, and that inhibition of crystal growth is of fundamental importance to the preservation of pore spaces in dolomites. His model of pore geometry evolution is that initial polyhedral pores are reduced to tetrahedral pores, which in turn may be eliminated to leave interboundary-sheet pores at the sites of compromise boundaries. The occurrence of solid bitumen residues as intergrain sheets, and the relatively large volume occupied by interboundary-sheet pores in some dolomites, provides evidence both direct and indirect, that these pores actually exist in the subsurface and are not the result of depressuring during core recovery (Wardlaw, 1976).

The present study found no relationship between throat size and throat shape for the upper Red River dolomites. Even very small throats were found to have highly complex shapes (Figure 29). Interboundary-sheet pores occur within reservoir rocks of both large and small mean throat size.

FIGURE 23

A. Finely crystalline, hypidiotopic dolomite crystals of the U4 supratidal zone. Cabin Creek 41-28, 9043 ft. Scanning electron micrograph.

B. Pore cast of above sample. Dolomite has been completely dissolved by acid so that plastic resin cast of pore throats stands in relief. Pore throats of this sample are tabular (sheet-like) and polyhedral in shape. Scanning electron micrograph.

C. Mercury capillary pressure curve for above sample. Curve shape indicates good reservoir properties. Mean throat size = 1.8 micron. Throats are poorly sorted (Sp = 1.12) and coarse-skewed (Skp = -0.04).

D. Thin section photomicrograph for above sample. Pore space (black areas) consists of vug and interpelletal types. Crossed nicols.

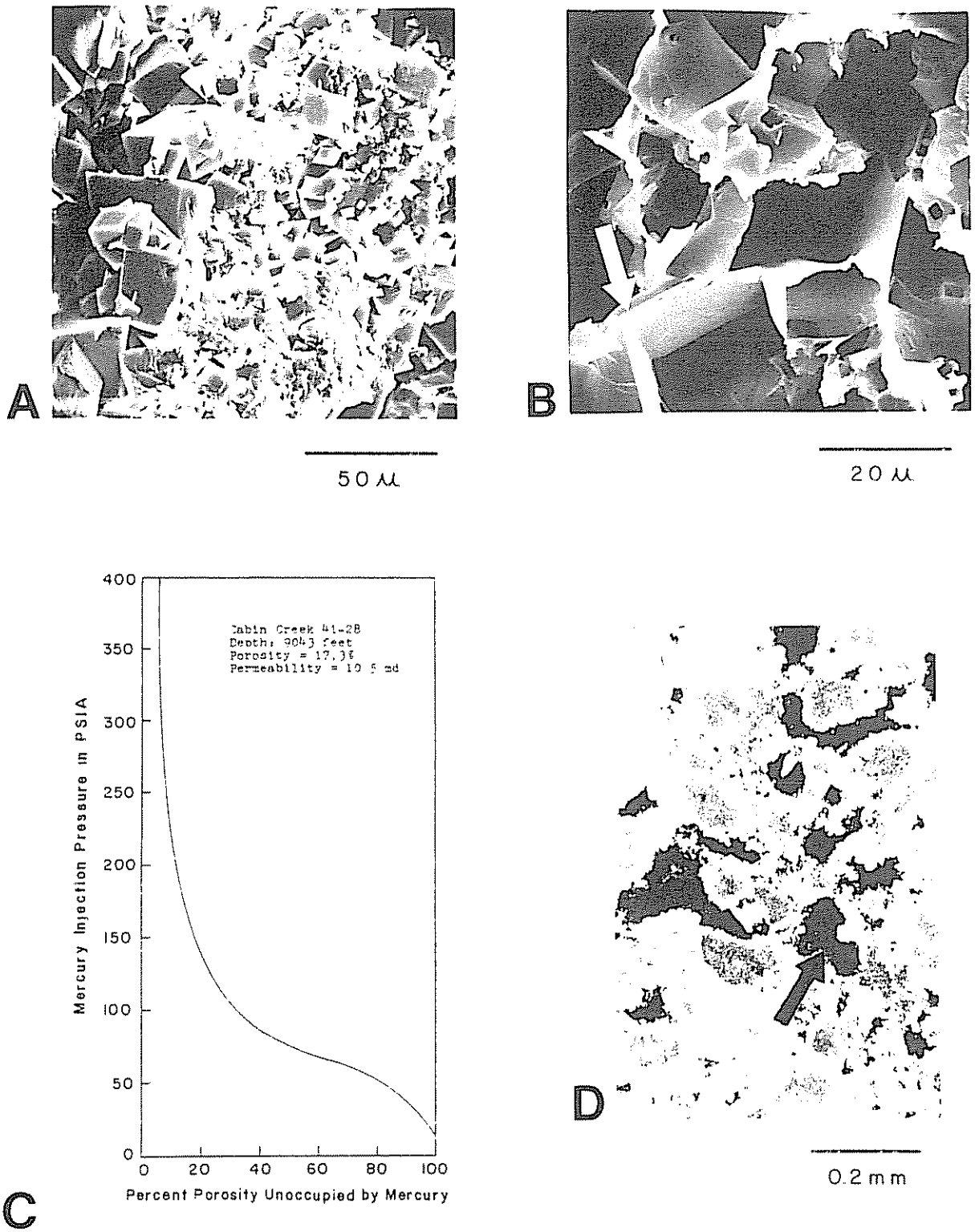
A
50 μ
B
20 μ
Cabin Creek 41-28
Depth: 9043 feet
Porosity = 17.3%
Permeability = 10.5 md
Mercury Injection Pressure in PSIA
400
350
300
250
200
150
100
50
0
0
20
40
60
80
100
Percent Porosity Unoccupied by Mercury
C
D
0.2 mm

Figure 23

FIGURE 24

A. Finely crystalline, hypidiotopic dolomite crystals of the U4 supratidal zone. Cabin Creek 41-28, 9040 ft. Scanning electron micrograph.

B. Pore cast of above sample. Pore throats are narrow, tabular to polyhedral in shape, due to close packing of the matrix dolomite crystals. Scanning electron micrograph.

C. Mercury capillary pressure curve for above sample. Curve shape indicates poor reservoir properties despite 9.6% porosity. Irreducible water saturation is 45%. Mean throat size = 0.52 micron. Throats are moderately well sorted (Sp = 0.68) and fine-skewed (Skp = +0.43).

D. Thin section photomicrograph for above sample. Pore space consists of vugs. Crossed nicols.

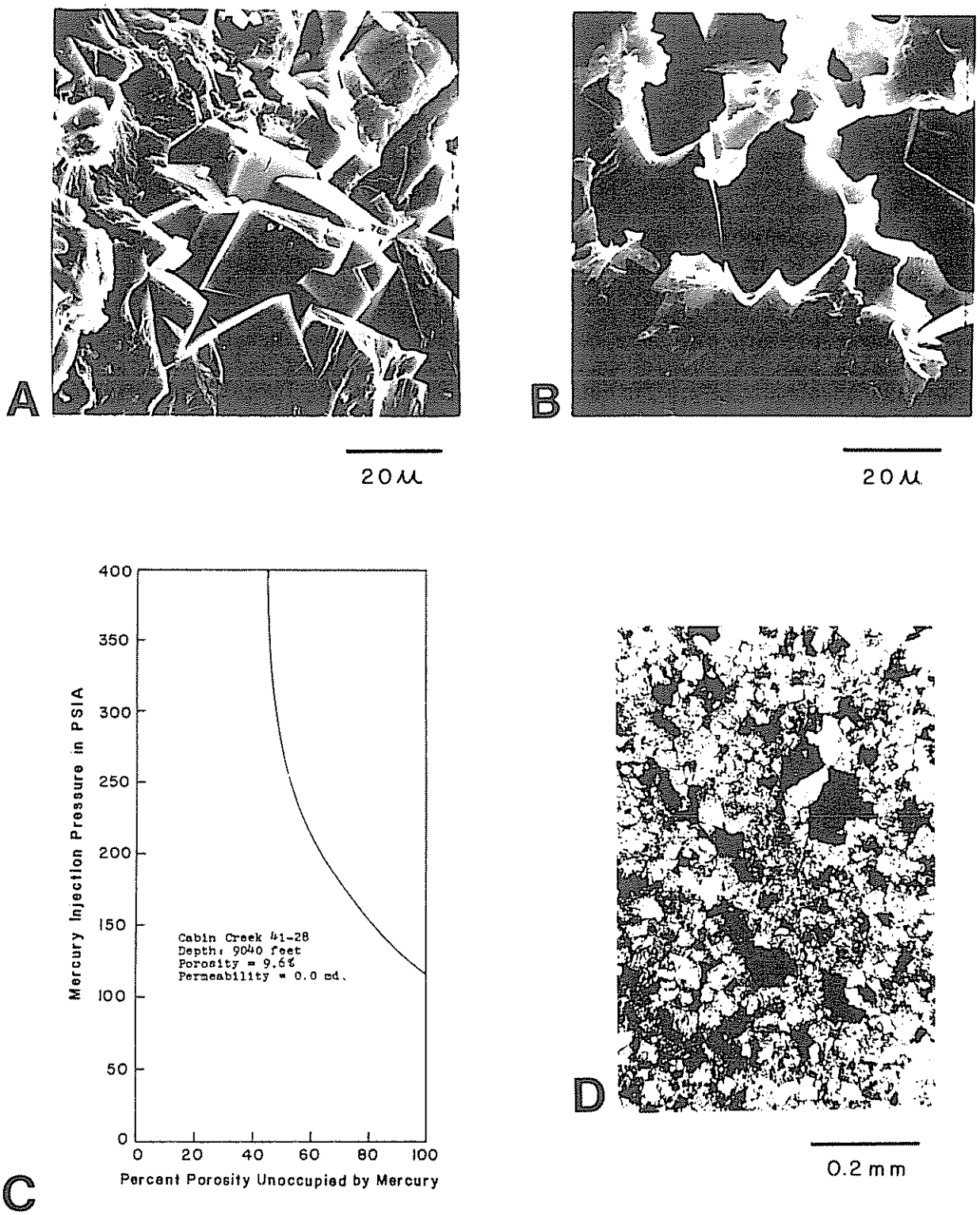
A
20μ
B
20μ
400
350
300
250
200
150
100
50
0
Mercury Injection Pressure in PSIA
Cabin Creek 41-28
Depth: 9040 feet
Porosity = 9.6%
Permeability = 0.0 md.
0
20
40
60
80
100
Percent Porosity Unoccupied by Mercury
C
D
0.2 mm

Figure 24

FIGURE 25

A. Microcrystalline, xenotopic dolomite crystals of the U6 supratidal zone. Cabin Creek 23-20, 8838 ft. Scanning electron micrograph.

B. Pore cast of above sample. Pore throats are tabular to irregular and tube-like in shape, much smaller than throats of the U4 supratidal zone. Scanning electron micrograph.

C. Mercury capillary pressure curve for above sample. Curve shape indicates poor reservoir quality within the range of injection pressures shown. Mean throat size = 0.36 micron. Throats are very well sorted (Sp = 0.30) and coarse-skewed (Skp = -0.12).

D. Thin section photomicrograph for above sample. Pore space consists of small vugs. Crossed nicols.

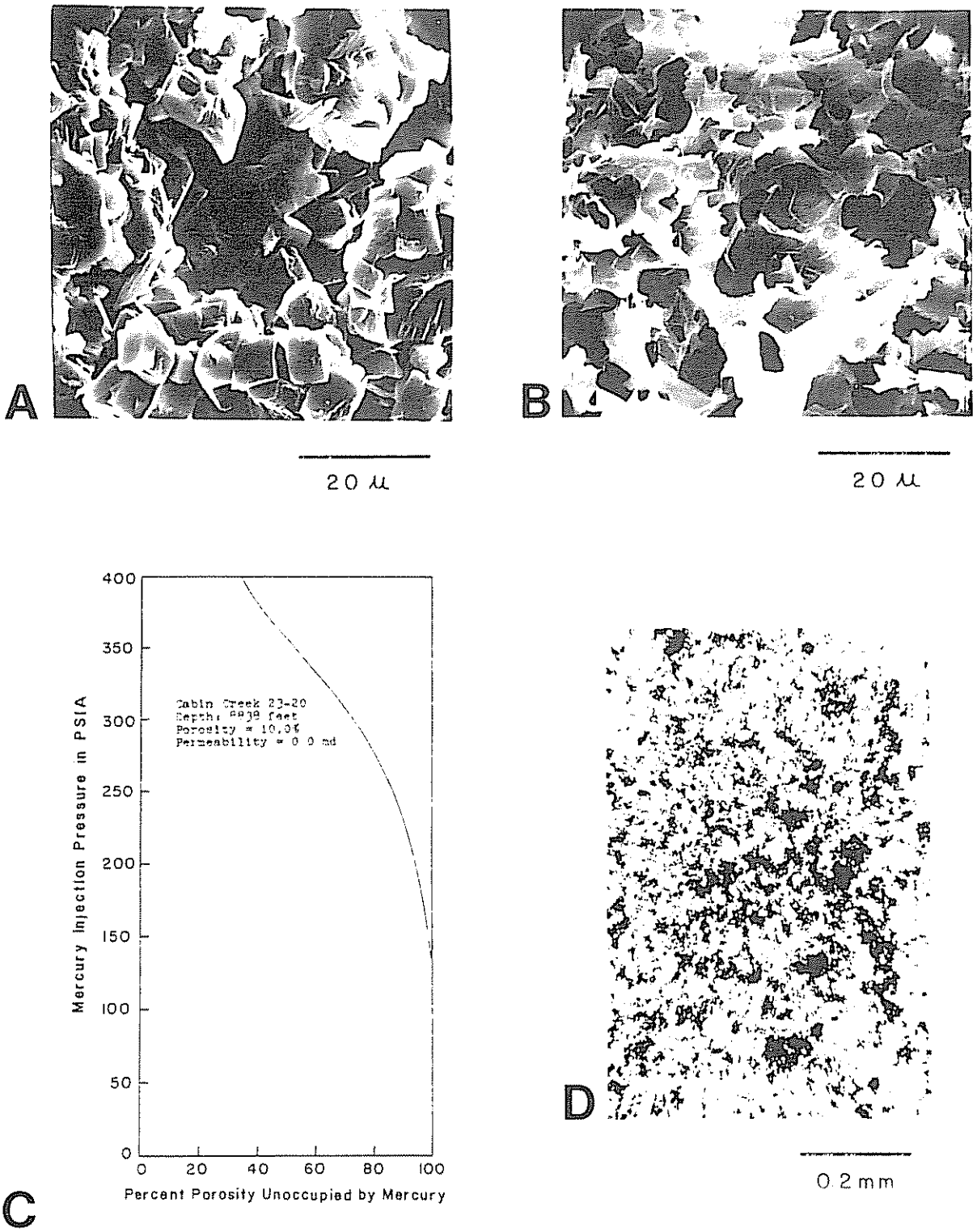
A
20 μ
B
20 μ
400
350
300
250
200
150
100
50
0
Mercury Injection Pressure in PSIA
Cabin Creek 23-20
Depth: 8838 feet
Porosity = 10.0%
Permeability = 0.0 md
0
20
40
60
80
100
Percent Porosity Unoccupied by Mercury
C
D
0.2 mm

Figure 25

FIGURE 26

A. Microcrystalline, hypidiotopic dolomite crystals of the U6 supratidal zone. Cabin Creek 23-20, 8843 ft. Scanning electron micrograph.

B. Pore cast of above sample. Pore throats have many planar boundaries and thus are tetrahedral and polyhedral in shape. Scanning electron micrograph.

C. Mercury capillary pressure curve for above sample. Curve shape indicates good reservoir properties. Mean throat size = 0.70 micron. Throats are well sorted (Sp = 0.49) and fine-skewed (Skp = +0.33).

D. Thin section photomicrograph for above sample. Pore space consists of vug and moldic types. Note shell fragment (arrow). Crossed nicols.

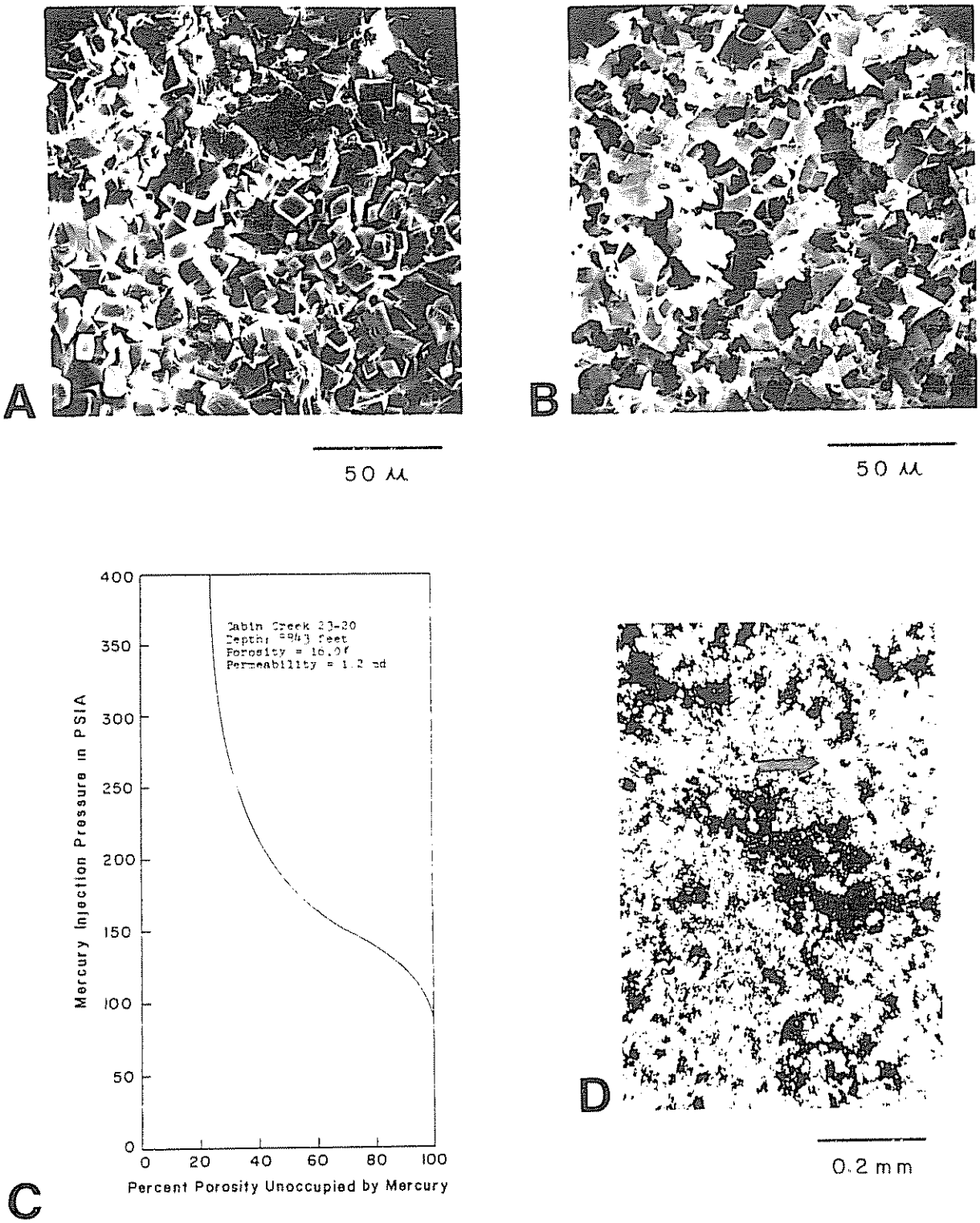
A
50 µ
B
50 µ
Cabin Creek 23-20
Depth: 5843 feet
Porosity = 16.0%
Permeability = 1.2 md
Mercury Injection Pressure in PSIA
400
350
300
250
200
150
100
50
0
0
20
40
60
80
100
Percent Porosity Unoccupied by Mercury
C
D
0.2 mm

Figure 26

FIGURE 27

A. Finely crystalline, hypidiotopic to xenotopic dolomite crystals of the U4 intertidal zone. Cabin Creek 41-28, 9048 ft. Scanning electron micrograph.

B. Pore cast of above sample. Pore throats are irregular in shape and occur in a wide range of sizes due to the poor sorting of the matrix dolomite crystals. Large throat in lower-left of photo is over 10 microns in width. Scanning electron micrograph.

C. Mercury capillary pressure curve for above sample. Curve shape indicates excellent reservoir properties. Irreducible water saturation is only 10%. Mean throat size = 10.0 microns. Throats are very poorly sorted (Sp = 2.36) and coarse-skewed (Skp = -0.15).

D. Thin section photomicrograph for above sample. Pore space consists of molds and enlarged molds. Crossed nicols.

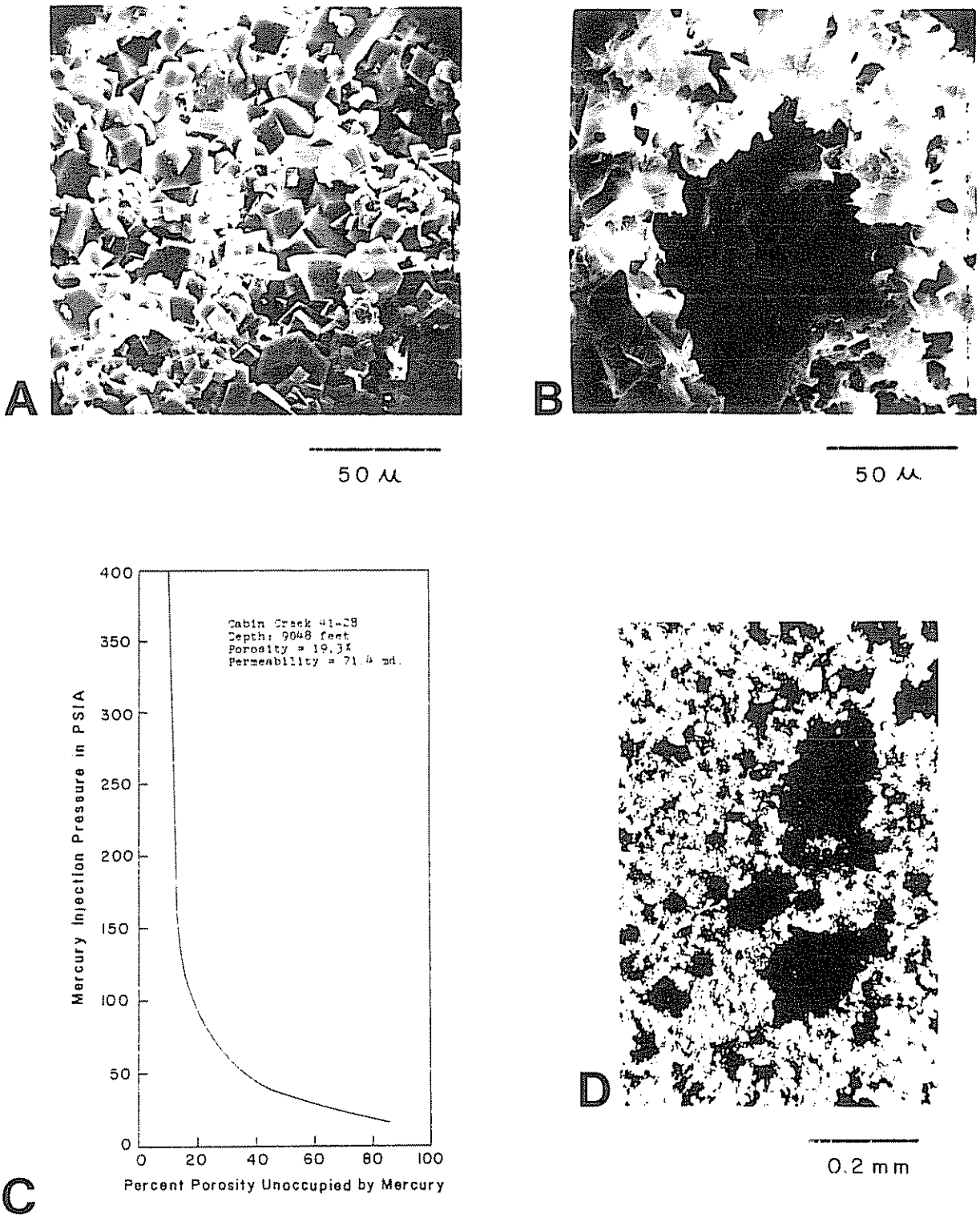
A
50 μ
B
50 μ
Cabin Creek 41-28
Depth: 9048 feet
Porosity = 19.3%
Permeability = 71.4 md.
Mercury Injection Pressure in PSIA
400
350
300
250
200
150
100
50
0
0
20
40
60
80
100
Percent Porosity Unoccupied by Mercury
C
D
0.2 mm

Figure 27

FIGURE 28

A. Bimodal, hypidiotopic dolomite crystals of the U4 subtidal zone. Cabin Creek 41-28, 9060 ft. Scanning electron micrograph.

B. Pore cast of above sample. Throats are irregular in shape, exhibit a wide range of sizes, and have a heterogeneous distribution. Note large throats along left margin of photo. Scanning electron micrograph.

C. Mercury capillary pressure curve for above sample. Curve shape indicates good penetration by mercury, but high pressure is needed for maximum saturation. Note that threshold pressure is only 30 psia. Mean throat size = 1.6 micron. Throats are poorly sorted (Sp = 1.70) and unskewed (Skp = 0.00).

D. Thin section photomicrograph for above sample. Pore space is moldic. Crossed nicols.

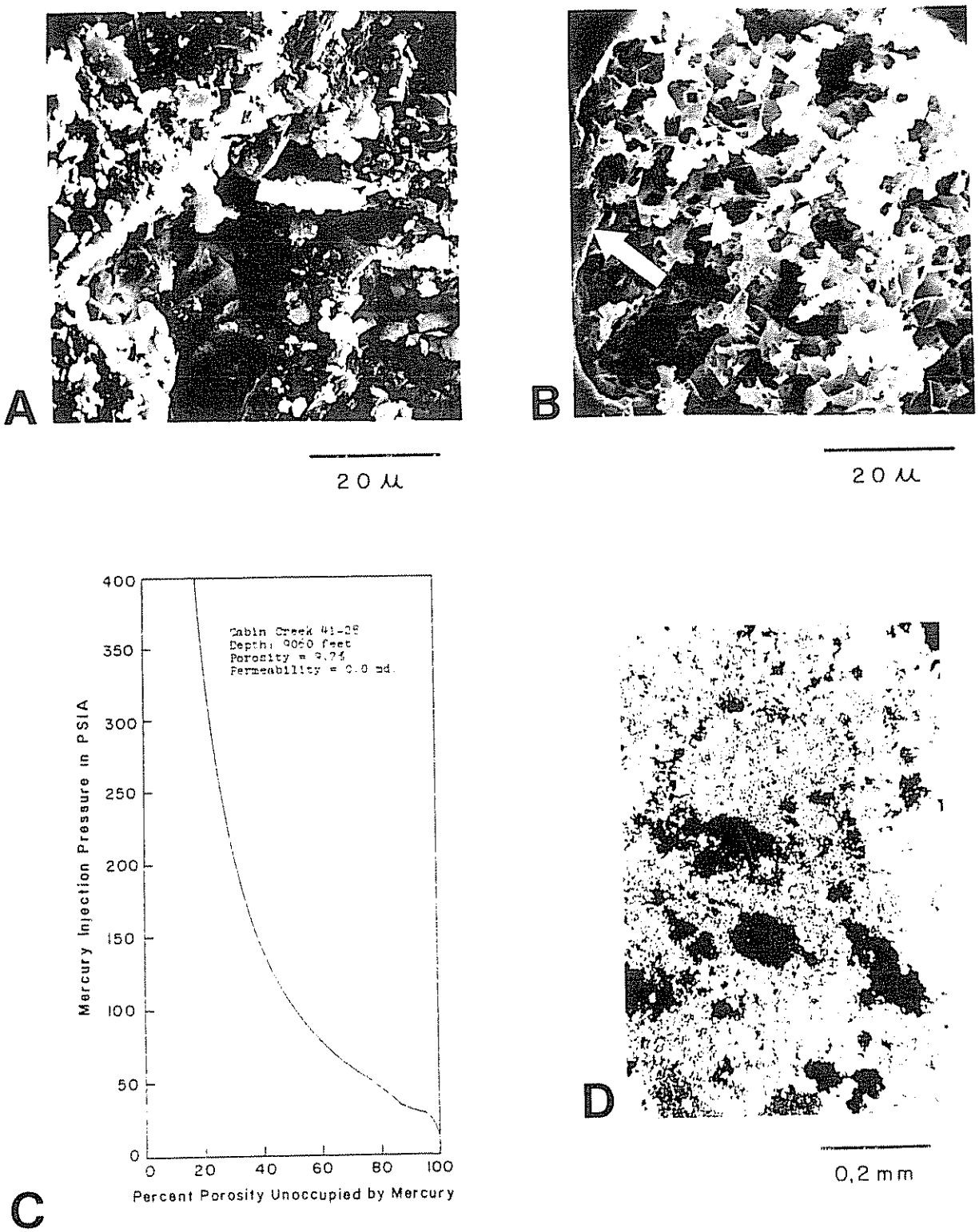
A
20 μ
B
20 μ
C
Cabin Creek 41-28
Depth: 9060 feet
Porosity = 9.7%
Permeability = 0.0 md.
Mercury Injection Pressure in PSIA
400
350
300
250
200
150
100
50
0
0
20
40
60
80
100
Percent Porosity Unoccupied by Mercury
D
0,2 mm

Figure 28

FIGURE 29

A. Bimodal but predominantly microcrystalline, xenotopic dolomite crystals of the U4 subtidal zone. Cabin Creek 32-17, 9019 ft. Scanning electron micrograph.

B. Pore cast of above sample. Pore throats are of complex polyhedral shapes and very small. Scanning electron micrograph.

C. Mercury capillary pressure curve for above sample. Curve shape indicates extremely poor reservoir properties. Mercury saturation is only 5% at maximum test pressure of 400 psia. Mean throat size = 0.6 micron. Throats are very poorly sorted (Sp = 2.24) and coarse-skewed (Skp = -0.73).

D. Thin section photomicrograph for above sample. Pore space consists of molds, enlarged molds, and some interparticle types. Crossed nicols.

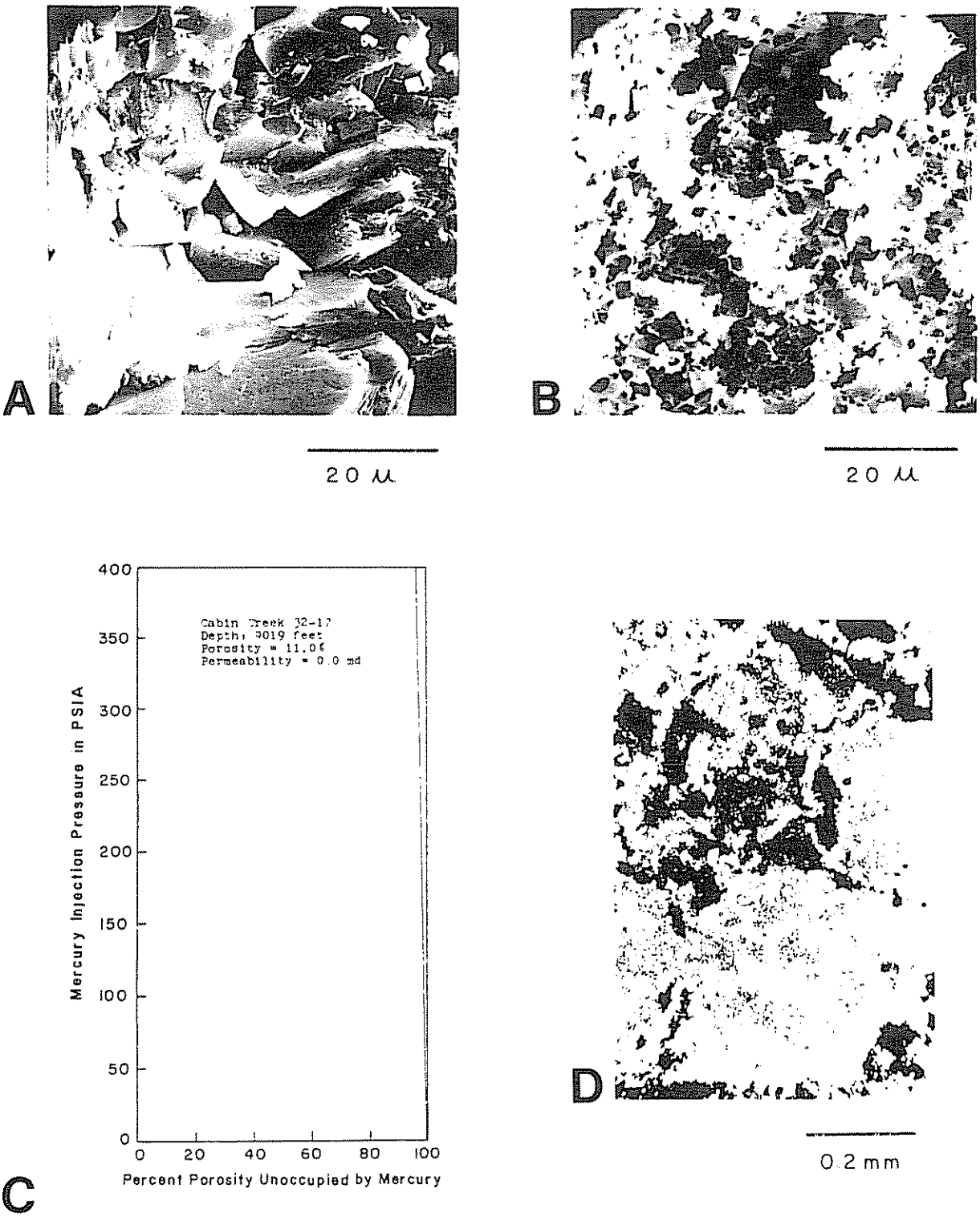
A
20 μ
B
20 μ
Cabin Creek 32-17
Depth: 9019 feet
Porosity = 11.0%
Permeability = 0.0 md
Mercury Injection Pressure in PSIA
400
350
300
250
200
150
100
50
0
0
20
40
60
80
100
Percent Porosity Unoccupied by Mercury
C
D
0.2 mm

Figure 29

FIGURE 30

A. Finely crystalline, idiotopic dolomite crystals of the U6 upper subtidal zone. Cabin Creek 23-20, 8870 ft. Scanning electron micrograph.

B. Pore cast of above sample. Pore throats are tabular to polyhedral and quite large. Wide separation of matrix dolomite crystals has resulted in tabular throats up to several microns in thickness. Areas of close-packed matrix dolomite crystals resulted in thin tabular throats (interboundary sheet-pores). Scanning electron micrograph.

C. Mercury capillary pressure curve for above sample. Curve shape indicates excellent reservoir properties. Mean throat size = 1.4 microns. Throats are moderately well sorted (Sp = 0.60) and fine-skewed (Skp = +0.73).

D. Thin section photomicrograph for above sample. Pore space consists of intercrystalline type. Crossed nicols.

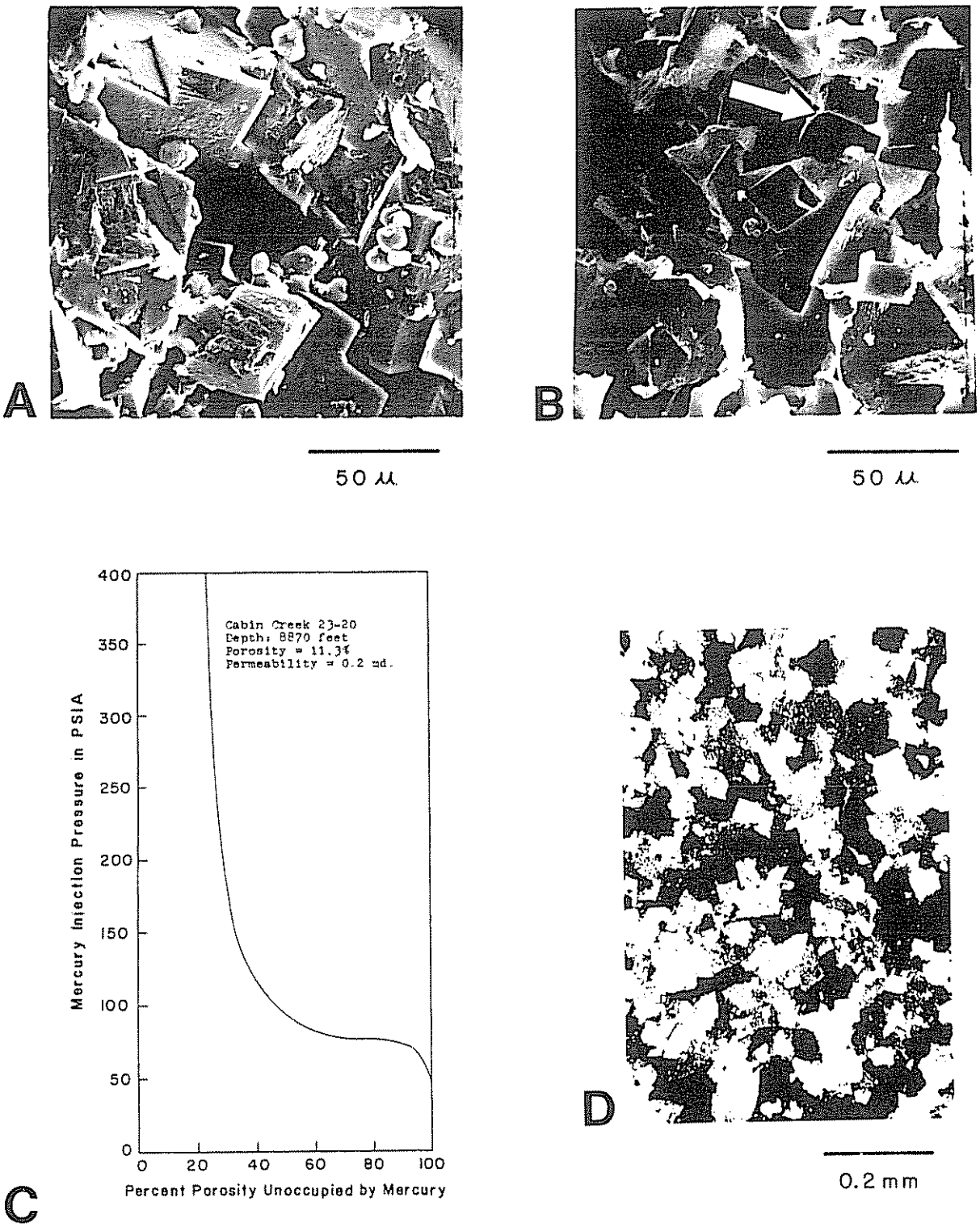
A
50 μ
B
50 μ
Cabin Creek 23-20
Depth: 8870 feet
Porosity = 11.3%
Permeability = 0.2 md.
Mercury Injection Pressure in PSIA
400
350
300
250
200
150
100
50
0
0
20
40
60
80
100
Percent Porosity Unoccupied by Mercury
C
D
0.2 mm

Figure 30

PETROPHYSICAL RELATIONSHIPS OF UPPER RED RIVER RESERVOIRS

In order to determine the distribution of reservoir properties within Cabin Creek or any other oil field, it is necessary to establish relationships among the various petrophysical parameters determined from core analysis, and those determined from electric logs. This permits interpolation of important reservoir data from cored wells to uncored wells. Porosity, permeability, and saturation data from core-plug analyses were available at one-foot sampling intervals for essentially all cored reservoir rock in Cabin Creek Field. Capillary-pressure data were available for five wells of the U4 reservoir and two wells of the U6 reservoir. Using core and capillary-pressure data, plots were made of permeability versus porosity, permeability versus mean throat size (Dm), and porosity versus mean throat size for both the U4 and U6 reservoir data.

Permeability Versus Porosity

Two separate plots of permeability versus porosity were made for the U4 reservoir using data for lithofacies 3 samples only (Figure 31), and using data for lithofacies 5 samples only (Figure 32). Both plots indicate that permeability tends to increase as porosity increases. However, the lithofacies 5 data is much more scattered than lithofacies 3 data. Scattering of this nature has been reported in upper Red River reservoirs by Kohm and Louden (1978). Their plot of porosity versus permeability for the "C" Burrowed Member (equivalent to lithofacies 5)

exhibited a large scattering of points, while the same plot for the "C" Laminated Member (equivalent to lithofacies 3) showed much less scattering. Kohm and Louden attribute the large scattering of the "C" Burrowed Member to the complex combination of intercrystalline, vug, and fracture-controlled vug porosity of this unit.

Figure 33 is a plot of permeability versus porosity for all data of the U6 reservoir. Data for lithofacies 4 and 5 are undifferentiated as both were found to exhibit the same amount of scattering. As in the case of the U4 reservoir, there is a general trend of increasing porosity with increasing permeability shown by this plot. However, there is a wide range of permeability for any given porosity, and permeability values in general are much lower than those of the U4 reservoir.

Permeability Versus Mean Throat Size

Figure 34 is a plot of permeability versus mean throat size (Dm) for the U4 reservoir. All data are included and no differentiation is made between lithofacies 3 and lithofacies 5. This plot indicates that mean throat size increases as permeability increases. Relatively little scatter occurs and thus the range of throat sizes occurring at any given permeability is small, about ± 1 micron. This relationship between permeability and mean throat size is highly significant, since mean throat size is one of the important measures of pore-system geometry.

A similar relationship exists between permeability and mean throat size of the U6 reservoir (Figure 35). In contrast to the U4 reservoir,

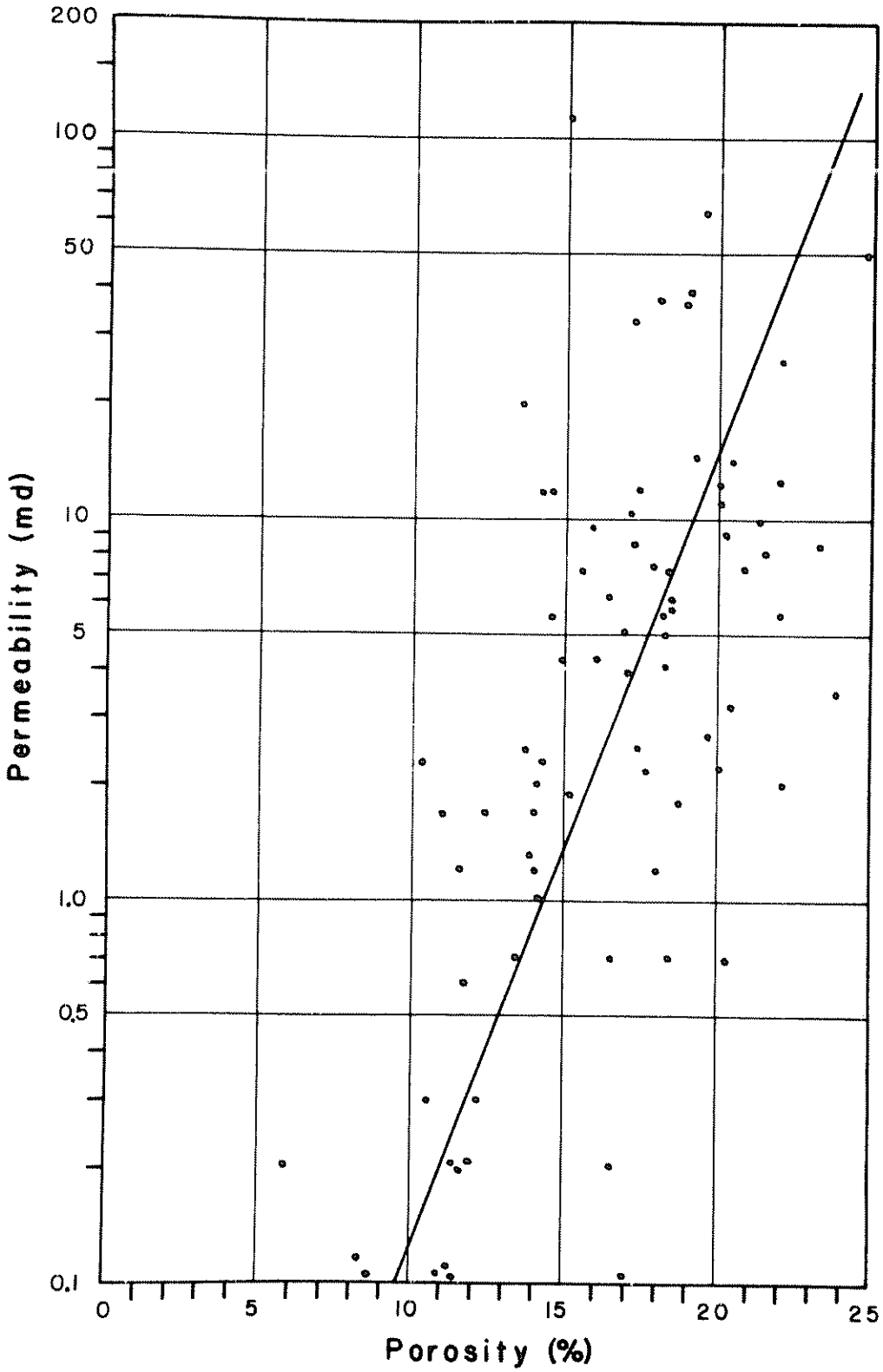

FIGURE 31. Plot of permeability versus porosity for U4 reservoir lithofacies 3 only.

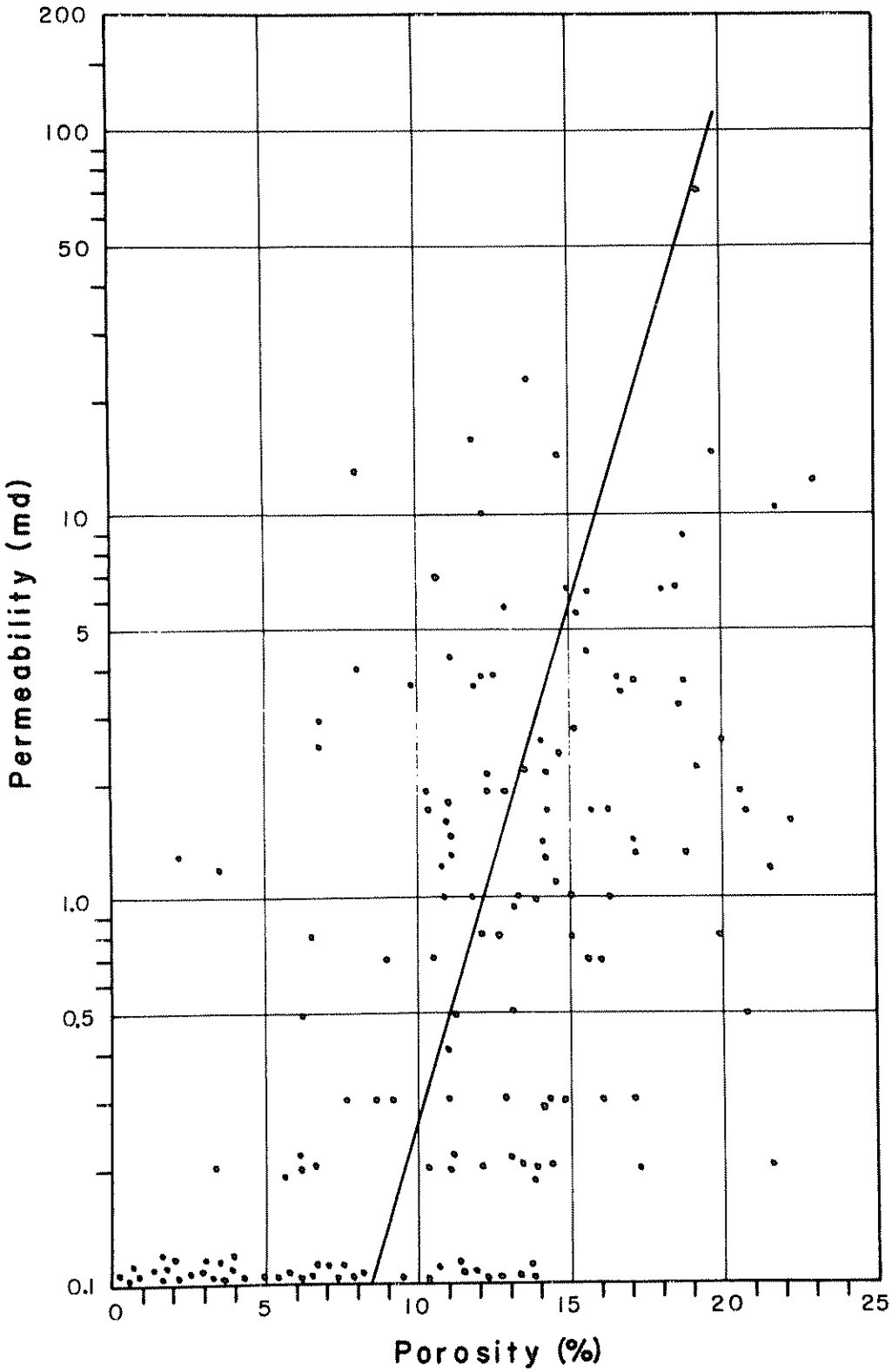

FIGURE 32. Plot of permeability versus porosity for U4 reservoir lithofacies 5 only.

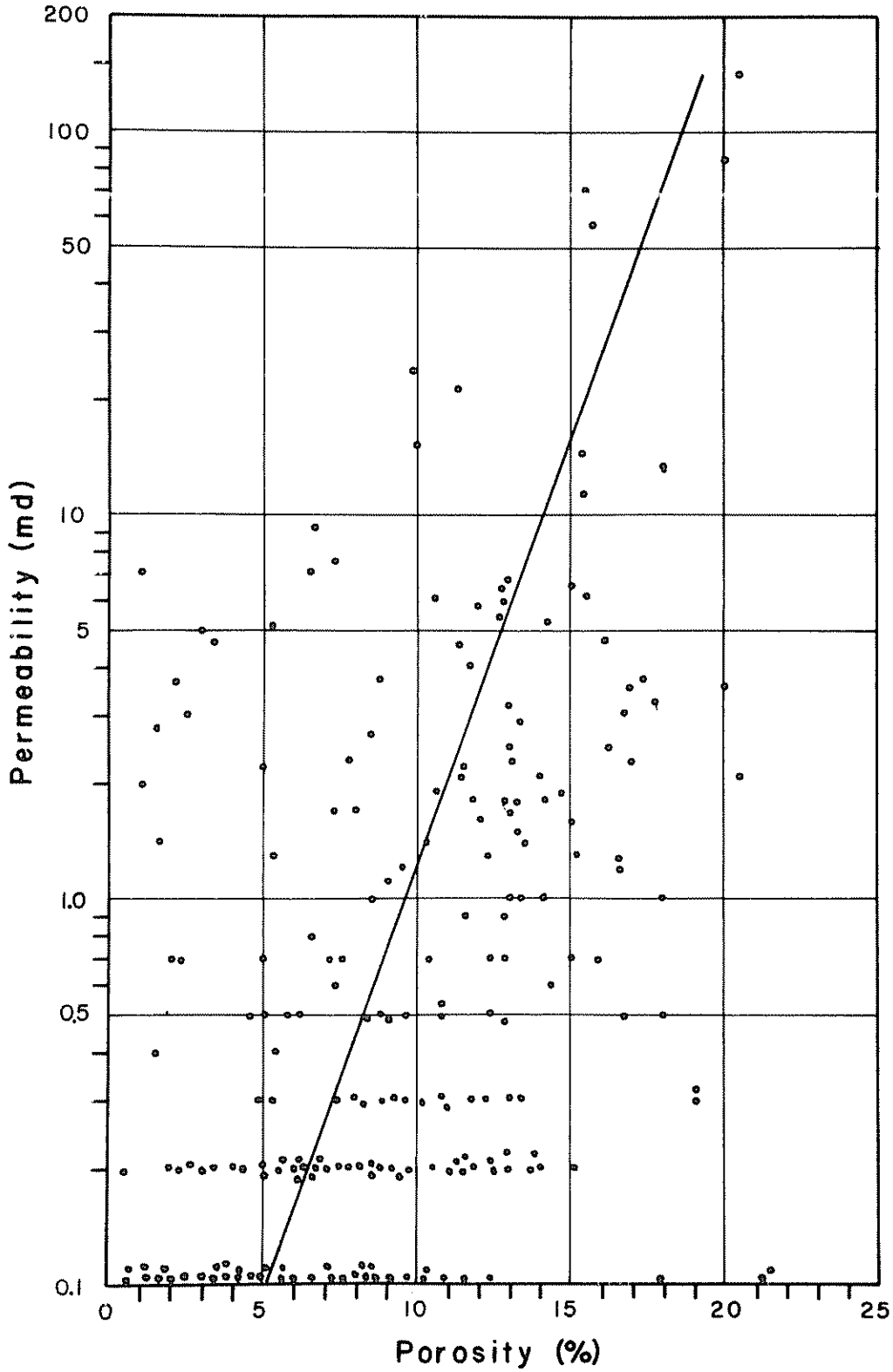

FIGURE 33. Plot of permeability versus porosity for all data of the U6 reservoir.

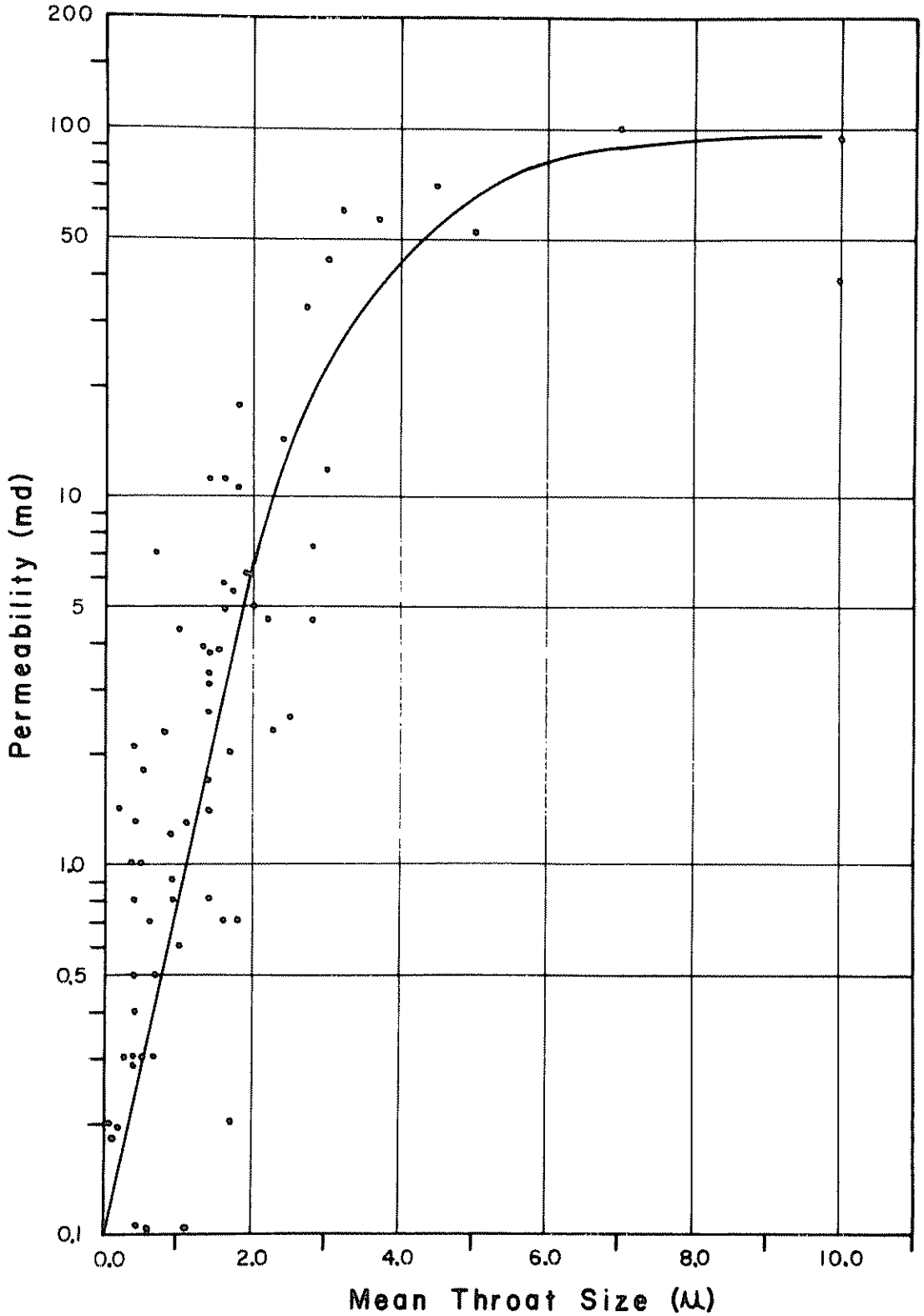

FIGURE 34. Plot of permeability versus mean throat size for all data of the U4 reservoir.

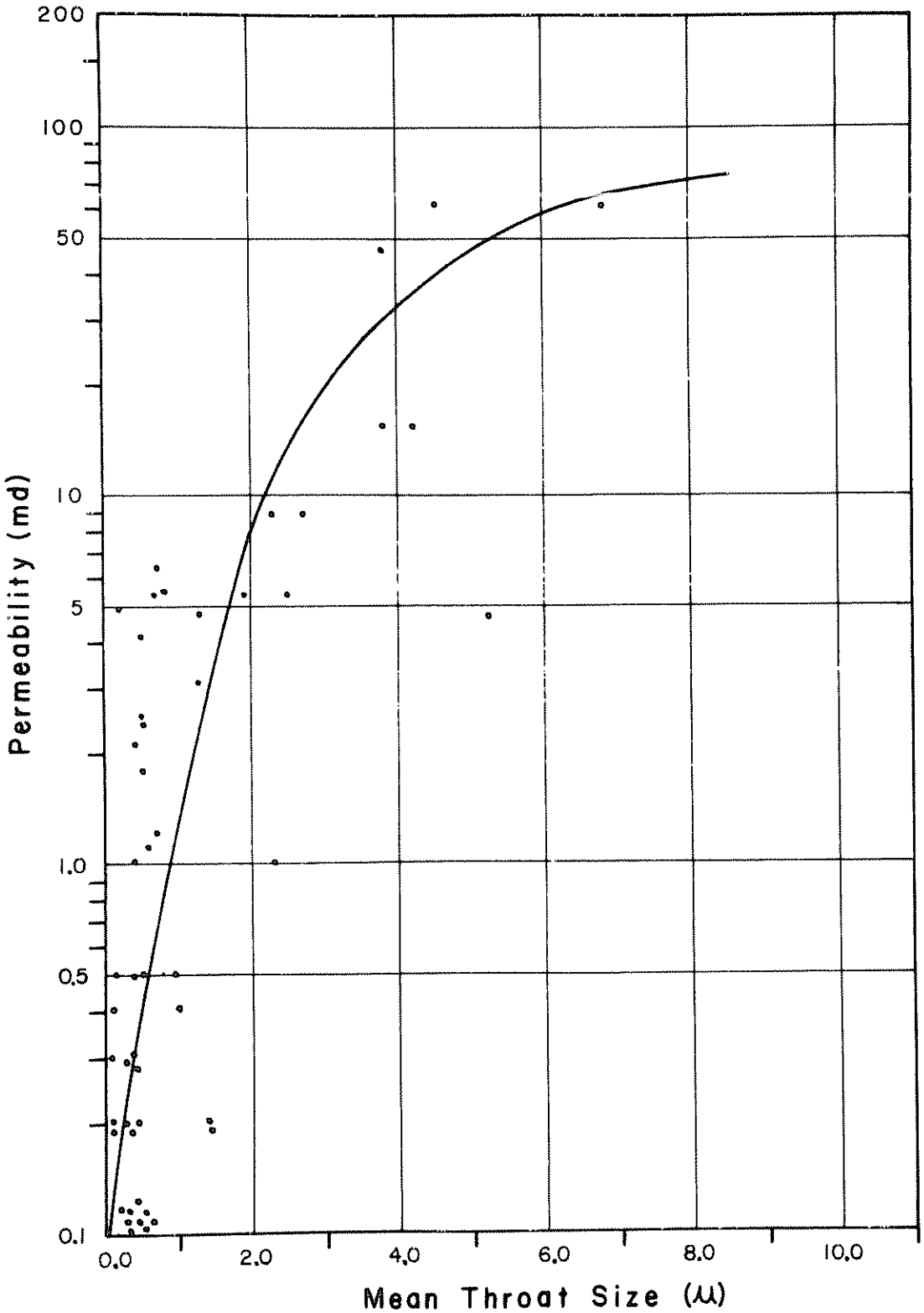

FIGURE 35. Plot of permeability versus mean throat size for all data of the U6 reservoir.

data for the U6 exhibits slightly more scatter; however, the curves are quite similar in shape and magnitude. In comparison to other plots, the relative lack of data scatter in Figures 34 and 35 suggests that the relationship between permeability and mean throat size is independent of lithofacies type.

Porosity Versus Mean Throat Size

Figures 36 and 37 are plots of porosity versus mean throat size for the U4 reservoir. Figure 36 includes only data for lithofacies 3 samples and shows a general increase in mean throat size as porosity increases. The larger values of Dm, over 1.0 micron, occur mostly in cases where porosity exceeds 15%. Figure 37 includes only the data for lithofacies 5 samples. In comparing Figures 36 and 37, note that porosity values of lithofacies 3 tends to be greater than 10% and exhibit a more pronounced increase in throat size as porosity increases. The relationships displayed in Figures 36 and 37 are important as they relate mean throat size, a measure of pore-system geometry, to porosity value, which can be obtained from neutron logs in uncored wells.

Figure 38 is a plot of porosity versus mean throat size (Dm) for all data of the U6 reservoir. Much of the data for Figure 38 is from the #23-x-28 well, for which no core was available for study. However, based on neutron log correlation with nearby cored wells, data from samples within the subtidal intercrystal porosity zone have been differentiated from other U6 porosity data in this plot. Two different trend lines are shown on the graph. In either case, mean throat size

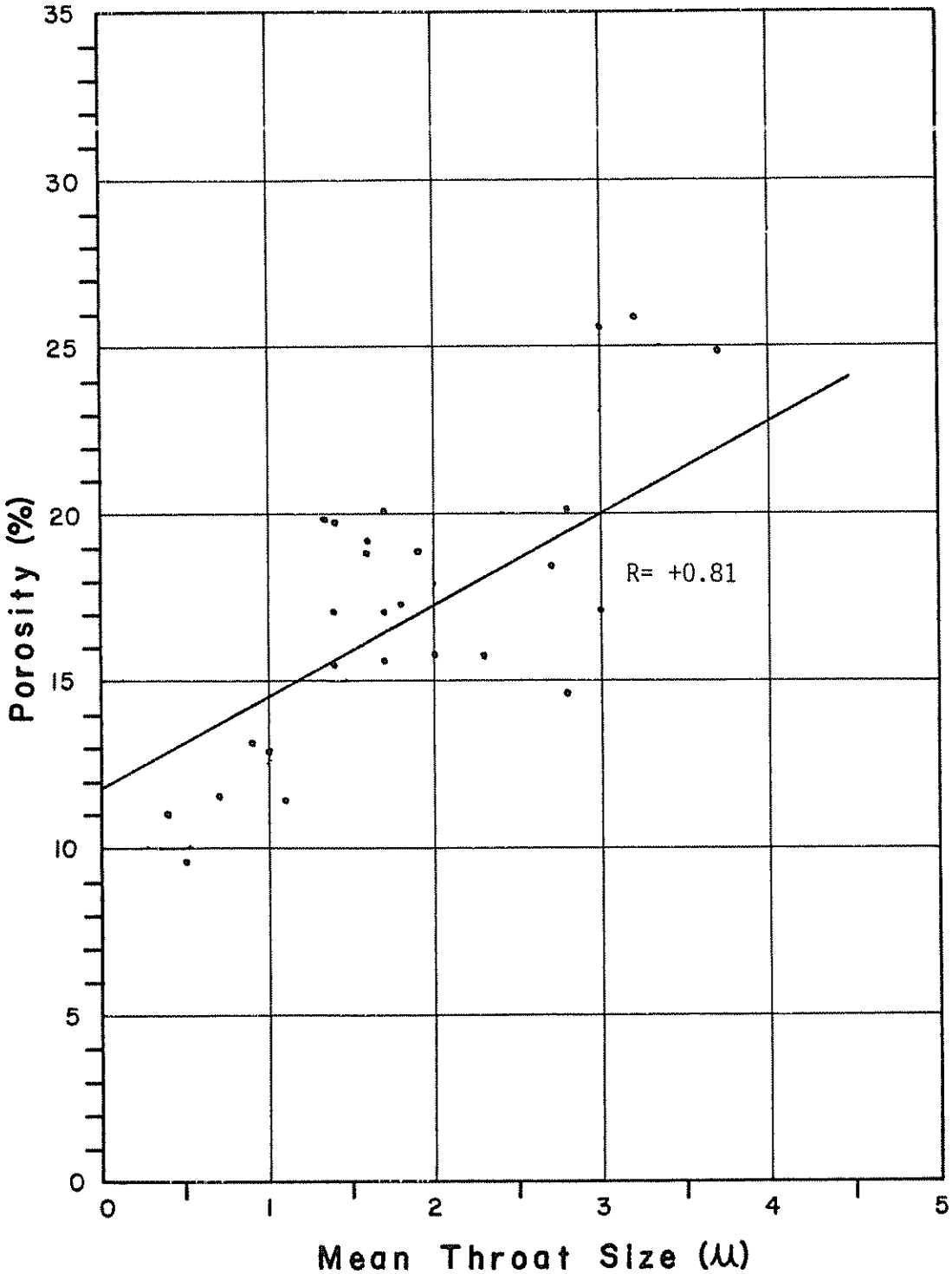

FIGURE 36. Plot of porosity versus mean throat size for U4 reservoir lithofacies 3 only.

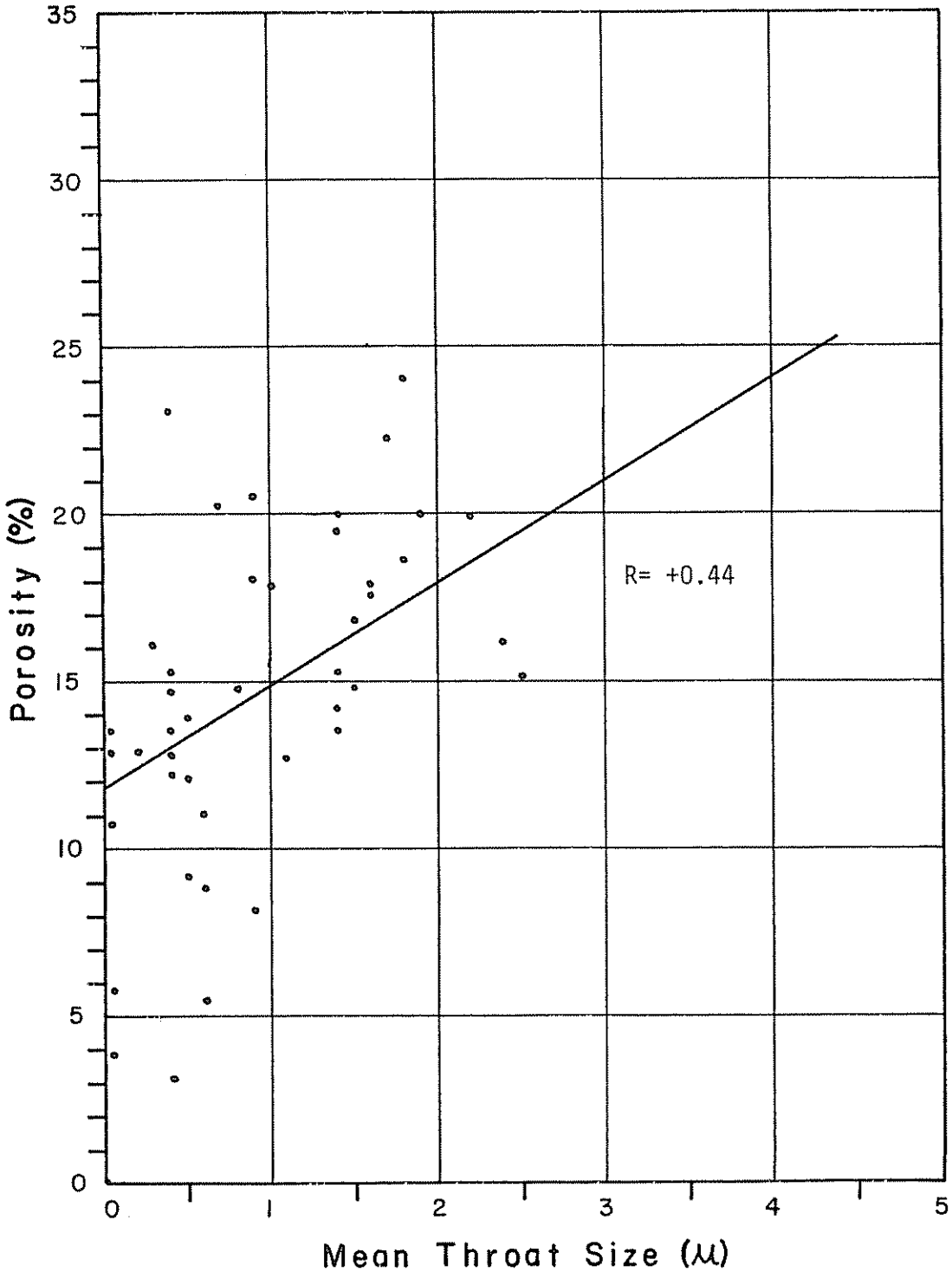

FIGURE 37. Plot of porosity versus mean throat size for U4 reservoir lithofacies 5 only.

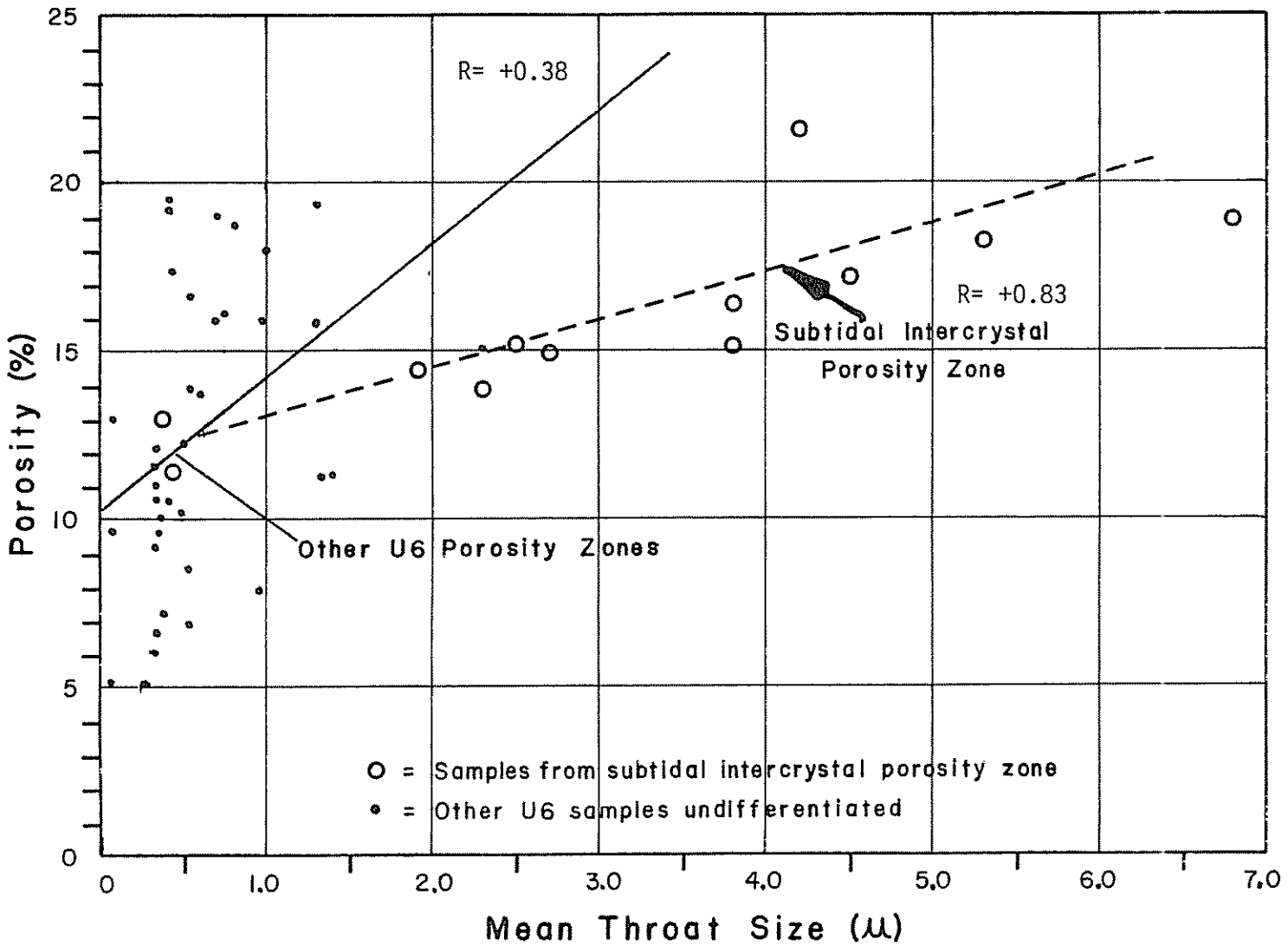

FIGURE 38. Plot of porosity versus mean throat size for all data of the U6 reservoir.

increases as porosity increases. However, the relationship exhibited by the subtidal intercrystal porosity zone data is quite different from that exhibited by other U6 porosity data. Samples of the subtidal intercrystal porosity zone exhibit very high mean throat size values.

Influence of Lithology and Depositional Environment On Reservoir Petrophysics

The above relationships among porosity, permeability, and pore geometry underscore the importance of depositional environment and diagenetic processes in determining the distribution of reservoir properties. If lithofacies type, depositional environment, and neutron log porosity are known, an approximation of permeability and pore geometry of upper Red River reservoirs can be made by using the graphs shown in Figures 31 through 38. This is possible because permeability and pore geometry are largely dependent on porosity, which in turn is largely dependent on depositional environment.

The relationship of porosity to permeability and pore geometry is most well defined for lithofacies 3. This is because the finely crystalline dolomite composing this lithofacies is relatively homogeneous across the field and the pore geometry of this lithofacies is also relatively homogeneous; consisting primarily of vugs formed by anhydrite dissolution. This same porosity type predominates in lithofacies 4; however, the microcrystalline dolomite composing the matrix of lithofacies 4 profoundly affects pore geometry in an adverse way. As a result, permeabilities tend to be lower and have a greater range than those of lithofacies 3.

Pores of lithofacies 5 consist mostly of molds and enlarged molds created by the dissolution of a large assortment of skeletal and non-skeletal particles and also gypsum crystals. Matrix material between pores consists of microcrystalline dolomite. The resulting pore system is heterogeneous and exhibits a wide range of permeability values.

The high porosity and mean throat size values exhibited by samples of the U6 subtidal intercrystal porosity zone result from the homogeneous nature of pore geometry in this zone. The dolomite crystals composing the matrix of this porosity zone are mostly idiotopic and finely crystalline in size, creating large pores and throats. The occurrence of this porosity zone appears to have been environmentally controlled, as previously discussed.

Petrophysical relationships of the upper Red River reservoirs may be summarized as follows:

(1) Permeability tends to increase as porosity increases for both the U4 and U6 reservoirs. This relationship is most evident in the case of lithofacies 3 samples. The permeability range of lithofacies 5 is greater than that of lithofacies 3 for a given porosity. This finding concurs with that of Kohm and Louden (1978).

(2) Mean throat size (Dm) increases as permeability increases for both the U4 and U6 reservoirs. This relationship appears to be independent of lithofacies type.

(3) Mean throat size increases as porosity increases for both the U4 and U6 reservoirs. This relationship is most pronounced in the case of lithofacies 3 samples. The relationship between porosity

and mean throat size is markedly different for samples of the U6 subtidal intercrystal porosity zone, and reflects the unique geometry of this pore system. Subtidal intercrystal porosity zone samples of the U6 reservoir exhibit abnormally large mean throat size values relative to porosity and permeability.

(4) Since mean throat size is a measure of pore geometry, it is possible to predict pore geometry and other petrophysical properties of the U4 and U6 reservoirs in uncored wells. This can be done by determining porosity value from neutron logs, and by using the shape of the neutron curve to determine lithofacies type and general porosity type. Once these are known, the appropriate plots can be used to approximate permeability and mean throat size values.

DIAGENETIC CONTROLS ON THE DEVELOPMENT AND GEOMETRY OF UPPER RED RIVER PORE SYSTEMS

The role of various diagenetic processes in the development of upper Red River pore systems is summarized in Figure 39. Porosity development was controlled largely by diagenetic overprint, which in turn is closely related to environment of deposition. The combined effects of these processes resulted in the creation of four basic pore-system types. Classification of pore systems is based on pore type, lithological association, stratigraphic association, environmental association, pore geometry, and reservoir characteristics (Table 6).

Pore System Development

Type I Pore System

The Type I pore system consists of vugs in a finely crystalline, hypidiotopic dolomite. The parent sediment was composed of laminated, mud to sand-sized calcium-carbonate particles, largely devoid of skeletal debris. The vugs resulted from vadose leaching of anhydrite crystals in the syngenetic supratidal U4 dolomite (lithofacies 3). The Type I pore system has the highest average value of porosity, 17.4%. The size and predominant subhedral shape of the matrix dolomite crystals has resulted in large, moderately sorted pore throats of rather homogeneous distribution. Reservoir properties of this pore system are excellent.

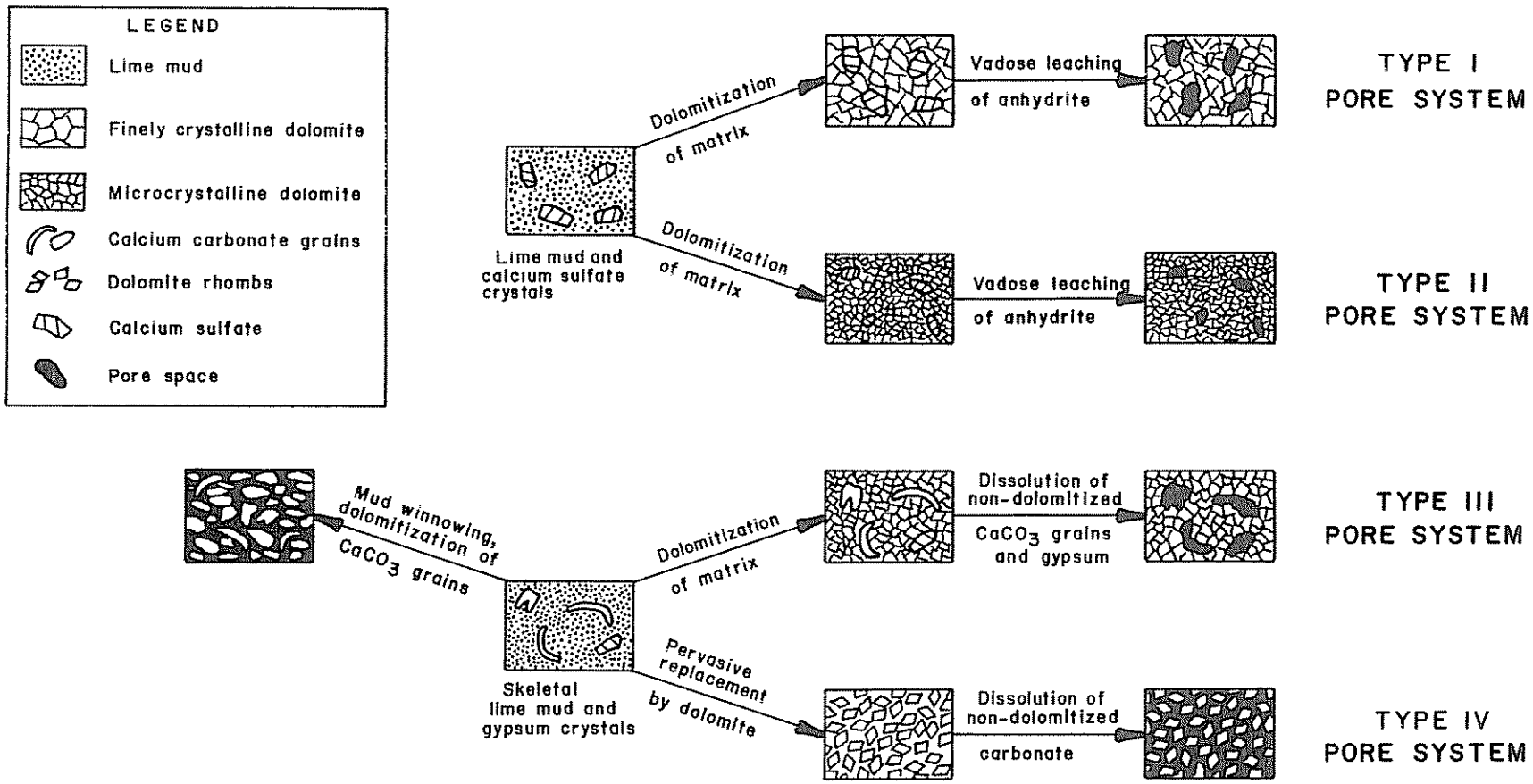

FIGURE 39. Diagenetic processes involved in the development of upper Red River pore systems.

Table 6. Classification and reservoir characteristics summary of upper Red River pore systems

Pore System	Porosity Type and Lithological Association	Stratigraphic and Environmental Association	Ave. ϕ (%)	Ave. K(md.)	Pore Throat Geometry	Reservoir Characteristics
Type I	Vug pores occurring in a finely crystalline, hypidiotopic dolomite.	Supratidal zone of U4 dolostone	17.4	13.5	Ave. Dm = 2.4μ Ave. Sp = 0.89 Moderately sorted Fine skewed Thin-tabular to polyhedral shaped	Ave. Swi = 12%. Large throats and homogeneous pore system provide excellent reservoir quality. Low irreducible oil saturation is indicated by low Swi and moderate throat sorting.
Type II	Vug pores occurring in a microcrystalline, xenotopic dolomite.	Supratidal zone of U6 dolostone	13.5	1.9	Ave. Dm = 0.7μ Ave. Sp = 0.46 Well sorted fine skewed tabular to highly irregular	Ave. Swi = 21%. Small throats and low permeability provide poor reservoir quality. Combination of small throat size, good sorting, and Swi values indicate moderate irreducible oil saturation.
Type III	Moldic, enlarged moldic, and interparticle pores occurring in microcrystalline to finely crystalline, xenotopic to hypidiotopic dolomite.	Intertidal to subtidal zones of U4 and U6 dolostones.	14.9	6.2	Ave. Dm = 1.0μ Ave. Sp = 0.98 Moderate to poorly sorted, fine to coarse skewed irregular shaped, heterogeneous.	Ave. Swi = 44%. Heterogeneous pore system and small throats provide poor reservoir quality. Poorly sorted throat geometry and high Swi indicate high irreducible oil saturation.
Type IV	Intercrystalline pores occurring in a finely crystalline, idiotopic to hypidiotopic dolomite.	Uppermost subtidal zone of U6 dolostone	16.2	23.8	Ave. Dm = 3.8μ Ave. Sp = 0.92 Moderately sorted Fine skewed Tabular to polyhedral shaped.	Ave. Swi = 13%. Pore system is homogeneous providing excellent reservoir quality. Pore geometry and low Swi indicate low irreducible oil saturation.

Type II Pore System

The Type II pore system consists of vugs in microcrystalline, xenotopic dolomite. This pore system is restricted to the supratidal zone of the U6 dolostone (lithofacies 4). The vugs resulted from vadose leaching of anhydrite in the same manner as those of the Type I pore system, except that Type II pore system vugs are much smaller in size and less abundant than vugs of the Type I pore system. This difference resulted from the fact that less anhydrite occurred in the parent sediment as a result of environmental conditions. Less evaporitic sulfate minerals (gypsum and anhydrite) were deposited in the U6 supratidal zone due to less favorable climatic conditions. The resulting average porosity of the Type II pore system is only 13.5%. The size and predominantly anhedral shape of the matrix dolomite crystals has resulted in small but well sorted throats of rather homogeneous distribution. Reservoir properties of the Type II pore system are rather poor due primarily to the small size of the pore throats. This pore system has the lowest average permeability, only 1.9 md.

Type III Pore System

The Type III pore system consists of molds, moldic pores enlarged to vugs, and interparticle pores, in microcrystalline to finely crystalline, xenotopic to hypidiotopic dolomite. This pore system is most common in the intertidal and subtidal zones of both U4 and U6 dolostones. The Type III pore system is the most complex, since any combination of the above pore types may occur together.

In most cases, interparticle pores appear to represent original pore space preserved between pellets, peloids, ooids, or intraclasts. Most pores of this system resulted from dissolution of calcium carbonate particles or gypsum crystals due to a solubility contrast, after dolomitization of the matrix lime-mud. Average porosity of the Type III pore system is 14.9%. Both pores and throats of this system are quite heterogeneous in shape, size, and distribution. This results from the variety of particle types dissolved to create the pores, and from the size and shape of the dolomite matrix. Throats of this system thus tend to be small and moderate to poorly sorted, providing poor reservoir properties.

Type IV Pore System

The Type IV pore system consists of intercrystalline pores in a finely crystalline, idiotopic to hypidiotopic dolomite. This pore system is best developed in the uppermost subtidal zone of the U6 dolostone. Pores of this system originated by dissolution of relict interstitial calcite occurring between rhombs of pervasive dolomite. Presence of skeletal debris in rocks immediately above and below the intercrystal porosity zone indicate that the parent rock was most likely a biomicrite. Average porosity of the Type IV pore system is 16.2%. Pore geometry of this system is rather homogeneous due to the fabric of the matrix dolomite crystals. Average throat size is larger than any of the other pore systems, and the throats are moderately sorted. Resulting reservoir properties of the Type IV pore system are excellent.

Pore Geometry as an Index to Carbonate Reservoir Characteristics

Correlation of Pore Geometry

The reservoir properties of any rock depend on how the pores are interconnected. In the case of dolomite reservoirs, pore throats are a function of the size, shape and arrangement of the dolomite crystals which form the rock matrix. In order to determine the reservoir characteristics of the rock with regard to either primary or enhanced recovery, it is necessary to know the geometry of the pore system and to define its continuity across the field. The relationship established between porosity percentage and mean throat size (see Figures 36, 37, and 38) makes it possible to correlate reservoir pore geometry by the use of neutron logs. However, such correlations can only be done if depositional environments, diagenetic history, and pore system types are known.

Mean throat size increases as porosity percentage increases because of the spatial relationship between pores and throats. In low porosity reservoir rocks, interconnections between pores are necessarily long (Figure 40A). In such a rock, fluids must travel a long distance to reach the next pore. In highly porous reservoir rocks, fluids forced through the throats have less distance to travel in order to reach the next available pore (Figure 40B). The greater the distance between pores, the longer the throats, and the greater the chance of encountering an obstruction going from one pore to the next. Thus highly porous

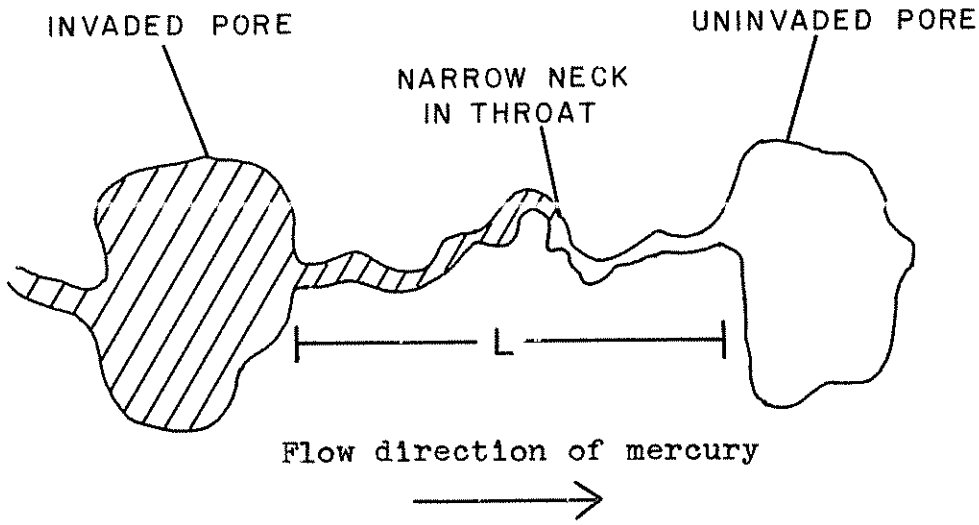

A. Low porosity reservoir rock.

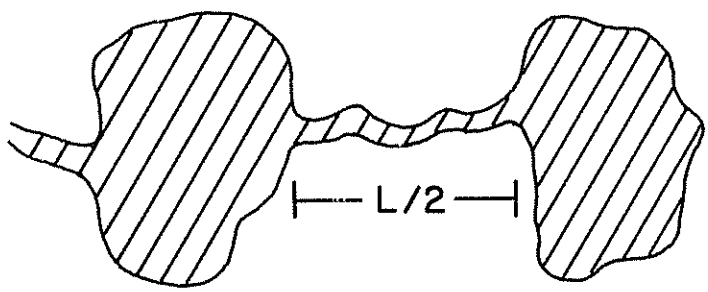

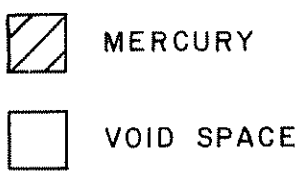

B. High porosity reservoir rock.

FIGURE 40. Schematic illustration of how porosity percentage can influence measurement of throat size in a heterogeneous pore system. In the case of A, a low porosity reservoir rock, mercury has been prevented from invading the adjacent pore by a constriction in the throat passage. In the case of B, a high porosity reservoir rock, distance between adjacent pores is half that of case A. Assuming throat shape to be the same in both cases, mercury is free to flow into the adjacent pore.

rocks tend to have a large mean throat size, as determined by mercury capillary-pressure data, because the smaller the distance between pores, the greater the chance of the mercury invading the pore system at the applied pressure.

Recovery Efficiency

Wardlaw and Cassan (1978) consider the most important characteristics of the pore system to be: pore-to-throat size ratio, pore-to-throat coordination number, and heterogeneity of the pore system. Using these characteristics, they devised a scheme to estimate recovery efficiency by visual observations made from resin pore casts of carbonate reservoir rock.

This method was not found to be practical because it is often difficult to distinguish pores from throats in a given sample; the difference between pores and throats being a matter of scale. Pores and throats may both be too small to be effectively measured by petrographic methods. In any case, pore-to-throat size ratio is, in effect, a measure of pore-system sorting. Pore-to-throat coordination number is also difficult to determine in a complex pore system, and a thin section or pore cast does not provide enough sampling area to effectively describe heterogeneities of the pore system.

It is more meaningful to describe reservoir characteristics and recovery efficiency in terms of statistical parameters obtained from capillary-pressure curves. These parameters can then be related to reservoir lithology, depositional environment, and diagenetic processes

in order to predict reservoir characteristics in parts of a field lacking adequate core control.

Effects of Pore Geometry On Residual Saturations

Pore-throat geometry is a function of the size, shape, and arrangement of the crystals composing the rock matrix. It has been determined experimentally that as matrix particle size distribution is made broader, or bi-modal, it is possible to develop local, small-scale packing heterogeneities which result in increased magnitude of residual wetting-phase saturation (Morrow, 1970, 1971). This is because heterogeneities of this nature result in small clusters of pores which remain entirely filled with the wetting-phase despite attempts of displacement by a non-wetting phase. The magnitude of irreducible wetting phase saturations is mostly a function of pore-system heterogeneity, the manner in which pores and throats of different sizes are distributed within the matrix (Morrow, 1970).

These relationships have been shown to exist for upper Red River reservoirs. Figure 41 is a plot of irreducible water saturation (Swi) versus mean throat size (Dm) for all data. Data points exhibit wide scattering, but for a given throat diameter, there is a maximum value of Swi that is not exceeded. Thus if throat size is known, an expected range of corresponding irreducible water saturation values can be determined (Table 7).

Figure 42 is a plot of irreducible water saturation (Swi) versus the ratio of mean throat size to throat sorting (Dm/Sp). Data points

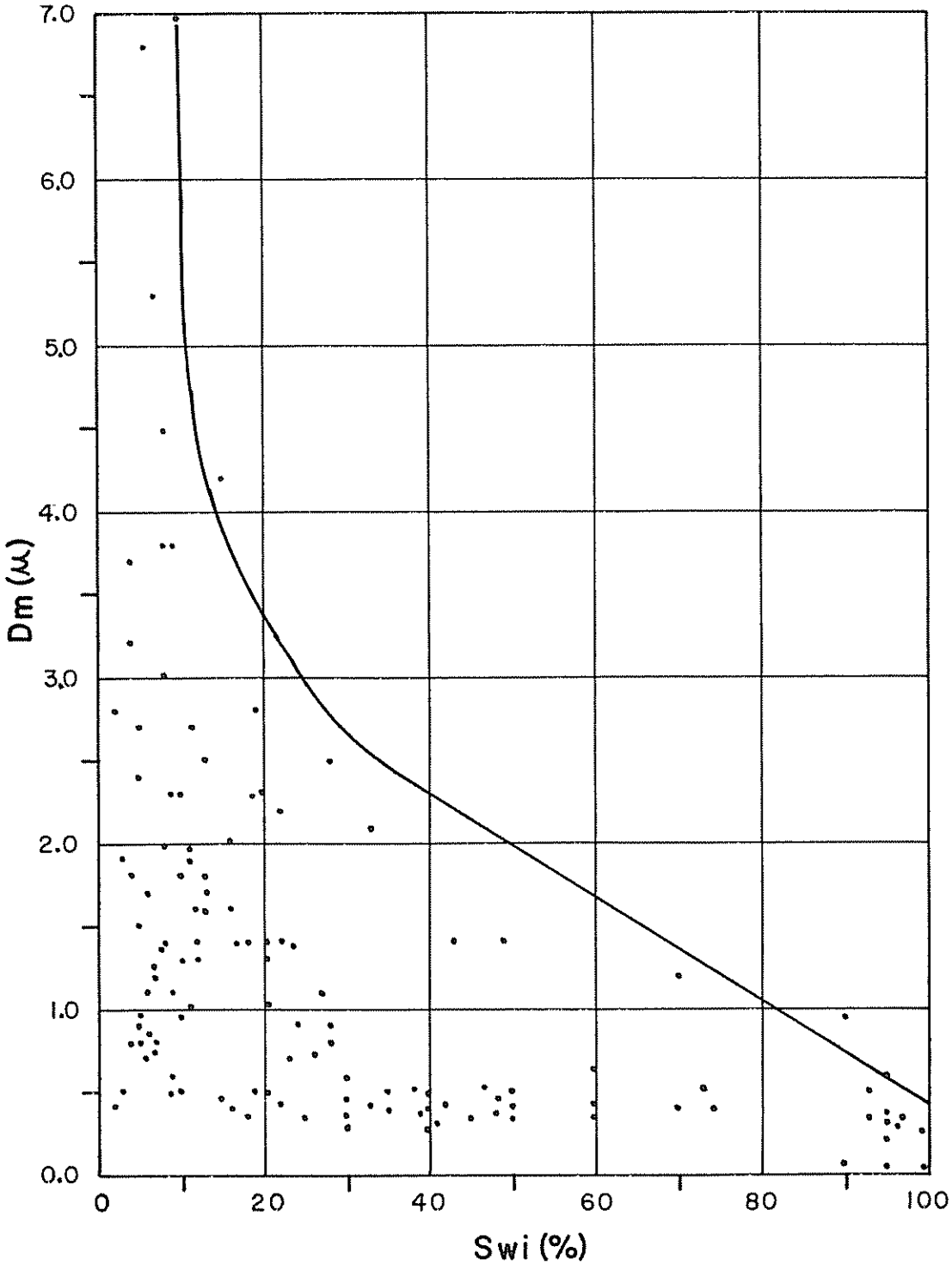

FIGURE 41. Plot of irreducible water saturation versus mean throat size for all data of U4 and U6 reservoirs combined.

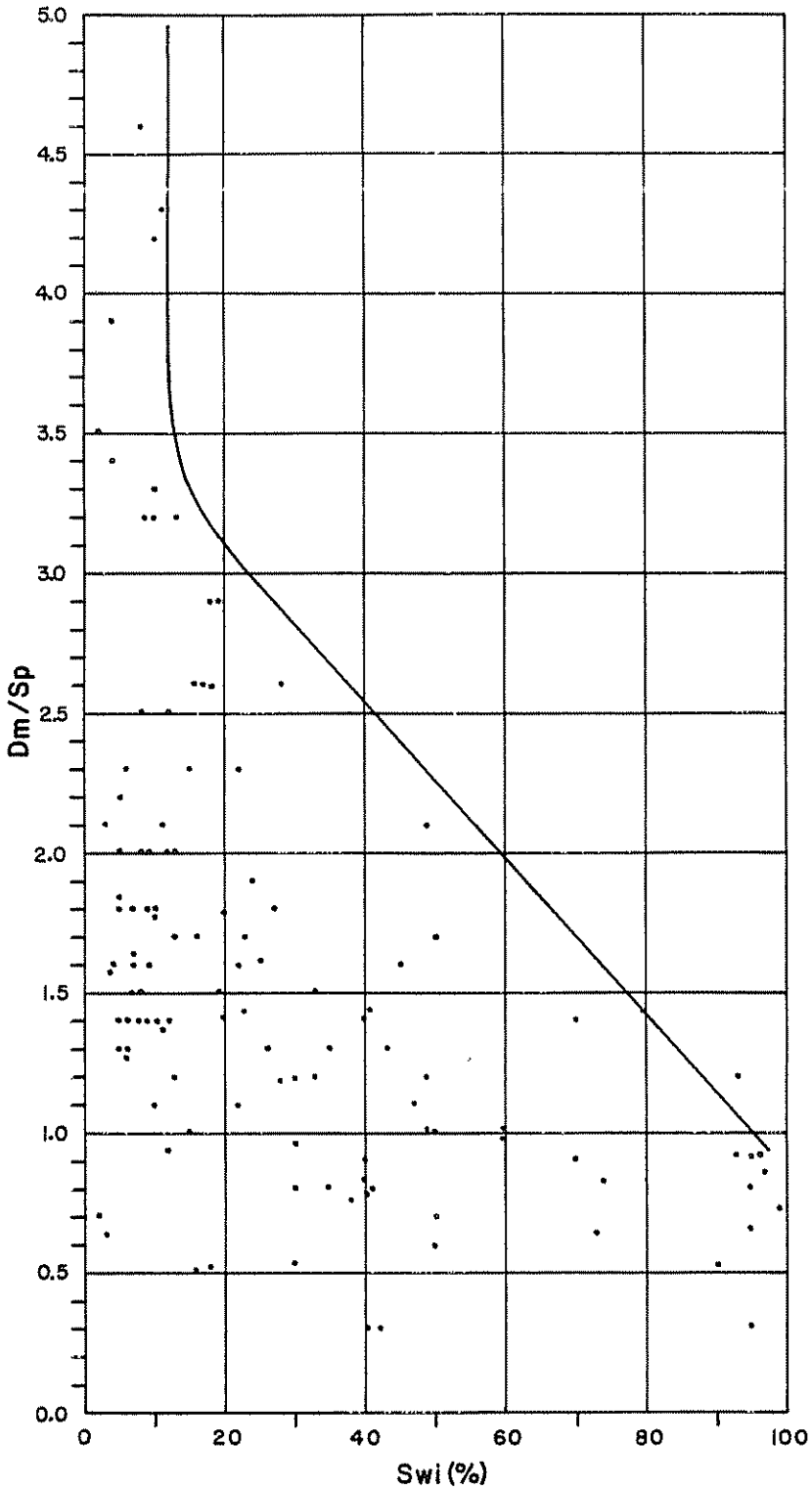

FIGURE 42. Plot of irreducible water saturation versus mean throat size to throat sorting ratio for all data of U4 and U6 reservoirs combined.

Table 7. Expected range of irreducible water saturation values for corresponding values of mean throat size.

Mean Throat Size (μ)	Expected Range of Swi
less than 0.5	0-98%
1.0	0-80%
1.5	0-65%
2.0	0-50%
2.5	0-35%
3.0	0-25%
3.5	0-20%
4.0	0-15%
4.5	0-12%
greater than 5.0	0-10%

Table 8. Expected range of irreducible water saturation values for corresponding values of mean throat size/throat sorting ratio.

Dm/Sp Ratio	Expected Range of Swi
less than 0.5	0-98%
1.0	0-95%
1.5	0-75%
2.0	0-60%
2.5	0-40%
3.0	0-25%
greater than 3.5	0-12%

of this plot also exhibit wide scattering, but for a given Dm/Sp ratio, there is a maximum value of Swi that is not exceeded. Expected range of irreducible water saturation values corresponding to a known Dm/Sp value are shown in Table 8.

Melrose and Brander (1974) have discussed the relationships between pore-system geometry and residual non-wetting-phase saturation. Because reservoir rocks are usually considered to be water-wet, this residual saturation corresponds to residual oil saturation. Non-wetting phase trapping (residual oil saturation) caused by capillary forces is strongly dependent on the characteristics of the reservoir rock pore system (Wardlaw and Cassan, 1978).

Experimental results clearly show that the broader the throat-size distribution, the larger the residual oil saturation (Melrose and Brandner, 1974). This is because oil within smaller throats and pores is bypassed. Any given pore has only a limited number of throats leading to other pores. Water being forced into a reservoir rock pore system thus may not have access to all the pores. This effect has been termed the accessibility factor (Wardlaw and Taylor, 1976).

Since both irreducible water saturation and irreducible oil saturation depend on the same variables, it is reasonable to assume that these two parameters are somewhat correlative. This is to say that high values of irreducible oil saturation are likely to occur in reservoir rocks which display high values of irreducible water saturation. This assumption must be used cautiously, however, since irreducible water saturation (Swi) and irreducible oil saturation (Soi) are two different

measures. Relative irreducible oil saturation of each of the upper Red River pore systems is indicated in Table 6.

Implications For Tertiary Recovery

The key to a tertiary recovery study is to determine the saturation of residual oil after waterflood (Herbeck et al, 1976). Most of the unrecovered oil remaining after waterflooding consists of microscopic droplets of residual oil. The fraction of original oil saturation that has been displaced from the pores by waterflood defines the displacement efficiency of the reservoir. The poorer the throat size sorting, the lower the displacement efficiency. Thus areas of potentially high residual oil saturation can be identified by knowledge of the pore geometry. Reservoir heterogeneities resulting from pore geometry can cause parts of the reservoir to be bypassed during waterflood.

CONCLUSIONS

The Upper Ordovician Red River Formation at Cabin Creek Field, Montana, consists of several carbonate peritidal sequences deposited on a broad, shallow-marine, carbonate bank under arid conditions. Sediments of the upper part of the Red River Formation were deposited as shoaling-upwards cycles which display diagenetic overprinting. Diagenetic processes important to the development of porosity were early vadose leaching of anhydrite, dolomitization, and post-depositional leaching of calcite and gypsum. Local occlusion of porosity resulted from late diagenetic anhydrite and chert cementation.

The predominant pore types are vug, moldic, interparticle, and intercrystal. Vug pores originated in supratidal sediments as a result of vadose leaching of evaporitic sulfate minerals. Moldic porosity occurs most abundantly in the intertidal and subtidal zones, and resulted from leaching of calcium-carbonate grains remaining after dolomitization of matrix material. Moldic pores also developed by leaching of gypsum crystals in the phreatic zone. Interparticle porosity is of primary origin and occurs most commonly in intertidal and lower supratidal zones. Intercrystal porosity resulting from pervasive dolomitization is best developed in the uppermost part of the subtidal zone.

Pore geometry of the upper Red River carbonate reservoirs is a function of depositional environment and diagenetic history. The size, shape, and sorting of pores are mostly a function of porosity type. For example, the size, shape, and sorting of moldic pores depends on the

size, shape, and sorting of skeletal grains and other particles leached to produce the pores. Geometry of pore throats is primarily a function of the size and shape of dolomite crystals composing the matrix of the reservoir rock. It was found that mean throat size tends to increase as porosity percentage increases, depending on reservoir rock type. This relationship occurs because of the spatial relationship between pores and throats. The greater the distance between pores, the less the chance of fluid communication between them. Mean throat size tends to increase as permeability increases regardless of rock or porosity type. No relationship was found between throat size and throat shape. Even the smallest throats may have highly complex shapes.

The most important pore geometry factors affecting reservoir character are size and sorting of pore throats. Using the relationship established between mean throat size and porosity percentage, it is possible to predict pore geometry and, as a consequence, recovery efficiency, if lithofacies distribution, porosity type, and diagenetic history are known for the reservoir. This approach to predicting reservoir pore geometry is capable of identifying areas of potentially high residual oil saturation which can be targeted for enhanced recovery.

LITERATURE CITED

Aitken, J.D., 1967, Classification and environmental significance of cryptalgal limestones and dolomites: Jour. Sedimentary Petrology, v. 37, no. 4, p. 1163-1178.

Aschenbrenner, B.C., and Achauer, C.W., 1960, Minimum conditions for migration of oil in water-wet carbonate rocks; Am. Assoc. Petroleum Geologists Bull., v. 44, p. 235-243.

Asquith, G.B., 1979, Subsurface carbonate depositional models: a concise review: 121 pp., The Petroleum Publishing Corp., Tulsa, OK.

Asquith, G.B., Parker, R.L., Gibson, C.R., and Root, J.R., 1978, Depositional history of the Ordovician Red River C and D zones, Big Muddy Creek Field, Roosevelt County, Montana: in Montana Geological Society Guidebook: Williston Basin Symposium, p. 71-76.

Aufricht, W.R., and Koepf, E.H., 1957, The interpretation of capillary pressure data from carbonate reservoirs: Trans. Amer. Inst. Metallurgical Engin., v. 210, p. 402-405.

Beales, F.W., and Oldershaw, A.E., 1969, Evaporite-solution brecciation and Devonian carbonate reservoir porosity in Western Canada: Am. Assoc. Petroleum Geologists Bull., v. 53, no. 3, p. 503-512.

Carroll, W.K., 1978, Depositional and paragenetic controls on porosity development, upper Red River Formation, North Dakota: in Montana Geological Society Guidebook: Williston Basin Symposium, p. 79-94.

Clement, J.H., 1976, Geologic history - key to accumulation at Cedar Creek (abs): Am. Assoc. Petroleum Geologists Bull., v. 60, p. 2067-2068.

Clement, J.H., 1978, Depositional sequences and characteristics of Ordovician Red River producing zones, Pennel Field, Cedar Creek Anticline, Fallon County, Montana (abs): in Montana Geological Society Guidebook: Williston Basin Symposium, p. 97.

Cussey, R., and Friedman, G.M., 1977, Patterns of porosity and cement in ooid reservoirs in Dogger (Middle Jurassic) of France: Am. Assoc. Petroleum Geologists Bull., v. 61, no. 4, p. 511-518.

Dow, W.G., 1974, Application of oil-correlation and source rock data to exploration in Williston Basin: Am. Assoc. Petroleum Geologists Bull., v. 58, no. 7, p. 1253-1262.

Dowling, P.L., Jr., 1970, Application of carbonate environmental concepts to secondary recovery projects: Soc. of Petroleum Engin. of AIME, paper no. SPE 2987.

Dullien, F.A.L., and Dhawan, G.K., 1974, Characterization of pore structure by a combination of quantitative photomicrography and mercury porosimetry: Jour. of Colloid and Interface Science, v. 47, no. 2, p. 337-349.

Dullien, F.A.L., and Dhawan, G.K., 1975, Bivariate pore-size distributions of some sandstones: Jour. of Colloid and Interface Science, v. 52, no. 1, p. 129-135.

Evamy, B.D., 1967, Dedolomitization and the development of rhombohedral pores in limestones: Jour. Sedimentary Petrology, v. 37, p. 1204-1215.

Fisk, H.N., 1959, Padre Island and the Laguna Madre Flats, coastal south Texas, in 2nd Coastal Geogr. Conf., R.J. Russell, Ed: Washington, D.C., Natl. Acad. Sci., p. 103-152.

Folk, R.L., 1974, The natural history of crystalline calcium carbonate: effect of magnesium content and salinity: Jour. Sedimentary Petrology, v. 44, no. 1, p. 40-53

Friedman, G.M., 1959, Identification of carbonate minerals by staining methods: Jour. Sedimentary Petrology, v. 29, no. 1, p. 87-97.

Friedman, G.M., and Sanders, J.E., 1967, Origin and occurrence of dolostones, p. 267-348 in Chilingar, G.V., Bissell, H.J., and Fairbridge, R.W., eds, Carbonate rocks, origin, occurrence, and classification: Amsterdam, Elsevier Publ. Co., 471 p.

Friedman, G.M., and Sanders, J.E., 1978, Principles of sedimentology: New York, John Wiley & Sons, 792 p.

Fuller, J.G.C.M., 1961, Ordovician and contiguous formations in North Dakota, South Dakota, Montana, and adjoining areas of Canada and United States: Am. Assoc. Petroleum Geologists Bull., v. 45, p. 1334-1363.

Gvirtzman, G., and Friedman, G.M., 1977, Sequence of progressive diagenesis in coral reefs: Am. Assoc. Petroleum Geologists Studies in Geology no. 4, p. 357-380.

Herbeck, E.F., Heintz, R.C., and Hastings, J.R., 1976, Fundamentals of tertiary oil recovery: Petroleum Engineer, May 1976, p. 114-120.

Imbt, W.C., and Ellison, S.P., 1946, Porosity in limestone and dolomite petroleum reservoirs, in Drilling and production practice: Amer. Petroleum Inst., New York, p. 364-372.

Jardine, D., Andrews, D.P., Wishart, J.W., and Young, J.W., 1977, Distribution and continuity of carbonate reservoirs: Jour. Petroleum Technology, July 1977, p. 873-885.

Jodry, R.L., 1972, Pore geometry of carbonate rocks (Basic geologic concepts), p. 35-82 in Chilingar, G.V., Mannon, R.W., and Rieke, H.H., eds, Oil and gas production from carbonate rocks: Amsterdam, Elsevier.

Kendall, A.C., 1976, The Ordovician carbonate succession (Bighorn Group) of southeastern Saskatchewan: Sask. Dept. Miner. Resour. Rept. 180.

Kinsman, D.J.J., 1969, Modes of formation, sedimentary associations, and diagnostic features of shallow-water and supratidal evaporites: Am. Assoc. Petroleum Geologists Bull., v. 53, p. 830-840.

Kohm, J.A., and Louden, R.O., 1978, Ordovician Red River of Eastern Montana and Western North Dakota: relationships between lithofacies and production: Montana Geological Soc. Guidebook, Williston Basin Symposium, p. 99-117.

Laporte, L.F., 1967, Carbonate deposition near mean sea-level and resultant facies mosaic: Manlius Formation (Lower Devonian) of New York State: Am. Assoc. Petroleum Geologists Bull., v. 51, no. 1, p. 73-101.

McBride, E.F., and Folk, R.L., 1977, The Caballos novaculite revisited: part 2: chert and shale members and synthesis: Jour. Sedimentary Petrology, v. 47, no. 3, p. 1261-1286.

Melrose, J.C., and Brandner, C.F., 1974, Role of capillary forces in determining microscopic displacement efficiency for oil recovery by waterflooding: Jour. Canadian Petrol. Tech., v. 13, p. 54-62.

Monty, C., 1976, The origin and development of cryptalgal fabrics: P. 193-249, in Walter, M.R., ed, Stromatolites: Developments in Sedimentology 20, Amsterdam, Elsevier Scientific Pub. Co., 790 p.

Morrow, N.R., 1970, Irreducible wetting-phase saturations in porous media: Chem. Engin. Science, v. 25, p. 1799-1815.

Morrow, N.R., 1971, Small-scale packing heterogeneities in porous sedimentary rocks: Am. Assoc. Petroleum Geologists Bull., v. 55, p. 514-522.

Murray, R.C., 1960, Origin of porosity in carbonate rocks: Jour. Sedimentary Petrology, v. 30 p. 59-84.

Murray, R.C., and Pray, L.C., 1965, Dolomitization and limestone diagenesis - an introduction, p. 1-3 in Pray, L.C., and Murray, R.C., eds, Dolomitization and limestone diagenesis, a symposium: Tulsa, Okla., Soc. Econ. Paleontologists and Mineralogists, Spec. Pub. No. 13, 180 p.

Pickell, J.J., Swanson, B.F., and Hickman, W.B., 1966, Application of air-mercury and oil-air capillary pressure data in the study of pore structure and fluid distribution: Soc. of Petrol. Engin. Jour., March, 1966, p. 55-61.

Pickett, G.R., and Artus, D.S., 1970, Prediction from logs of recoverable hydrocarbon volume, Ordovician carbonates: Williston Basin: Geophysics, v. 35, no. 1, p. 113-123.

Porter, J.W., and Fuller, J.G.C.M., 1959, Lower Paleozoic rocks of northern Williston Basin and adjacent areas: Am. Assoc. Petroleum Geologists Bull., v. 43, p. 124-189.

Reitzel, G.A., and Callow, G.O., 1977, Pool description and performance analysis leads to understanding Golden Spike's miscible flood: Jour. Petroleum Tech., July, 1977, p. 867-872.

Rieke, H.H., III, Chilingar, G.V., and Mannon, R.W., 1972: Application of petrography and statistics to the study of some petrophysical properties of carbonate reservoir rocks, p. 340-354, in Chilingar, G.V., Mannon, R.W., and Rieke, H.H., eds, Oil and gas production from carbonate rocks: Amsterdam, Elsevier.

Robinson, R.B., 1966, Classification of reservoir rocks by surface texture: Am. Assoc. Petroleum Geologists Bull., v. 50, no. 3, p. 547-559.

Roehl, P.O., 1967, Stony Mountain (Ordovician) and Interlake (Silurian) facies analogs of recent low energy marine and subaerial carbonates, Bahamas: Am. Assoc. Petroleum Geologists Bull., v. 51, p. 1979-2032.

Schmidt, V., 1965, Facies, diagenesis, and related reservoir properties in the Gigas Beds (Upper Jurassic), Northwestern Germany, p. 124-168, in Pray, L.C., and Murray, R.C., eds, Dolomitization and limestone diagenesis, a symposium: Tulsa, Okla., Soc. Econ. Paleontologists and Mineralogists, Spec. Pub. no. 13, 180 p.

Shinn, E.A., Robbin, D.M., and Steinen, R.P., 1980, Experimental compaction of lime sediment: Am. Assoc. Petroleum Geologists Bull., v. 64, no. 5, p. 783 (abs).

Stout, J.L., 1964, Pore geometry as related to carbonate stratigraphic traps: Am. Assoc. Petroleum Geologists Bull., v. 48, p. 329-337.

Thomeer, J.H.M., 1960, Introduction of a pore geometrical factor defined by the capillary pressure curve: Jour. Petroleum Tech., Tech. Note 2057, March issue, p. 73-77.

Wanless, H.R., 1979, Limestone response to stress: Pressure solution and dolomitization: Jour. Sedimentary Petrology, v. 49, no. 2, p. 437-462.

Wardlaw, N.C., 1976, Pore geometry of carbonate rocks as revealed by pore casts and capillary pressure: Am. Assoc. Petroleum Geologists Bull., v. 60, no. 2, p. 245-257.

Wardlaw, N.C., and Cassan, J.P., 1978, Estimation of recovery efficiency by visual observation of pore systems in reservoir rocks: Bull. Canadian Petroleum Geologists, v. 26, no. 4, p. 572-585.

Wardlaw, N.C., and Cassan, J.P., 1979, Oil recovery efficiency and rock-pore properties of some sandstone reservoirs: Bull. Canadian Petroleum Geology, v. 27, no. 2, p. 117-138.

Wardlaw, N.C., and Taylor, R.P., 1976, Mercury capillary pressure curves and the interpretation of pore structure and capillary behavior in reservoir rocks: Bull. Canadian Petroleum Geologists, v. 24, no. 2, p. 225-262.

Washburn, E.W., 1921, Note on a method of determining the distribution of pore sizes in a porous material: Proc., National Academy of Science, v. 7, p. 115-116.

Wayhan, D.A., and McCaleb, J.A., 1969, Elk Basin Madison heterogeneity - its influence on performance: Jour. Petroleum Tech., February, 1969, p. 153-159.

Williams, J.A., 1974, Characterization of oil types in Williston Basin: Am. Assoc. Petroleum Geologists Bull., v. 58, no. 7, p. 1243-1252.

APPENDIX

Mercury Capillary-Pressure Curves

Mercury capillary-pressure curves provide data for the determination of pore throat size and the percentage of total pores effective under varying pressure conditions in the reservoir rock. The mercury injection method best reproduces reservoir conditions (Stout, 1964) and is commonly used to construct a capillary-pressure curve. With this method, the core sample to be used is cleaned, placed in a chamber, and evacuated. Mercury, which acts as a non-wetting agent equivalent to oil entering a water-wet reservoir, is forced into the sample at low pressure. This pressure is maintained until no more mercury enters the sample. The volume of mercury which has entered the pore system of the sample at this initial pressure is recorded. The process is then repeated through a range of increasingly higher and higher pressures to the highest pressure desired. The volume of mercury injected into the sample pore system at each pressure level is used to calculate directly the percentage of total pore space which has been saturated. The saturation at each pressure level is plotted on a graph with the vertical axis as capillary pressure in pounds per square inch, and the horizontal axis as percent of porosity unoccupied by mercury (equivalent to percent water saturation). The injected mercury represents oil, and thus the amount of mercury entering the sample can be considered as oil saturation.

Water saturations as plotted on the graph are computed by subtracting the percentage of total pore space filled by mercury from the total pore space of the sample. A capillary-pressure curve results by connecting the points computed at each pressure level (Figure A-0). The changing position of the mercury/mercury vapor interface within a single capillary pore as pressure increases is shown in the inset (M = mercury, V = mercury vapor).

Capillary pressure measurements should not be confused with measurement of permeability. Permeability refers to the extent of interconnection between an unknown number of pores in a reservoir rock. A capillary pressure curve on the other hand, indicates the percentage of total pores connected by pore throats of sufficient size to permit oil entry at a given capillary pressure (Jodry, 1972).

Interpretation of Capillary-Pressure Curves

In the example given (Figure A-0), mercury does not begin to enter the pore system of the reservoir rock until a pressure of 25 psia is reached. Prior to this, 100% of the pore space is unoccupied by mercury (or 100% water saturated). At a pressure of 50 psia, an abrupt change in gradient of the curve occurs as a substantial volume of mercury begins to enter the sample. This point on the curve is defined as the threshold pressure (Pt). As the pressure is increased, more and more mercury enters the pore space. At 65 psia, 50% of the pore space in the reservoir rock has been occupied by mercury.

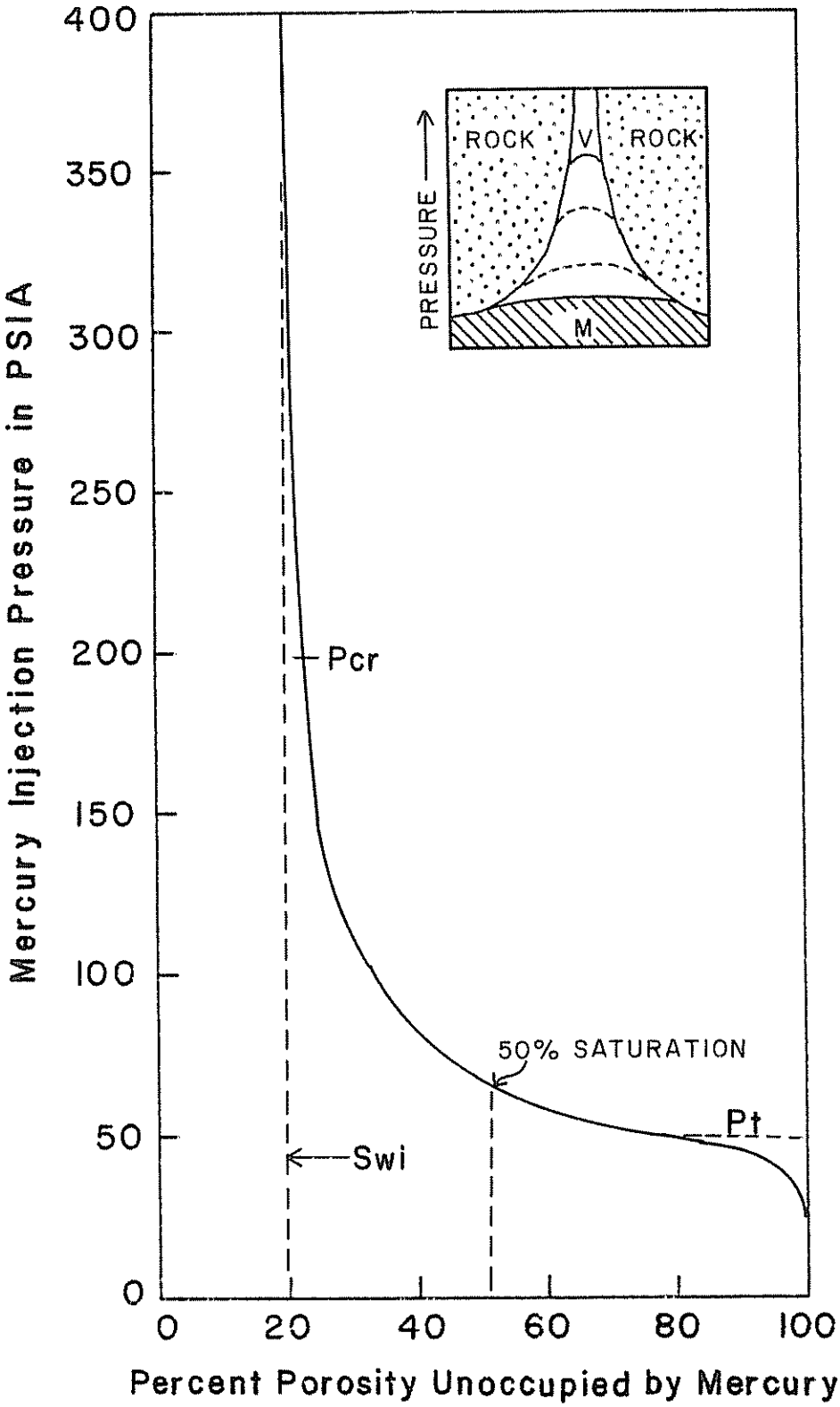

FIGURE A-0. Capillary-pressure diagram illustrating terms defined in the text. Inset diagram illustrates the changing position of the mercury/mercury vapor interface as pressure increases. M = mercury, V = mercury vapor.

The point at which the curve becomes essentially vertical is defined as the critical pressure (Pcr). Beyond this pressure, essentially no additional mercury will enter the sample. After critical pressure has been attained, the amount of pore space which remains unoccupied by mercury indicates the irreducible water saturation (Swi) of the reservoir rock. In the case of the example (Figure A-0), the irreducible water saturation is 20% and the critical pressure is about 200 psia. Thus it takes a pressure of about 200 psia to saturate the available pore space of this reservoir rock with mercury, and 20% of the total pore space cannot be invaded due to lack of sufficiently large interconnections (throats) between pores.

Determination of threshold pressure, critical pressure, and irreducible water saturation provide a means of describing reservoir petrophysics. In addition to such data, capillary-pressure curves are useful for determining the pore geometry of a reservoir rock. The curve indicates total pore volume invaded by mercury as increasing pressure forces it through successively smaller pore throats. Pores deep within the reservoir rock are invaded by mercury only via the pore throats. Thus the shape of the curve is determined by the size, sorting, and skewness of the pore throats (Thomeer, 1960, Jodry, 1972). The statistical methods used to investigate cumulative curves from sediment seive analysis may also be used to investigate capillary-pressure curves (Stout, 1964). It should be understood that the use of such methods for capillary-pressure curve analysis measures not only the influence of the deposited carbonate particles, but also the effects of diagenesis.

Determination of Pore Throat Size

The size of invaded pore throats can be calculated from capillary-pressure curve data by use of the Washburn (1921) equation:

$$Pc = \frac{-2\gamma\cos\Theta}{d}$$

where: Pc = pressure

γ = surface tension of mercury = 465 dynes/cm

Θ = contact angle of mercury = 140°

d = pore throat diameter

The measurement of pore throats by this method is discussed by Gvirtzman and Friedman (1977), Wardlaw (1976), Wardlaw and Cassan (1979), and Rieke (1972). According to Wardlaw (1976) the above equation is appropriate for sheetlike pore throats, as are found in dolomites. The capillary pressure of any point on the curve can thus be converted to the equivalent pore throat diameter. Determination of mean throat size (Dm) is particularly useful for the comparison of different reservoir rock samples, as it is an important indication of pore-throat geometry. In addition, the throat size which is equivalent to the capillary pressure at 50 percent saturation of the pore volume by mercury (d_{50}) may also be used to express pore-throat geometry (Wardlaw and Cassan, 1979).

Statistical Measures of Pore Geometry

The statistical measures used to determine pore geometry from capillary-pressure curves have been discussed by Rieke et al (1972).

Pore-throat size statistics are the same as those used in grain-size analysis. The measures employed in the present study are mean throat size (Dm), sorting (Sp), and skewness (Skp). The mean (Dm) is the measure of the overall average throat size. Throat sorting (Sp) is a measure of dispersion about the mean, or standard deviation, of the throat sizes in the sample. Skewness (Skp) is a measure of asymmetry, or non-normality, of a throat-size distribution. Sorting and skewness measures, as they relate to capillary-pressure curves, have been discussed by Jodry (1972). The equations used are shown below.

$$Dm = \frac{D_{16} + D_{50} + D_{84}}{3}$$

$$Sp = \frac{(D_{84} - D_{16})}{4} + \frac{(D_{95} - D_5)}{6.6}$$

$$Skp = \frac{(D_{84} + D_{16} - 2D_{50})}{2(D_{84} - D_{16})} + \frac{(D_{95} + D_5 - 2D_{50})}{2(D_{95} - D_5)}$$

EXPLANATION OF LITHOLOGY, PORE TYPE, AND BOREHOLE SYMBOLS

Lithology Symbols

- limestone
- dolomite
- shale
- M mudstone
- W wackestone
- P packstone
- X crystalline
- fossil debris
- intraclasts
- peloids
- ooids
- conglomerate
- chert
- nodular chert
- anhydrite
- nodular anhydrite

Pore-Type Symbols

- M moldic
- V vug
- Ip interparticle
- Ic intercrystal
- F fracture
- C channel

Borehole Symbols

- cored well
- oil well
- injection well
- shut in well
- water supply well
- abandoned well

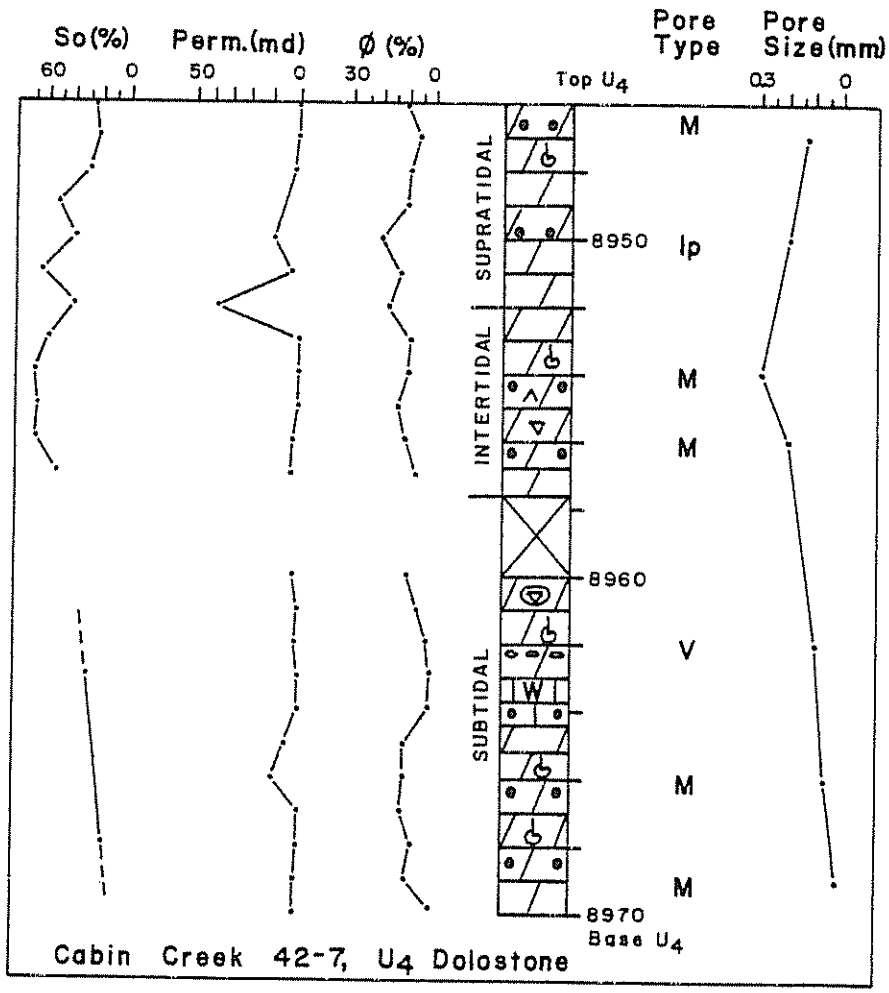

FIGURE A-1. Diagram illustrating oil saturation (So), permeability, porosity percentage (Ø), lithology, pore type, and pore size for the U4 reservoir of the Cabin Creek 42-7 well. Location: Sec.7-10N-58E, SE-NE.

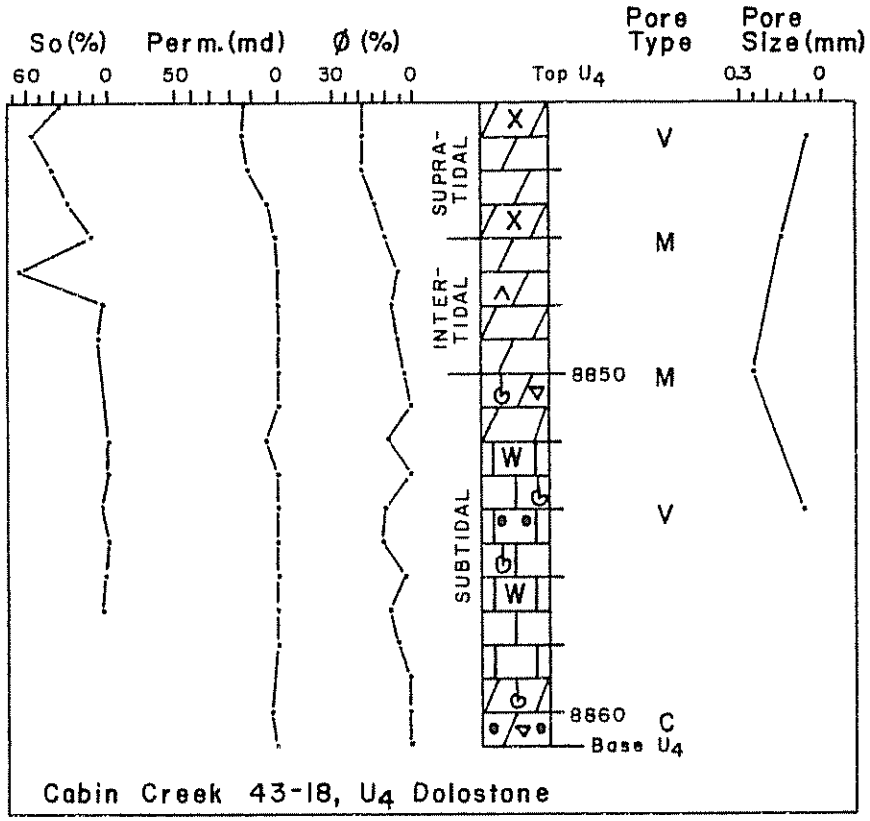

FIGURE A-2. Diagram illustrating oil saturation (So), permeability, porosity percentage (Ø), lithology, pore type, and pore size for the U4 reservoir of the Cabin Creek 43-18 well. Location: Sec.18-10N-58E, NE-NE-SE.

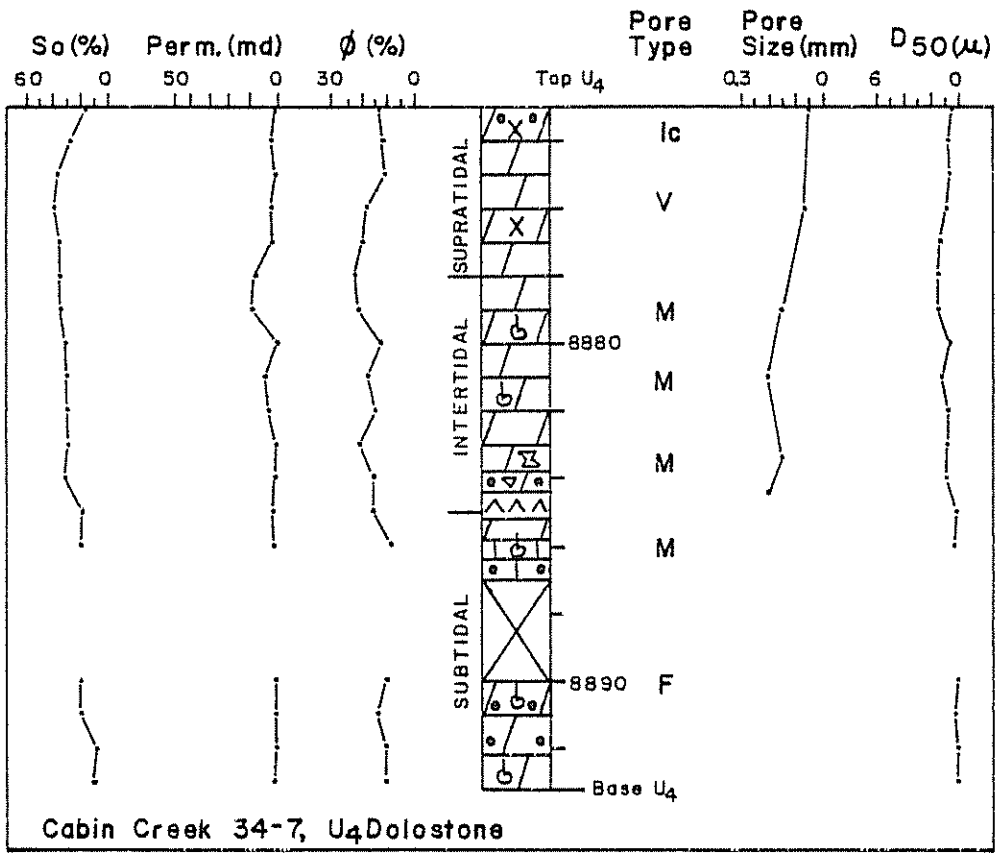

FIGURE A-3. Diagram illustrating oil saturation (So), permeability, porosity percentage (ϕ), lithology, pore type, pore size, and throat size (D_{50}) for the U4 reservoir of the Cabin Creek 34-7 well. Location: Sec.7-10N-58E, SW-SE.

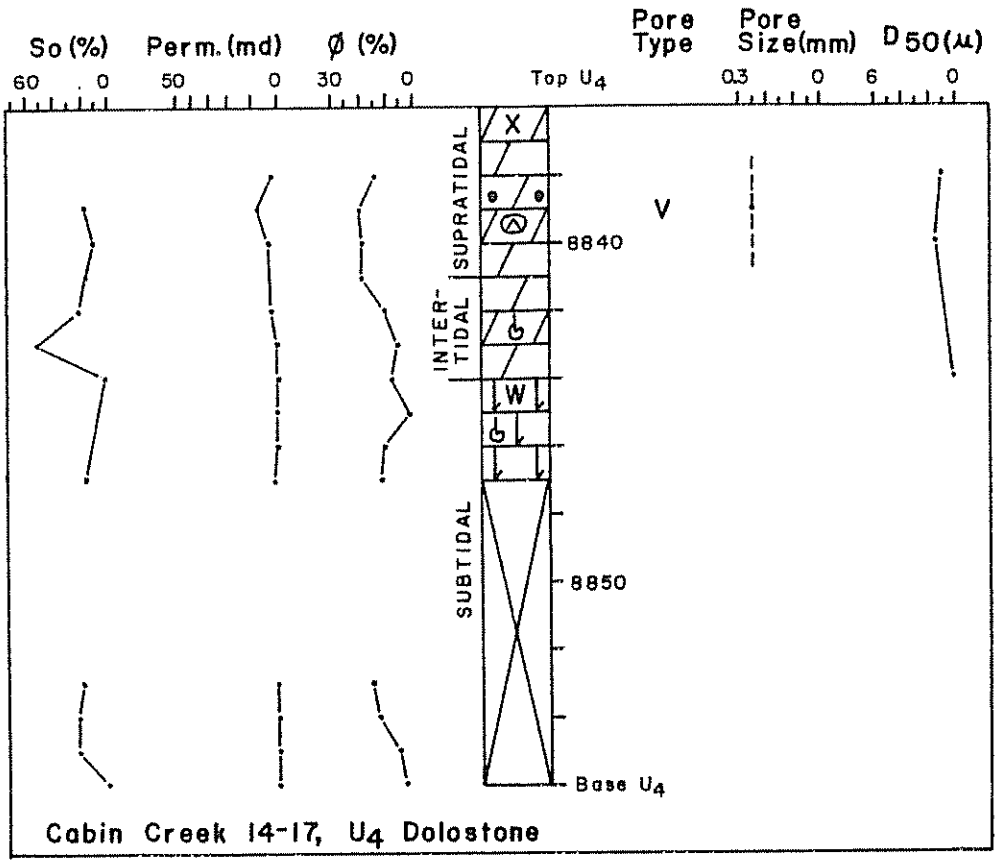

FIGURE A-4. Diagram illustrating oil saturation (So), permeability, porosity percentage (Ø), lithology, pore type, pore size, and throat size (D50) for the U4 reservoir of the Cabin Creek 14-17 well. Location: Sec.17-10N-58E, SW-SW-SW.

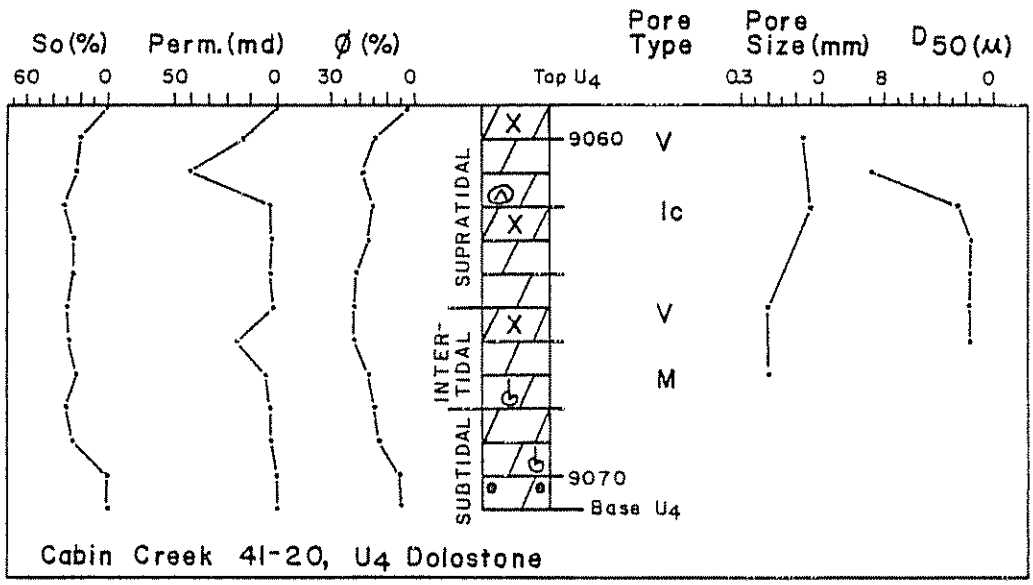

FIGURE A-5. Diagram illustrating oil saturation (So), permeability, porosity percentage (Ø), lithology, pore type, pore size, and throat size (D_{50}) for the U4 reservoir of the Cabin Creek 41-20 well. Location: Sec.20-10N-58E, NW-NE-NE.

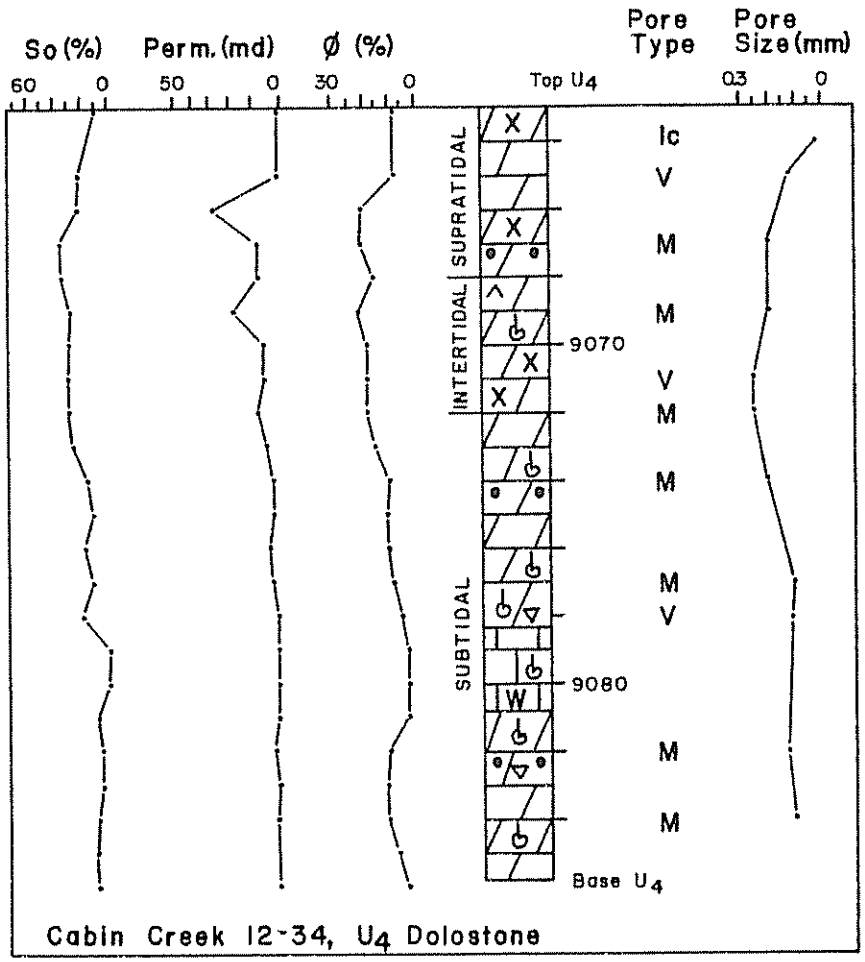

FIGURE A-6. Diagram illustrating oil saturation (So), permeability, porosity percentage (ϕ), lithology, pore type, and pore size for the U4 reservoir of the Cabin Creek 12-34 well. Location: Sec.34-10N-58E, SW-NW.

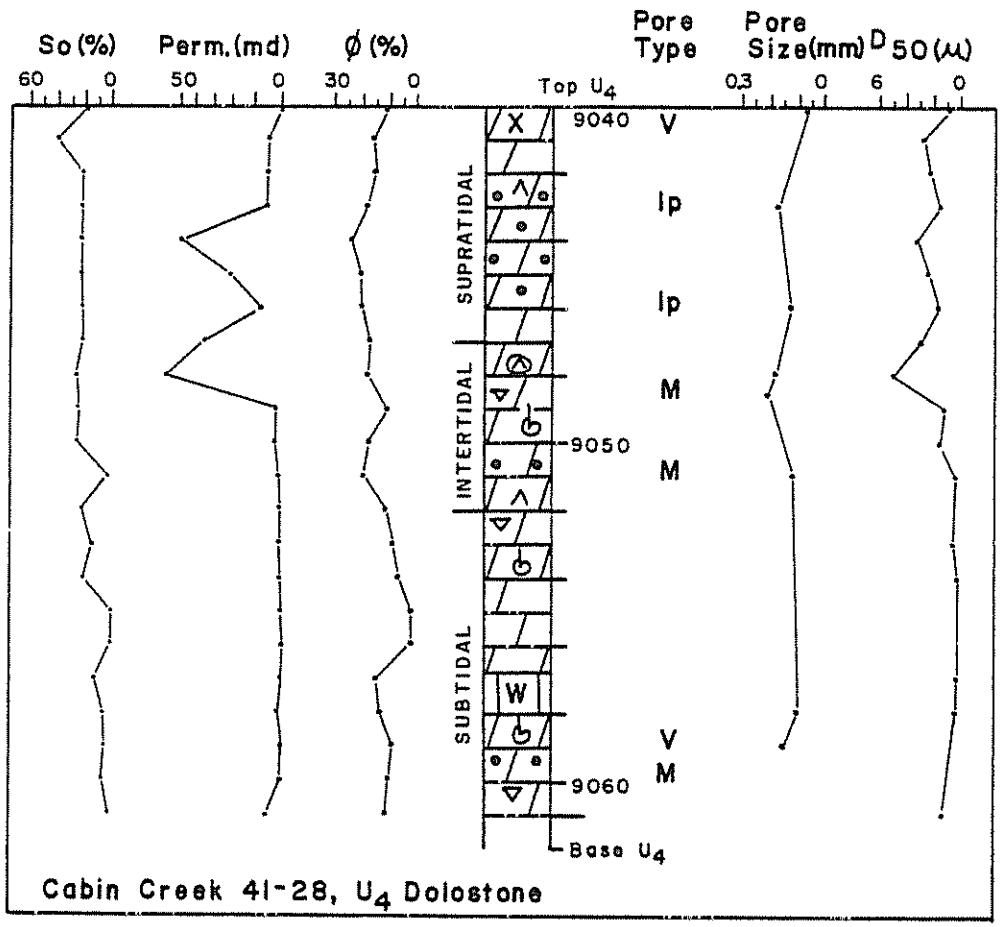

FIGURE A-7. Diagram illustrating oil saturation (So), permeability, porosity percentage (ϕ), lithology, pore type, pore size, and throat size (D_{50}) for the U4 reservoir of the Cabin Creek 41-28 well. Location: Sec.28-10N-58E, C-NE-NE.

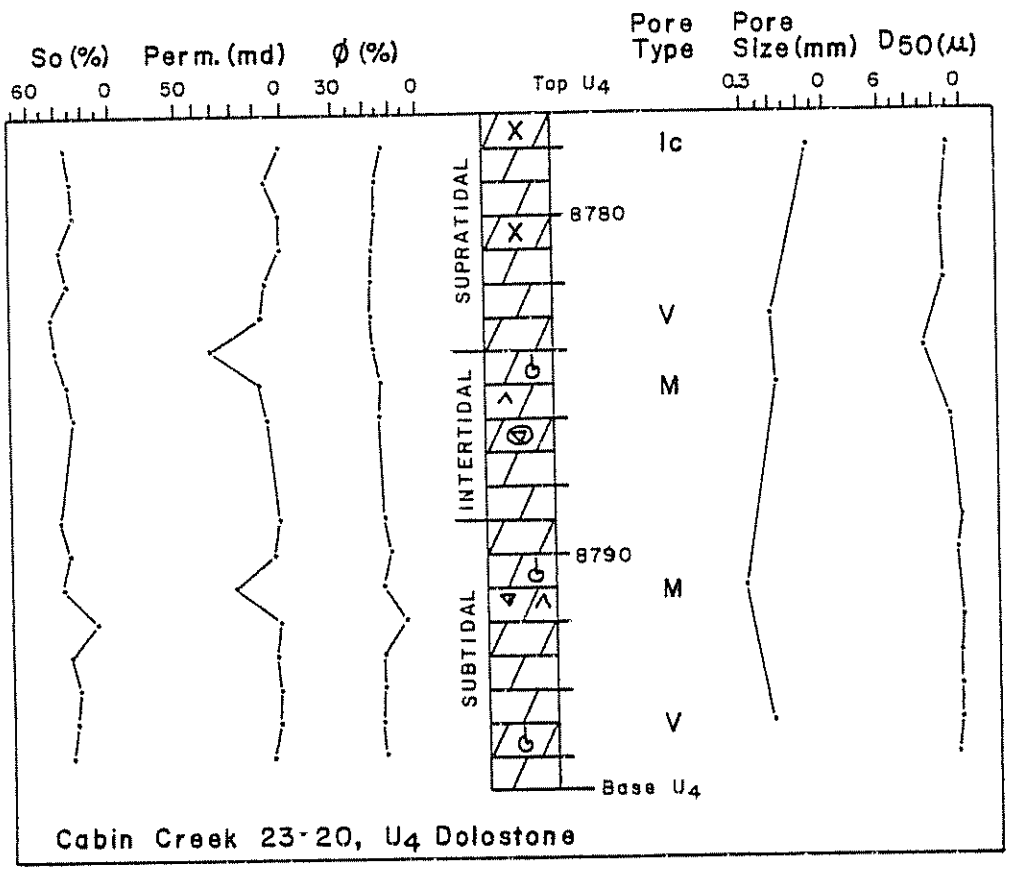

FIGURE A-8. Diagram illustrating oil saturation (So), permeability, porosity percentage (ϕ), lithology, pore type, pore size, and throat size (D_{50}) for the U4 reservoir of the Cabin Creek 23-20 well. Location: Sec.20-10N-58E, C-NW-SW.

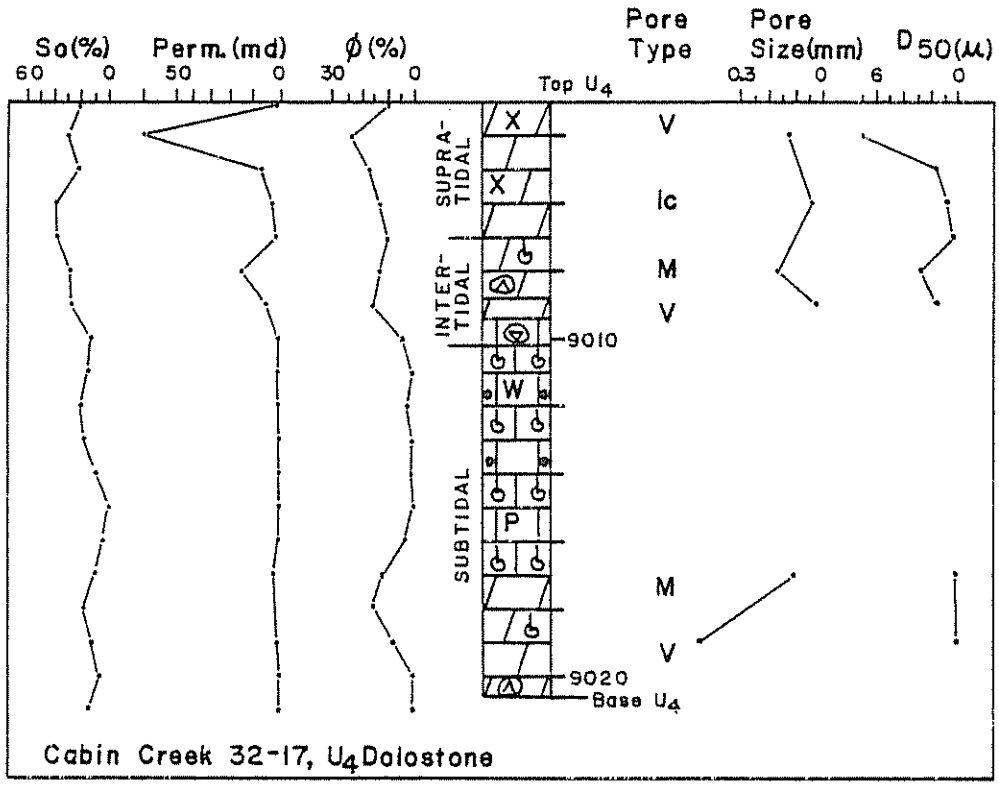

FIGURE A-9. Diagram illustrating oil saturation (So), permeability, porosity percentage (Ø), lithology, pore type, pore size, and throat size (D_{50}) for the U4 reservoir of the Cabin Creek 32-17 well. Location: Sec.17-10N-58E, SW-NE.

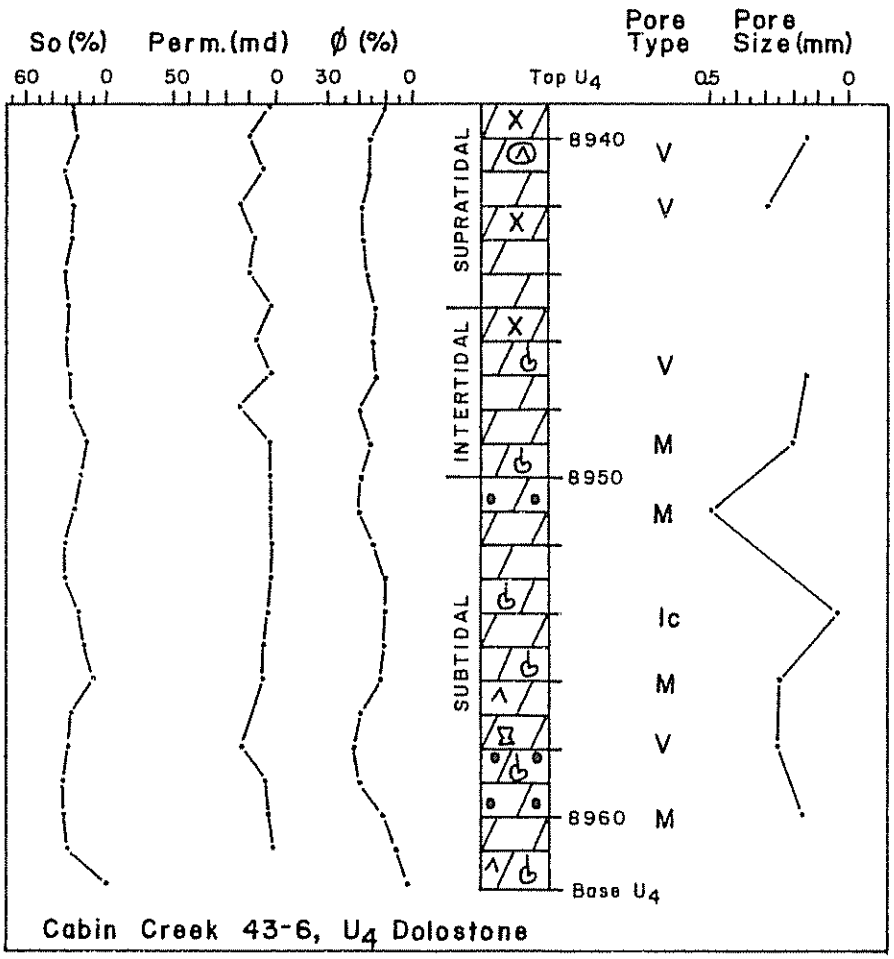

FIGURE A-10. Diagram illustrating oil saturation (So), permeability, porosity percentage (Ø), lithology, pore type, and pore size for the U4 reservoir of the Cabin Creek 43-6 well. Location: Sec.6-10N-58E, SW-NE-SE.

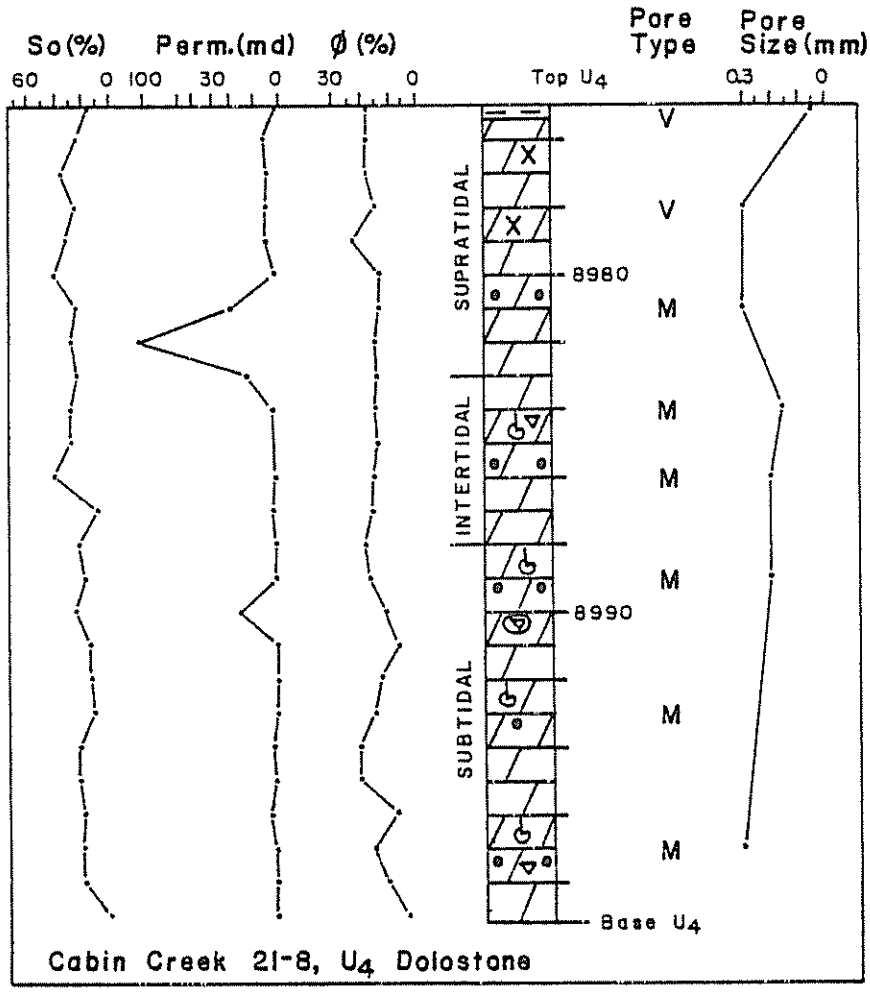

FIGURE A-11. Diagram illustrating oil saturation (So), permeability, porosity percentage (Ø), lithology, pore type, and pore size for the U4 reservoir of the Cabin Creek 21-8 well. Location: Sec.8-10N-58E, NE-NW.

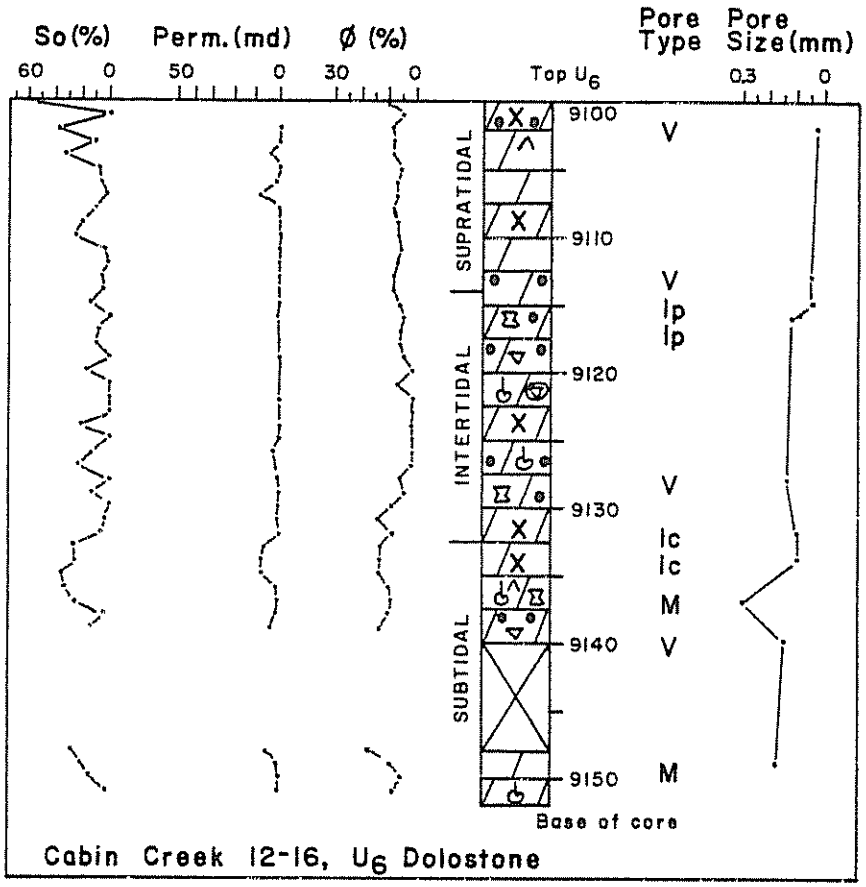

FIGURE A-12. Diagram illustrating oil saturation (So), permeability, porosity percentage (Ø), lithology, pore type, and pore size for the U6 reservoir of the Cabin Creek 12-16 well. Location: Sec.16-10N-58E, SW-NW.

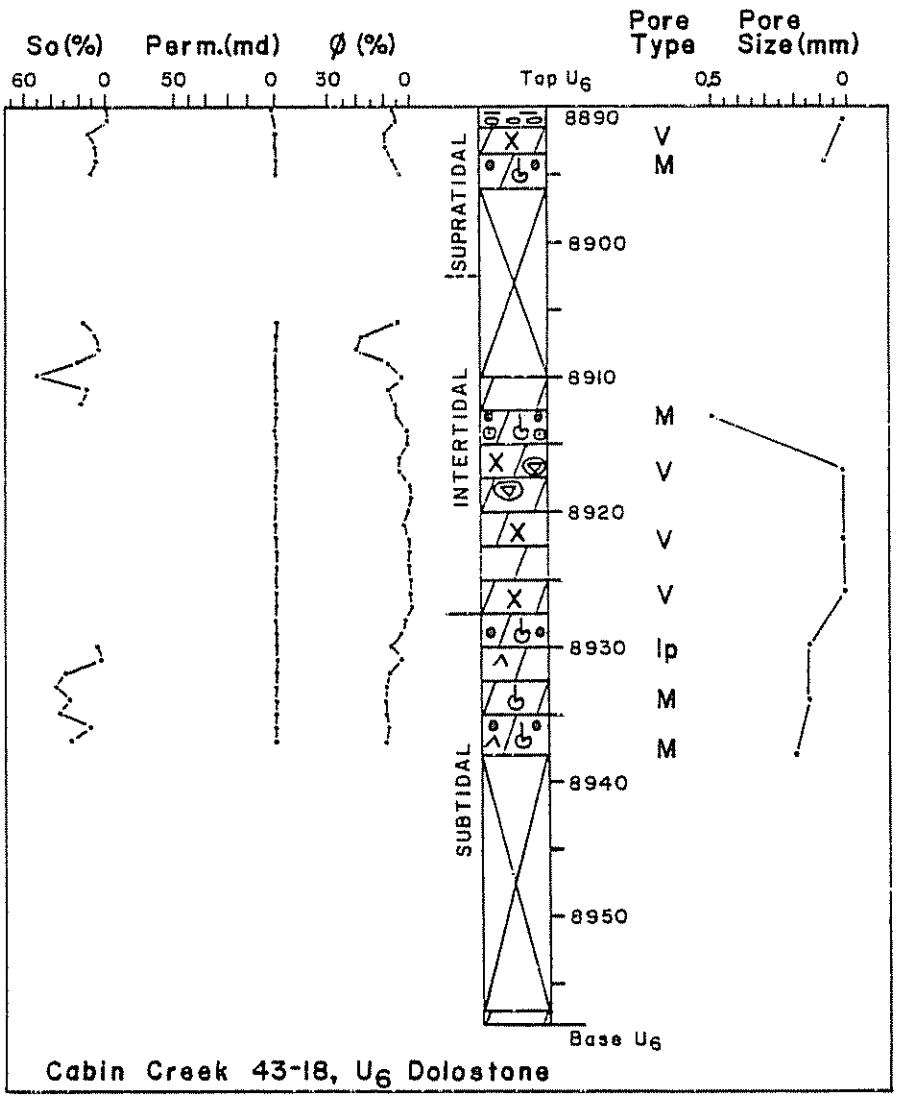

FIGURE A-13. Diagram illustrating oil saturation (So), permeability, porosity percentage (Ø), lithology, pore type, and pore size for the U6 reservoir of the Cabin Creek 43-18 well. Location: Sec.18-10N-58E, NE-NE-SE.

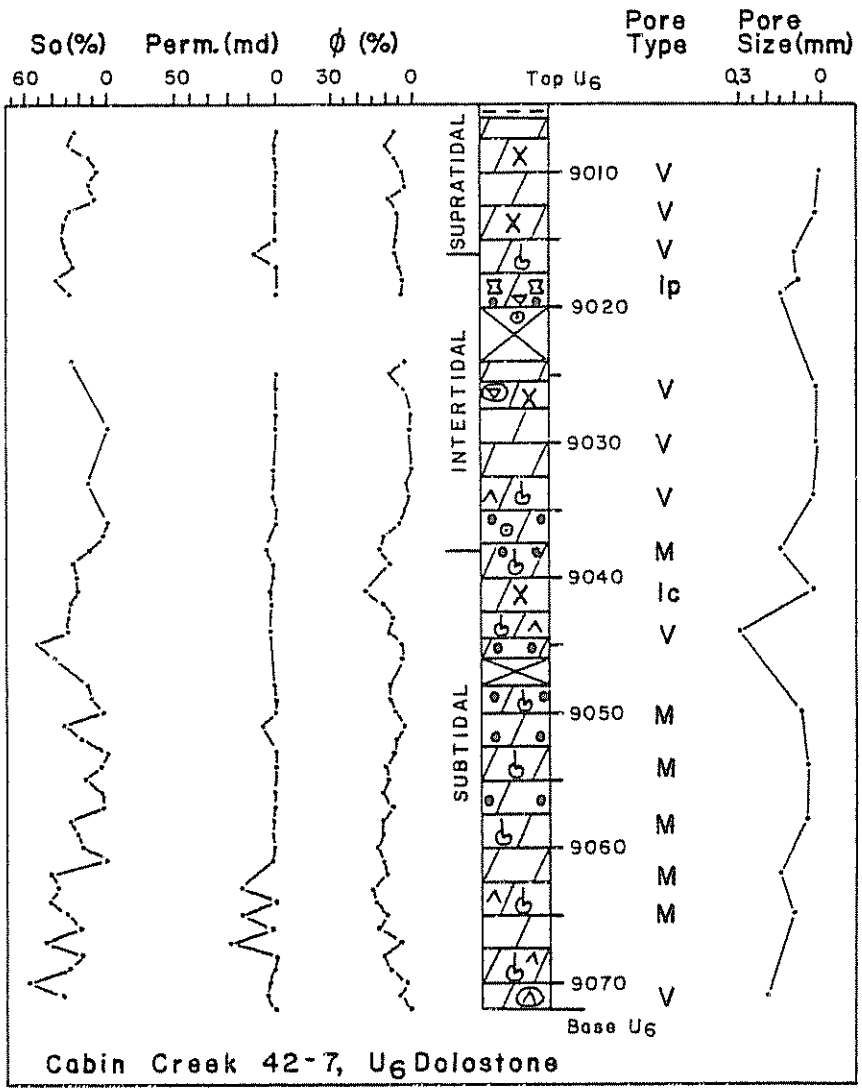

FIGURE A-14. Diagram illustrating oil saturation (So), permeability, porosity percentage (ϕ), lithology, pore type, and pore size for the U6 reservoir of the Cabin Creek 42-7 well. Location: Sec.7-10N-58E, SE-NE.

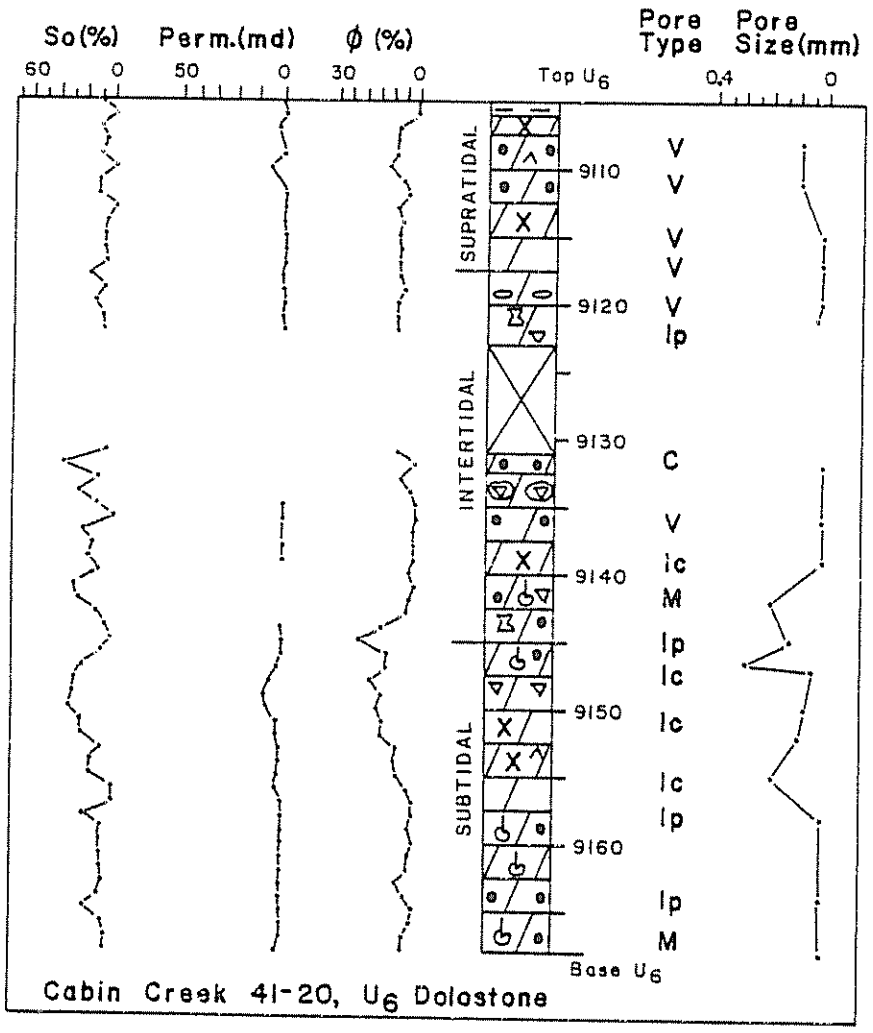

FIGURE A-15. Diagram illustrating oil saturation (So), permeability, porosity percentage (ϕ), lithology, pore type, and pore size for the U6 reservoir of the Cabin Creek 41-20 well. Location: Sec.20-10N-58E, NW-NE-NE.

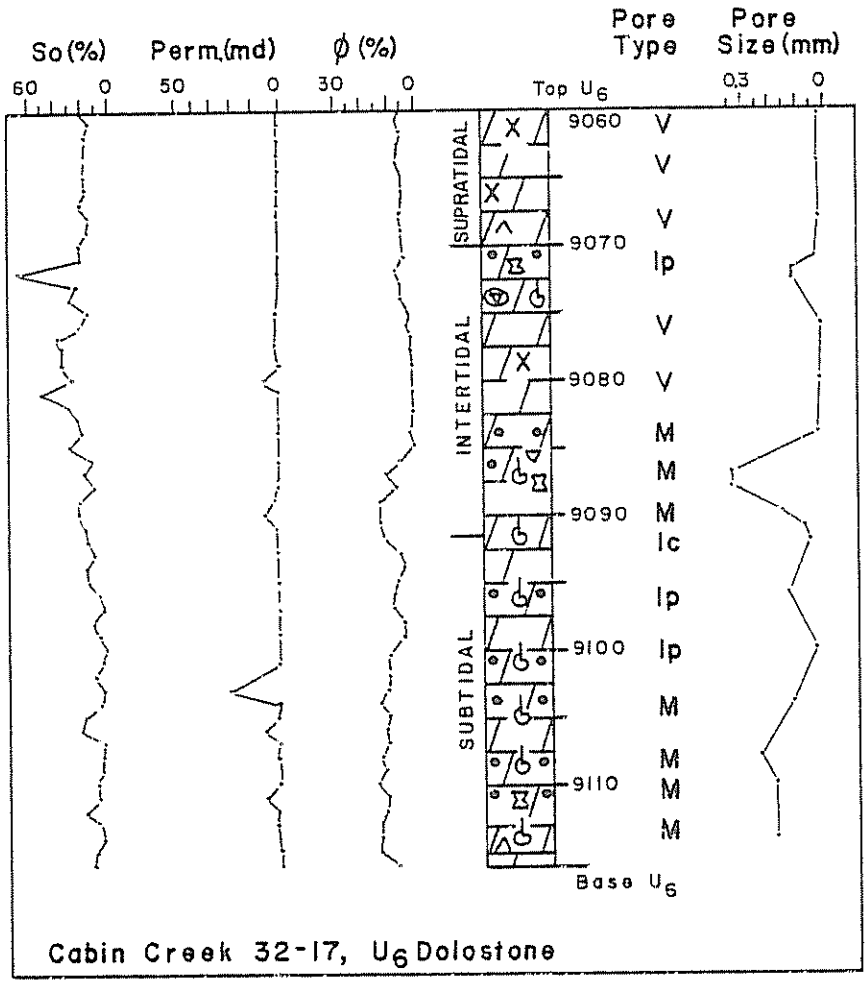

FIGURE A-16. Diagram illustrating oil saturation (So), permeability, porosity percentage (ϕ), lithology, pore type, and pore size for the U6 reservoir of the Cabin Creek 32-17 well. Location: Sec.17-10N-58E, SW-NE.

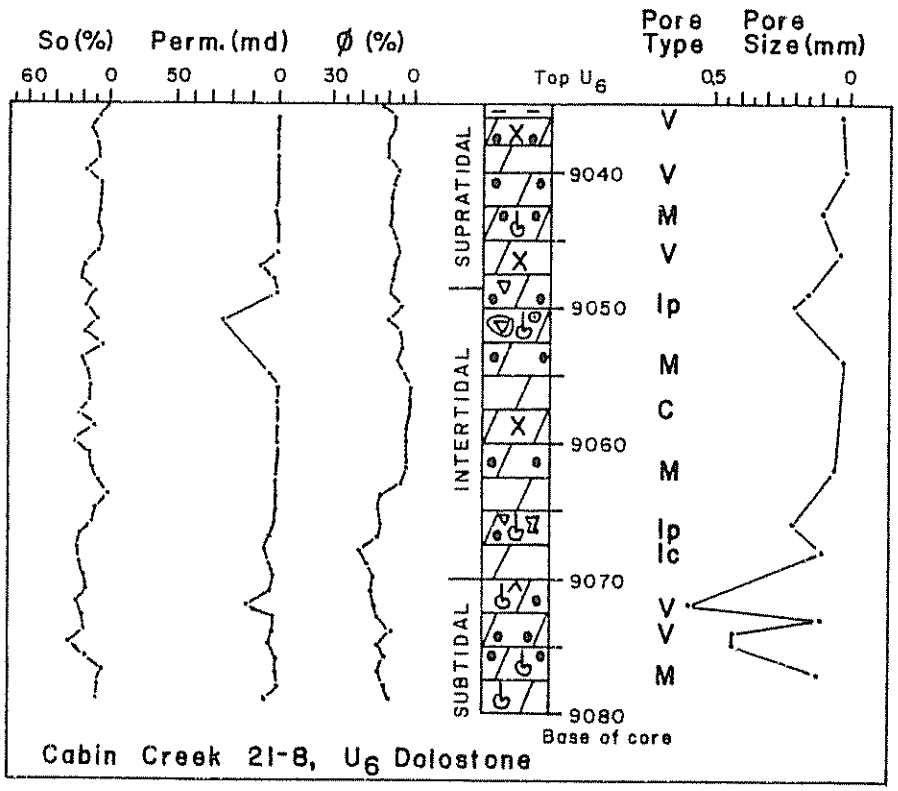

FIGURE A-17. Diagram illustrating oil saturation (So), permeability, porosity percentage (Ø), lithology, pore type, and pore size for the U6 reservoir of the Cabin Creek 21-8 well. Location: Sec.8-10N-58E, NE-NW.

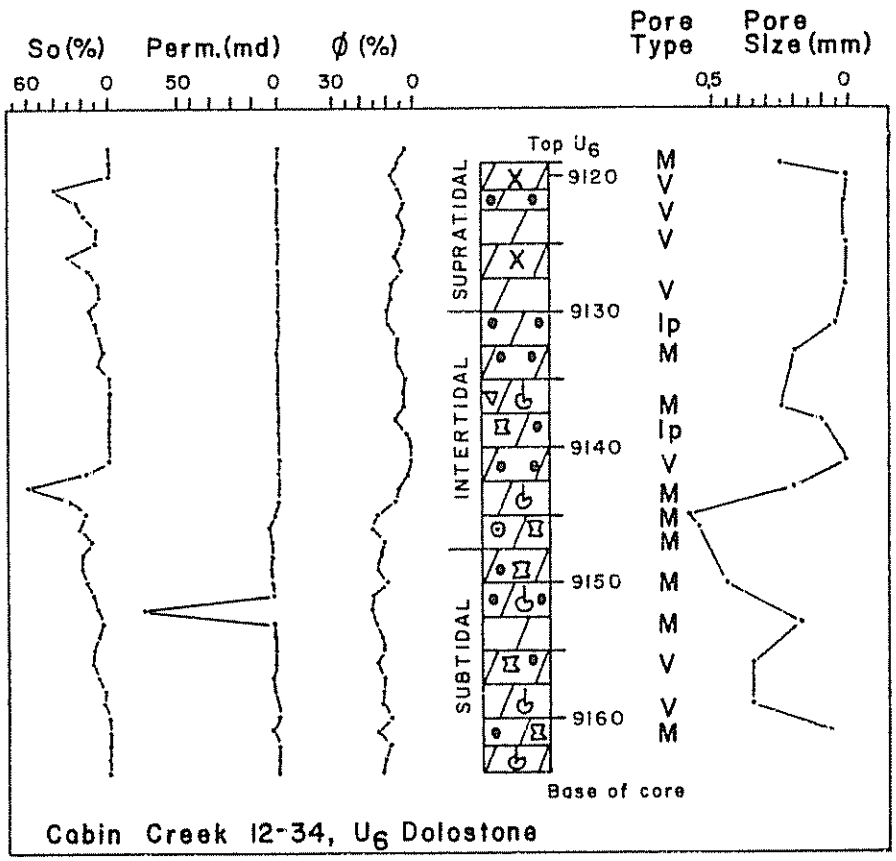

FIGURE A-18. Diagram illustrating oil saturation (So), permeability, porosity percentage (Ø), lithology, pore type, and pore size for the U6 reservoir of the Cabin Creek 12-34 well. Location: Sec.34-10N-58E, SW-NW.

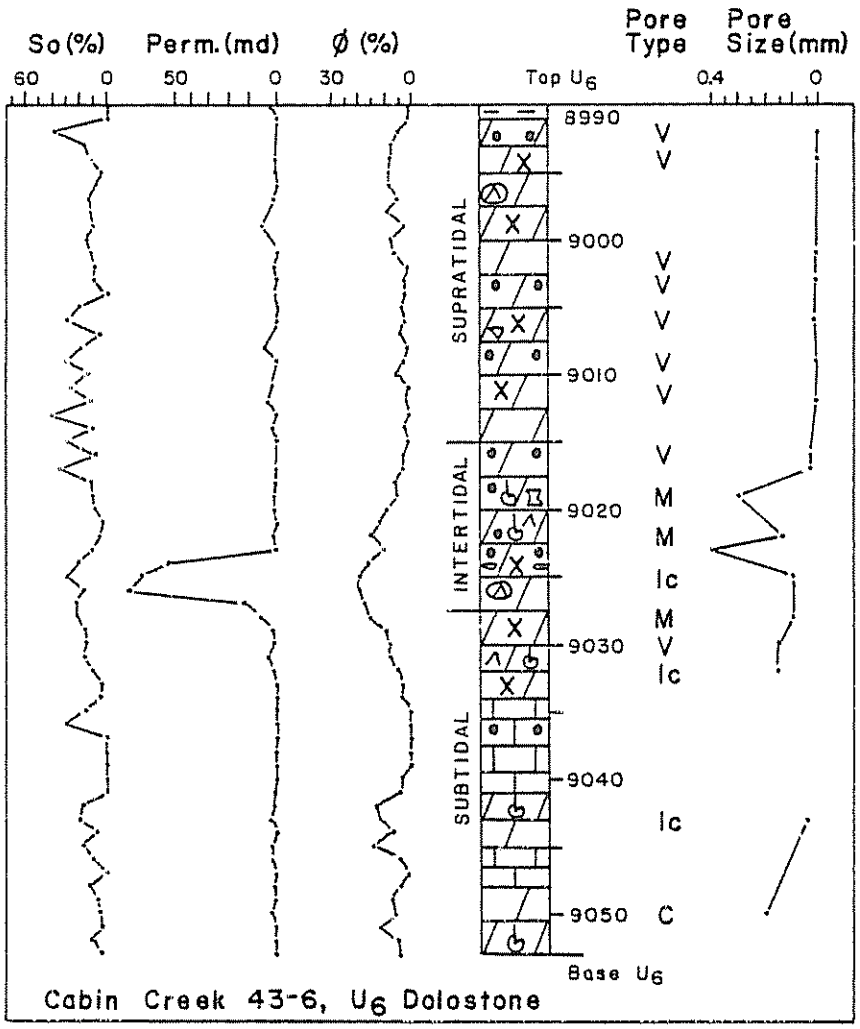

FIGURE A-19. Diagram illustrating oil saturation (So), permeability, porosity percentage (Ø), lithology, pore type, and pore size for the U6 reservoir of the Cabin Creek 43-6 well. Location: Sec.6-10N-58E, SW-NE-SE.

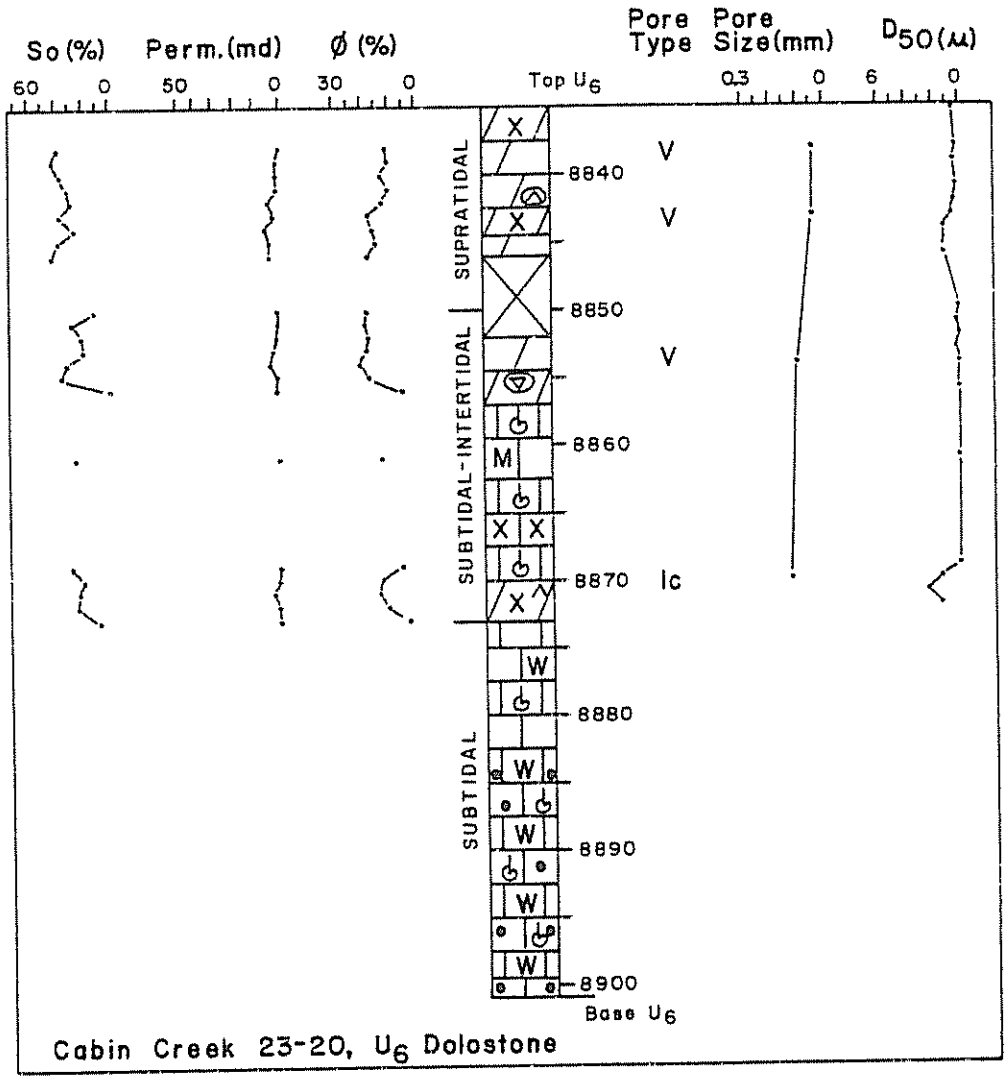

FIGURE A-20. Diagram illustrating oil saturation (So), permeability, porosity percentage (Ø), lithology, pore type, pore size, and throat size (D50) for the U6 reservoir of the Cabin Creek 23-20 well. Location: Sec.20-10N-58E, C-NW-SW.

Computer Analysis of Production from the Cabin Creek Field

Introduction

The Cabin Creek Field has been producing oil and gas from Silurian and Ordovician reservoirs since 1953. Prior to April 1964, production was primary, but after this date secondary recovery was commenced using water flood techniques.

Approximately 70 wells from the Cabin Creek Field were used as a basis for the analysis of production *versus* reservoir porosity *versus* reservoir structure in order to test what correlations may occur between reservoir characteristics and production. Porosity was chosen as the reservoir property for use in this analysis because:

(1) it is the only reservoir characteristic which can be determined in most wells across the field (based on electric log and core data), and

(2) because the study presented in this report has shown that porosity in the Red River Formation can be closely correlated with other reservoir characteristics such as permeability and pore throat size.

The aim of the production analysis was to find:

(1) what, if any correlation exists between the production of oil, water and gas from a particular well and the reservoir porosity or

structure; and

(2) if any relationship exists between the amount and location of production during primary and secondary recovery.

The wells chosen for the study were the ones for which all the relevant production and reservoir data was available.

Production Data

Production sheets for the Cabin Creek Field for March 1964, give cumulate production figures for oil, gas and water from individual wells prior to the commencement of secondary recovery. Oil and water production is expressed in barrels x 10^3 (variables 6 and 7, Table 1-A and 2-A) and gas production is expressed in m.c.f. x 10^3 (variable 8). A further variable -- the productivity -- is also calculated. This is the sum of oil, water and gas production over the period of primary recovery and is considered to represent the total amount of material which passed through the pore network of the reservoir rock (variable 9, Table 1-A and 2-A).

The production data for the Cabin Creek Field during May 1980, gives the closest available approximation to the present cumulative production of oil, water and gas. Subtracting the cumulative production figures for March 1964, from these figures for 1980, gives the total production of oil, water and gas during secondary recovery (variables 10, 11, and 12). The productivity was also calculated for secondary

recovery and is the sum of total oil, water and gas production from April 1964, to May 1980 (variable 13).

In order to highlight any change in the location of oil production and the relative amount of oil produced during secondary recovery, the ratio and difference of oil produced during secondary and primary recovery were calculated (variables 14 and 15).

TABLE 1-A - List of Variables

1. RR = Top of the Red River Formation below sea level (measured in feet).

2. IL = Top of the Interlake Formation below sea level (measured in feet).

3. PFRR = Thickness of the Red River Formation with porosity greater than 10% (measured in feet).

4. PFIL = Thickness of the Interlake Formation with porosity greater than 10% (measured in feet).

5. PFTOTAL = Total reservoir thickness (Red River Formation plus Interlake Formation) with porosity greater than 10% (measured in feet).

6. OIL64 = Total oil production until the commencement of secondary recovery (barrels X 10^3).

7. WATER64 = Total water production until the commencement of secondary recovery (barrels X10^3).

8. GAS64 = Total gas production until secondary recovery (M.C.F.X10^3).

Table 1-A - Cont'd

9. PROD64 = Total productivity (sum of oil, water and gas produced) until secondary recovery commenced.

10. OIL80 = Total oil produced since secondary recovery began in 1980 (barrels $X10^3$).

11. WATER80 = Total water produced since the commencement of secondary recovery (barrels $X10^3$).

12. GAS80 = Total gas production since the commencement of secondary recovery (M.C.F. $X10^3$).

13. PROD80 = Total productivity since water flood (oil plus gas plus water produced).

14. RATIO = Ratio of oil produced during water flood/oil produced prior to water flood (secondary/primary recovery).

15. DIFF = Total oil production during water flood minus total primary oil production (measured in barrels $X10^3$).

TABLE 2-A - Description of Variables

VARIABLE	N	MINIMUM	MAXIMUM	MEAN	STD DEV
1. RR	73	-6302.00	-5846.00	-6128.00	142.12
2. IL	73	-5858.00	-5347.00	-5658.20	143.36
3. PFRR	73	9.00	58.00	34.63	12.70
4. PFIL	73	43.00	230.00	127.56	43.69
5. PFTOTAL	73	85.00	256.00	162.64	41.34
6. OIL64	73	11.45	906.70	295.86	191.25
7. WATER64	73	1.08	404.07	63.54	82.36
8. GAS64	73	1.82	596.14	127.70	128.17
9. PROD64	73	16.99	1323.00	487.10	315.06
10. OIL80	55	9.14	1413.00	389.60	289.26
11. WATER80	55	3.07	2857.10	750.93	704.99
12. GAS80	55	28.45	1468.80	331.97	329.96
13. PROD80	55	47.07	4773.10	1490.20	1063.40
14. RATIO	55	.10	3.65	1.36	.83
15. DIFF	55	-350.36	606.80	69.10	228.00

N = Number of Values of Each Variable Used

Reservoir Data

The main reservoir horizons in the Cabin Creek Field are the Upper Ordovician Red River Formation and the Silurian Interlake Formation, and their production is comingled. Based on log and core analyses, the thickness of Red River Formation with greater than 10% porosity was calculated in all the wells for which production data was available (Variable 3, Tables 1-A and 2-A). A similar compilation of strata with greater than 10% porosity was made for the Interlake Formation throughout the Cabin Creek Field (Variable 4). A total thickness of reservoir rock with greater than 10% porosity was also calculated in all wells by adding those values obtained for the Interlake and Red River Formations (Variable 5). The Interlake Formation has a mean of 127 feet with greater than 10% porosity while the Red River formation has a mean of only 34 feet (Table 2-A). Thus the total thickness of reservoir rock with greater than 10% porosity is mostly made up of Interlake Formation.

Using information from the well logs, the depths below sea level to the top of the two reservoir formations were measured (Variables 1 and 2, Table 1-A and 2-A). This information was used to construct structure contour maps on the formations' tops (Figs. 2-A and 3-A).

Computer Mapping and Correlation Study

The variables listed in Table 1-A were plotted on contour maps which covered much of the Cabin Creek Field (Figure 1-A). The plots were generated by computer using the computer graphics program SURFACE II (developed by the Kansas Geological Survey).

TABLE 3-A Correlation Matrix

	1.RR	2.IL	3.PFRR	4.PFIL	5.PF TOTAL	6.OIL64	7.WATER 64	8.GAS64	9.PROD 64	10.OIL 80	11.WATER 80	12.GAS 80	13.PROD 80	14. RATIO	15.DIFF
1.RR	1.0000														
2.IL	.9550	1.0000													
3.PFRR	-.0468	-.1299	1.0000												
4.PFIL	.0368	.1745	-.2296	1.0000											
5.PFTOTAL	.0525	.1679	.0356	.9598	1.000										
6.OIL64	.6315	.7118	.0390	.1320	.1654	1.0000									
7.WATER64	-.1504	-.0559	.2371	.0411	.1033	.1211	1.0000								
8.GAS64	.6448	.7035	-.0860	.1616	.1555	.7697	-.2006	1.0000							
9.PROD64	.6262	.7216	.0406	.1588	.1906	.9652	.2141	.8511	1.0000						
10.OIL80	.3226	.3097	.0315	.0758	.0959	.6500	.1022	.4573	.6143	1.0000					
11.WATER80	-.0702	-.0122	.0864	.0432	.0655	.3520	.4219	.0785	.3432	.6432	1.0000				
12.GAS80	.6096	.6151	.0079	.0486	.0571	.7272	-.1462	.8744	.7837	.6074	.1541	1.0000			
13.PROD80	.2192	.2525	.0738	.0388	.0618	.6161	.2480	.4331	.6163	.8822	.8722	.5658	1.0000		
14.RATIO	-.3411	-.4315	.1176	-.0493	-.0230	-.3052	.0123	-.2569	-.2929	.4278	.3464	-.0378	.3660	1.0000	
15.DIFF	-.1384	-.2342	-.0045	-.0183	-.0248	-.0528	-.0026	-.0872	-.0701	.7156	.5000	.1454	.5823	.8316	1.0000

Figures 2-A and 3-A are the structure contour maps drawn on the top of the Red River and Interlake Formations respectively. The similiarity of the plots together with the high linear correlation of the depths to the top of the two formations in each well (0.955, Table 3-A) shows that the surfaces of the two reservoir formations are virtually parallel across the field.

Figures 4-A and 5-A are contour maps of the reservoirs showing thickness of strata with greater than 10% porosity. There is no obvious pattern to porosity distribution in either formation reflecting the general unpredictability and heterogeneity of pore distribution typical of carbonate reservoirs.

Contour maps showing oil, water and gas production prior to and during water flood were also generated (Figure 6-A to 12-A inclusive). These maps delineate the individual zones of the Cabin Creek Field where highs in production occurred during primary and secondary recovery. Production data was available only for wells down the central axis of the field and so the maps generated are slightly longer and more narrow than the structure contour or porosity maps (Figure 1-A).

The correlation matrix given in Table 3-A shows the degree of linear correlation between the variables defined for this study. The correlation matrix was calculated using MIDAS (Michigan Interactive Data Analysis System), a program of the Michigan Terminal System (M.T.S.) which is used at Rensselaer Polytechnic Institute.

Obvious correlations exist (0.6 to 0.7 and higher) between the production of oil and gas prior to April 1964, and during water flood.

There is very little correlation (0.4) between high water production prior to April 1964 and wells with high water production during water flood, however, a correlation of 0.6 occurs between the production of water and oil during water flood.

The most interesting lack of linear correlation occurs between the production of oil, water and gas and the thickness of porous reservoir rock. Correlation coefficients of 0.16 and 0.09 respectively, relate production of oil during primary and secondary recovery to thickness of reservoir rock with greater than 10% porosity. Similar low correlation is shown for both gas and water during primary and secondary recovery and thickness of porous reservoir rock (Table 3-A).

The most interesting correlation occurs between the amount of oil and gas produced and the height of the reservoir above sea level (correlation coefficients of 0.6 for the Red River Formation and 0.7 for the Interlake Formation). From this it can be concluded that the best production of oil and gas from the Cabin Creek Field during both primary and secondary recovery is found on the structural highs regardless of the thickness of reservoir rock with greater than 10% porosity.

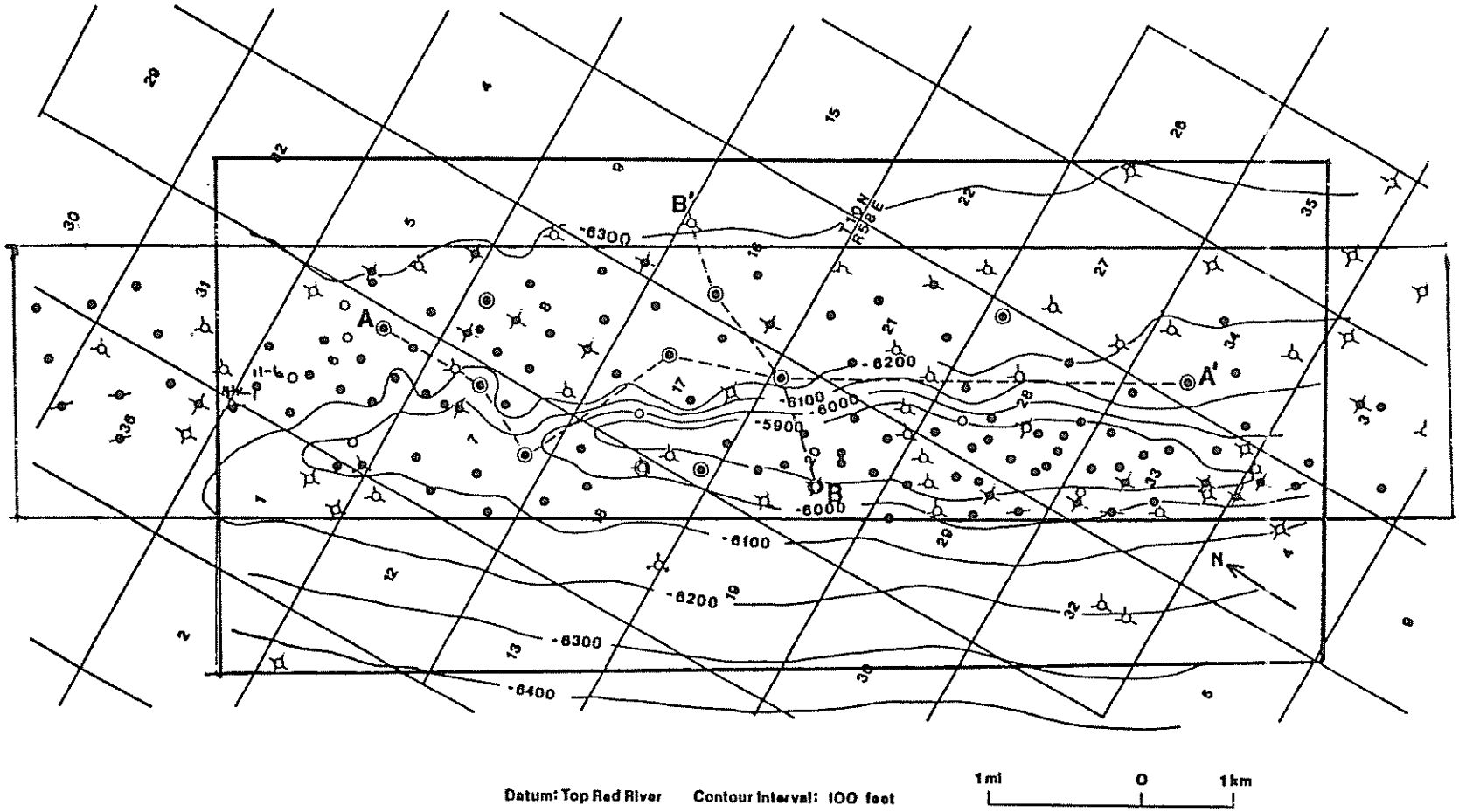

FIGURE 1-A: Structure contour map (hand produced) of Cabin Creek Field showing location of wells and areas covered by figures.

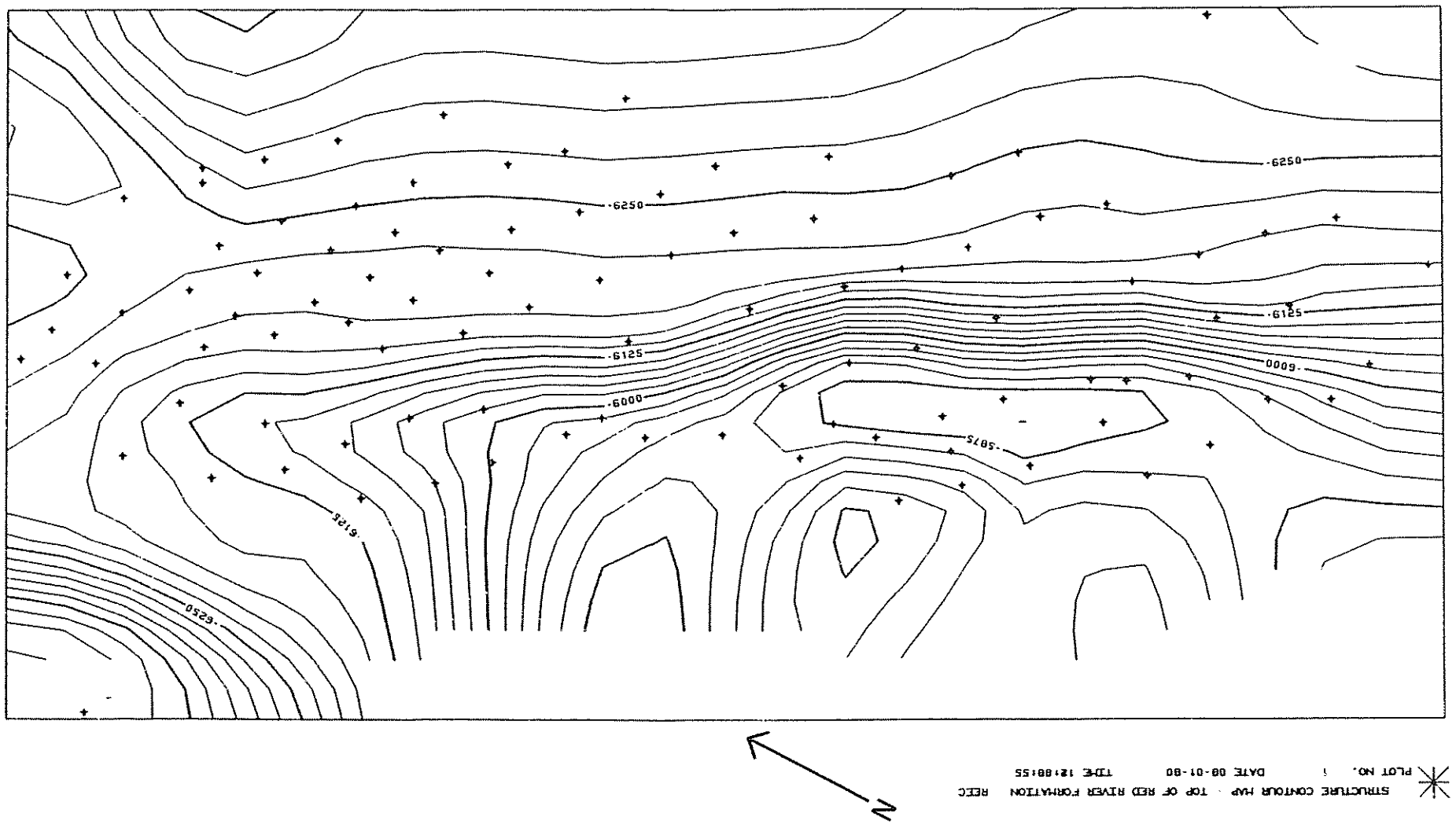

FIGURE 2-A: Computer-generated structure contour map of top of Red River Formation.

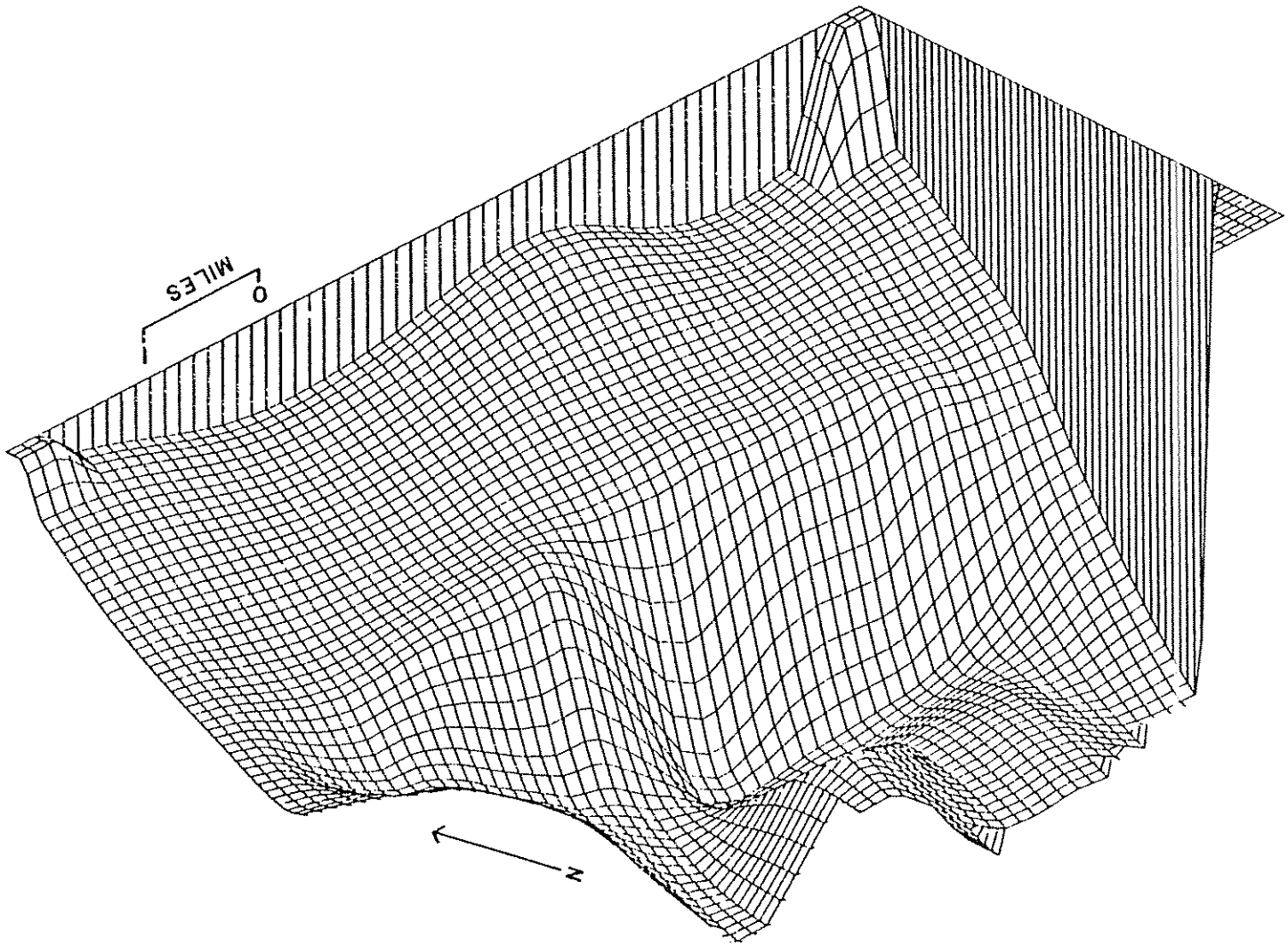

FIGURE 2-A Supplement: 3-D block diagram showing structure of the top of the Red River Formation.

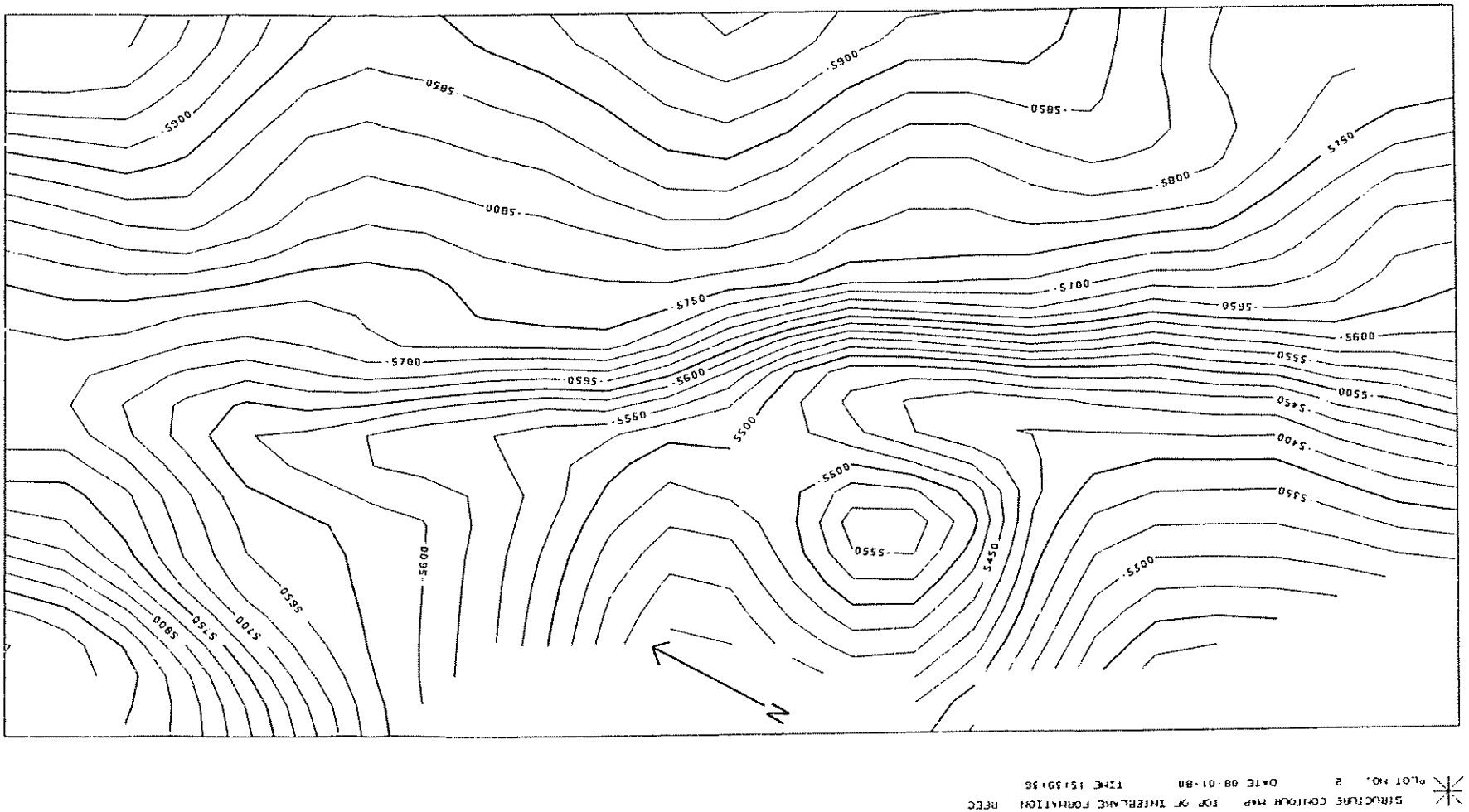

FIGURE 3-A: Structure contour map of the top of the Interlake Formation.

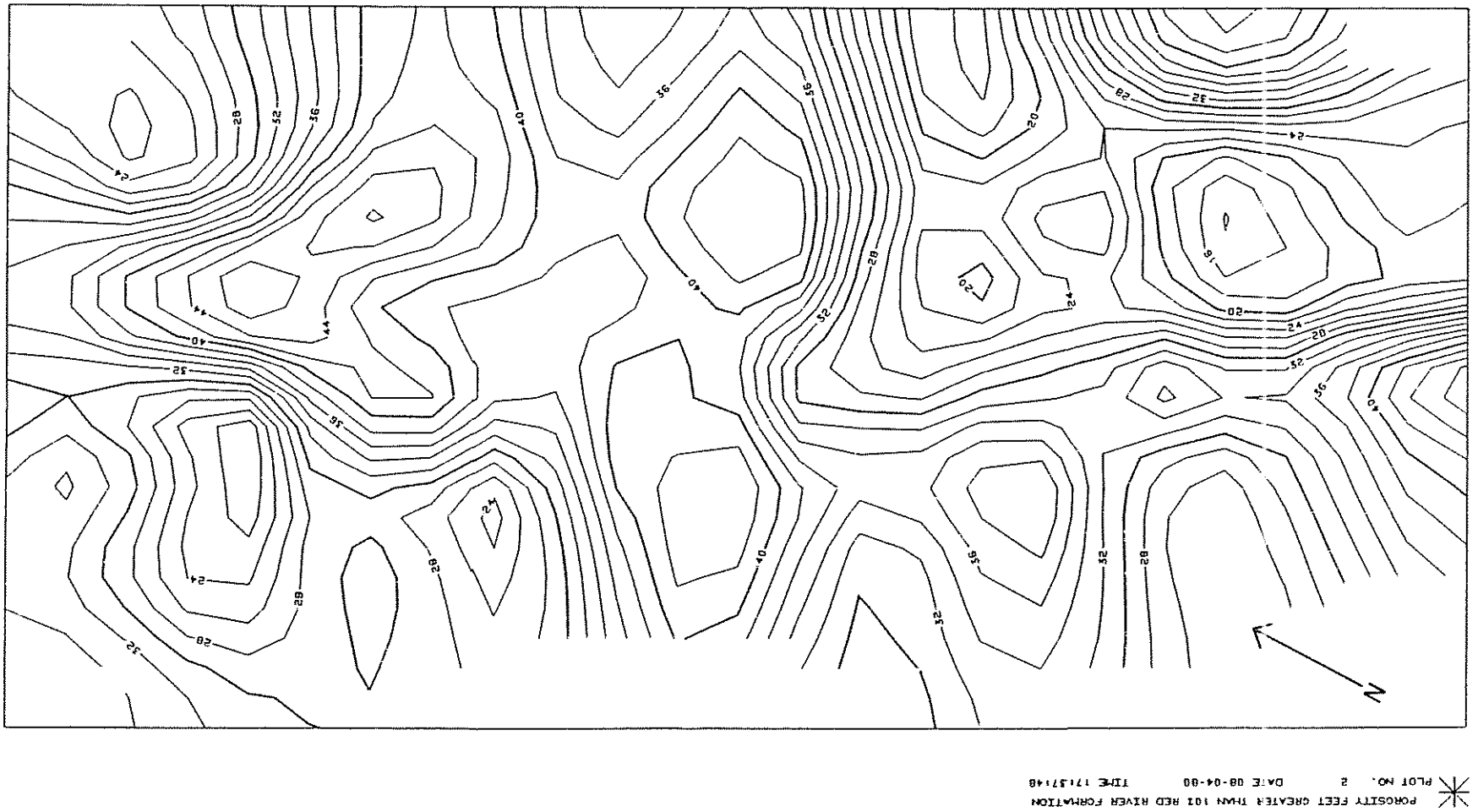

FIGURE 4-A: Map showing feet of Red River Formation having greater than 10% porosity.

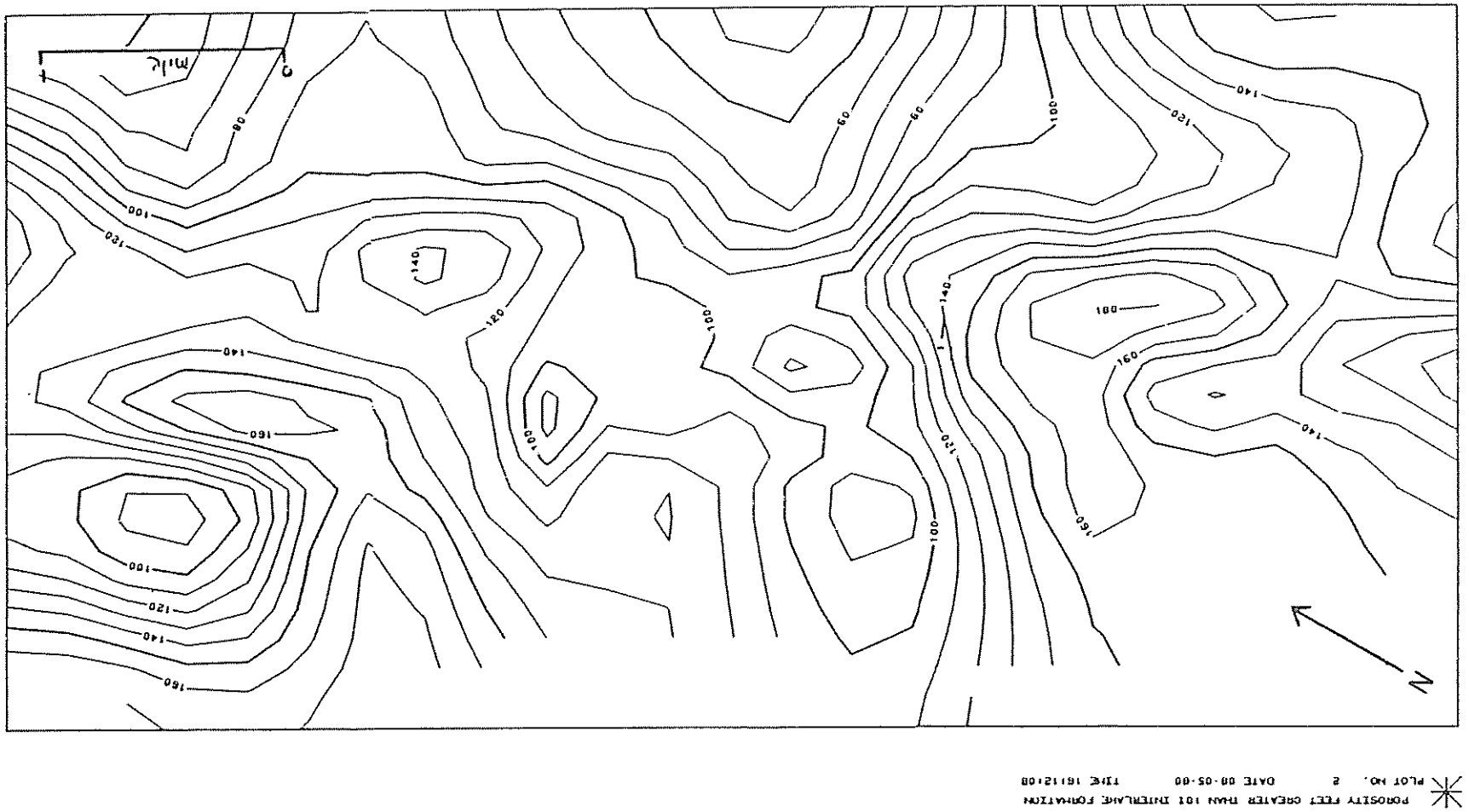

FIGURE 5-A: Map showing feet of Interlake Formation having greater than 10% porosity.

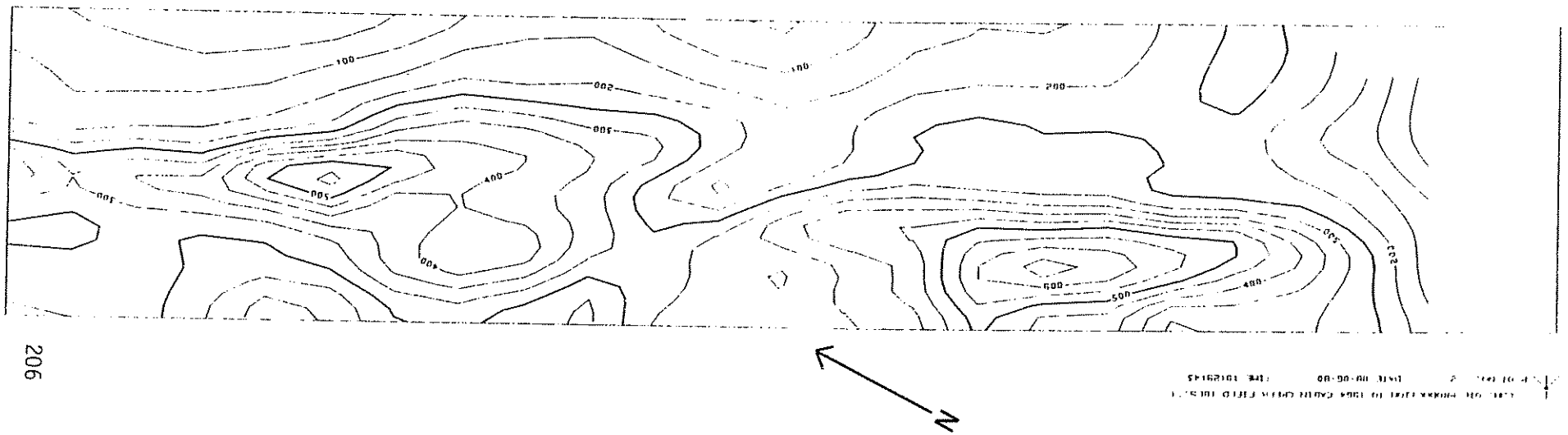

FIGURE 6-A: Map showing cumulative oil production in Cabin Creek Field up to 1964 (prior to waterflood). Contour lines indicate barrels X 10^3.

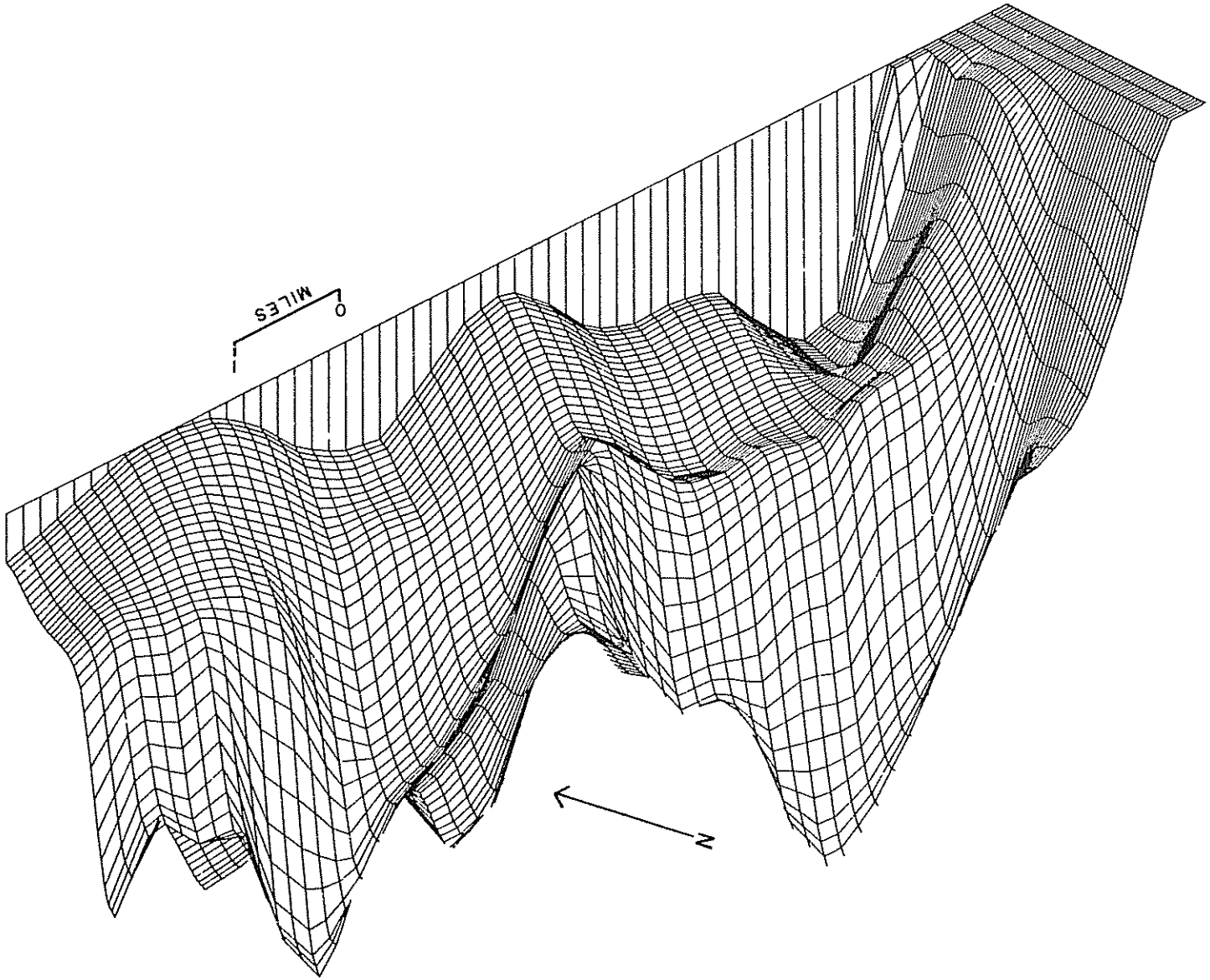

FIGURE 6-A Supplement: 3-D block diagram showing cumulative oil production from Cabin Creek Field prior to water flood (1964 and earlier).

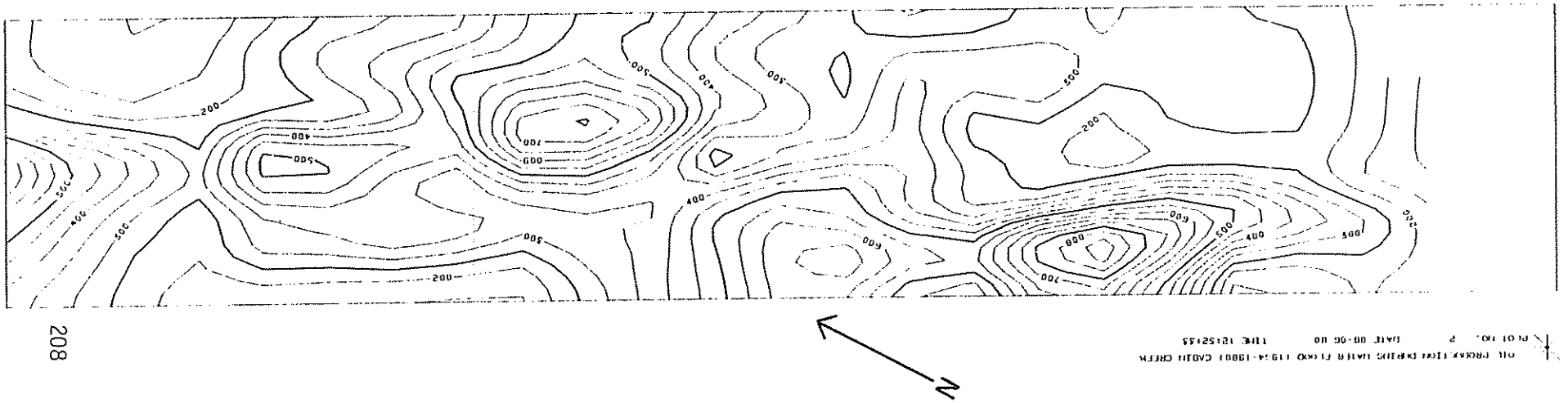

FIGURE 7-A: Map showing oil production during water flood (1964-1980) at Cabin Creek Field (in barrels X 10^3).

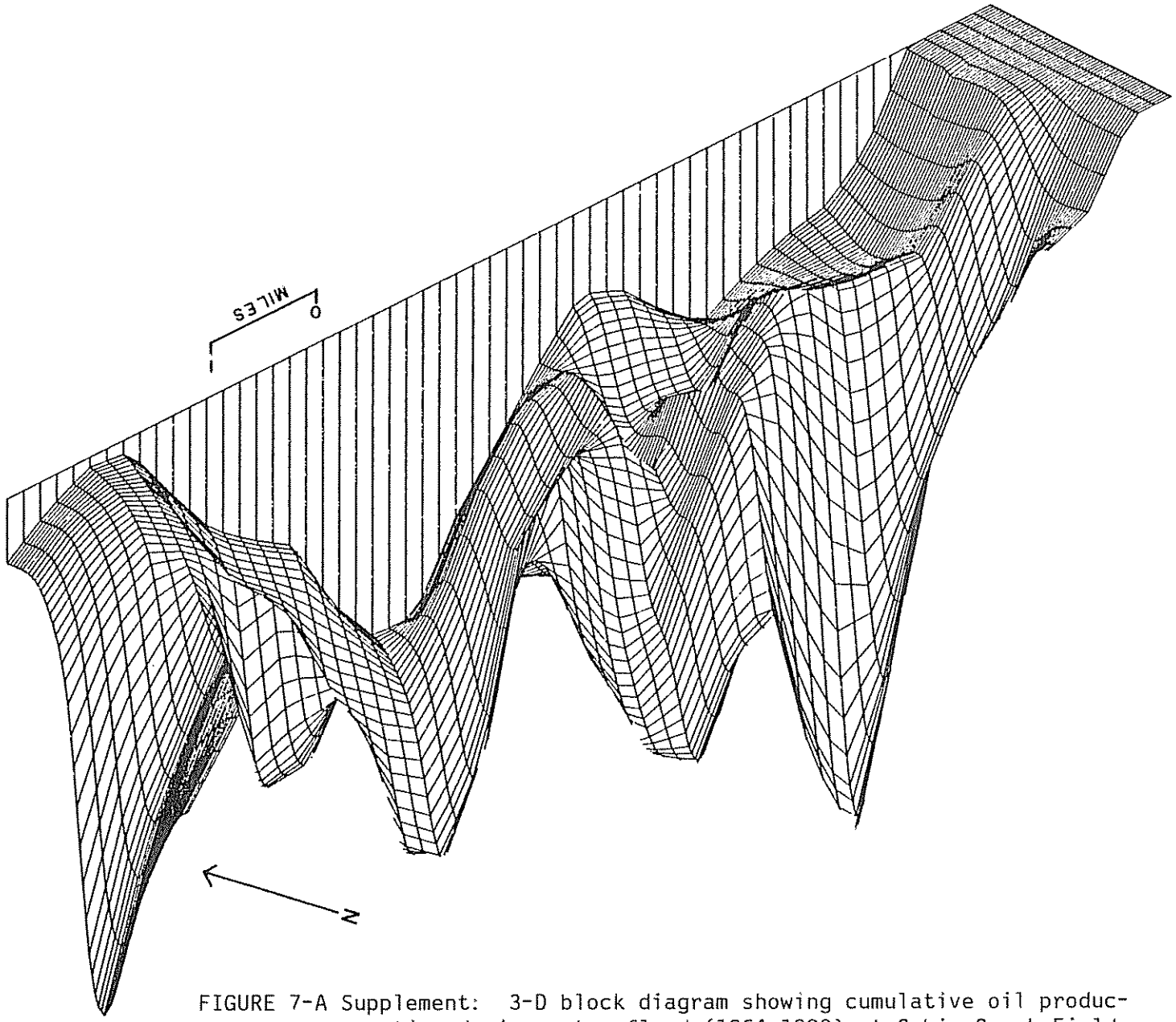

FIGURE 7-A Supplement: 3-D block diagram showing cumulative oil production during water flood (1964-1980) at Cabin Creek Field.

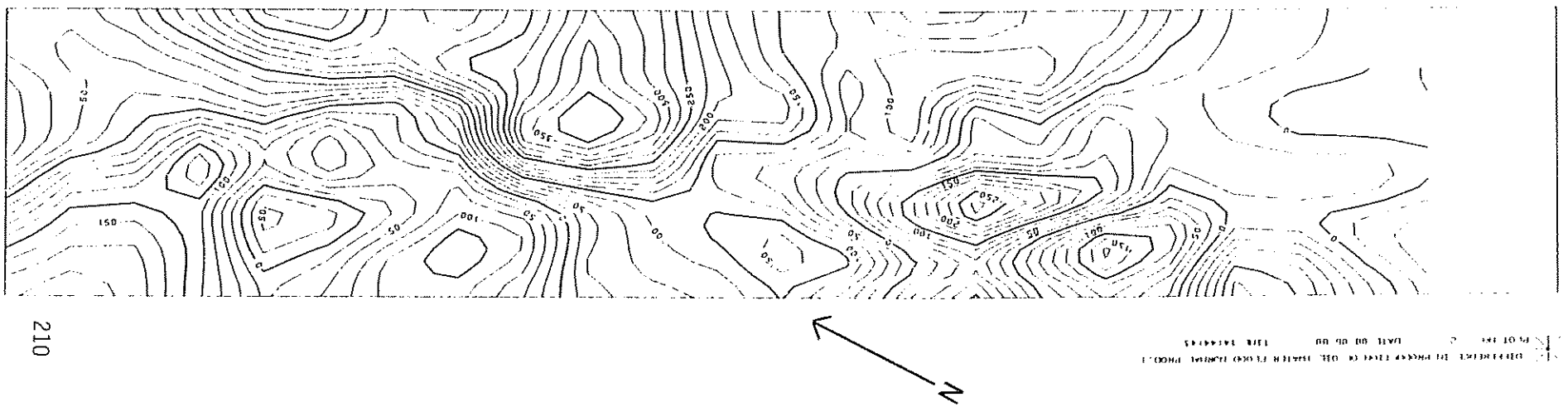

FIGURE 8-A: Map showing difference in production of oil by primary and secondary methods at Cabin Creek Field (water flood recovery minus primary recovery in barrels X 10^3).

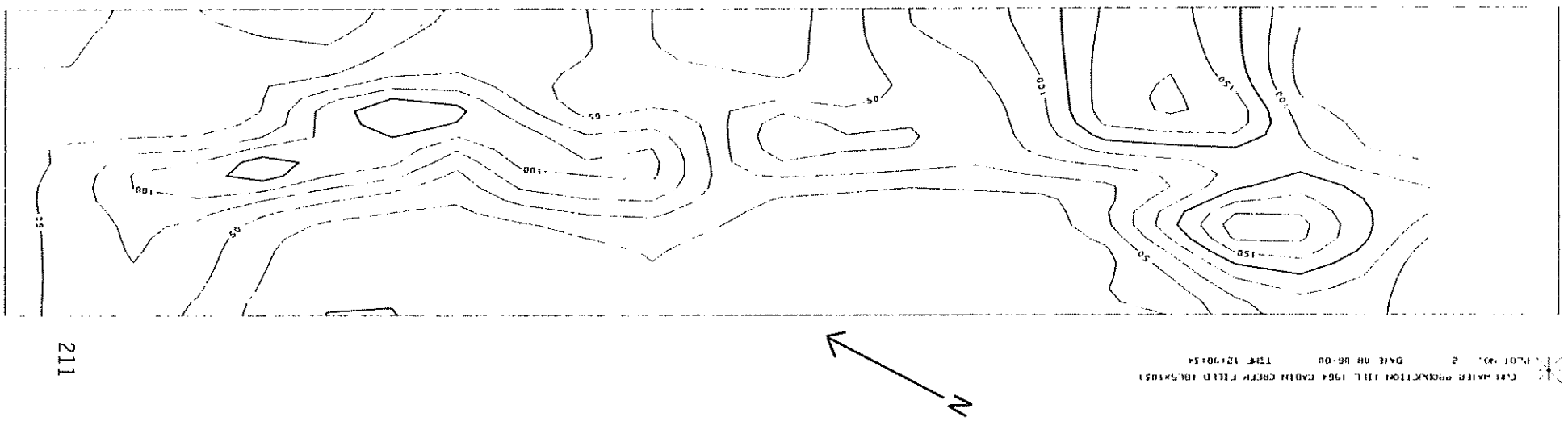

FIGURE 9-A: Map showing cumulative water production (in barrels X 10^3) in Cabin Creek Field prior to water flood.

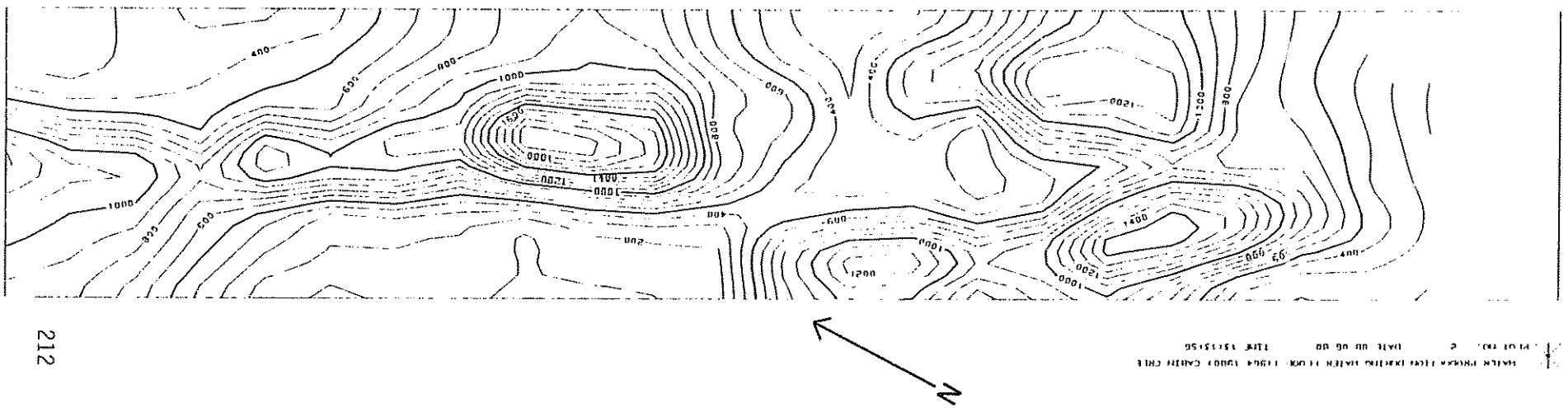

FIGURE 10-A: Map showing cumulative water production (in barrels X 10^3) in Cabin Creek Field during water flood (1964-1980).

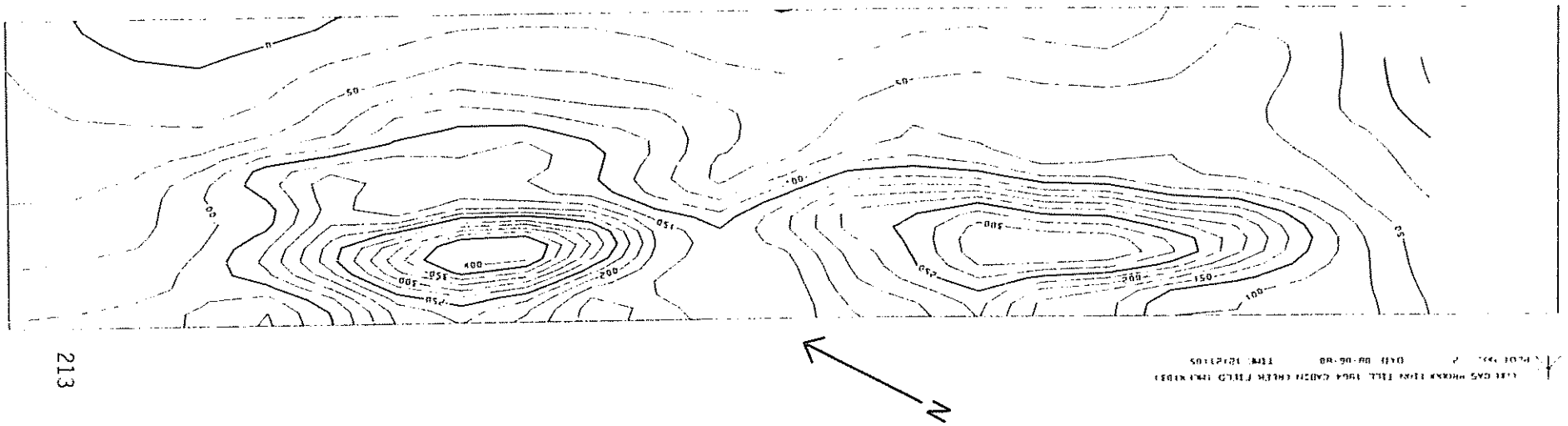

FIGURE 11-A: Map showing cumulative gas production (in MCF X 10^3) in Cabin Creek Field prior to water flood.

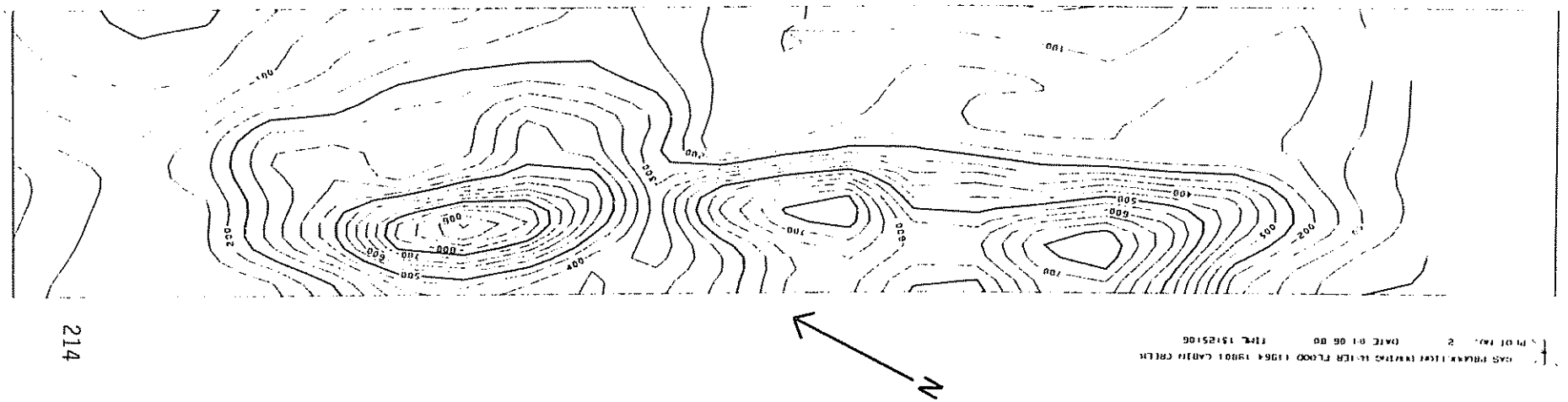

FIGURE 12-A: Map showing cumulative gas production (in MCF X 10^3) in Cabin Creek Field during water flood (1964-1980).

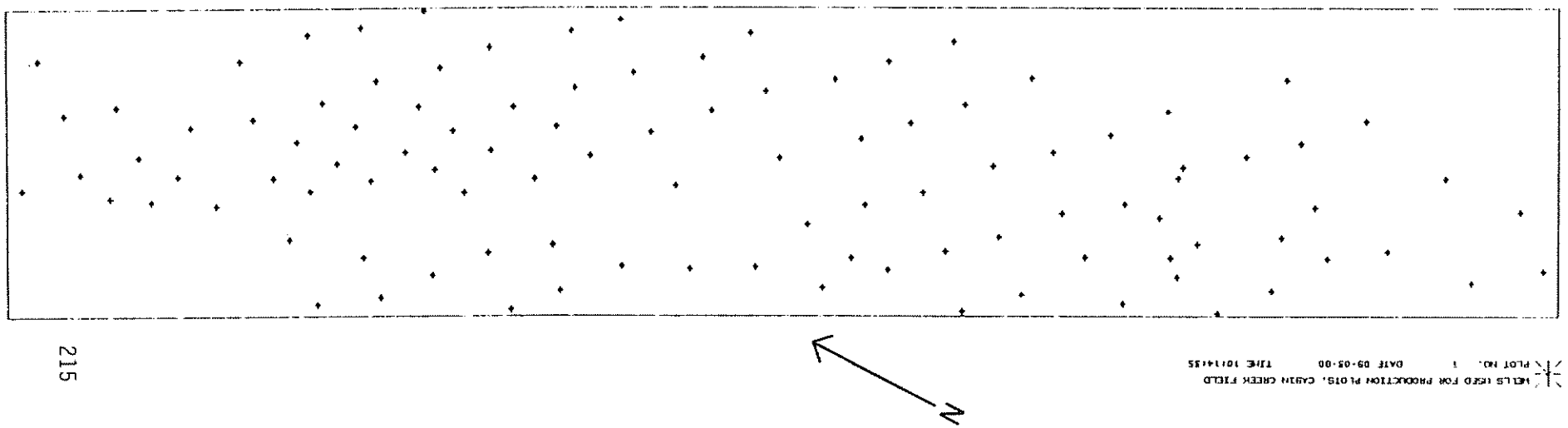

FIGURE 13-A: Map showing wells used for production plots in Cabin Creek Field.

Location map and overlay for figures 2A, 3A, 4A, and 5A

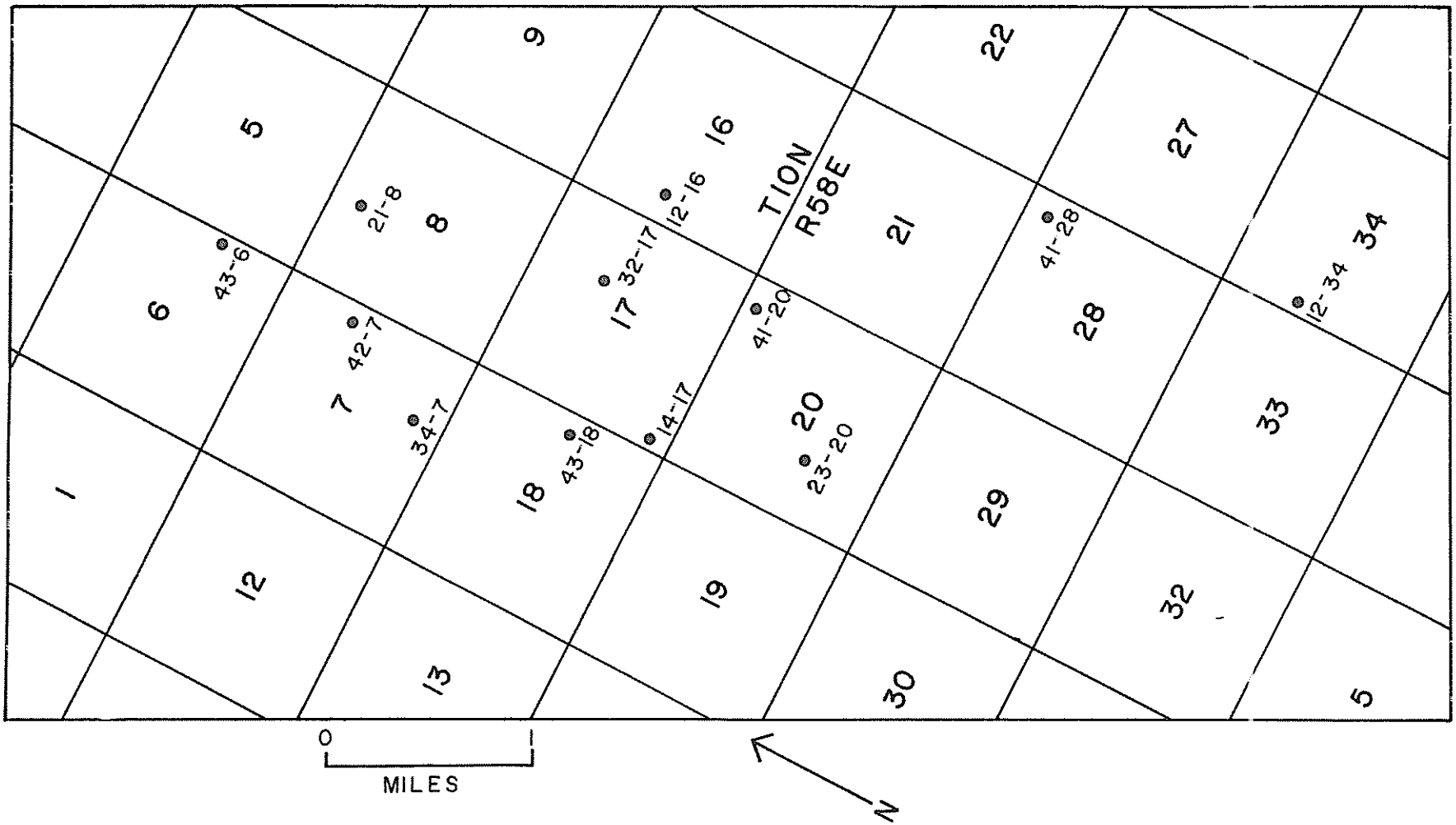

Location map and overlay for figures 6A, 7A, 8A, 9A, 10A, 11A, 12A, and 13A

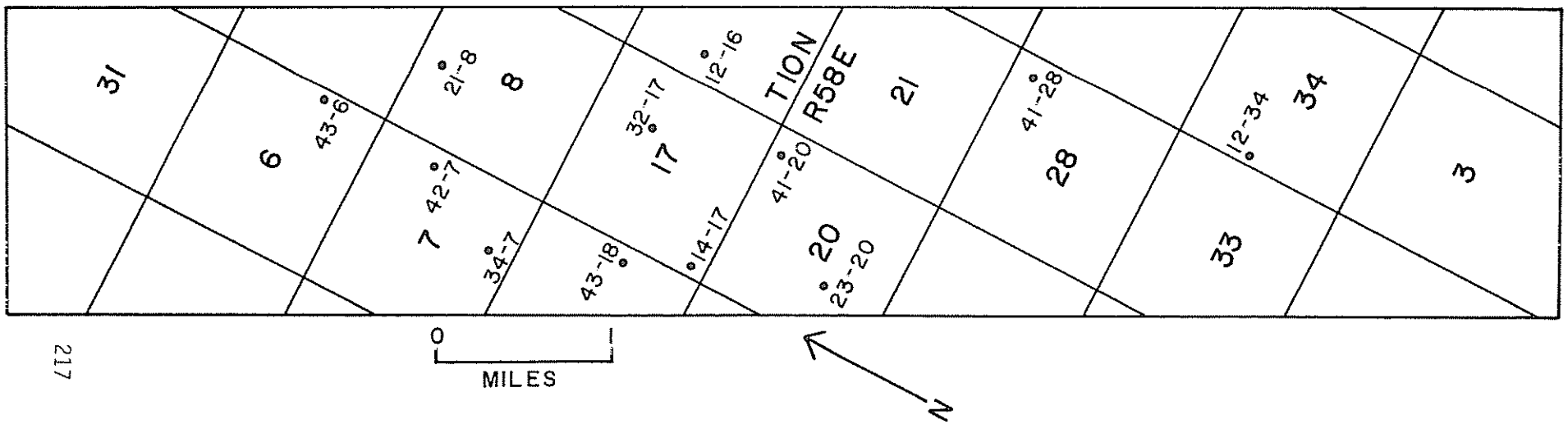

☆ U.S. GOVERNMENT PRINTING OFFICE: 1981—771-031/85